THE UNIVERSITY OF QUEENSLAND

AUSTRALIA

Numerical investigation of conjugate heat transfer and temperature-dependent viscosity in non-Brownian suspensions with application to hydraulic fracturing

Jon William Shaw McCullough

BE(Mechanical, Hons 1)

BSc(Mathematics)

A thesis submitted for the degree of Doctor of Philosophy at The University of Queensland in 2018

School of Mechanical and Mining Engineering

Abstract

Particle suspensions are relevant in a number of scientific and engineering fields, where they can occur at a wide range of scales. Examples of these include blood flow, flood debris, crystal formation, mineral processing plants and pharmaceutical production. One particular application occurs within the hydraulic fracturing process used in the oil and gas industry. Here, a fracturing fluid with a solid proppant component (typically sand) is pumped into a reservoir to increase low permeability. The fluid pressure fractures the reservoir allowing transport of proppant within the rock. On removal of the fluid, the proppant prevents the closure of fractures leading to increased reservoir permeability and enhanced production of hydrocarbons. To meet ongoing demand for fossil fuels, a growing number of unconventional oil and gas reservoirs are being exploited. One example of this is the coal seam gas industry that has emerged in Queensland, Australia. To facilitate continuing improvement of the hydraulic fracturing performance, the ongoing development of modelling techniques to better understand the physical processes occurring during a treatment is an important goal.

The performance of a hydraulic fracturing treatment depends on the physical properties (e.g. density, viscosity) of the fluid to transport the proppant throughout the fracture network and maximise the permeability of the reservoir. Temperature variations from the surface to the reservoir, via the well, can alter these properties and result in unexpected performance of a fracturing operation. Current models for hydraulic fracturing fluids often simplify aspects of the fundamental physics that occurs within the suspension such as heat transfer between components, thermal variation of physical properties, or the physical geometry of the solid component. This work seeks to capture the behaviour of hydraulic fracturing fluids under thermal influences through a more detailed modelling approach.

This thesis presents the development, evaluation and application of a coupled numerical framework for particle suspension modelling using a thermal lattice Boltzmann method (TLBM) for the fluid component and the discrete element method for the solid component. The thermal behaviour of both components is also accounted for using the lattice Boltzmann method. Studies conducted in this research examine a range of topics including methods for conjugate heat transfer, flows with temperature-dependent viscosity, numerical rheometry, and flows within idealised fracture geometries.

Initially, this work develops a 2D model using a passive scalar interpretation of the double distribution function TLBM. A local and a non-local method for the calculation of conjugate heat transfer between disparate media have been included within the model. This allows a more accurate representation of the transient thermal behaviour within a multicomponent system to be captured. However, 2D studies of modelling fluids with temperature-dependent viscosity show that a total energy

formulation of TLBM is necessary to capture these flows accurately. This is demonstrated through comparison to analytical results for a Couette flow with an imposed temperature gradient. The change in viscosity is also demonstrated to have an impact on the transport of particles suspended within such fluids. To ensure conjugate heat transfer can still be captured, this is also implemented for the total energy based formulation.

The developed model is extended to 3D to study the rheometry of sheared suspensions. Model performance is verified against flow of a single particle through fluid and compared against validated correlations for the relative viscosity observed in suspensions experiencing shear. Within a fluid featuring temperature-dependent viscosity, the perturbation of the velocity field within the numerical rheometer due to the presence of particles is reduced in areas of thinner fluid. Temperature profiles became non-linear due to viscous heating stemming from the presence of particles. This increased when conjugate heat transfer was allowed to take place within the flow.

To complete the research, the model is applied to case studies of suspension flow through three proppant transport problems. These relate to settling in a straight fracture and transport through leaking or stepped geometries. In all cases, the results for a fluid with temperature-dependent viscosity are compared to a constant-viscosity fluid to identify variations in behaviour. The settling velocity of particles in a straight fracture is observed to significantly increase in the presence of temperature-dependent viscosity. In the leaking geometry, temperature-dependent viscosity is observed to reduce the number of particles travelling along the side channel. The stepped geometry is used to demonstrate how blockages may develop in practice. In all cases, a reduction of particle size illustrates the particle motion becoming dominated by the fluid flow.

This work demonstrates the potential of the developed model in providing new insights on the micromechanics of suspension flows in the presence of temperature gradients. In conjunction with continued model development, future applications in the area of hydraulic fracturing include assessment of graded proppant injection, non-Newtonian carrier fluids, and particle straining in porous media.

Declaration by author

This thesis is composed of my original work, and contains no material previously published or written by another person except where due reference has been made in the text. I have clearly stated the contribution by others to jointly-authored works that I have included in my thesis.

I have clearly stated the contribution of others to my thesis as a whole, including statistical assistance, survey design, data analysis, significant technical procedures, professional editorial advice, financial support and any other original research work used or reported in my thesis. The content of my thesis is the result of work I have carried out since the commencement of my higher degree by research candidature and does not include a substantial part of work that has been submitted to qualify for the award of any other degree or diploma in any university or other tertiary institution. I have clearly stated which parts of my thesis, if any, have been submitted to qualify for another award.

I acknowledge that an electronic copy of my thesis must be lodged with the University Library and, subject to the policy and procedures of The University of Queensland, the thesis be made available for research and study in accordance with the Copyright Act 1968 unless a period of embargo has been approved by the Dean of the Graduate School.

I acknowledge that copyright of all material contained in my thesis resides with the copyright holder(s) of that material. Where appropriate I have obtained copyright permission from the copyright holder to reproduce material in this thesis and have sought permission from co-authors for any jointly authored works included in the thesis.

Publications included in this thesis

1. McCullough, J. W. S., Leonardi, C. R., Jones, B. D., Aminossadati, S. M. and Williams, J. R. (2018) Investigation of local and non-local lattice Boltzmann models for transient heat transfer between non-stationary, disparate media, Computers and Mathematics with Applications, *In press*, Submitted 28/03/17, Revisions submitted 06/11/17, Accepted 20/01/18, `https://doi.org/10.1016/j.camwa.2018.01.018`.

2. McCullough, J. W. S., Leonardi, C. R., Jones, B. D., Aminossadati, S. M. and Williams, J. R. (2016) Lattice Boltzmann methods for the simulation of heat transfer in particle suspensions, International Journal of Heat and Fluid Flow, vol. 62, part B, pp. 150-165.

Submitted manuscripts included in this thesis

No manuscripts submitted for publication.

Other publications during candidature

Peer-reviewed Papers

1. Leonardi, C. R., McCullough, J. W. S., Wang, D., and Aminossadati, S. M. (2018) Evaluation of the temperature-dependent rheology of non-Brownian particle suspensions via direct numerical simulation, 21st Australasian Fluid Mechanics Conference, Adelaide, 10-13 December 2018, Paper accepted 2 October 2018.

2. McCullough, J. W. S., Leonardi, C. R., Jones, B. D., Aminossadati, S. M. and Williams, J. R. (2018) Investigation of local and non-local lattice Boltzmann models for transient heat transfer between non-stationary, disparate media, Computers and Mathematics with Applications, *In press*, Submitted 28/03/17, Revisions submitted 06/11/17, Accepted 20/01/18, `https://doi.org/10.1016/j.camwa.2018.01.018`.

3. McCullough, J. W. S., Leonardi, C. R., Jones, B. D., Aminossadati, S. M. and Williams, J. R. (2016) Lattice Boltzmann methods for the simulation of heat transfer in particle suspensions, International Journal of Heat and Fluid Flow, vol. 62, part B, pp. 150-165.

4. Leonardi, C. R., Regulski, W., McCullough, J. W. S., Wang, D., Mitchell, T.R., Jones, B. D., and Williams, J. R. (2016) Characterising the behaviour of hydraulic fracturing fluids via direct numerical simulation, SPE-182458-MS, SPE Asia Pacific Oil & Gas Conference and Exhibition 2016, Perth, 25-27 October 2016.

Conference Abstracts and Presentations

1. McCullough, J. W. S., Leonardi, C. R. and Aminossadati, S. M. (2018) An LBM-DEM study of the shearing thermo-rheology of dense particle suspensions. 27^{th} International Conference on Discrete Simulation of Fluid Dynamics (DSFD 2018), Worcester (USA), 25-29 June 2018.

2. McCullough, J. W. S., Leonardi, C. R. and Aminossadati, S. M. (2017) Capturing the transient characteristics of thermally varying particle suspensions. V International Conference on Particle-Based Methods (PARTICLES 2017), Hannover (Germany), 26-28 September 2017.

3. McCullough, J. W. S., Leonardi, C. R. and Aminossadati, S. M. (2017) An analysis of approaches for including temperature dependent viscosity within the thermal lattice Boltzmann method. 14^{th} International Conference for Mesoscopic Methods in Engineering and Science (ICMMES 2017), Nantes (France), 17-21 July 2017.

4. McCullough, J. W. S., Leonardi, C. R. and Aminossadati, S. M. (2017) Modelling temperature dependent viscosity in particle suspensions using the lattice Boltzmann method. 26^{th} International Conference on Discrete Simulation of Fluid Dynamics (DSFD 2017), Erlangen (Germany), 10-14 July 2017.

5. McCullough, J. W. S., Leonardi, C. R., Jones, B. D., Aminossadati, S. M. and Williams, J. R. (2016) Transient heat transfer modelling at straight and curved interfaces of disparate media using DDF-TLBM. 13^{th} International Conference for Mesoscopic Methods in Engineering and Science (ICMMES 2016), Hamburg (Germany), 18-22 July 2016.

6. McCullough, J. W. S., Leonardi, C. R., and Aminossadati, S. M. (2015) Application of thermal lattice Boltzmann methods at fluid-solid interfaces, 2^{nd} Australasian Conference on Computational Mechanics (ACCM2015), Brisbane (Australia), 30 November – 1 December 2015.

Other Papers

1. Faff, Robert W. and Babakhani, Nazila and Carrick, Robin and Chen, Angel and Dallest, Kathy and Daunt, Lisa and Escobar, Marisol and Foley, Gabe and Gill, Chelsea and Khong, Bo Xuan and Liu, Maggie and Mahmud, Siti and McCullough, Jon and Ndugwa, Zina and Nguyen, Bao and O'Brien, Shari and Orole, Felix and Qureshi, Asma and Rad, Hossein and Rekker, Saphira and Shahzad, Syed and Smith, Marita and Tran, Tran Le and Tunny, William and Wallin, Ann, Motivating Postgrad Research Students to Pitch Their Ideas: What Have We Learned from 'Pitching Research' Competitions at UQ? (January 15, 2017). Available at SSRN: `https://ssrn.com/abstract=2899942`.

2. Faff, Robert W. and Gill, Chelsea and McCullough, Jon and Noh, Jae-Eun and Mahmud, Siti and Ndugwa, Nakazinga and Eats, Patricia and Gorji, Sara, Book of Pitches: UQAPS 2015 Pitching Research Competition Final (April 17, 2017). Book of Pitches: UQAPS 2015 Pitching Research Competition Final, UQ Busness School, 2017. Available at SSRN: `https://ssrn.com/abstract=2953842`.

Contributions by others to the thesis

- Dr Christopher Leonardi - Initial directions of research, refinement of project design, revision of written content in capacity as Principal Advisor.
- A/Prof Saiied Aminossadati - Revision of written content in capacity as Associate Advisor.
- Dr Lukasz Llaniewski-Wollk - Developing the coupling between the open-source TCLB and ESyS-Particle codes. This was further developed and utilised in the work conducted in Chapters 5 and 6.
- Dr Bruce Jones - Revision of written content in capacity as co-author of publications included in Chapters 2 and 3.
- Prof John Williams - Revision of written content in capacity as co-author of publications included in Chapters 2 and 3.

Statement of parts of the thesis submitted to qualify for the award of another degree

No works submitted towards another degree have been included in this thesis.

Research Involving Human or Animal Subjects

No animal or human subjects were involved in this research.

Acknowledgements

For those who have completed a PhD, it is well understood that, whilst attributed to an individual, there are many supporting roles that get filled along the road to its completion. This work has been no different.

I would firstly like to thank the academic advisors for my PhD at UQ: Dr. Christopher Leonardi (principal) and Associate Professor Saiied Aminossadati (associate). Your assistance along the way, no matter how big or small, has always been gratefully received. In particular, Chris I wish to thank and acknowledge your optimism, encouragement and general good opinion of my work; particularly when I was not sharing these views. I have enjoyed working under your guidance.

To my various officemates at UQ, thank you for experiencing the PhD journey with me. Our time spent in solving each other's research problems, or finding a distraction from them, has been much appreciated. Particular thanks go to Travis Mitchell, Ed Hay, Amin Kamyar and Duo Wang.

During 2017 I was fortunate enough to spend three months on research visits to Germany and the USA. I would like to thank the Institute for Computational Modelling in Civil Engineering (Institut für rechnergestützte Modellierung im Bauingenieurwesen) at Technische Universität Braunschweig and the Geonumerics Group at Massachusetts Institute of Technology for making me feel welcome within your groups. In particular thanks to Professor Manfred Krafczyk and Anna Wedler (TUB) and Professor John Williams and Dr Bruce Jones (MIT) for permitting my visits and assisting with the organisation of them. Thank you also to Professor Martin Geier and Stephan Lenz for sharing your office with me in Braunschweig and to Dr Bruce Jones, Sam Raymond, Dr Fabian Spreng and Dr Ranjan Pramanik for extending the same favour at MIT.

The Australian Petroleum Production and Exploration Association (APPEA) K.A. Richards Scholarship provided me with means to travel overseas a number of times during my PhD for conferences and research visits. These have allowed me to develop both professionally and personally. I'd like to thank the APPEA group for the opportunities afforded by this scholarship.

I would also like to acknowledge and thank Dr Lukasz Llaniewski-Wollk (TCLB) and Dr Dion Weatherley (ESyS-Particle) for their instruction and guidance for using their respective codes. Special thanks should go to Lukasz for his work in coupling the two codes together into a usable framework - something I wouldn't have been able to achieve alone in the time I had available.

Finally, I would like to thank my family: my parents, Peter and Marcia, and brothers, Harry and Seb. For being sounding boards to talk to, making me laugh, ongoing patience and everything else along the way. Thank you so much, I cannot say it enough.

Financial Support

This research was supported by an Australian Government Research Training Program Scholarship.

This research was supported by the School of Mechanical and Mining Engineering, The University of Queensland.

This research was supported by a Graduate School International Travel Award (GSITA) provided by the Graduate School of The University of Queensland.

This research was supported by the Australian Petroleum Production and Exploration Association (APPEA) K.A. Richards Scholarship.

This work was supported by resources provided by The Pawsey Supercomputing Centre with funding from the Australian Government and the Government of Western Australia.

These contributions are all gratefully acknowledged, without which this research would not have been possible.

Research classifications

Keywords

thermal lattice Boltzmann method, particle suspensions, transient analysis, hydraulic fracturing, proppant transport, suspension rheology

Australian and New Zealand Standard Research Classifications (ANZSRC)

ANZSRC code: 091406, Petroleum and Reservoir Engineering , 25%

ANZSRC code: 091501, Computational Fluid Dynamics, 35%

ANZSRC code: 091502, Computational Heat Transfer, 40%

Fields of Research (FoR) Classification

FOR code: 0914, Resources Engineering and Extractive Metallurgy, 25%

FOR code: 0915, Interdisciplinary Engineering, 75%

To those who believed when I did not

Contents

List of Figures

List of Tables

Chapter 1

Introduction

Much of the development of humankind over the past 200 years can be attributed to the exploitation of fossil fuel reserves. Oil and gas has not only provided the energy to drive the development of industry and the spread of personal transport to the greater populace but also the raw material needed for the plastics prevalent throughout today's society. In Australia, approximately 62% of total energy consumption in 2014-15 originated from oil and gas resources [1]. Such is the dependence on these finite resources that, even though there is a general consensus that their use is contributing to changes in climate, there is a drive to ensure that the access and production of these continues into the medium term. One option for doing this is to develop ways of economically obtaining oil and gas resources from reserves that had not previously been considered viable, otherwise known as uncoventional resources.

The term 'conventional resources' is generally applied to reservoirs that produce oil or gas once a well has been drilled into it without the need for further adaptation (see Figure 1.1). In these reservoirs, the pressure at which the hydrocarbons are stored is sufficient, once released, to drive material to the surface and beyond for further processing and transport to consumers. The traditional oil and gas producing regions of the world e.g. the Persian Gulf states, southern USA and the Gulf of Mexico; are all based on the development of conventional resources. Further driving the interest in the development of unconventional resources is the fact that the productiveness of reservoirs diminishes as material is removed due to the background pressure reducing to an equilibrium state. This fact is becoming more important as the production from some historical sites are declining.

Unconventional reservoirs are those that require some level of artificial modification in order for them to produce hydrocarbon resources effectively. This requirement is generally due to the source rock having a low permeability that inhibits the flow of oil or gas out of the reservoir. From a mechanical point of view this is often due to the oil or gas being physically trapped, or chemically bonded,

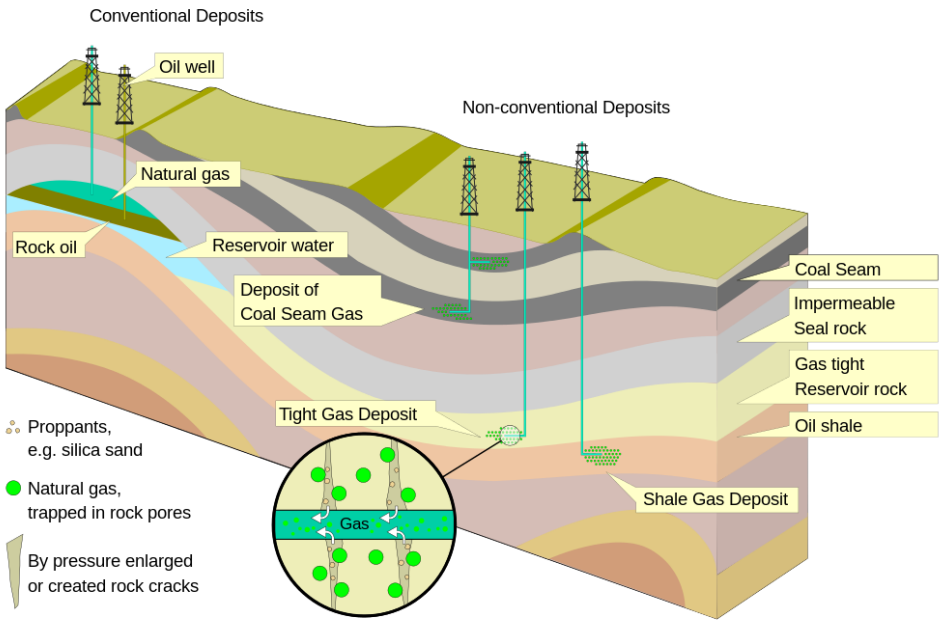

Figure 1.1: Schematic diagram of a range of conventional and unconventional hydrocarbon reservoirs. Image from [2]

.

in the pore spaces within the reservoir rock. In contrast, conventional reservoirs may be highly permeable formations that readily permit flow of oil or gas but this is trapped by surrounding layers of impermeable material. Common formations that contain unconventional gas include coal seams, shale and some sandstones (see Figure 1.1). The depth at which these latter two may be found is another contributing factor to the challenges associated with extracting these resources. Whatever the situation, the economic case for being able to make use of unconventional resources is based on being able to artificially alter the properties of such reservoirs to a point where the trapped hydrocarbons are able to flow in useful quantities. With respect to increasing permeability, hydraulic fracturing is one method of achieving such an outcome.

From an Australian point of view, the development of coal seam gas (CSG) reserves in Queensland is a local example of the utilisation of unconventional resources. These are particularly focused in the Bowen and Surat Basins that stretch through central and southern QLD (see Figure 1.2) with early production commencing in 1996 [3]. Capitalisation of these resources has been the driving force behind recent growth in Australian natural gas production. This has occurred to such an extent that CSG contributed 18% of national gas production in 2014-15 [1]. New wells and export facilities meant that this figure represented an annual increase of 50% to a value of 462PJ. This growth has continued with QLD CSG fields producing a total of 1,358PJ across 5,759 wells in the year to 30

June 2017 [4]. This made Australia the second largest exporter of liquefied natural gas behind Qatar in 2015 [5]. By way of comparison, Australian conventional resources produced a total of 705PJ in 2014-15, with this figure reducing annually due to the age of the fields. It is estimated that, as production continues, up to 40% of CSG wells may require hydraulic fracturing to remain viable [6].

On a global scale, the production from unconventional shale gas plays throughout the USA since the mid-2000s has meant that it will likely become a net energy exporter within the next 10-15 years [7]. Shale gas reservoirs have been identified in a number of basins spread across the country. These are, in particular, located east of the Rocky Mountains as shown in Figure 1.3. The production of shale gas has increased by a factor of five in the last decade to a current annual production level of around 17,500PJ [7]. This is predicted to more than double again by 2050, with most of this occurring in the north-eastern states [7]. In 2016, it was estimated that about 84% of USA onshore oil and gas wells were hydraulically fractured to some extent [8]. An illustration of the rate of hydraulic fracturing procedures performed in USA wells is given in Figure 1.4. Note that this data is valid for the 12 months to September 2010 [9]. Whilst somewhat out of date, it does illustrate regions where the technique is being used.

It is also important to distinguish between CSG and shale gas. CSG refers to the gas stored within coal seams themselves. It is often the water that is also trapped in the coal that inhibits the natural flow of gas from a seam [11]. Once dewatered, the gas will generally flow naturally. Despite this, hydraulic fracturing is still necessary for CSG production. This is related to the low and variable porosity of coal across regions. Shale, on the other hand, refers to a sedimentary rock layer that consists of fine-grained earth material such as mud, silt, clay and some organic matter [12]. Compression of these substances leads to a material with very low natural permeability. Stimulation of shale through hydraulic fracturing is generally required. This will also be true for any future production of Australian shale gas resources.

1.1 The hydraulic fracturing process

The hydraulic fracturing process is used to increase the permeability of unconventional reservoirs and better enable trapped hydrocarbons to be extracted. The first use of hydraulic fracturing as a production tool occurred in 1949 [13]. The technology developed rapidly over the following decades, particularly in the USA, for it to become a widely used method today. In a simple description of the process, a slurry mixture is pumped into an unconventional reservoir well prior to production. This slurry is largely composed of water carrying solid proppant particles (often sand but other materials are also used due to properties of strength or shape composition). Extra chemicals may be added to

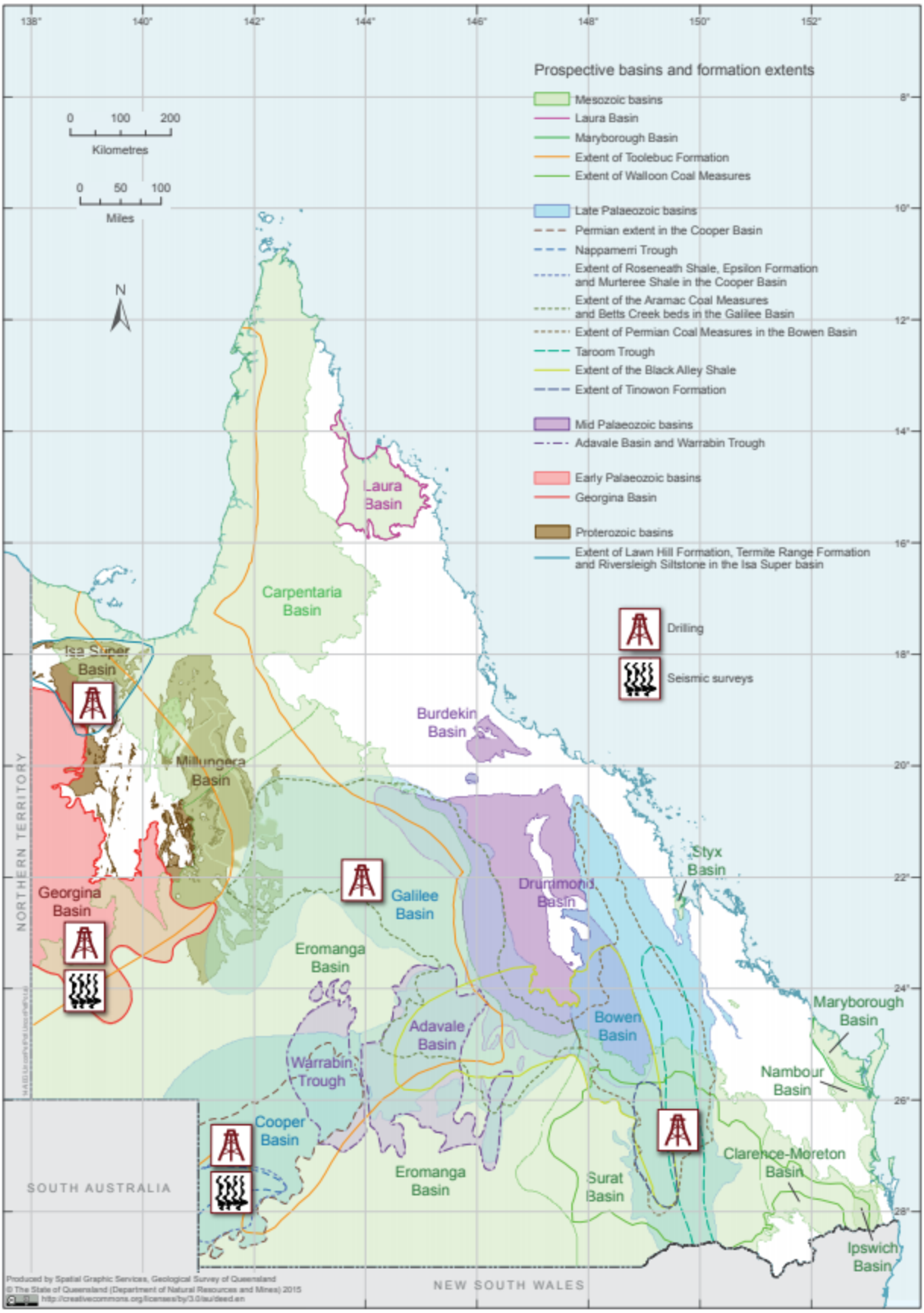

Figure 1.2: Identified geological basins throughout QLD, Australia. Significant CSG production has occurred in the Bowen and Surat Basins in central and southern QLD. Image from [3].

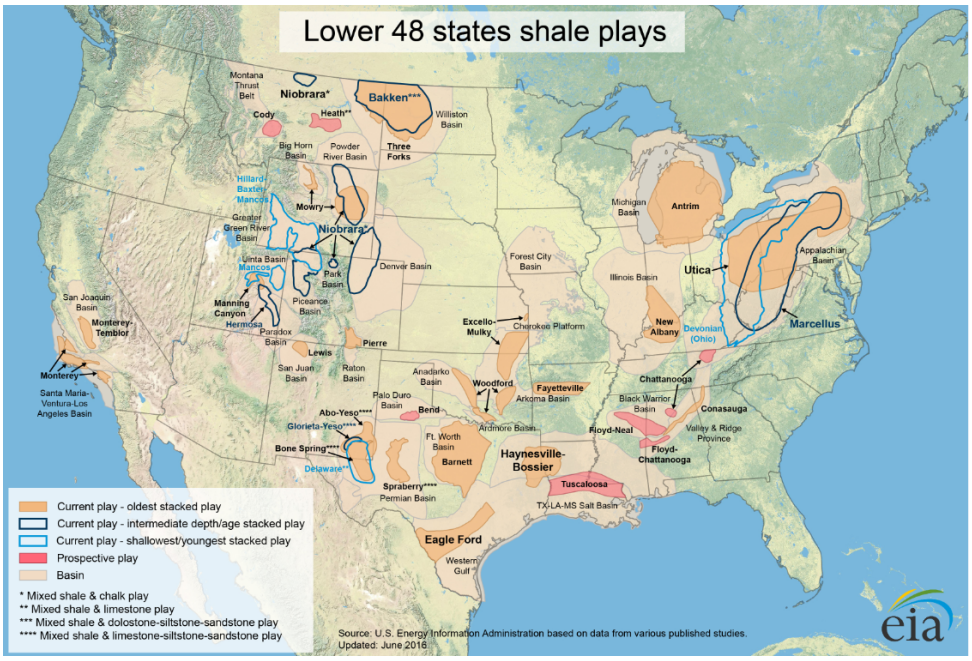

Figure 1.3: Shale gas basins located throughout the conterminous 48 states of USA. Image from [10].

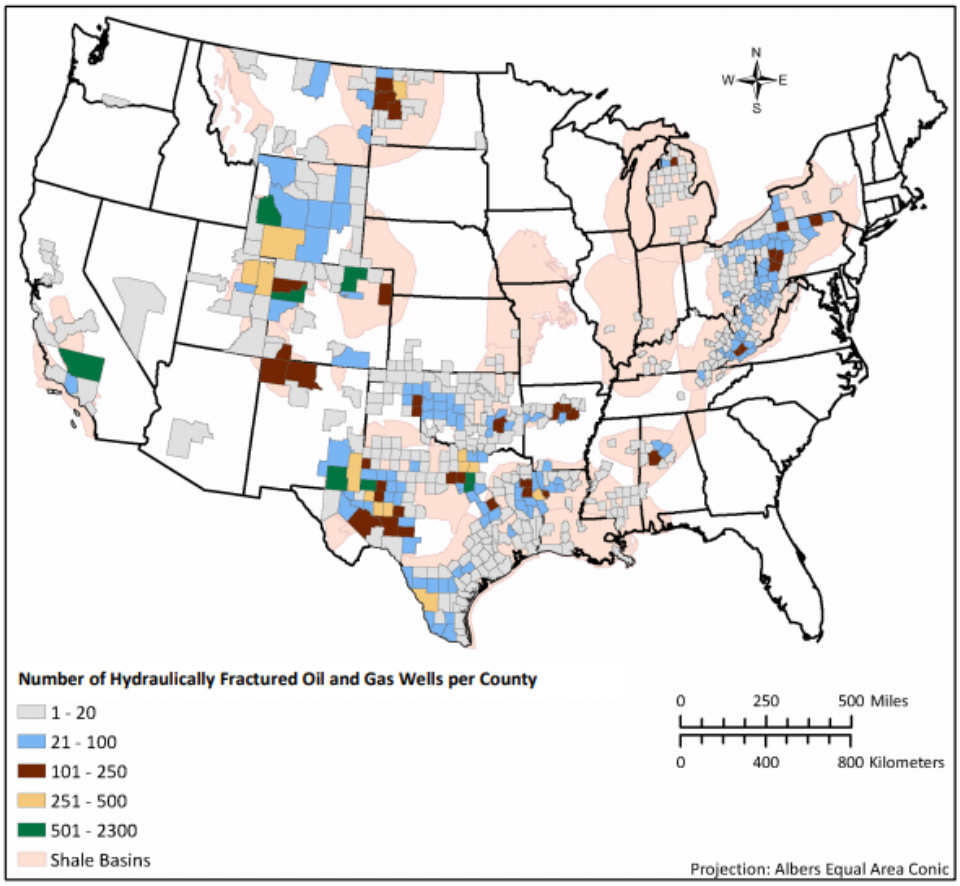

Figure 1.4: County based rates of hydraulic fracturing throughout the conterminous 48 states of USA. This map was derived from data in the 12 months to September 2010. Image from [9].

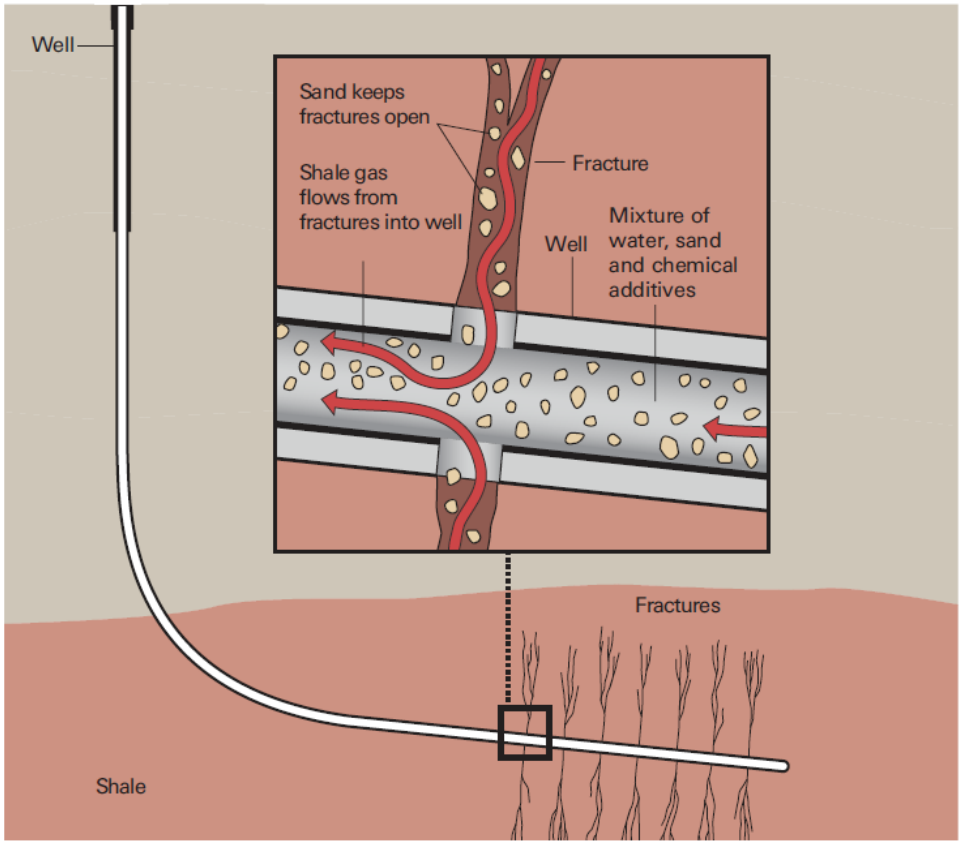

Figure 1.5: Generalised schematic of a producing shale gas well after a hydraulic fracturing treatment. Image source from [12], original source Al Granberg (ProPublica). The fractures are generated by pumping fluid into the reservoir at high pressure at specially initiated locations called perforations.

the mixture to enable it to achieve desired performance characteristics relating to proppant transport and longevity of piping. The induced pressure generates fractures within the reservoir that increases its overall permeability. On removal of the fluid component the proppant remains to hold the fractures open and permit the flow of oil and gas. Pumps may then be used to ensure that the produced material reaches the surface. A schematic of a producing well after a hydraulic fracturing treatment is presented in Figure 1.5.

In practice however, the hydraulic fracturing procedure is more detailed. The process begins through the drilling of a well into the source reservoir. This may often be done directionally (i.e. the well intentionally veers away from vertical and may reach a fully horizontal orientation) to help maximise the volume of reservoir being accessed. At predetermined locations within the reservoir, explosive charges are then used to perforate the wellbore casing and initiate fractures within its surrounds. These are propagated deeper into the reservoir by pumping an initial pad of fluid. Since the reservoir being treated is permeable to some degree, fluid can be naturally absorbed into it. This mostly occurs at the fracture tip in a process termed ‘leak-off’. To overcome this, fluid must be con-

tinuously pumped at sufficient rates to ensure that sufficient pressure is maintained for fractures to grow. Once fractures are large enough, the proppant laden slurry mixture is introduced to the treatment. A combination of fluid flow and settling causes the proppant to be transported and placed along the length of the fracture. A final fluid volume is used to remove unused proppant from the wellbore. Prior to production commencing, the well is 'shut-in'. This gives remaining fluid in the fracture a chance to leak-off or be removed to the surface in a 'flowback' operation. As this occurs, the fractures close on the placed proppant. The proppant's purpose is to prevent full closure of the generated fracture and provide a more permeable pathway through the reservoir to the wellbore. A typical fracture generated by this process may be on the order of tens or even hundreds of metres long but only a few millimetres wide. These may require a few hours of pumping before shut-in occcurs in order to be created. These summaries have been modified from [13, 11, 12].

Ultimately, the purpose of a hydraulic fracturing treatment is to increase the surface area of the reservoir that has a free pathway to the wellbore. Maximising this quantity increases the volume of material that is able to escape from the pore space of the unconventional reservoir and be extracted to the surface. In addition to its use in making unconventional reservoirs productive, Economides and Nolte [13] note that hydraulic fracturing may also be employed in conventional reservoirs. It can be used to negate the impact of drilling damage near a wellbore, enhance production by creating new pathways for hydrocarbons to flow through or alter flow routes as part of a greater reservoir management plan.

1.2 Design and modelling of hydraulic fracturing fluids

1.2.1 Composition of hydraulic fracturing fluids

The total volume of a typical hydraulic fracturing treatment consists of approximately 95% fluid, 4% proppant and the remaining portion as chemical additives [11, 12]. The additives generally serve the purpose of preventing corrosion and modifying the viscosity of the fluid [11, 12]. During the proppant injection stage, localised solid volume fractions of 30% or greater may be observed within the system.

The fluid component of the hydraulic fracturing process is the component most amenable to modification and performance optimisation. Early pioneers of hydraulic fracturing experimented with numerous fluids including crude oil and combinations of napalm and petroleum [13]. In modern treatments, such fluids may include water, 'slickwater' - water with friction reducing agents, or a water-gel mixture [11]. Pumping a thinner slickwater has advantages relating to the energy required to transport the fluid through the well and extracting it once the treatment is complete. A thicker

water-gel mixture, however, is better suited to generating fractures and transportation of proppant [13]. Balancing these two design requirements has led to complex treatment strategies with differing mixes of components to achieve an optimal completion.

Sand has been used as proppant since it was first included in fracturing treatments [13]. The main functional requirements of proppant are that it is robust enough to support the closing pressure of the fracture and that this compressed pack is significantly more permeable than the reservoir. Sand remains a popular choice as it is cheap and widely available. Synthetic proppants, manufactured from ceramics or other suitable materials, provide a more uniform particle size than sand [13, 11]. The size of proppant particle used is another consideration in the design, planning and scheduling a fracturing treatment. Larger proppant particles create more permeable fractures but require larger initial fractures to flow through [13]. However, larger particles are also relatively weaker and settle faster than smaller counterparts [13]. Proppant choice is, ultimately, a balance between costs of use and production returns gained.

1.2.2 Characterisation of hydraulic fracturing fluids

The performance of the fluid component is arguably the most important aspect in the effectiveness of a hydraulic fracturing treatment. In *Reservoir Stimulation*, edited by Economides and Nolte [13], it is observed that characterisation of hydraulic fracturing fluids is needed for:

- additive and system development
- obtaining input data for use in fracture design simulators
- quality control before or during treatment.

This is reiterated in *Effective and Sustainable Hydraulic Fracturing*, edited by R. Jeffrey [14], where several performance characteristics are noted. These need to be taken into account when a fluid is being designed and include the geometry of the created fracture, the rate at which leak-off occurs, safety concerns for operators and the environment, flowback characteristics and cost. Both sources, however, recognise that the viscosity of the fluid is the most significant physical characteristic of the fluid relating to treatment performance.

A fluid is rheologically classified as Newtonian if the shear stress generated in the fluid is linearly proportional to shear rate. In this case, the viscosity of the fluid describes the proportionality constant. Non-Newtonian fluids may exhibit changing viscosity with shear rate or possess a yield stress that needs to be overcome before the fluid flows. In many hydraulic fracturing treatments, the rheology of the fluid is controlled through the use of additives in the base water. This leads to fluids that can be

strongly non-Newtonian with respect to shearing rate, temperature and/or chemical composition. The most common modelling assumption of non-Newtonian fluids is that viscosity changes with shear rate, $\dot{\gamma}$, in a power law model as,

$$\mu = \bar{K}\dot{\gamma}^n, \tag{1.1}$$

where the constants $\bar{K}$ and n respectively represent a consistency coefficient and the degree of shear thinning ($n < 1$) or thickening ($n > 1$). Newtonian behaviour occurs when $n = 1$. Proppant concentration is also another factor that can significantly impact the apparent viscosity of hydraulic fracturing fluid. This has been studied widely in the literature with some of the earliest work done by Albert Einstein [15] who applied a linear change in viscosity for a dilute particle fraction. Other models that account for higher particle fractions have also been developed for application to non-Newtonian fluids [16]. Figure 1.6 illustrates the change in viscosity due to particle volume fraction as predicted by the Krieger-Dougherty model cited in [16] and compares this to the Einstein model modified for non-Newtonian fluids by Laven and Stein, also noted in [16].

Prior to being marketed to industry, a campaign of laboratory experiments is performed to develop reference data describing the fluid's behaviour [13, 14]. Tests conducted aim to both gather basic information on the viscosity change of the fluid, usually through the use of a 'cup and bob' rheometer. This apparatus contains the fluid between a rotating cup and stationary bob held at its centre [13, 14]. The torque experienced by the bob is used to infer the fluid's viscosity. By testing at various shear rates, these experiments provide empirical values for coefficients in fluid rheology models. For example, the coefficients $\bar{K}$ and n of a power law fluid can be found from,

$$\mu_{apparent} = \frac{C\bar{K}}{\dot{\gamma}^{1-n}}. \tag{1.2}$$

Here, $\mu_{apparent}$ is the viscosity measured by the rheometer and C is a constant related to the units of measurement being used. Plotted on a log-log scale of shear rate against shear stress, n is the slope of the data points and $\bar{K}$ the intercept on the shear stress axis [13, 14]. Independent testing and experimentation may still be required for practitioners to determine the fluid characteristics being displayed within a given hydraulic fracturing treatment. It is recognised though that such bespoke testing can be costly in terms of both dollars and time [13].

Temperature can also significantly affect the behaviour of a fluid. In general, the viscosity of a fluid will decrease with temperature. However, many models assume the fluid to possess properties based on a steady-state reservoir temperature [13, 14]. In practice, the fluid will enter a formation at a relatively cool (surface) temperature and be heated to reservoir temperature over the length of

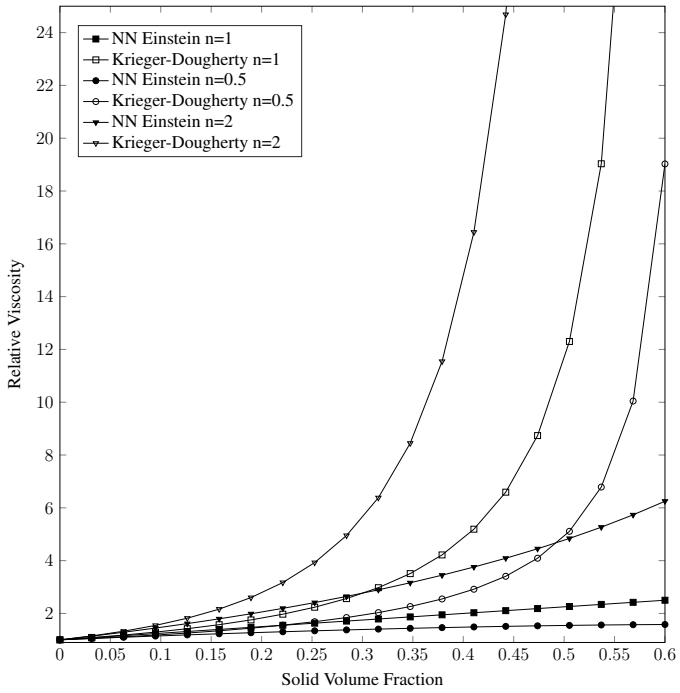

(a) Relative viscosity of concentrated suspensions

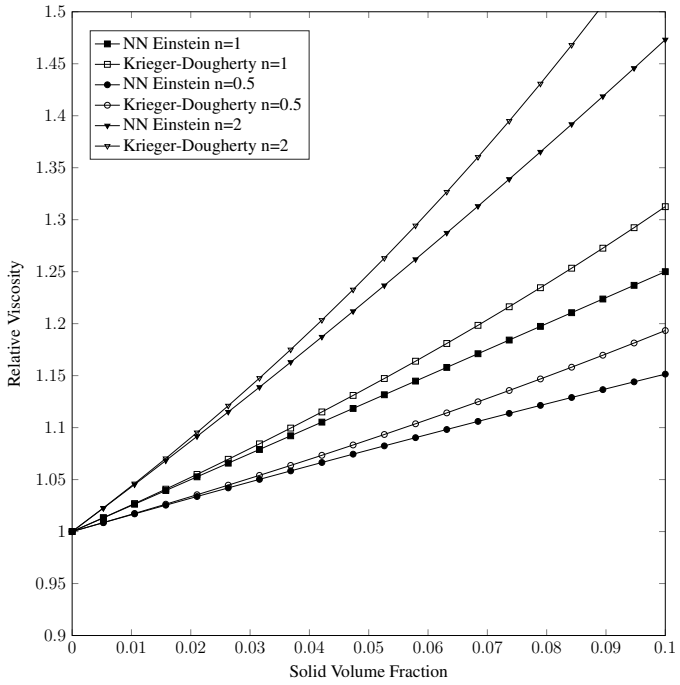

(b) Relative viscosity of dilute suspensions

Figure 1.6: Comparison of relative viscosity of non-Newtonian fluids with the modified Einstein model and the Krieger-Dougherty model described in [16]. Newtonian fluid behaviour is represented by the $n = 1$ cases for comparison. The relative viscosity refers to the magnitude of change induced by particles as compared to the viscosity of the base fluid.

the fracture. Although figures may vary with specific fracture geometry, temperature affects can be a serious consideration for the flow of fracturing fluid in the near-wellbore region. Indeed, depending on the leak-off properties of the system, temperature transience may be present for 50% or more of a fracture's length [13]. The temperature of the fluid also can impact on the chemistry of additives that are used to control fluid behaviour [13]. For example, the compounds may break down at elevated temperatures or reaction rates may vary.

The thermal environment also has an effect on proppant transport. In particular, this relates to the ability of the fluid to carry proppant through the fracture with its changing viscosity [13, 14]. Generally speaking, a reduced viscosity due to temperature means that a particle settles to the bottom of the domain sooner than in an unchanged fluid. Heat transfer effects will also occur between the fluid and proppant, particularly in the transient temperature regions near to the wellbore. Generally, this is not regarded as a significant component of heat transfer within a hydraulic fracturing treatment [13]. However, as the materials science of both the fluid and proppants used in hydraulic fracturing develop, it could become an exploited feature to optimise performance. For example, proppant that takes longer to be heated by the fluid may help to keep the fluid component at a lower temperature for a greater duration of the fracture length. This means that the fluid would maintain a higher viscosity for a longer period and potentially reduce the amount of additives needed for a treatment.

1.2.3 Numerical modelling of hydraulic fracturing fluids

To predict and plan a hydraulic fracturing treatment, experimental calibration data for a fluid is used as input data for a fracture simulator. This allows attributes such as pumping time, rates and volumes to be analysed to generate the desired fracture growth and proppant placement.

The numerical modelling of various aspects of this process were developed with advancing computational abilities through the 1980s [17, 18, 19]. The models developed in these studies were wide in scope with factors such as fracture growth, fluid flow, proppant transport and heat transfer from the surrounding formation all being considered. However, the models are typically finite difference approximations of the fundamental equations to be solved. When these models consider proppant transport, a continuous approximation was used to conform the equations to the finite difference approach. This approach stipulates a proppant concentration term based on volume fraction and views the solid component as an entity dispersed through the fluid rather than being constructed of individual particles [19, 20, 21]. Even in more recent works [22, 23] the fluid flow is solved through a numerical solution of the classical Navier-Stokes equations of,

$$\nabla \cdot \mathbf{v}_f = 0, \tag{1.3}$$

for continuity of fluid velocity ($\mathbf{v}_f$) and,

$$\rho_f \left(\frac{\partial \mathbf{v}_f}{\partial t} + (\mathbf{v}_f \cdot \nabla)\mathbf{v}_f \right) = -\nabla P + \mu_f \nabla^2 \mathbf{v}_f, \tag{1.4}$$

for momentum conservation of a Newtonian fluid. This is used when there is no-slip between solid and fluid components or only the fluid phase is being modelled.

Within a continuous solid model, where gravitational slip may occur between the solid and fluid components, the combined fluid-solid slurry is transported according to,

$$\frac{\partial cw}{\partial t} + \nabla \cdot (cw\mathbf{v}_p) = 0, \tag{1.5}$$

where c is the concentration of the proppant, w the fracture width and $\mathbf{v}_p$ particle velocity [24, 23, 25]. A source term may be added to the right hand side to assist in modelling leak-off [26]. The use of Stokes drag correlations guide the estimation of proppant settling behaviour within the fluid [19, 27] of this approach. In particular, the particle velocity for a small sphere settling in isolation due to gravity, $\mathbf{g}$, in an infinite fluid can be estimated as [21, 23, 25]

$$\mathbf{v}_p = \frac{\mathbf{g}(\rho_p - \rho_f)D^2}{18\mu_f}. \tag{1.6}$$

The diameter of the particle, D, and physical parameters of density, ρ, and dynamic viscosity, μ, are chosen such that the Reynolds number of the flow is smaller than unity. The subscripts of p and f refer to the respective properties of the particle and fluid components. To account for the width of the surrounding fracture and the local proppant concentration, empirical modifications have been proposed with,

$$\mathbf{v}_p = \frac{\mathbf{g}(\rho_p - \rho_f)D^2}{18\mu_f} \left(0.563 \left(\frac{D}{w} \right)^2 - 1.563 \left(\frac{D}{w} \right) + 1 \right) \left(2.37c^2 - 3.08c + 1 \right), \tag{1.7}$$

noted in [26] and,

$$\mathbf{v}_p = \mathbf{v}_f + (1 - c)^{5.65} \frac{\mathbf{g}(\rho_p - \rho_f)D^2}{18\mu_f}, \tag{1.8}$$

cited in [25] as containing the Richardson and Zaki correlation.

The use of these approximations neglects the interacting behaviours that occur between multiple particles within a suspension. For example, a group of particles may clump together and effectively act as a much larger particle and violate the Stokes settling assumptions. Such variations could serve to extend the distance which proppant is transported through a fracture. It was noted by Nolte [20] that the Stoke's law formulations may not be the governing equation needed for the complex fracturing fluids used in industry. Both of these observations were affirmed in the work by Barree and Conway [21]. These authors further used an empirical relation to account for the 'hindered settling' of

a particle within a suspension. The concentration parameter was further used in empirical correlations that govern non-Newtonian behaviours of a system and to control the material properties of the suspension. Although computational performance has improved such that some resolved fluid-particle models have been introduced [28, 22], this approach remains a common strategy in the hydraulic fracturing literature.

From a precise thermodynamics perspective, there will be a conjugate heat transfer (CHT) process controlling the heating of the fluid by the reservoir. This dictates that both the heat flux and temperature are continuous at the interface between the solid and fluid components. This may be simplified to models based on convection and conduction models that can achieve adequate results [13].

The motivation for the inclusion of heat transfer effects from the surrounding formation varies among these early publications. In the work by Ben-Naceur and Stephenson [17] the focus is on how the heat source of the reservoir impacts fracture propagation. The temperature-dependence of the viscosity of the fracturing fluid is included and its effect on proppant transport is noted but received only passing mention in this study.

The problem of fluid temperature distribution along a fracture was considered by Biot *et al.* [18]. This was approached by developing and solving partial differential equations for fluid temperature under the considerations of a growing fracture and leak-off of fluid into the surrounding reservoir. With the focus on temperature, leak-off was modelled as a constant flow of fluid away from the centre of the fracture. This study also treated the proppant as a continuous volume fraction property of the fluid. The impact of this on the thermal conductivity and heat capacity of the suspension occurs using the volume fraction to create a weighted average of the constituent components. These properties are held to be temperature independent however the non-Newtonian rheology of the fluid component does vary with temperature. With temperature only varying along the length of the fracture a linear approximation is found to be valid for a range of fracture growth scenarios and is suggested to be useful for practical application. This model can be described as,

$$T(x) = \begin{cases} \dfrac{T_R - T_W}{0.47} + T_W & 0 \leq x \leq 0.47 \\ T_R & 0.47 \leq x \leq 1 \end{cases} \tag{1.9}$$

where T_R is the reservoir temperature, T_W the temperature at the wellbore and x is the normalised fracture length; it is plotted in Figure 1.7. The effect of higher dimensions on the temperature distribution are not considered here but could have a notable impact on the flow behaviour as the properties of the fluid can have significant dependence on temperature. Clifton *et al.* [19] build on the work of Biot *et al.* [18] by noting that the one-dimensional fracture temperature is the average temperature across the fracture width at a given location. This is justified based on the narrowness of the fracture (and

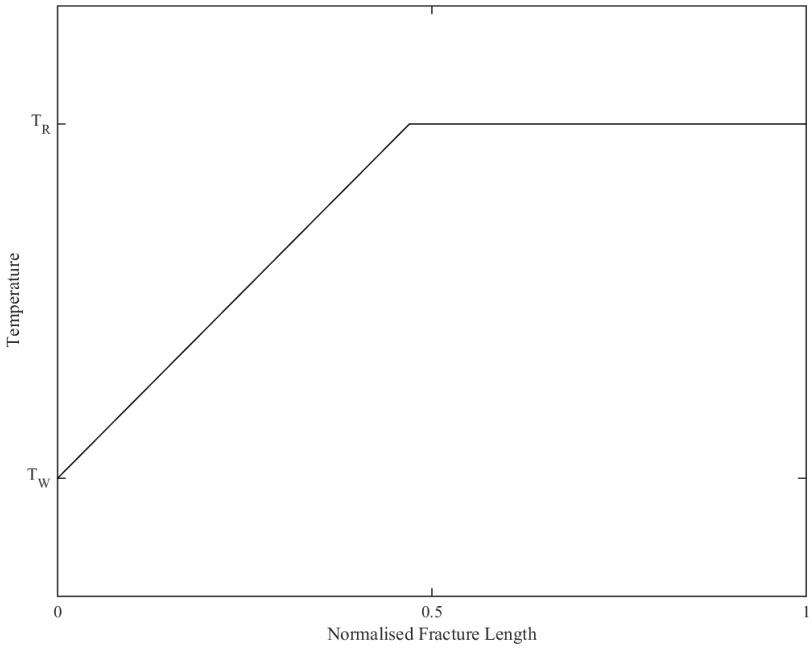

Figure 1.7: Plot of the generalised fracture temperature against normalised fracture length as estimated by Biot *et al*. [18]. T_R is the reservoir temperature and T_W is the temperature at the wellbore.

small temperature change) compared to its length. This is used in the development of a 3D fracture model where viscosity changes with temperature. A case study of fracture generation and proppant settling indicated that, in the variable viscosity case, it generated a preferential proppant distribution compared to a constant viscosity model. Meyer [29] performed a similar analysis in 2D that further considered more sophisticated models for the description and nature of fracture itself.

More recently, the efforts to capture the complex behaviour of fracturing fluids and proppants have continued to develop the available models. For example, Linkov [30] investigated the comparison of Newtonian and non-Newtonian fluids in the hydraulic fracturing context. This study looked at the fluid itself and does not consider the impact of proppant. Its purpose is to develop a framework for comparing the performance of hydraulic fracturing fluids with differing rheologies in a systematic way. Proppant effects are however considered in the works of Eskin and Miller [31, 32]. These studies account for proppant behaviour using kinetic theory [31] or a diffusive flux model [32]. In both situations, migration of particles away from the walls of a channel, and into the centre, occur for non-Newtonian fracturing fluids due to differences in flow around a particle. Similar particle migration has also been observed in Newtonian fluids. In [32], it was observed that the centre concentration of a non-Newtonian slurry may be more than double that at the walls. This is a result of shearing at the walls changing the fluid viscosity in these regions, increasing away from the wall. Viscosity

was relatively constant in the channel centre. This viscosity difference, and subsequent impact on fluid velocity profile, were reasoned to cause the particle migration. These models are, however, still fundamentally based on a volume fraction term to describe the proppant distribution rather than a rigorous resolution of particles.

The main difference in the modelling used in the more recent works is not so much in the fundamental formulations used but in how the large scale problem is broken down and resolved. Adachi *et al*. [24] advance the earlier models by considering the vertical layering of a formation and implementing a more realistic characterisation of fracture geometry. This study has not included temperature effects and proppant modelling is still based on volume fraction assumptions. It was further noted that gravitational settling of particles is the only slip mechanism to occur between the components despite the presence and effect of shear flows. The consequence of this assumption is that the proppant concentration is uniform across the width of a fracture when gravity is neglected.

The effect of proppant choice was studied by Kong *et al*. [26] using similar techniques to those already mentioned (e.g. corrected Stokes drag for settling velocity, proppant location treated with a volume fraction term). This found that, particularly in low permeability reservoirs, settling of proppant and the choice of proppant size and density can all have a significant impact on its productivity. Thermal effects on the rheology of the suspension and the overall transport of the proppant particles were not considered in this study.

In a study of particle migration (however not in the context of hydraulic fracturing), Chen *et al*. [33] used a finite difference approach to study particle migration in non-isothermal suspensions in a tube with wall slip conditions. This study does not capture heat transfer between the solid and fluid components, but particle motion is impacted by temperature gradients within the fluid. The particle component adjusts the local thermal conductivity of the fluid, altering the temperature profiles calculated. Particle migration within this model, however, is restricted by an assumption that each radial plane of the flow possesses the same volume fraction as initially stipulated.

As a final consideration, Richardson and Chhabra [34] observe that when particulates are involved in pipe flows, the avoidance of blockage and wear are greater concerns than the power needed to drive the flow. In the context of the design of proppants and fracturing fluids, it is desired for the proppant to be transported deep into a fracture in order to maximise its production potential. Avoiding blockage of a fracture ensures that the greatest area of a fracture can be propped open.

1.2.4 Summary of modelling hydraulic fracturing fluids

A common theme among the modelling studies highlighted in this section is that the transport of particles is calculated using a continuum equation. The hydrodynamic interactions of the proppant with the fluid are generally implemented through a modified Stokes drag law. Whilst this approach does allow for larger scale calculations to be performed it does make many approximations on how the proppant component behaves. In particular, the collision dynamics and thermohydrodynamics occurring around individual particles are lost. This loss of detail motivates the research conducted in this thesis, in particular the development of numerical models that can study proppant at a fully resolved scale with significant numbers of particles.

1.3 Advanced computational modelling and analysis

Modern science has been founded on an ongoing cycle of experimentation and observation of results. This has led to an increasing array of sophisticated tools and techniques that allow data to be gathered from complex physical experiments. However, there still remains many situations where performing experiments and gathering the required data is difficult, expensive or hazardous. Gathering repeated observations of such scenarios is another challenge continually facing experimental campaigns. As an example, consider airflow over a racing car. The direction, velocity and pressure of this flow is fundamental to the performance of vehicle. However if these were to be directly measured using a pitot probe this physical protrusion into the flow would locally disturb the flow in a fashion that would not otherwise occur.

One approach to gaining insight of physical phenomena is to develop computational models that enable prediction of the state of parameters of interest at difficult to reach locations. The applicability of such models has increased with the growth of computing power. Faster and cheaper processors, increased memory capacity and parallel computation have all enabled models to be solved and solutions projected for larger and larger problem cases, at higher resolution and with more detail. Whilst still needing a justifiable grounding based on fundamental phenomena, such models allow scientific investigation to occur in directions that may not be safe, affordable or practical to undertake from a purely experimental standpoint. Another advantage of using such numerical models is in the area of prototyping and component design. As experiments can be performed repeatedly and at low cost, a wide design space encompassing geometry, material property and implementation strategy can be investigated and optimal solutions identified before more costly physical experiments or prototyping is undertaken. This strategy additionally reduces material waste and can improve the overall perfor-

mance of the system being studied.

This thesis develops computational techniques for the analysis of the effects of temperature on the behaviour of particle suspensions. From a physical point of view, a particle suspension is a multiple component problem where a number of solid particles are immersed within a fluid. Such systems have a number of applications throughout scientific and engineering fields; targeting problems with both an industrial and academic focus and over a range of length scales. Such applications include:

- Biology - red blood cells immersed within plasma.
- Chemistry - water treatment processes.
- Civil engineering - aggregate within unset concrete.
- Environmental studies - debris carried by a flood.
- Industrial processing - grinding mills.

The hydraulic fracturing process, which is the particular focus in this research, is another example of particle suspension flows (i.e. proppant being transported by the fracturing fluid).

Due to the interactions between the solid and fluid components, modelling of particle suspensions requires a number of different areas of study to be combined. This is further complicated when thermal interactions of both components are taken into account. These fields all have complexities in their own right and include:

- Hydrodynamics of the fluid flow moving through a geometry.
- Contact mechanics of how particles interact with each other and physical boundaries.
- Hydrodynamic forces acting on particles, which suspend and transport them within fluid.
- Thermodynamic behaviours of the fluid component such as conduction and convection.
- Thermodynamics of how physical and material properties of both components vary with temperature.
- Heat transfer between the solid and fluid components and between objects in physical contact.

As an illustration, consider the flow of fluid and particles through a heated channel depicted in Figure 1.8. In this scenario, the fluid flow forms a non-linear velocity profile, particles are carried by the flow colliding with each other and heat is transferred from the boundary wall to the fluid and between the fluid and solid. Although a conceptually simple problem, the contributions of all these factors makes

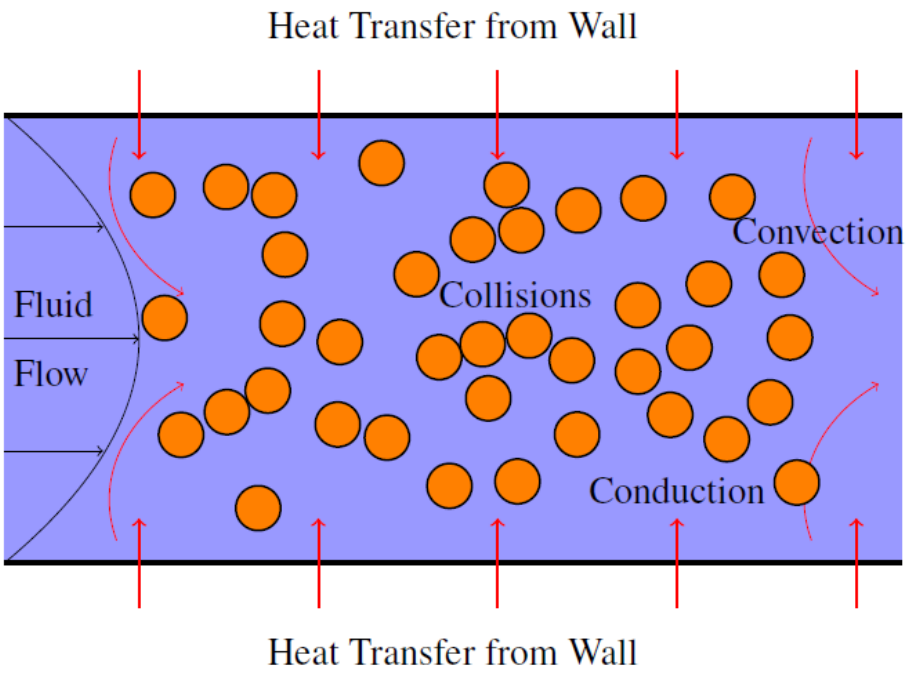

Figure 1.8: Modelling of thermal particle suspension flows requires a number of complex physical phenomena to be taken into account. This includes components of hydrodynamics, contact mechanics and thermodynamics.

determining an analytical expression for describing the flow at a given point in time intractable, even in two dimensions. If investigated experimentally, any observations would be required to be made from an external point of view to prevent disrupting the flow. Internal flow features may be obscured in this reference frame by particles closer to the edge. A computational model would allow all features of interest of the flow to be recorded without hindrance.

In light of these complexities, careful articulation of the parameter space being studied in this research is required. This is needed both in terms of the numerics and from the industrial context of hydraulic fracturing in which this work has been framed.

1.4 Thesis aims and objectives

The transport of hydraulic fracturing fluids in unconventional reservoirs is a complex process, involving numerous physical and chemical phenomena. Current analytical, numerical and experimental tools for studying this process each exhibit their own limitations. Therefore the aim of this thesis is:

To investigate the effect of geothermal temperature gradients on the rheology, transport and placement of particle suspensions in hydraulically fractured, unconventional reservoirs

To achieve this, a number of key objectives were identified as targets to be met during the development of the research. These were to:

- Develop, verify and validate a computational model of coupled fluid and particle mechanics at the particle scale.
- Incorporate a temperature field and associated boundary conditions for conjugate heat transfer in the developed model.
- Implement a temperature-dependent, non-Newtonian rheological model to account for temperature-dependent characteristics of the fluids of interest.
- Apply the developed model to characterise the macroscopic behaviour of particle suspensions as a function of temperature, temperature gradient and solid volume fraction.
- Apply the developed model to investigate the transport of suspended particles when injected into synthetic fracture geometries subject to geothermal gradients.

From a numerical standpoint in particular, many existing models for proppant transport take a macroscopic viewpoint of the solid component by treating it as a continuum phase. The strategy proposed in this thesis allows for resolution of individual proppant particles and, as such, a more detailed study of their transport through complex geometries. This also allows for particle-scale thermal effects to be studied in greater detail, providing a point-of-difference to these previous studies.

1.5 Methodology and scope

In this research, three areas are required to be solved in a coupled manner: the hydrodynamics, the particle mechanics and the thermal behaviour of the system. A natural choice for explicitly computing the particle mechanics is the discrete element method (DEM). This method computes the forces acting on point particles and integrates their motion according to Newton's second law. This is a mature technique that has been applied to a wide variety of problems including the granular flow of individual particles and the study of fracture mechanics through the use of particle bonds. To capture the fluid flow, a method is needed that is able to efficiently capture the transient motion of fully resolved particles moving through it. The lattice Boltzmann method (LBM) is an ideal candidate in this regard as, in a suitable formulation, it is able to solve fluid flow at a local point in space without information from neighbouring locations. This means that once a point is identified to be covered by a DEM

particle, the appropriate behaviour of fluid flow can be calculated. A second advantage of the LBM is that, due to it being a strategy for solving partial differential equations, it can also be used to solve the thermodynamics of the system. In this study, the thermal LBM solver is used to compute the thermal state of the entire suspension system, simplifying the thermal interactions between the two components. As the LBM is an intrinsically dynamic solver, it is also able to efficiently capture the transient nature of particle suspensions. Greater detail on the formulation of these algorithms and their application to thermal particle suspensions will be provided over the duration of this thesis.

A brief survey of the petroleum engineering literature has demonstrated that the hydraulic fracturing process is both complex and broad. This research focuses on the transport of spherical proppant particles through a fracture of fixed dimension. These particles are assumed to be large enough such that their motion is not affected by Brownian processes. The rheology of the fluid is assumed to be temperature-dependent only, with this being described by simple analytic expressions. The base fluid exhibits Newtonian behaviour at the appropriate reference temperature. Conjugate heat transfer is modelled in the thermal description of the two components within a suspension. These restraints will allow the general trends of suspension characteristics when transported within a temperature-dependent viscosity fluid to be most clearly identified. It is important to note that the following factors relating to hydraulic fracturing are not considered in this work:

- The initiation, propagation and closure of a fracture within a reservoir.
- The composition of the fracturing fluid through the use of additives.
- Fluid leak-off to the reservoir.
- Mechanical performance of the proppant particles under loading.
- Influences of pumping strategy.

1.6 Thesis structure

The remaining chapters of this thesis articulate how the research has been developed to meet its aims and objectives. In particular, they focus on the development of the numerics required to analyse the problems of interest as well as the study of thermal influences on suspension flow within sheared and fracture-like geometries. Chapter 2 describes the fundamentals of coupled fluid-particle modelling within a thermal LBM-DEM framework. This is extended in Chapter 3 to discuss the development and analysis of LBM techniques that account for conjugate heat transfer between the two components.

The model development is concluded in Chapter 4 with a discussion on how temperature-dependent viscosity can be included within a thermal LBM-DEM model. Chapters 5 and 6 extend the model to 3D and analyse the behaviour of particle suspensions in the respective contexts of shearing rheology and fracture-like geometries. Finally, Chapter 7 summarises the outcomes of the thesis, highlighting its contributions and identifying areas where this work can be continued.

Chapter 2 - Modelling thermal particle suspensions with coupled lattice Boltzmann and discrete element methods

McCullough, J. W. S., Leonardi, C. R., Jones, B. D., Aminossadati, S. M. and Williams, J. R. (2016) Lattice Boltzmann methods for the simulation of heat transfer in particle suspensions, International Journal of Heat and Fluid Flow, vol. 62, part B, pp. 150-165.

Significant portions of this chapter have been adapted from Sections 1-4 of the above paper. As the lead author of this paper, I was responsible for significant portions of the following aspects:

- literature review presented in Sections 1-4
- model development discussed in the later sections of the paper
- analysis of results presented in the later sections of the paper
- drafting of the manuscript and its review.

Estimated Contributions by Candidate	
Conception and design	70%
Analysis and interpretation	75%
Drafting and production	70%

Chapter 2

Modelling thermal particle suspensions with coupled lattice Boltzmann and discrete element methods

From a numerical perspective, the treatment of the solid component within particle suspensions can be approached in a number of ways. One way is to assume that particles are a continuous property of the fluid with a distribution that evolves with a convection-diffusion equation. This approach allows for efficient modelling of large scale particle systems as the relatively small particles do not need to be fully resolved. However, as particles are not being fully resolved, their behaviour can only ever be computed in an approximate manner. Features of particle motion that are not driven by the convective motion of the suspending fluid - collisions and lubrication driven agglomeration for example, can be difficult to resolve with this approach [35, 36, 31].

Choosing techniques that resolve particles can also be unsuitable. Mesh based approaches require the fluid domain to be frequently recomputed as the solids move through the domain. The computational expense of this makes this approach unrealistic for suspensions beyond a few particles in size. A completely fundamental approach to modelling particle suspensions would be to use molecular dynamics to explicitly resolve the behaviour of the system at all length scales. This approach however becomes a impractically large when approaching realistic systems, even for modern computers [37, 38, 32].

To get the best compromise for suspension modelling, a balance between the extremes of resolved and homogenised techniques needs to be reached. Approaches based on the lattice Boltzmann method (LBM) however offer an attractive compromise by treating the fluid as probability distributions moving throughout a domain. This is is mesoscale point of view that avoids full modelling at the

molecular level but is still sufficiently resolved to couple directly to motion of individual solid particles [39]. The discrete element method (DEM) provides a similar approach to the modelling of solid particles by capturing their interactions with each other and their surroundings from a fundamental perspective.

2.1 Lattice Boltzmann method for fluid flow modelling

The LBM was proposed in the late 1980s as an evolution of the lattice gas automaton developed to capture the molecular behaviour of gas flows [40, 41, 42, 43]. Since then the LBM has seen a rapid uptake and development for a wide variety of flow regimes and scenarios. These include multiphase [39, 43, 42] and multicomponent [39, 44, 42, 45, 46] flows, thermal modelling [39, 47], turbulent flow [39, 42], reactive flow [39, 48], porous media flows [44, 43], particle suspensions with electromagnetic effects [45, 46] and nano-scale regimes [44, 42, 49]. Situations that involve complex or evolving physical boundaries can be challenging to capture using conventional finite difference/volume/element methods. The implementation of boundary conditions in the LBM means that such scenarios are more straightforward to model with this approach [39, 43]. Furthermore, the LBM also has the advantage of locally solving the macroscopic flow properties at each time step. This can allow parallel implementation of the calculation process over multiple processors whilst still retaining fundamental flow relations [39, 42, 43].

2.1.1 General methodology

Conventional finite difference schemes solve flow problems by focusing on representative elements of fluid over which the conservation equations are maintained. In contrast, the development of lattice Boltzmann based methodologies start by regarding the fluid as being constructed of distribution functions, $f_i(\mathbf{x}, t)$, that represent the probability of an amount of fluid moving on a grid of nodes in the direction of propagation, i, at a given location, $\mathbf{x}$, and time, t.

The evolution of the distribution functions at a location can then be described as,

$$f_i(\mathbf{x} + \mathbf{c}_i \Delta t, t + \Delta t) - f_i(\mathbf{x}, t) = \Omega_i(f_i(\mathbf{x}, t)), \tag{2.1}$$

which is known as the lattice Boltzmann equation (LBE). In Equation 2.1, $\Omega_i\left(f_i\left(\mathbf{x}, t\right)\right)$ is a collision function that controls the interaction of distribution functions at a node. The $\mathbf{c}_i$ term represents the velocity with which motion occurs between nodes in a propagation direction. This is determined from the lattice spacing, the time step and the lattice displacement vector to the destination node, $\boldsymbol{\xi}_i$,

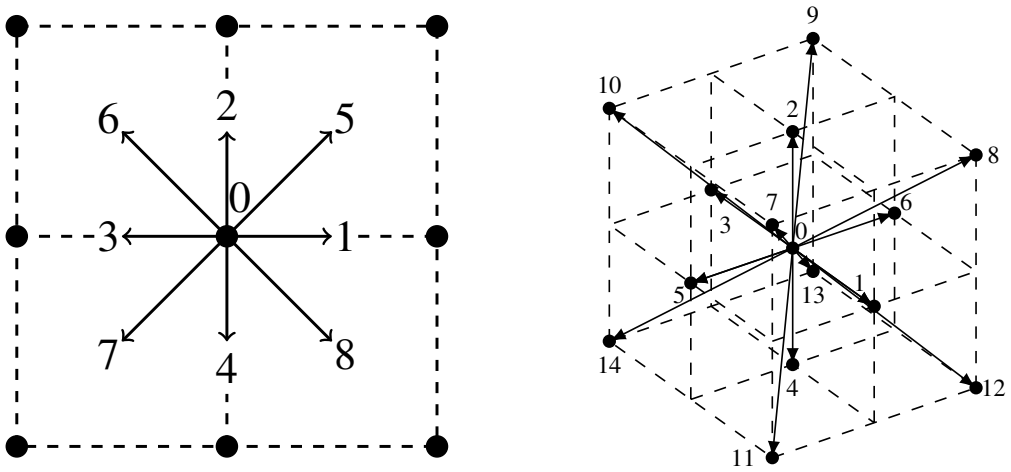

(a) D2Q9 lattice

(b) D3Q15 lattice

Figure 2.1: The velocity set of the D2Q9 and D3Q15 lattices which are commonly used LBM models for 2D or 3D studies. The D3Q27 lattice is also often used and adds velocities to the centre of the outer cubic edges of the D3Q15 lattice.

as $\mathbf{c}_i = \boldsymbol{\xi}_i \Delta x / \Delta t$. When implemented numerically, this evolution is separated into two processes, namely: streaming between nodes and collision at nodes. The order of evaluating these two stages at each iteration does not impact the overall end result.

The streaming and collision processes of the LBE are applied to the flow problem by discretising the entire possible fluid domain into a planar (2D) or prismatic (3D) array of point locations. The complexity of such a model is described as D*n*Q*m* where *n* is the number of dimensions in the model and *m* refers to the number velocities available to redistribute populations from a given node. This velocity set relocates populations to the surrounding nodes based on the lattice configuration implemented. Sets often also include a stationary velocity to allow some of the population to remain at a node. Widely used models are the D2Q9 and D3Q15 variants (see Figure 2.1) for reasons of ease of computational implementation and acceptable accuracy [50]. The D3Q27 lattice is also often used for three-dimensional flows. It is important to note that the numbering of the lattice directions varies within the literature for reasons of convention or convenience of implementation.

The macroscopic properties of the flow at each nodal location are determined from summation conditions on the populations and the given velocity set. In particular, these are found as density,

$$\rho = \sum_{i=0}^{m-1} f_i(\mathbf{x}, t), \tag{2.2}$$

and mass flux (**u** is the flow velocity),

$$\rho \mathbf{u} = \sum_{i=0}^{m-1} f_i(\mathbf{x}, t)\mathbf{c}_i. \tag{2.3}$$

There exists two predominant methods of implementing the collision function in the LBE (Equation 2.1), known as the single relaxation time (SRT) and multiple relaxation time (MRT) techniques. The SRT implementations are generally based on the work of Bhatnagar, Gross and Krook [51] where the evolution of the distribution functions occurs based on comparison to an equilibrium state.

The SRT collision function (also referred to as the BGK operator) is based on the relaxation of the distribution functions towards an equilibrium state, $f_i^{eq}(\mathbf{x}, t)$, and was introduced early in LBM development [52, 53]. This process can be defined as,

$$\Omega_i(f_i(\mathbf{x}, t)) = -\frac{\Delta t}{\tau_f}(f_i(\mathbf{x}, t) - f_i^{eq}(\mathbf{x}, t)). \tag{2.4}$$

The equilibrium state is most often computed as a polynomial approximation of the Maxwell-Boltzmann velocity distribution function. A relaxation parameter, τ_f, is used to control the evolution of the populations towards equilibrium within the collision process. The value of this parameter is typically restricted to $\tau_f \in (0.5, 1.5]$ due to stability and accuracy considerations.

The MRT was introduced by d'Humieres in 1992 [54] to provide a more stable method of solving the LBE. As its name suggests, MRT models control the updating of the LBM populations by imposing multiple relaxation rates upon them. The collision process of particles is performed in the domain of physically meaningful moments of the distribution functions. The outcome of this is then transformed back to the distribution function domain to complete the propagation phase [43]. Prosperetti and Tryggvason [43] summarise that whilst the MRT approach is slightly more involved and expensive to implement computationally than SRT (approximately 15% slower [55]) this is overcome by its advantages in the areas of numerical stability and boundary condition development.

As it deals with distribution functions instead of flow variables, the relationship between the LBM approach to the fundamental conservation laws needs to be demonstrated for the desired velocity set and collision function being implemented. This can be performed in detail through the use of a Chapman-Enskog expansion to an appropriate order as is widely illustrated in the literature (for example in the works of He and Luo [56] or Chen and Doolan [39]).

Within SRT and MRT models an isothermal equation of state is used to relate the pressure, p, and density of the system as,

$$p = \rho RT = \rho c_s^2 = \frac{\rho}{3}\left(\frac{\Delta x}{\Delta t}\right)^2, \tag{2.5}$$

in which c_s is the speed of sound on the lattice and typically assigned a value of $1/\sqrt{3}$ as a consequence of the Chapman-Enskog procedure. The gas constant, R, and system temperature, T, are chosen and held constant in isothermal flows such that $c_s = RT$. The kinematic viscosity of the system in the SRT-LBM is also revealed through the Chapman-Enskog expansion as,

$$\nu = \frac{1}{3}\left(\tau_f - \frac{1}{2}\right)\frac{(\Delta x)^2}{\Delta t}. \tag{2.6}$$

It is shown via the Chapman-Enskog expansion that, in the low Mach number limit ($Ma = |\mathbf{u}|/c_s \ll 1$), the expressions in Equations 2.5 and 2.6 are valid and the equilibrium distributions can be defined. The equilibrium function depends on the lattice geometry being used and the distribution direction of interest. Equation 2.7 is a result for the D2Q9 lattice as a second-order velocity expansion. The weightings, w_i, vary based on the direction chosen with it being 4/9 for $i = 0$, 1/9 for $i = 1, 2, 3, 4$ and 1/36 for $i = 5, 6, 7, 8$ in the D2Q9 case [52]. For D3Q15, the stationary direction has a weight of 2/9, 1/9 is used for the next six nearest neighbour directions and the remaining eight have 1/72. In D3Q27, the groups of lattice directions from the current node use weights of 8/27, 2/27, 1/54 and 1/216 based on increasing distance [57].

$$f_i^{eq}(\mathbf{x}, t) = w_i \rho(\mathbf{x}, t)(1 + 3\mathbf{c}_i \cdot \mathbf{u} + \frac{9}{2}(\mathbf{c}_i \cdot \mathbf{u})^2 - \frac{3}{2}u^2) \tag{2.7}$$

The LBM process is constrained to low speed flows in order to retain the low Ma required to satisfy fundamental conservation laws (see [39, 42] for example). To overcome this limitation, an approach to solving more general flow problems with the LBM was proposed by Karlin *et al.* [58] based upon an entropy function. Minimisation of this function as part of determining the equilibrium distribution provided an H-theorem for the calculation thus guaranteeing its stability within the range of applicable approximations. Over the following years, this entropic LBM (ELBM) has been adapted to a wide range of situations including combustion and turbulence ([59, 60] among others). Ansumali and Karlin [61] record that the ELBM approach is approximately ten times more expensive than the conventional SRT approach in terms of both run time and nodal computations. Whether the extra computational effort justifies the stability benefits is dependent on the scenario under investigation.

In order to further improve the accuracy and stability of the LBM alternate collision techniques are still being developed. The most prominent of these are the cascaded [62] and cumulant [63] methods. These seek to improve LBM performance by modifying collision parameters to reduce Galilean invariance and increase accuracy for traditionally difficult problems such as low viscosity and high Reynolds number flows.

2.1.2 LBM boundary conditions

To implement boundary conditions within the LBM the desired constraint needs to be expressed as a function of the local distribution populations at the target location. Assumptions are made to accommodate the unknown values streamed from outside the domain. The most common LBM boundary condition is the bounce-back technique for solid, non-slip walls. On such boundaries the unknown populations are assumed to possess the same values as those incoming from the opposite direction. Variants of this approach can include features such as variable physical wall location [47, 64], boundary velocity [65, 66] or porous media [67]. Improved accuracy of the method was developed by Ladd and Verberg [37] in the link or continuous bounce-back approaches. These still encounter inaccuracies for some boundaries as curves are viewed in a stepwise rather than continuous fashion [37, 68].

The boundary condition proposed by Zou and He [69] aimed to provide exact values of velocity or pressure (via density) along a given boundary. This was achieved through rearranging the macroscopic property laws (Equations 2.2 and 2.3) and assuming a non-equilibrium bounce-back condition of, $f_i - f_i^{eq} = f_{-i} - f_{-i}^{eq}$, to obtain unknown population values. Here '$-i$' signifies the distribution acting in the opposite direction to i. The Zou-He condition has been found to be accurate at low Reynolds numbers but can become unstable as this increases [70].

2.2 Lattice Boltzmann methods for non-isothermal settings

The challenge of extending the LBM to non-isothermal scenarios (thermal LBM, TLBM) can be summarised as determining methods that account for the necessary extra degrees of freedom of the system required to solve for both energy and hydrodynamics. Various approaches to this problem were highlighted and explained by Guo and Shu [47], however no consensus has been reached here or in the wider literature as to an optimal approach.

2.2.1 Multispeed methods

Within multispeed methods, the velocity set being considered is greatly expanded to allow conservation of moments necessary to satisfy energy conservation equations in addition to those of continuity and momentum. McNamara and Alder [71] note that to fully resolve the 3D thermal Navier-Stokes equations at least 26 velocities are necessary to meet the constraints imposed (13 in two dimensions). An example of a D2Q13 model is illustrated in Figure 2.2, while a D3Q21 model can be analogously constructed by adding an extra velocity along the positive and negative Cartesian axes directions of a D3Q15 model. The size of the velocity set being implemented varies depending on assumptions

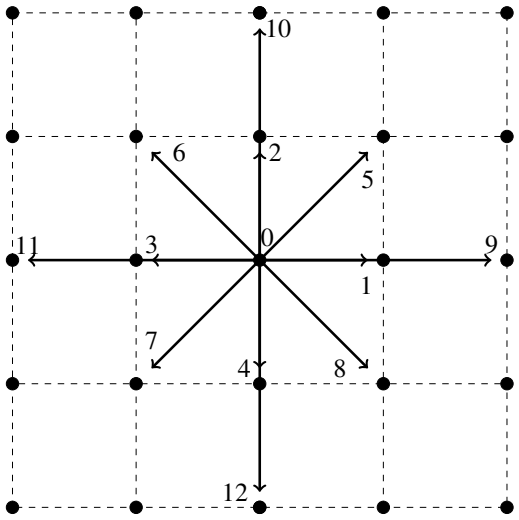

Figure 2.2: Example of a multispeed TLBM lattice using a D2Q13 layout, derived from [71].

made on the isotropy of the flow and accuracy to which some moments are conserved [71, 72, 73]. Larger sets however may be necessary to improve the numerical stability of such an implementation. Smaller sets may be used when the non-conservation of a moment set does not unacceptably impact on accuracy of the overall solution. This, with a double relaxation time collision scheme, was used by McNamara *et al*. [72] to improve a multispeed TLBM application. The isothermal D2Q9 lattice can be formed within this framework by neglecting higher order velocity moments, which is a suitable approximation for low Ma flows, and the energy equation from the thermal Navier-Stokes restrictions.

The multispeed approach to thermal flows is widely noted in the literature to encounter problems with numerical stability [71, 72, 73, 47]. The source of this problem has been determined to be a result of modal coupling of energy and shearing [74, 47]. This instability causes the multispeed approach to the TLBM to be restricted in the range of temperatures that it can validly model.

The use of a single distribution population however does have a key strength in that the hydrodynamic and thermodynamic behaviours of the fluid system are intrinsically linked. As such, the introduction of forcing terms for phenomena such as buoyancy and internal viscous heating is not required. This strength however can lead to problems in implementing boundary conditions. McNamara *et al*. [72] discuss a technique that enforces no-slip velocity and isothermal conditions simultaneously via an extrapolation process based on the desired boundary values. This approach was based on methods used in finite-difference numerical methods and uses up to three interior nodes to determine the equilibrium distributions necessary to implement the boundary values. A layer of exterior nodes is also needed to complete this approach.

Other approaches to multispeed boundary conditions include the regularised boundary condition

[75]. This work deals with very large velocity sets for use with isothermal flows rather than also accounting for the extra restrictions imposed by energy. This method replaces unknown populations with an approximation (a perturbation from the equilibrium distribution) sourced from the Chapman-Enskog expansion process. This method was found to be second-order accurate for the investigated cases.

The implementation of diffuse boundary conditions in multispeed models were discussed by Meng and Zhang [76]. These boundary types are desirable in that they can replicate slip velocities and temperature jumps at interfaces. These authors provide a method of implementing such conditions while still retaining the collision and streaming processes characteristic of the LBM. Their condition is constructed through the use of ghost nodes to represent those outside the fluid domain. A mass balance is observed in conjunction with scattering rules to reflect particle behaviour at the wall to determine the necessary values for populations originating from ghost nodes to replace the unknown populations within the fluid.

A boundary condition for the multispeed TLBM was proposed by Frapolli *et al.* [77] and is based on the Tamm-Mott-Smith conditions for Dirichlet velocity and temperature restrictions. Here, unknown populations are first estimated through the bounce-back technique. A correction is then applied to them to ensure that the desired target values are met. The authors further note that such a formulation cannot produce slip conditions at a wall and that only applying the corrections to unknown populations reduces the amount of flow information that is lost by the boundary condition. It must be noted though that the equilibrium formulation from which the correction is determined is of a different form to Equation 2.7 due to the larger velocity set being used. This high-order polynomial form (with terms up to the power of eight for velocity and 11 for temperature) would not be straightforward to implement in practice.

2.2.2 Double distribution function methods

In the double distribution function (DDF) approach to the TLBM, a second distribution population, $g_i(\mathbf{x}, t)$, is introduced to compute energetic aspects of the flow. This population follows similar conservation rules and principles to the hydrodynamic population. In this case, however, the Chapman-Enskog expansion yields a conservation of energy equation. The assumptions made regarding the energetics determine the function formed. For example, if viscous heating and compression work are ignored the energy and hydrodynamics completely decouple and,

$$\frac{\partial T}{\partial t} + \mathbf{u} \cdot \nabla T = \nabla(\alpha \nabla T), \tag{2.8}$$

is the conservation equation solved. Temperature is solved directly in this passive scalar approach. The thermodynamic population behaves in a similar manner to the hydrodynamic population with a collision and streaming rule,

$$g_i(\mathbf{x} + \mathbf{c}_i\Delta t, t + \Delta t) - g_i(\mathbf{x}, t) = -\frac{\Delta t}{\tau_g}(g_i(\mathbf{x}, t) - g_i^{eq}(\mathbf{x}, t)), \tag{2.9}$$

and definition of macroscopic temperature,

$$T = \sum_{i=0}^{m-1} g_i(\mathbf{x}, t). \tag{2.10}$$

The equilibrium functions are also similarly calculated as,

$$g_i^{eq}(\mathbf{x}, t) = w_i T(\mathbf{x}, t)(1 + 3\mathbf{c}_i \cdot \mathbf{u} + \frac{9}{2}(\mathbf{c}_i \cdot \mathbf{u})^2 - \frac{3}{2}u^2). \tag{2.11}$$

In the SRT collision approach of Equation 2.9, the relaxation parameter, τ_g, is related to the thermal diffusivity of the material, α, by the relation,

$$\alpha = \frac{1}{3}\left(\tau_g - \frac{1}{2}\right)\frac{(\Delta x)^2}{\Delta t}. \tag{2.12}$$

Although it makes the solution process straightforward, the decoupling of the thermohydrodynamic behaviour means the temperature field has no influence on the velocity field. This drawback, and the lack of viscous heating and compression work, was overcome by He *et al.* [78] by using the second distribution function to conserve internal energy. This approach also provided some coupling between the two populations in a one-way manner in that velocity influenced energy but not vice-versa. This coupling occurs both in the equilibrium distribution as in the passive-scalar point of view and via a source term.

From both He *et al.* [78] and Guo and Shu [47] the main change to the system of equations is in the macroscopic interpretation of the g_i population which for this model is,

$$\frac{\rho nRT}{2} = \rho\epsilon = \sum_{i=0}^{m-1} g_i(\mathbf{x}, t) - \frac{\Delta t}{2}\sum_{i=0}^{m-1} \bar{f}_i(\mathbf{x}, t)q_i(\mathbf{x}, t), \tag{2.13}$$

where,

$$\bar{f}_i = \frac{(\tau_f - 0.5\Delta t)f_i + 0.5\Delta t f_i^{eq} + 0.5\Delta t(\tau_f - 0.5\Delta t)F_i}{\tau_f}, \tag{2.14}$$

and,

$$q_i(\mathbf{x}, t) = (\mathbf{c}_i - \mathbf{u}) \cdot [\frac{1}{\rho}(-\nabla p + \nabla \cdot \hat{\mathbf{T}}_{stress}) + (\mathbf{c}_i - \mathbf{u}) \cdot \nabla \mathbf{u}]. \tag{2.15}$$

Here ϵ is the internal energy of the system at a node and $\bar{f}_i q_i$ constitutes a forcing term to account for viscous heating. An external forcing term of,

$$F_i = \frac{\mathbf{G} \cdot (\mathbf{c}_i - \mathbf{u})}{RT} f_i^{eq}, \tag{2.16}$$

in which $\mathbf{G}$ is the force per mass is also introduced. Finally $\hat{\mathbf{T}}_{stress}$ is the viscous stress tensor at the given node. This can be found through computing the second-order moment of the term $f_i - f_i^{eq}$ [57].

A result of the non-localities within q_i (calculating the pressure and velocity gradients, ∇p and $\nabla \mathbf{u}$ respectively) is that this method is not necessarily used to solve general thermal behaviour of a fluid [79]. Another version of the DDF approach can be attained by conserving total, $E = \epsilon + u^2/2$, rather than internal energy with the second population. This has benefits of including viscous heating without the need for non-local derivative terms. The derivation of the system equations is described by Guo *et al*. [80] and Guo and Shu [47]. Firstly, a change of variables was implemented to retain the explicit properties of the formulation (this was also done in the internal energy model). These changes yield,

$$\tilde{f}_i = f_i - \frac{\Delta t}{2}\left[\frac{f_i^{eq} - f_i}{\tau_f} + F_i\right], \tag{2.17}$$

and,

$$\tilde{g}_i = g_i - \frac{\Delta t}{2}\left[\frac{g_i^{eq} - g_i}{\tau_g} + Z_i \frac{f_i^{eq} - f_i}{\tau_f}\left(\frac{1}{\tau_g} - \frac{1}{\tau_f}\right) + q_i\right]. \tag{2.18}$$

The fluid population is then able to be relaxed by,

$$\tilde{f}_i(\mathbf{x} + \mathbf{c}_i \Delta t, t + \Delta t) - \tilde{f}_i(\mathbf{x}, t) = -\omega_f \left(\tilde{f}_i(\mathbf{x}, t) - f_i^{eq}(\mathbf{x}, t)\right) + \frac{2 - \omega_f}{2} \Delta t F_i, \tag{2.19}$$

and the thermal population with,

$$\tilde{g}_i(\mathbf{x} + \mathbf{c}_i \Delta t, t + \Delta t) - \tilde{g}_i(\mathbf{x}, t) = -\omega_g \left(\tilde{g}_i(\mathbf{x}, t) - g_i^{eq}(\mathbf{x}, t)\right) + \frac{2 - \omega_g}{2} \Delta t \tilde{q}_i + (\omega_g - \omega_f) Z_i \Phi_i. \tag{2.20}$$

These results are supported with the expressions,

$$\omega_f = \frac{2\Delta t}{2\tau_f + \Delta t}, \tag{2.21}$$

$$\omega_g = \frac{2\Delta t}{2\tau_g + \Delta t}, \tag{2.22}$$

$$Z_i = \mathbf{c}_i \cdot \mathbf{u} - \frac{u^2}{2}, \tag{2.23}$$

$$\Phi_i = \tilde{f}_i - f_i^{eq} + \frac{\Delta t F_i}{2}, \tag{2.24}$$

and,

$$\tilde{q}_i = \left[w_i \frac{\rho E}{RT_0} + f_i^{eq}(1 - \frac{\omega_f}{2})\Phi_i \right] \mathbf{c}_i \cdot \mathbf{G}. \tag{2.25}$$

The equilibrium distributions themselves are evaluated at a reference temperature, T_0, and pressure, p_0, as,

$$f_i^{eq} = w_i \rho \left[1 + \frac{\mathbf{c}_i \cdot \mathbf{u}}{RT_0} + \frac{1}{2}\left(\frac{\mathbf{c}_i \cdot \mathbf{u}}{RT_0} \right)^2 - \frac{u^2}{2RT_0} \right], \tag{2.26}$$

and,

$$g_i^{eq} = w_i p_0 \left[\frac{\mathbf{c}_i \cdot \mathbf{u}}{RT_0} + \left(\frac{\mathbf{c}_i \cdot \mathbf{u}}{RT_0} \right)^2 - \frac{u^2}{2RT_0} + \frac{1}{2}\left(\frac{\mathbf{c}_i^2}{RT_0} - n \right) \right] + E f_i^{eq} i \tag{2.27}$$

recalling that n refers to the number of spatial dimensions in the problem.

This use of a fixed reference temperature rather than the local one again removes the influence of the thermal distribution on the velocity field as in the previous models. Guo and Shu [80] note that this decoupling limits the application of the total energy formulation to situations in which the variation in temperature is small (Boussinesq flows). This is a consequence of the equation of state implemented in these DDF models being independent of the local temperature [80, 47].

As energy and hydrodynamics are conserved separately in the DDF formulation, the linking of the two quantities and associated phenomena needs to be made explicit through the forcing terms noted previously. For example, He *et al*. [78] use,

$$\rho \mathbf{G} = -\rho \mathbf{g} \eta (T - T_0), \tag{2.28}$$

to allow convection behaviour to be modelled with a buoyancy forcing term added to the collision operator of the LBE (right hand side of Equation 2.1). Here T_0 is an appropriate reference temperature for to the system. As convection examples in the literature generally examine Rayleigh-Benard type convection where there the fluid is contained in a box with a hot wall and a cold wall, T_0 is often stipulated as the average of these two quantities. A coefficient of fluid thermal expansion, η, and gravity, $\mathbf{g}$, are also considered. The key assumption that is made in using this term is the Boussinesq

approximation whereby density variations within the fluid are only significant if they are multiplied by a gravitational term.

Finally, it should be noted that both multispeed [77] and total energy DDF [79] formulations of the ELBM have been developed to model thermal flows.

2.2.3 Hybrid methods

A third approach that has been advocated within the literature is to couple the fluid problem solved by the LBM to an alternate solution method for the thermal problem in a hybrid approach [74, 47, 81]. This typically would involve an appropriate finite difference formulation to solve the convection-diffusion equation on a domain similar to the LBM grid under consideration. Such an approach would have similar implementation benefits and drawbacks to the DDF approaches already discussed. In addition, this approach can leverage the considerable existing body of knowledge pertaining to such numerical techniques for solution accuracy and boundary conditions. The drawback of such an approach is that finite difference approaches are inherently non-local. A key strength of the LBM is that macroscopic properties can be found locally so coupling the solution process to the surrounding nodes with a finite difference solver would negate one reason for selecting the LBM originally. Lallemand and Luo [74], however, do implement a coupling parameter to link the temperature field to the velocity field, a feature not seen in other dual approaches.

Another hybrid approach was implemented by Metzger *et al.* [82] who captured a passive-scalar representation of the thermal behaviour of a fluid by releasing a population of Brownian tracer particles into a Couette flow which follow a discretised advection-diffusion equation. The concentration of such particles at a given location within the flow corresponds to its temperature.

2.2.4 Thermal LBM boundary conditions

Having the energetic aspects of the flow being solved by a population distribution of similar form to that used for the hydrodynamics means that a similar approach to boundary conditions can be used. Boundary conditions analogous to those used in isothermal cases can be implemented in the TLBM to obtain rules for both Dirichlet and Neumann constraints. Such examples include those by Guo *et al.* [83], Huang *et al.* [84] and Monfared *et al.* [85].

The 'nonequilibrium extrapolation' boundary method proposed by Guo *et al.* [80] provides a general computation for Dirichlet conditions for both fluid (fixed velocity) and thermal LBM populations. The drawback of this method however is that it is non-local in format. For a general population h_i, the boundary nodes are updated using values from adjacent interior nodes using

$$h_i(boundary) = h_i^{eq}(boundary) + h_i(adjacent) - h_i^{eq}(adjacent). \tag{2.29}$$

The boundary node equilibrium values are determined from the fixed conditions desired at that location. It is noted in [80] that using the density of the adjacent node is a good approximation for the boundary node.

2.3 Discrete element method for particle motion

Regardless of the specific numerical methodology being employed, the motion of particles reduces to an integration procedure being applied to Newton's second law. The forces acting on a particle may include those arising from contact with walls or other particles, hydrodynamic forces from the surrounding fluid, gravitational forces and external forces such as those from an externally applied electromagnetic field [86, 46]. The approach for particles of finite size, with a detailed contact identification and resolution process, is typically a form of discrete element method (DEM).

The numerical procedure of the DEM can be briefly summarised as a procedure of four fundamental steps [87, 88]:

1. Contact search - particles that are in close proximity to one another and may be touching are identified.

2. Contact resolution - each near neighbour pair has the distance between particles computed and determines the magnitude and orientation of any overlap between them.

3. Force resolution - based on the overlap and properties of the particles forces that are acting on the particles are calculated. Other forces such as hydrodynamic, gravitational or electromagnetic effects are also resolved here.

4. Kinematic integration - the position and velocity of the particles are updated based on the forces and an appropriate numerical scheme for solving Newton's second law.

The contact and force resolution steps of this procedure are most efficiently performed when the particles are spheres (or circles in 2D). This is due to analytical equations that describe the boundary of the particle in a concise and straightforward manner. The problem with spheres though is that most real objects are not truly spherical. To overcome this, strategies such as clumping multiple spheres together to generate complex shapes or performing DEM with superquadric or polyhedra-based particles have been employed [87]. Although these approaches better capture particle behaviours such as bouncing or rolling, they do so at significantly greater computational expense [87].

2.4 Coupling of particle and fluid behaviour

In the analysis of particle suspensions, the method of linking particle and fluid behaviour will have significant impacts on the overall flow behaviour and computation time of the system.

2.4.1 Hydrodynamic coupling of particle and fluid behaviour

The calculation of the hydrodynamic forces acting on a particle is of specific interest in the linking of suspension components. The simplest way to couple the two components is to apply hydrodynamic forces through the use of a drag correlation (such as by Jahanshaloo *et al*. [89]) as part of the force resolution step. These are typically in the form,

$$\mathbf{F}_f = 0.5 C_D A_p \rho (|\mathbf{u} - \mathbf{u}_p|(\mathbf{u} - \mathbf{u}_p)) \tag{2.30}$$

with dependence on a drag coefficient, C_D, that is a function of the particle Reynolds number, Re_p, the cross-sectional area of the particle, A_p, the particle velocity, $\mathbf{u}_p$, and the fluid density and velocity. Such an approach is useful in the case of suspensions where Stokes flow is valid (i.e. Re_p being less than unity) [90].

The partially saturated method (PSM) developed by Noble and Torczynski [91] has been utilised in this work as the strategy for coupling DEM to LBM. Further details on the method can be found in [88, 46]. Here, locations of the DEM particles are firstly mapped onto the LBM grid to identify fluid nodes covered by the solid. The nodes covered by the interior of the particle are assigned the same velocity as the particle. The consequences of this are imposed upon the population distributions through a modified relaxation process as,

$$f_i(\mathbf{x} + \mathbf{c}_i \Delta t, t + \Delta t) - f_i(\mathbf{x}, t) = -\frac{\Delta t}{\tau_f} [1 - B] \left(f_i(\mathbf{x}, t) - f_i^{eq}(\mathbf{x}, t) \right) + B \Omega_i^s. \tag{2.31}$$

The summation of momentum differences for the LBM nodes assigned as the boundary of a particle are converted to the hydrodynamic force acting on the particle through,

$$\mathbf{F}_f = \frac{\Delta x^2}{\Delta t} \sum_r B_r \left(\sum_i \Omega_i^s \mathbf{c}_i \right). \tag{2.32}$$

The torque on a particle centred at $\mathbf{x}_p$ can be found by [88],

$$\mathbf{T}_f = \frac{\Delta x^2}{\Delta t} \sum_r (\mathbf{x} - \mathbf{x}_p) \times B_r \left(\sum_i \Omega_i^s \mathbf{c}_i \right). \tag{2.33}$$

In these expressions, r counts the nodes that map an obstacle to the lattice and B is a weighting factor dependent on the coverage of the cell surrounding a node by the particle. The calculation of this

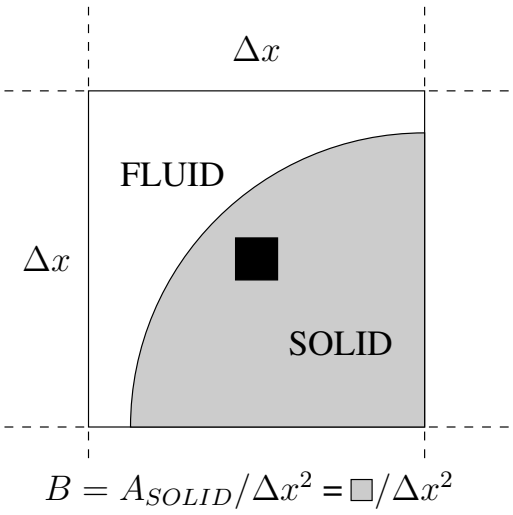

Figure 2.3: Strategy for calculating the nodal coverage fraction B for use in the PSM method. Interface nodes for particle boundaries are identified as $B \in (0, 1)$. Note that the solid and dotted lines in this figure are offset from the lattice grid linking nodes by $\Delta x/2$.

term is illustrated in Figure 2.3. Although more computationally expensive than a drag correlation implementation, such a process does calculate the hydrodynamic force acting on a finite particle from the LBM point of view for a general flow state.

The collision function,

$$\Omega_{id}^{s} = f_{-i}(\mathbf{x}, t) - f_i(\mathbf{x}, t) + f_i^{eq}(\rho, \mathbf{u}_p) - f_{-i}^{eq}(\rho, \mathbf{u}), \tag{2.34}$$

is chosen from the options tested by Noble and Torczynski [91] and is based on a non-equilibrium bounce-back and the particle velocity, $\mathbf{u}_p$.

Other options for applying hydrodynamic forces to particles in a LBM-DEM framework include variants of Ladd's link bounce-back method [65, 66] across a number of works [37, 92, 93, 94, 95], the ALD method [96, 42, 81] or modifications on the momentum exchange method of Equation 2.32 [97, 98, 99].

2.4.2 Thermal coupling of particle and fluid behaviours

Within particle suspensions the heat transfer within and between components could potentially include conduction between solid particles during collision, conduction between walls and solid particles during contact, convection between both wall boundaries and the fluid and the solid particles and the fluid, and internal viscous heating within the fluid. As was noted in Section 2.2, viscous heating behaviour within a fluid can be implemented as a feature within the TLBM model either implicitly (multispeed) or explicitly (internal energy DDF). Radiative effects are generally not considered.

The solution for heat transfer at the interface of two media (both between solid and fluid components in a particle suspension as well as between contacting particles) with no thermal resistance between them requires the continuity of both temperature and heat flux to be maintained with consideration of the varying material properties (conjugate heat transfer). Chen and Han [100] outline a number of methods of doing this from a finite difference approach on a common grid for a steady state solution. Their 'pseudo-density' approach treats the ρC_p term that arises in the conservation of energy equation as the ρ term in the conservation of momentum equation and applies conventional techniques to solve for temperature. A slight rearranging of the energy equation leads to their 'pseudo-solid-specific-heat' method where the thermal diffusivity of the solid and fluid components is found based on the conductivity of the local medium and the density and specific heat of the fluid term only.

Given the constant immersion of the solids within the fluid component in a particle suspension the convective heat transfer process between the two should be a significant factor. Some studies however assume the particles to have adiabatic surfaces [81, 98]. Potential justification for this could be that given the solid particles are generally small in comparison to the overall system that they would, firstly, quickly reach an equilibrium with the surrounding fluid and secondly have a minimal impact on the thermal properties of the fluid itself. It should be noted though that neither Khiabani *et al.* [81] nor Hashemi *et al.* [98] provide this justification. In suspensions within confining geometries, or in a confined pure fluid, the convective process between walls and the fluid is necessarily going to be a significant influence on its behaviour. The convective process in either of these cases can be implemented through an appropriately developed thermal boundary condition.

In the hybrid technique implemented by Metzger *et al.* [82], the heat transfer between the respective components is governed by the advective mechanism of the tracer particles. The redistribution of these tracer particles is influenced by the velocity of the component the particle is in at a given instant.

Hashemi *et al.* [97] update the temperature of an immersed particle at each time step by numerically integrating the energy balance occurring between the solid and fluid at the interface. This procedure was performed for cases with a single particle and 30 individual particles.

The work of Chen and Han [100] has been recognised in the development of steady-state solvers within a LBM framework [101, 102]. The 'pseudo-solid-specific-heat' approach was utilised by Wang *et al.* [102] to determine the thermal conductivity of a fibre composite body. Although numerically convenient, this approach does not capture the correct local material properties of the respective components. The steady-state limitation of such approaches was noted by Wang *et al.* [101] in the development of their conjugate heat transfer model. Here the interface of the components is placed between nodes, with the thermal relaxation parameter at a node being determined by the local ma-

terial properties. A modified bounce-back model is used to capture the development of flow at this interface.

Both Seddiq *et al*. [103] and Mohamad *et al*. [104] consider the conjugate heat transfer problem in a LBM framework with the interface located at a node. In both cases the temperature at the interface is determined through an energy balance to ensure that the flux condition is met. This is done on the interface populations by Seddiq's group [103] but from a macroscopic perspective by Mohamad's group [104] with this temperature then acting on the interface populations through the equilibrium functions. The relaxation of populations crossing the interface is dependent on the respective material properties. Mohamad's work [104] relaxes populations on the interface with an average relaxation parameter whilst those in Seddiq's work [103] evolve based on the difference between pre- and post-streaming values.

The work of Karani and Huber [105] ensures that the flux interface restriction is met through the application of a forcing term to the relaxation of the thermal populations adjacent to the interface. This approach assumes that the interface is straight or stair-cased and located halfway between nodal locations. In order to retain the locality of the LBM, the effect of the change in material properties at the interface is only calculated in a one-sided manner. Whilst demonstrated in a SRT setting, the approach of Karani and Huber [105] is applicable to other relaxation schemes. Another forcing-term-based approach was presented by Hu *et al*. [106] that focused on an implementation within an MRT scheme. This method is able to resolve conjugate heat transfer on both straight boundaries and curved interfaces that can be represented by a staircase boundary. A key point to note in the approach of Hu *et al*. [106] is that it is a non-local scheme. Moment-space information from the surrounding nodes is utilised to calculate heat fluxes present at the boundary of two media.

2.4.3 Heat transfer between particles

Due to the simplicity of their implementation, most numerical simulations model the solid particles as spheres. A consequence of this however is that when collisions occur the contact area is very small compared to the overall surface area of the sphere and collision times are generally short. These two factors mean that some previous studies have assumed the conduction heat transfer mechanism to be negligible [89]. Whilst this may be true for dilute suspensions where the interaction between particles (and indeed between particles and walls) is relatively rare, such a process would become appreciable in suspensions with higher solid volume fractions. In the dense suspension situation, the contact area between particles would remain small but the time of contact would be extended as particles remain touching as part of aggregates or due to geometrical considerations (internal or external to the system).

To tackle this problem, Feng *et al*. [99] outlined their development of a so-called thermal DEM (TDEM) procedure. Here, a system of touching particles is modelled as a nodal framework, with temperatures being recorded at the centre of particles and at the points of contact. The conductive heat transfer between touching particles is then set up as a series of linear equations and the temperature at each location solved. The algorithmic procedure necessary to set up and solve the equation set for a large number of particles with multiple changing or separate contacting sets is a possible challenge in implementing this approach. The authors also note that the heat transfer mechanism proposed in the TDEM model in a discrete form is compatible with the dynamic system in terms of coupling the two processes together. Feng's work [99] approaches convective heat transfer between suspended particles and the surrounding fluid by summing the difference in the link-wise internal energy populations over the boundary of a solid particle and using this to replace the flux term within the general fluid population. The TDEM assumes no heat transfer from the fluid.

In this work, the thermal LBM population is used to compute the temperature behaviour for both components. Transient solid-fluid and solid-solid interactions can be resolved through modification of the local relaxation properties to represent individual materials. In particular, the relaxation of LBM nodes at the interface of separate materials can be adjusted to permit different boundary conditions. The implementation of conjugate heat transfer at the interface is discussed in further detail in Chapters 3 and 4. When required, the temperature of a particle can be found through determining the average value of the LBM nodes it covers.

2.5 Summary

This chapter has provided a brief outline of the main numerical methodologies used in this thesis to study particle suspensions with thermal effects. The LBM is an alternative numerical approach for modelling fluid flow to conventional finite difference, element or volume based methods. By considering the streaming and collision of probability distribution functions on a regular grid of nodes, the LBM solves the fundamental conservation equations of fluids. This technique has matured to be able to successfully capture a range of complex phenomena including thermal flows. The LBM is well-suited to studying particle suspensions as only the collision behaviour requires modification in the presence of solids. This is more efficient than recalculating a mesh, as is required in traditional techniques. This collision modification also allows the forces on individual particles to be explicitly resolved. The DEM is a straightforward approach to modelling the motion of solid particles. The availability of the hydrodynamic forces acting on particles in the LBM means that coupling it to the DEM can be readily performed using techniques such as the PSM. Additionally, within a thermal

setting, a second LBM population can be used to capture the thermal interactions between both solid and fluid components of a suspension. These features will be utilised within the remaining chapters of this thesis.

Chapter 3 - Conjugate heat transfer in the LBM

1. McCullough, J. W. S., Leonardi, C. R., Jones, B. D., Aminossadati, S. M. and Williams, J. R. (2018) Investigation of local and non-local lattice Boltzmann models for transient heat transfer between non-stationary, disparate media, Computers and Mathematics with Applications, *In press*, Submitted 28/03/17, Revisions submitted 06/11/17, Accepted 20/01/18, `https://doi.org/10.1016/j.camwa.2018.01.018`.

2. McCullough, J. W. S., Leonardi, C. R., Jones, B. D., Aminossadati, S. M. and Williams, J. R. (2016) Lattice Boltzmann methods for the simulation of heat transfer in particle suspensions, International Journal of Heat and Fluid Flow, vol. 62, part B, pp. 150-165.

Significant portions of this chapter have been adapted from Sections 3 onwards of Paper 1 above and from Sections 5-7 of Paper 2. As the lead author of both of these papers, I was responsible for significant portions of the following aspects:

- literature review presented in both papers (see also use of Paper 2 in Chapter 2)
- model development discussed in both papers
- analysis of results presented in both papers
- drafting of the respective manuscripts and their review.

The listed co-authors provided contributions towards the final review of the paper and suggestions as well as towards developing and improving the discussed results both in terms of analyses conducted and their presentation.

Estimated Contributions by Candidate		
	Paper 1	Paper 2
Conception and design	70%	80%
Analysis and interpretation	75%	75%
Drafting and production	70%	70%

Chapter 3

Conjugate heat transfer in the LBM

Consideration of conjugate heat transfer (CHT) ensures that thermal energy is correctly exchanged between two components of differing material properties. Capturing the behaviour of CHT requires the continuity of temperature, $T^{I,+} = T^{I,-}$, and heat flux, $\mathbf{n} \cdot (k\nabla T + \rho C_p \mathbf{u} T)^{I,+} = \mathbf{n} \cdot (k\nabla T + \rho C_p \mathbf{u} T)^{I,-}$, to be maintained at the boundary between disparate media. Here, the $+$ and $-$ indicate the two sides of interface I and $\mathbf{n}$ indicates the interface normal. Accounting for this numerically requires that information from the two components be swapped at interface locations, a process that can be difficult or expensive to perform. This chapter discusses and analyses methods for computing CHT within a D2Q9 passive scalar TLBM model. The single thermal population is used to capture heat transfer between the separate components in the studied system. Test cases that have been examined incorporate straight, curved and moving boundaries. Some preliminary tests were carried out to demonstrate the performance of TLBM in capturing CHT. A broader range of test cases were then examined in a more parametric study of model performance.

3.1 Approaches for conjugate heat transfer in TLBM

There exists two approaches for solving CHT in the LBM literature. The first method involves the calculation of an extra forcing term that is added to the nodal populations after the collision process has been calculated. This has been examined by Karani and Huber [105] for the SRT and by Hu *et al.* [106] for the MRT collision operators. This calculation can be performed based on local information only, particularly when the material properties and geometry of the boundary between them is known. The second approach adapts the populations of nodes at the interface of two components to enforce the continuity restrictions at these locations [104, 107, 83, 103, 108]. This computation is non-local in that information (in particular temperature) from the neighbouring nodes is needed to ensure these

conditions are met correctly. These modifications may take place before or after the collision process but serve to make use of information from both adjacent media.

One CHT method of each type mentioned above has been explored in this study. Both of these have been extended to identify the changes in material properties through the implementation of local values of τ_g based on the B value for a nodal cell. The thermal population is thus used to determine for the thermal state of the entire system, including both solid and fluid components in suspensions.

At interfacial locations where the coverage of the nodal cell by material 1 is $B \in (0, 1)$, the local value of property $\phi = \rho, C_p, k, \tau_g$ is found by $\phi_{local} = B\phi_1 + (1 - B)\phi_2$. Here 1 and 2 represent the values of ϕ in the respective components.

3.1.1 Local CHT calculation method

The first method of CHT calculation considered here is a modification of the local forcing term approach outlined by Karani and Huber [105] (KH method). Here the quantity,

$$F_i = w_i \frac{\partial}{\partial x_j}\left(\frac{1}{\rho C_p}\right)_l \cdot \left[\left(1 - \frac{1}{2\tau_g}\right)\sum_m (f_m - f_m^{eq})\mathbf{c}_m - u_j T_l\right], \tag{3.1}$$

is added to Equation 2.4 at boundary nodes of the particle where $B \in (0, 1)$ and at adjacent nodes. At these locations the term describing the gradient of $1/\rho C_p$ in the Cartesian direction j,

$$\frac{\partial}{\partial x_j}\left(\frac{1}{\rho C_p}\right)_l = \frac{((\rho C_p)_{l+1} - (\rho C_p)_{l-1})}{2(\rho C_p)_{l+1}\rho C_p)_{l-1}\Delta x_j}, \tag{3.2}$$

is non-zero. The subscript terms of $l - 1$, l and $l + 1$ refer to the node on the interface boundary and those neighbouring it in the normal direction. The locality of the method can be retained here if material properties and boundary geometry are known prior to calculation. The velocity term, u_j, within the convective component of the forcing term refers to the relative velocity of fluid at the interface location between two media. T_l refers to the local temperature at the boundary node. This forcing term has been calculated by determining the extra term needed to capture the conservative form of the energy equation when interfaces of disparate materials are present.

In [105], the forcing term was developed under the assumption that the interface is located halfway between two nodes. In this work it has been modified to assume that the interface is located at a node or, strictly, within its surrounding cell.

3.1.2 Non-local CHT calculation method

The non-local method for CHT studied here is based on the method of Mohamad *et al.* [104] (MTHB method). In this method, an energy balance is used to calculate the updated temperature at the interface nodes between two materials so as to ensure the continuity relationships for CHT are maintained. This occurs at each time step by,

$$T_{\text{int}}^{\text{new}} = \frac{E_{\text{int}}\Delta t}{(\rho C_p)_{\text{local}}(\Delta x)^2}, \tag{3.3}$$

where,

$$E_{\text{int}} = k_1 T_1 + k_2 T_2 + T_{\text{int}}^{\text{old}} \left(\frac{(\rho C_p)_{\text{local}}(\Delta x)^2}{\Delta t} - k_1 - k_2 \right). \tag{3.4}$$

The energy balance used here does not include the convective component of flux at the interface. In the current work, we have included such a term to Equation 3.4 to allow the MTHB method to be utilised in cases where a relative fluid flow velocity (u_{rel}) is incident upon an interface between two media. The form of E_{int} is then,

$$E_{\text{int}} = k_1 T_1 + k_2 T_2 + T_{\text{int}}^{\text{old}} \left(\frac{(\rho C_p)_{\text{local}}(\Delta x)^2}{\Delta t} - k_1 - k_2 - \Delta x u_{rel} \left((\rho C_p)_1 - (\rho C_p)_2 \right) \right). \tag{3.5}$$

This value for E_{int} is then used in the equilibrium function calculation for the thermal population to update the interface node populations via an SRT process. The relaxation parameter used for these populations varies based on the velocity direction. If the velocity is tangential to the interface then the local τ_g is used, otherwise the relaxation parameter corresponding to the material properties in the lattice velocity direction is used. This is graphically outlined in Figure 3.1. It can be further re-emphasised here that this method is regarded as non-local due to the requirement of retrieving temperature data from neighbouring nodes. Unlike the expression in Equation 3.2, this cannot be pre-computed from material or boundary information.

For more detailed derivations of the two basic methods used here for the calculation of CHT, the reader is referred to the source papers of [105] (KH) and [104] (MTHB) respectively.

3.2 Preliminary studies

Preliminary studies were carried out with the non-local MTHB approach to CHT. Being based on a finite difference approximation of the fundamental CHT equations makes this approach a natural

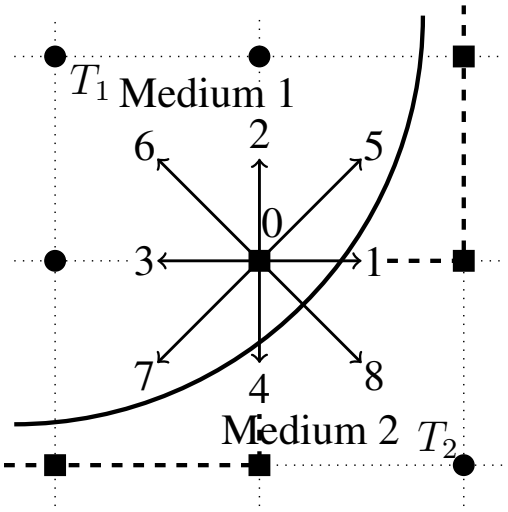

Figure 3.1: Relaxation strategy for the curved interface of a solid particle (solid line) and a surrounding fluid with the MTHB method. The dark dashed line is the numerical interface boundary. Populations g_0, g_5 and g_7 are relaxed according to local (coverage weighted) material properties; g_2, g_3 and g_6 with Medium 1 properties and g_1, g_4 and g_8 with Medium 2 properties. The target nodes for T_1 and T_2 in Equations 3.3, 3.4 and 3.5 are also identified.

choice to initially investigate. The test cases chosen have been selected to replicate situations that will need representation within a particle suspension.

The calculation of thermal interaction between two separate media within the MTHB framework was first tested through comparison to the analytic solution for a bar with a straight interface between the materials. This was then examined under two initial conditions, referred to as Case 1 and Case 2, as illustrated in Figure 3.2. The analytic solution for these situations has been developed from the results in Sun and Wichman [109]. This solution calculates a transient temperature profile for a three-layer slab, solving with two adjacent layers having the same material properties yields the desired two-layer solution. Converted to physical units the results from [109] can be expressed as,

$$T(x,t) = (T_H - T_C) * (\psi(x) - \phi(x,t)) + T_C, \tag{3.6}$$

where,

$$\psi(x) = \begin{cases} 1 - \Delta\theta_1 \frac{x}{d_1} & x \in (0, d_1) \\ 1 - \Delta\theta_1 - \Delta\theta_2 \frac{x-d_1}{d_2} & x \in (d_1, d_2) \\ 1 - \Delta\theta_1 - \Delta\theta_2 - \Delta\theta_3 \frac{x-d_1-d_2}{d_3} & x \in (d_2, d_3) \end{cases}, \tag{3.7}$$

and,

$$\phi(x,t) = \begin{cases} \sum_{n=0}^{\infty} A_n e^{-\alpha_1(\frac{\lambda_n}{d_1})^2 t} X_{1,n}(x) & x \in (0, d_1) \\ \Delta_1 \sum_{n=0}^{\infty} A_n e^{-\alpha_1(\frac{\lambda_n}{d_1})^2 t} X_{2,n}(x) & x \in (d_1, d_2) \\ \Delta_2 \sum_{n=0}^{\infty} A_n e^{-\alpha_1(\frac{\lambda_n}{d_1})^2 t} X_{3,n}(x) & x \in (d_2, d_3) \end{cases}, \tag{3.8}$$

with $\Delta\theta_i = \frac{d_i/k_i}{d_1/k_1+d_2/k_2+d_3/k_3}$; $\Delta_i = \frac{k_1 d_{i+1}}{d_1 k_{i+1}}\sqrt{\frac{\alpha_{i+1}d_1^2}{d_{i+1}^2\alpha_1}}$ and d_i being the thickness and k_i the thermal conductivity of layer i.

The eigenfunctions $X_{i,n}(x)$ are:

$$X_{i,n}(x) = \begin{cases} \sin(\lambda_n \frac{x}{d_1}) & x \in (0, d_1) \\ \cos(\lambda_n)\sin(\sqrt{\frac{\alpha_1 d_2^2}{d_1^2\alpha_2}}\lambda_n \frac{x-d_1}{d_2}) + \frac{\sin(\lambda_n)\cos(\sqrt{\frac{\alpha_1 d_2^2}{d_1^2\alpha_2}}\lambda_n \frac{x-d_1}{d_2})}{\Delta_1} & x \in (d_1, d_2) \\ \left[\frac{\cos(\lambda_n)\cos(\sqrt{\frac{\alpha_1 d_2^2}{d_1^2\alpha_2}}\lambda_n) - \sin(\lambda_n)\sin(\sqrt{\frac{\alpha_1 d_2^2}{d_1^2\alpha_2}}\lambda_n)}{\Delta_1}\right]\sin(\sqrt{\frac{\alpha_1 d_3^2}{d_1^2\alpha_3}}\lambda_n \frac{x-d_1-d_2}{d_3}) + \\ \quad \left[\frac{\cos(\lambda_n)\sin(\sqrt{\frac{\alpha_1 d_2^2}{d_1^2\alpha_2}}\lambda_n)\Delta_1}{\Delta_2} + \frac{\sin(\lambda_n)\cos(\sqrt{\frac{\alpha_1 d_2^2}{d_1^2\alpha_2}}\lambda_n)}{\Delta_2}\right]\cos(\sqrt{\frac{\alpha_1 d_3^2}{d_1^2\alpha_3}}\lambda_n \frac{x-d_1-d_2}{d_3}) & x \in (d_2, d_3) \end{cases}. \tag{3.9}$$

The eigenvalues themselves, λ_n, are found by numerically determining values that satisfy,

$$\tan(\lambda_n) = \frac{-(\Delta_1 \tan(\sqrt{\frac{\alpha_1 d_2^2}{d_1^2\alpha_2}}\lambda_n) + \Delta_2 \tan(\sqrt{\frac{\alpha_1 d_3^2}{d_1^2\alpha_3}}\lambda_n))}{1 - \frac{\Delta_2}{\Delta_1}\tan(\sqrt{\frac{\alpha_1 d_2^2}{d_1^2\alpha_2}}\lambda_n)\tan(\sqrt{\frac{\alpha_1 d_3^2}{d_1^2\alpha_3}}\lambda_n))}. \tag{3.10}$$

Finally, the terms A_n depend on the initial condition being implemented. For Case 1 it can be determined that,

$$A_n = (k_2k_3)/\Bigg(d_2d_3\lambda_n\left[\frac{k_2k_3}{2d_2d_3} + \frac{k_1k_3}{2d_1d_3}\left[\cos^2(\lambda_n) + \frac{\sin^2(\lambda_n)}{\Delta_1^2}\right] + \frac{k_1k_2}{2d_1d_2}\Bigg(\left[\cos(\lambda_n)\cos(\sqrt{\frac{\alpha_1 d_2^2}{d_1^2\alpha_2}}\lambda_n) - \frac{\sin(\lambda_n)\sin(\sqrt{\frac{\alpha_1 d_2^2}{d_1^2\alpha_2}}\lambda_n)}{\Delta_1}\right]^2 + \left[\frac{\cos(\lambda_n)\sin(\sqrt{\frac{\alpha_1 d_2^2}{d_1^2\alpha_2}}\lambda_n)\Delta_1}{\Delta_2} + \frac{\sin(\lambda_n)\cos(\sqrt{\frac{\alpha_1 d_2^2}{d_1^2\alpha_2}}\lambda_n)}{\Delta_2}\right]^2\Bigg)\Bigg]\Bigg). \tag{3.11}$$

.

To solve for Case 2, the A_n from Case 1 is multiplied by $\cos(\lambda_n)$.

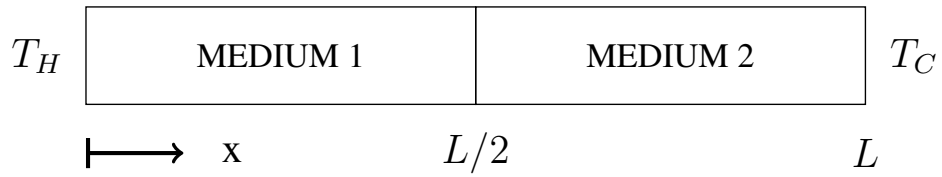

CASE 1:	CASE 2:
$T(x = 0, t = 0) = T_H$	$T(x \leq L/2, t = 0) = T_H$
$T(0 < x \leq L, t = 0) = T_C$	$T(x > L/2, t = 0) = T_C$

Figure 3.2: Layout of the two-medium bar test case used to examine the performance of the proposed TLBM interface model. The boundary conditions used with two separate cases of initial conditions are compared against analytic results from Sun and Wichman [109].

The heat transfer model was then applied to a suspension by examining the cooling behaviour of a single, stationary particle within a surrounding fluid. Both transient and steady-state behaviours were examined in this context. The transient system, illustrated in Figure 3.3, is compared to the analytic solution for such a layout by Jain *et al*. [110]. This solution, like that of Sun and Wichman for the bar tests, is a summation of terms generated through the separation of variables method for solving the appropriate partial differential equation with the given boundary and initial conditions. In the radial case, Bessel functions are required to be implemented instead of trigonometric functions. For further details the reader is referred to Jain *et al*. [110].

For steady-state testing, the outer circular boundary is replaced with a periodic square boundary. The steady-state results are evaluated through comparison to an energy balance of the solid and fluid initial temperatures (subscript I) and volumes (V). This is found by solving for the final temperature, T_f, in $(\rho C_p V)_F(T_{F,I} - T_f) = (\rho C_p V)_S(T_f - T_{S,I})$.

The material properties used for the two media in these tests are detailed in Table 3.1.

3.2.1 Results and discussion of preliminary study

In addition to the direct comparison of the model results with analytic solutions when possible, the L_2 and L_∞ norms were used as judgements of overall error. These metrics were calculated as,

$$L_2 = \sqrt{\frac{\sum_{j=1}^{N} |T_j - T_{j,analytic}|^2}{N}}, \tag{3.12}$$

and,

$$L_\infty = max|T_j - T_{j,analytic}|, \tag{3.13}$$

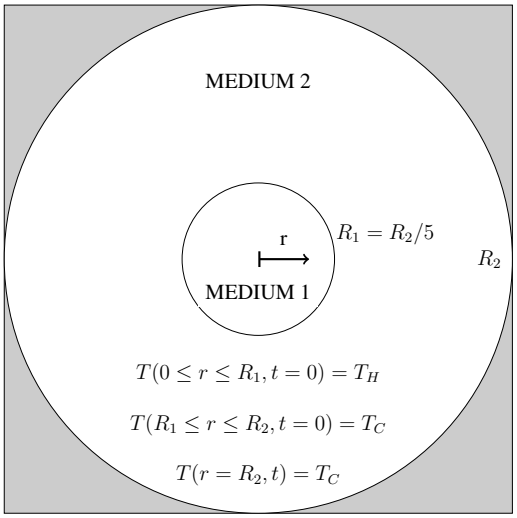

Figure 3.3: Layout of the two-medium radial test case used to examine the interface model on curved boundaries. The boundary and initial conditions used in these tests are compared against analytic results from Jain *et al.* [110]. To impose a circular boundary on the LBM grid, nodes in the shaded region were set to T_C as fixed temperature walls.

Property	**Medium 1**	**Medium 2**
Material	Solid	Fluid
$k\ [W/m.K]$	2.86	0.60
$\rho\ [kg/m^3]$	2,650	1,000
$C_p\ [J/kg.K]$	830	4,181
$\nu\ [m^2/s]$	-	1×10^{-6}

Table 3.1: Material data used for the two media in the heat conduction tests. The solid material values approximately represent sand and the fluid values water.

respectively. Both measures were compared to the appropriate analytic solution and defined using N data points along a profile with T_j being the temperature at location j.

Three levels of grid refinement were used for the two-medium bar test with Δx set to 5×10^{-5}m, 2.5×10^{-5}m and 1.25×10^{-5}m (coarse, medium and fine respectively). The relaxation parameters were held constant between each stage of refinement to minimise its impact on results. The time step was accordingly varied based on Equation 2.12 and the thermal diffusivity of the fluid component.

Two medium bar tests

The thermal response of the model over time for the test cases was compared to the analytic solution of Sun and Wichman [109], which examines three layer transient heat conduction in a 1D slab. The two layer problem examined here was generated by setting two adjacent layers to the same material properties. The initial condition used by Sun and Wichman was also adapted to allow the Medium 1 region to start at the T_H temperature rather than the entire domain being initialised at the T_C temperature.

Figures 3.4 and 3.7 illustrate the difference between the ideal and analytic initial conditions imposed on the bar cases. In these tests, T_H = 350K and T_C = 300K. The ideal initial condition (replicating that stated in Figure 3.2) was able to be applied to the numerical model but was not able to be captured accurately by the analytic model.

Figures 3.5 and 3.6 illustrate the transient behaviour of the relative errors and norms for the Case 1 scenario as it reaches steady-state. Figures 3.8 and 3.9 illustrate these measures for Case 2.

From Figure 3.5 the passage of heat through the bar can be noted as the reason for the delayed onset of error along the length of the bar. Upon reaching steady-state, the greatest error occurs at the interface itself where the -0.12% relative error indicates the model temperature being approximately 0.4K below the analytic solution. This slight error suggests that not enough heat is able to move through the bar from the high temperature end and may be a consequence of the relaxation parameters not being optimal for this problem.

Figure 3.6 illustrates the improvement in accuracy of results with grid resolution across the full duration of the experiments for both norm measures. The variation of the norm values (and magnitude of relative error, especially at the interface) may potentially be due to the computational time needed for the interface temperature condition to firstly impact on the surrounding nodes and secondly capture the appropriate flux continuity condition.

Similar to Case 1, the passage of heat dissipation from the interface in Case 2 can be noted by the delayed growth of error magnitude at the locations midway through each component in comparison to

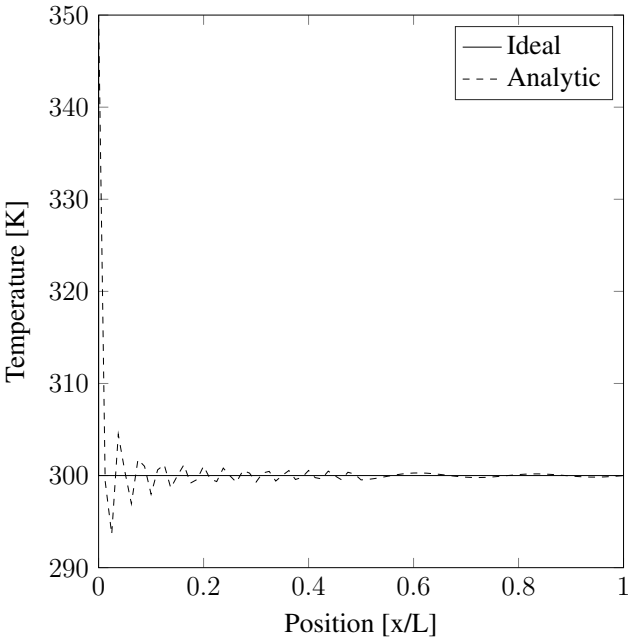

Figure 3.4: Difference in initial temperature between the ideal situation and that calculated by the analytic solution with 100 eigenvalues for the two-medium bar test and Case 1 initial condition.

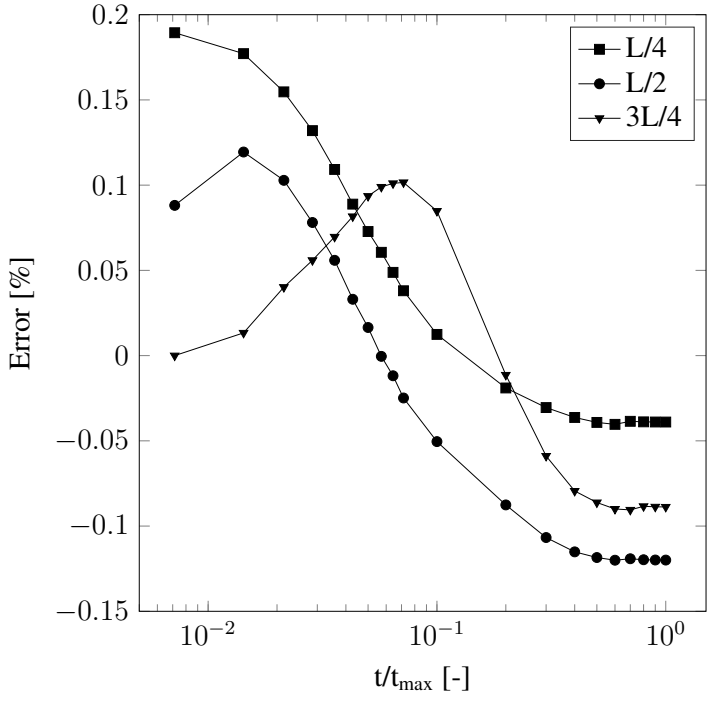

Figure 3.5: Development of the relative error between the model results and the analytic solution over time in the two-medium bar with Case 1 initial condition. The error has been measured at three locations the interface (L/2) and at the centre of the two media (L/4 for Medium 1 and 3L/4 for Medium 2). These results were observed with the fine level of grid refinement.

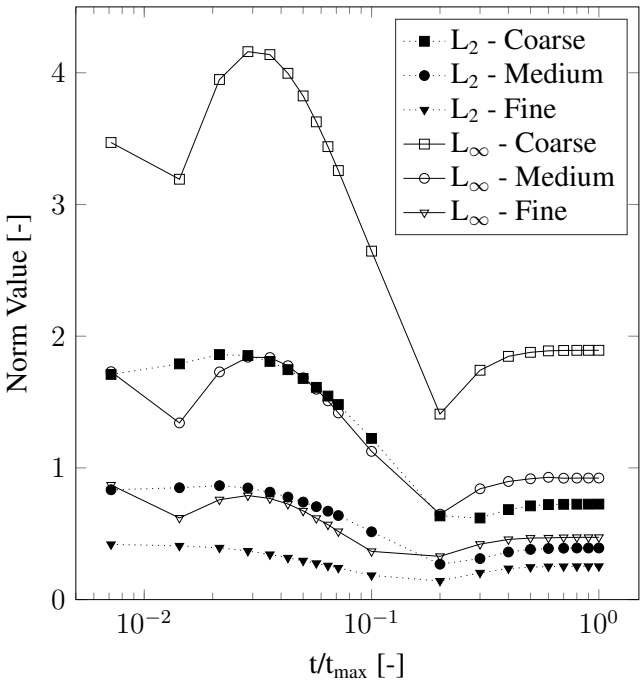

Figure 3.6: Development of the L_2 norm and L_∞ norm comparisons of the model results and analytic solution over time in the two-medium bar with Case 1 initial condition at the three levels of grid resolution.

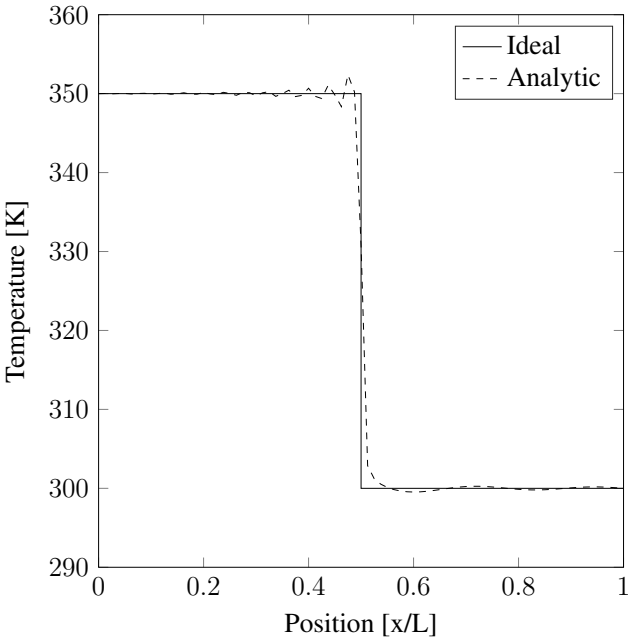

Figure 3.7: Difference in initial temperature between the ideal situation and that calculated by the analytic solution with 100 eigenvalues for the two-medium bar test and Case 2 initial condition.

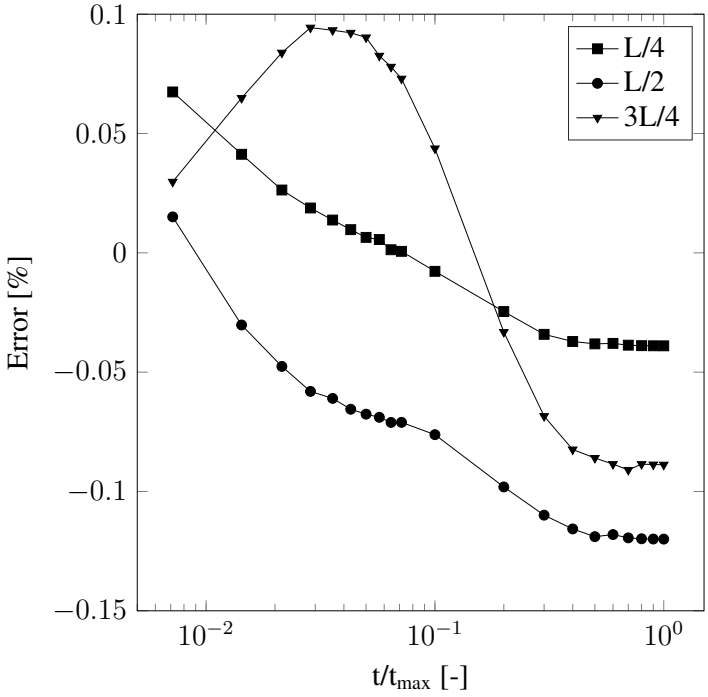

Figure 3.8: Development of the relative error between the model results and the analytic solution over time in the two-medium bar with Case 2 initial condition. The error has been measured at three locations the interface (L/2) and at the centre of the two media (L/4 for Medium 1 and 3L/4 for Medium 2). These results were observed with the fine level of grid refinement.

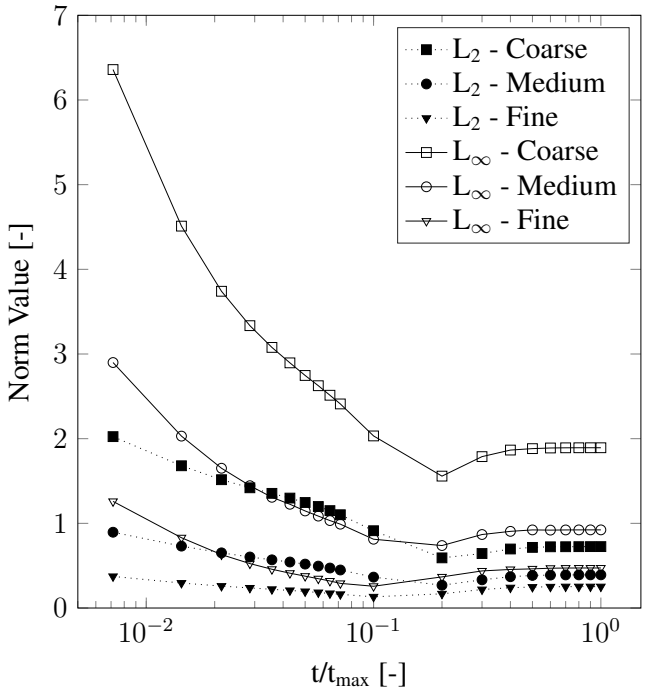

Figure 3.9: Development of the L_2 norm and L_∞ norm comparisons of the model results and analytic solution over time in the two-medium bar with Case 2 initial condition at the three levels of grid resolution.

that at the interface (Figure 3.8). Again, the steady-state solution reached by the model has converged to a profile slightly lower than the analytic outcome. However, an overall error magnitude of less than 0.1% over the duration of the simulation is an acceptable outcome for the model.

After generally starting at greater norm values than in Case 1, the convergence of the Case 2 numerical results proceeded more smoothly as is illustrated in Figure 3.9. The results improve with grid refinement as anticipated and generally reduce in time as the simulations reach the steady-state solution. Further analysis of the accuracy of the solution as a function of the relaxation parameter has been left as a future study. As expected, the same steady-state values as in Case 1 for the norms have been obtained in Case 2. This is because the steady-state solution is independent of the initial conditions.

The differing initial behaviour of the norms in Figures 3.6 and 3.9 would seem to be a result of how the applied initial condition interacts with the interface method. Case 1 allows heat to be transferred through the interface condition from an originally continuous state. The application of a jump in temperature at the interface in Case 2 provides an initial error that is required to be dissipated by the system. It is worth noting that the analytic equation set used in Case 2 calculates an initial temperature of approximately 331K at the interface of the two components compared to the ideal 350K which was implemented numerically.

The order of convergence of the bar tests can be seen to reflect the first order behaviour anticipated by the finite difference approximations made by the model. This behaviour can be more formally observed for both test cases in Figures 3.10. This convergence can be seen during both the transient dissipation of heat through the bar and when it has reached steady-state.

Two medium radial tests

The test layout illustrated in Figure 3.3 can be used to examine the transient behaviour of the model against the analytic situation proposed by Jain *et al.* [110]. This layout can be interpreted as a particle of Medium 1 immersed within Medium 2. The steady-state behaviour within this scenario is trivial however as it consists of the entire domain cooling to the outer wall temperature. To better examine the steady-state temperature evaluation of an immersed particle, a circular particle is placed in the centre of a square domain possessing periodic boundaries. This situation provides a non-trivial steady-state that the model must converge towards.

Figures 3.11 highlights the variation between the analytic and ideal (and numerically implemented) initial conditions imposed on the radial cases, in these tests $T_H = 350K$ and $T_C = 300K$. Figures 3.12 and 3.13 illustrate the relative errors and norms respectively this test case. Table 3.2

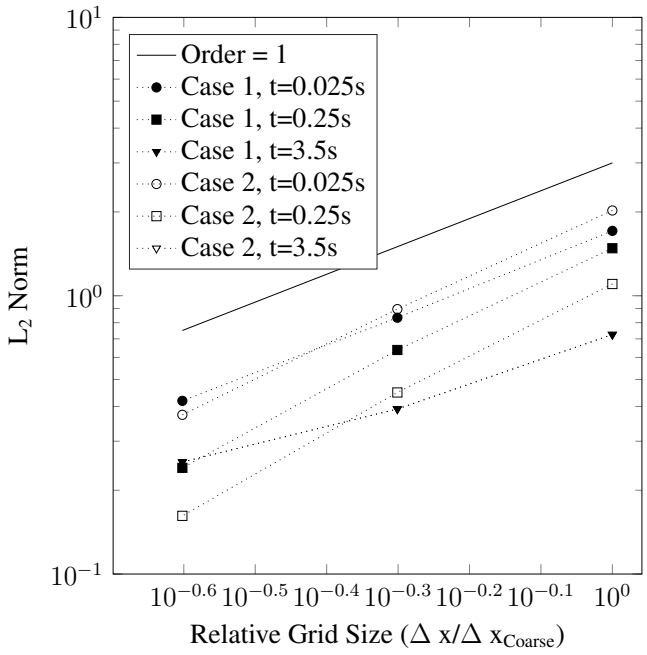

Figure 3.10: Change in L_2 norm with grid refinement at $t = 0.025, 0.25$ and $3.5s$ for the bar test cases. A slope indicating first order improvement is included for comparison. The steady-state results ($t = 3.5s$) are effectively identical for both cases.

T_F	T_S	$T_{f,Theory}$	$T_{f,Coarse}$	$T_{f,Medium}$	$T_{f,Fine}$
300	305	300.084	300.102	300.088	300.088

Table 3.2: Observed steady-state particle temperatures, T_f, compared to an energy balance model for a circular particle within a rectangular, periodic domain at three levels of grid resolution. The solid component started at $T_S = 305K$ and the fluid $T_F = 300K$ in an attempt to reduce the simulation time needed to reach equilibrium.

details the steady-state temperature results of a heated particle immersed within a fluid.

The approach used in Figure 3.3 to capture a radial domain on a Cartesian grid was observed to successfully maintain the desired angular symmetry of the temperature profiles. A contour plot of temperature illustrating this is presented in Figure 3.14.

The error seen in the radial system (Figure 3.12) compared to its analytic solution is larger than that seen in the bar problem but still of an acceptably small magnitude. This is not unexpected given the difficulties associated with replicating a curved surface on a Cartesian LBM grid despite the performance shown in Figure 3.14. The Medium 2 section of the domain does not deviate far from the initial temperature condition due to the larger volumetric heat capacity (ρC_p) and significantly larger area of this section combining to reduce the temperature gain associated with heat flow from Medium 1. The fixed temperature outer wall also more directly influences the temperature behaviour

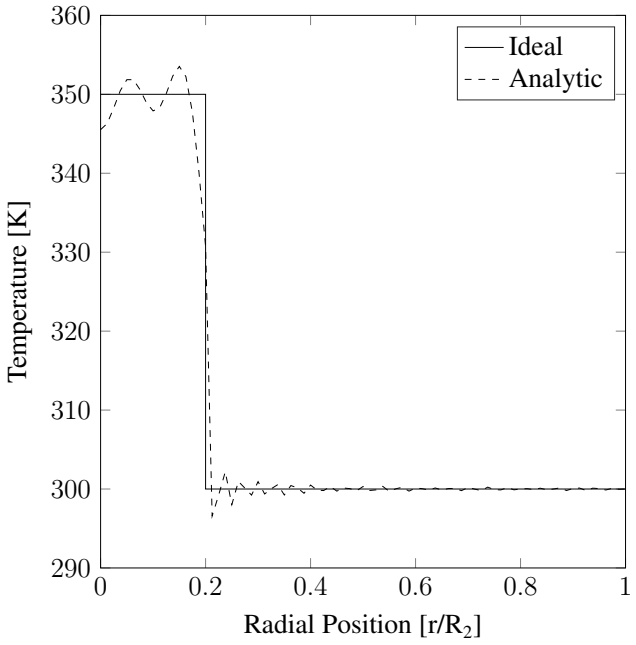

Figure 3.11: Difference in initial temperature between the ideal situation and that calculated by the analytic solution with 50 eigenvalues for the two-medium radial test.

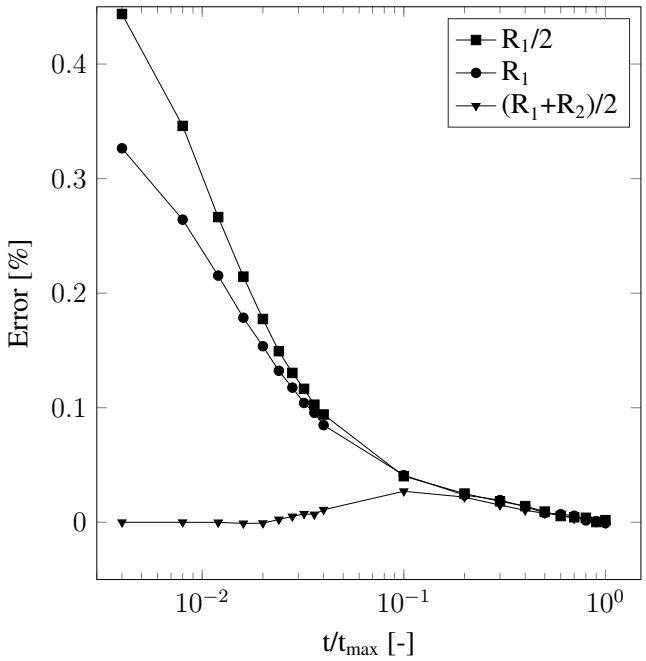

Figure 3.12: Development of the relative error between the model results and the analytic solution over time in the radial test case. The error has been measured at three locations: the interface (R_1) and at the centre of the two media ($R_1/2$ for Medium 1 and $(R_1 + R_2)/2$ for Medium 2). These results were observed with the fine level of grid refinement.

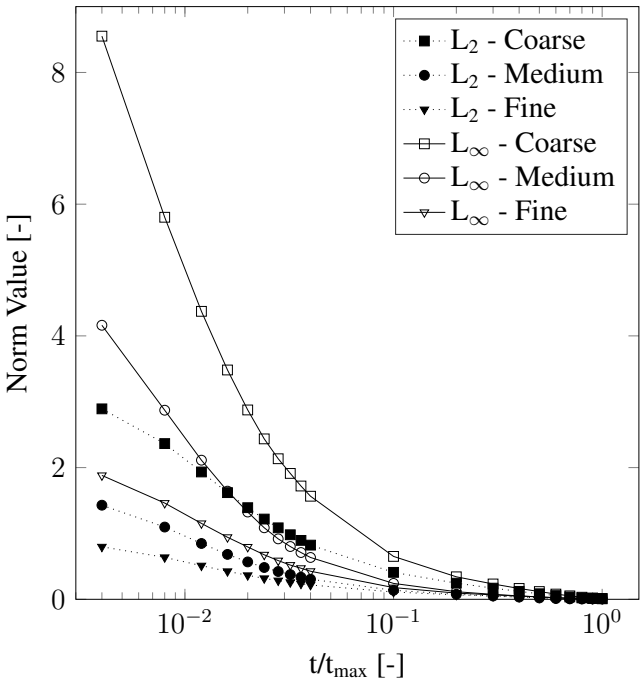

Figure 3.13: Development of the L_2 norm and L_∞ norm comparisons of the model results and analytic solution over time in the radial test case at the three levels of grid resolution.

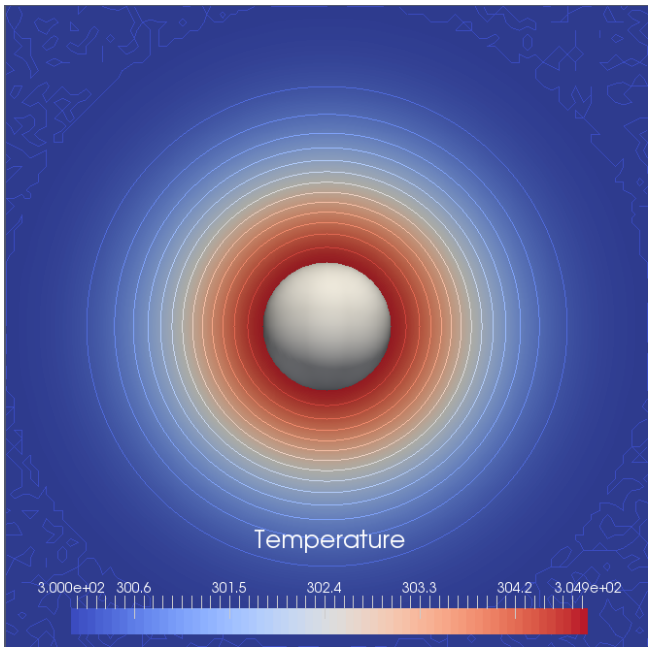

Figure 3.14: Temperature [K] contours for the cooling of a particle in a circular domain as per Figure 3.3. The desired symmetry of the temperature profiles has been maintained despite a rectangular grid being used. This figure was created from the medium grid resolution test case.

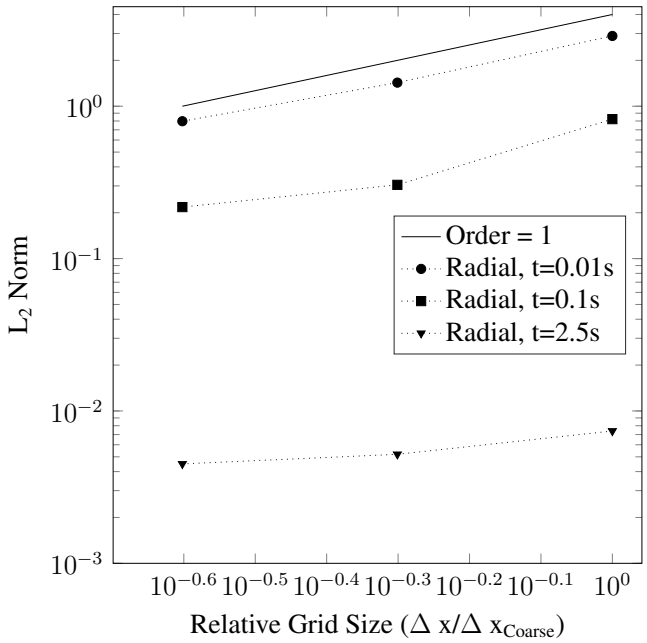

Figure 3.15: Change in L_2 norm with grid refinement at $t = 0.01, 0.1$ and $2.5s$ for the radial test cases. A slope indicating first order improvement is included for comparison.

in Medium 2 than in Medium 1. As the simulation progresses, the error across the domain becomes consistent and tending to zero as the simulation converges towards the steady-state.

The norms of the radial test, shown in Figure 3.13, again demonstrate the convergence of the solution to the steady-state solution with both measures tending towards zero. The simulations generate the anticipated first-order spatial convergence especially at shorter time scales. These results are presented in Figure 3.15. At longer time scales, the convergence behaviour becomes less than first order due to the constant temperature steady-state being consistently approached by all scales of grid refinement.

As was noted for the bar tests, the numerical tests were initialised using the ideal temperature profile. The initial population values were assigned at each nodal location based on the equilibrium distribution values i.e. the '0' population is $4T/9$, populations '1'-'4' are $T/9$ and populations '5'-'8' are $T/36$ where T is the assigned initial nodal temperature. In both test cases the LBM fluid is initialised as stationary with an equilibrium distribution (replacing T in the above notes with ρ). It is recognised that it may be possible to achieve improved results if a non-equilibrium initial distribution is utilised as noted by Caiazzo [111] and Mei *et al.* [112]. However, the equilibrium format is felt to be adequate for these test cases as it maintains generality of the modelling procedure.

The steady-state test with periodic boundary conditions (Table 3.2) illustrates the ability of the model to capture the particle temperature in a non-trivial situation. The model had an error of 0.018K for the coarse grid spacing and 0.004K for the medium and fine spacings. The result for the fine

spacing is slightly improved upon the medium test when the next significant digit of the particle temperature is considered. It would appear, however, that the limit of the model in terms of accuracy with grid refinement has been reached for this case.

Further observations

A further observation to make based on these results is that all test cases capture the analytic solution to an acceptable degree of accuracy. At very short time frames, the analytic solutions become more sensitive to the number (and accuracy) of eigenvalues used in the expansions. This is especially notable in the initial condition examples in Figures 3.4, 3.7 and 3.11. To attempt to alleviate this the first 100 eigenvalues were used for the bar tests and the first 50 for the radial tests. These quantities of eigenvalues are five times greater than those that the source papers used in their respective illustrations.

It is known that the performance of hydrodynamic LBM simulations is strongly dependent on the value of the relaxation parameter used [113]. It would be expected that such behaviours occur for thermal simulations as well. The ability to choose the relaxation parameters for each component being modelled is impacted by the difference in material properties of the system under consideration. In particular, as the time step and grid spacing is required to be constant within a system, the relaxation parameters of components 1 and 2 are related by their respective values of thermal diffusivity,

$$\frac{\alpha_1}{\alpha_2} = \frac{\tau_1 - 0.5}{\tau_2 - 0.5}. \tag{3.14}$$

Whilst the relaxation parameters used in this study have been held constant between each test, the values used were chosen largely for numerical convenience. It is quite likely that results could be improved through optimisation of the relaxation parameters.

In this study, the SRT approach has been utilised due to its advantages of efficiency and convenience of implementation. It has been recognised in the literature that the MRT version of the relaxation operator can provide more stable and accurate results for general fluid flows [114], thermal behaviours [74] and for particle suspension hydrodynamics [115]. Implementation of the MRT model would be another avenue worthy of future investigations of transient thermal behaviours within particle suspensions. In this study, the variation of material properties is determined through variation of the local relaxation parameter, in any generalisation to an MRT scheme this variation would need to be correctly replicated amongst the additional relaxation times.

What is also seen is that the steady-state solution is approached to an acceptable degree of accuracy regardless of the grid resolution tested. However, when modelling dense particle suspension flows,

the short time transient behaviours are typically of greater interest as the properties of the constituent components change too frequently for a steady-state to be achieved. In particular, such transience would arise from contact between particles and the thermal interaction of particles with a variable surrounding fluid.

3.3 Parametric studies

Based on the results of the preliminary studies, a parametric test campaign was conducted. This assessed the performance of a local and non-local version of CHT formulations. Understanding the comparative behaviour of two such schemes is critical to the overall performance of TLBM which, ideally, can be constructed as a purely local method. First, verification of the selected models was performed through comparison against transient, analytic solutions for two-medium test cases in one- and two-dimensions. The performance of the models in the presence of flow was also examined. Validation of the models was then been performed for static and dynamic particle suspensions.

3.3.1 Verification tests

The first set of verification tests examined the parametric variation of heat conduction through a two material system. These cases studied a one-dimensional bar and a two-dimensional radial system, with the layouts based on those used in the preliminary studies.

In addition to a reference case of the two regions possessing identical material properties, three permutations of parametric variations were conducted. These were defined based on differences in the thermal properties between the two layers of media as outlined in Table 3.3. For each test case, the varied ratio is altered to values of 2.5 and 5 whilst maintaining the constant property as equal between the two media. Here, these will be referred to as $P1, P2$ and $P3$ respectively. Thus $P1_{2.5}$ refers to case $P1$ with $\frac{k_1}{k_2} = 2.5$.

The reference problem and each test case in Table 3.3 were undertaken on a coarse, medium and fine grid spacing with an overall simulation time of 3,000 Δt_{coarse} for the bar scenario and 9,000 Δt_{coarse} for the radial simulation. For the coarse test cases, the total length of the bar and the outer radius of the larger radial domain were $10\Delta x_{coarse}$. This was doubled for each level of grid refinement. The bar test case was also separately run until a steady-state was reached. This was done in order to provide some further insight on the accuracy of the models being investigated. It should be noted here that the material properties and relaxation parameters used were held constant between the different levels of grid refinement. As such, the time step used in each simulation was simultaneously reduced

Test Case	Varied Ratio	Constant Property
$P1$	$\frac{k_1}{k_2}$	ρC_p
$P2$	$\frac{(\rho C_p)_1}{(\rho C_p)_2}$	α
$P3$	$\frac{\alpha_1}{\alpha_2}$	k

Table 3.3: Property variations of the three test cases used to parametrically evaluate the two CHT methods being investigated. These tests fix the varied ratio at values of 2.5 and 5 between the two media and hold the constant property as equal.

in a diffusive manner. If a specific time step reduction was desired than the result of such a trial could be determined from comparing the corresponding grid spacing to the coarse, medium and fine results.

In physical units, the base values for the thermal properties were taken as $k = 1W.m^{-1}.K^{-1}$, $\rho = 1,000kg.m^{-3}$ and $C_p = 1,000J.kg^{-1}.K^{-1}$. These values and ratios were not chosen to represent any real material or system, merely to illustrate the capabilities of the model.

In suspensions with moving particles, the short-term transient rather than steady-state behaviour may be of greater interest when observing how the system behaves. In order to quantify this behaviour in some manner, an integer weighted norm (IWN),

$$\text{IWN} = \sum_{out=1}^{out_{\max}} \frac{out_{\max} - out + 1}{\sum_{j=1}^{out_{\max}} j} L_{x,out} = I_{out} L_{x,out}, \tag{3.15}$$

has been used in this study. Here the output data of the desired norm, L_x, at chronological stages $out = 1, \ldots, out_{max}$ is weighted more heavily the earlier they are generated in the simulation. For example, if five (evenly spaced) outputs are generated during a simulation the earliest set of data will be weighted with a factor of $I_{out} = \frac{5}{15}$ and the final output with $I_{out} = \frac{1}{15}$. In this study, the L_2 norm from the preliminary study was utilised. The IWN has been implemented here so as to provide a measure of the early transient performance of the two models being compared within a single value. It should be noted here that as the IWN favours earlier time outputs, where a transient system may be changing considerably, it may be considered an tough measure of overall model performance.

Two medium bar test

This study analysed the Case 2 scenario presented in Figure 3.2. The IWN results calculated for the two methods were generated for the two medium bar test using the analytic solution described previously from Sun and Wichman [109]. These are presented for the transient case in Figure 3.16 and the L_2 norm results for the steady-state problem in 3.17. A graphical indication of convergence

performance for the tests is given in Figures 3.18 and 3.19.

During the transient tests (Figure 3.16), it can be seen that when replicating the behaviour of a single continuous medium (the 'Reference' case) both methods perform well. Improving results with grid refinement and independence from the average value of τ_g between the two media can be seen. Generally similar behaviour can be seen for the $P1$ and $P3$ test cases however the improvement between the medium and fine grid spacings has been reduced for the MTHB method. In the $P2$ case, the convergence behaviour for the KH model again behaves as expected however the MTHB method does present some unexpected convergence behaviour for the $P2_{2.5}$ case. There is also a greater dependence on the τ_g values used for both methods. For each of these cases, the average order of convergence is approximately one.

Once steady-state has been reached in these cases, different observations can be made (see Figure 3.17). Firstly, both models generate identical results for the reference case and exhibit no L_2 norm error when a value of $\tau_g = 1$ is used for the media. In the $P1$ case, it is the KH method that displays significantly more accurate and τ_g-invariant results. The MTHB results, though converging in the correct manner with grid refinement, departs from the analytic solution by an amount increasing with the average τ_g of the simulation.

At steady-state, the $P3$ behaviour of both models occasionally does not display conventional convergence behaviour. This is particularly noticeable for a property ratio of 5 for the KH model and at higher average τ_g for the MTHB model. As the $P1$ case (with the same average τ_g but with varying k and constant ρC_p) gives good results, it can be inferred that the variation of τ_g between the two media is not the cause of this. Instead it would appear that the change in ρC_p gives rise to the fine resolution returning poorer results than coarser grid spacings. The MTHB model however does display a much lower L_2 norm for the $P3$ case than the KH model. It also appears to be largely independent of τ_g at steady-state.

It has been noted in some studies, for example [100], using conventional numerical solution methods, specifically SIMPLE-like algorithms, that the variation of the ρC_p quantity between adjacent regions can lead to errors in the calculation of CHT behaviours. It seems likely from the results observed here that similar considerations should be taken into account when using LBM.

For the steady-state $P2$ case it appears that the performance of the KH model with respect to grid refinement is dependent on τ_g and the ratio value. In the $P2_{2.5}$ case, the medium and fine results are similar at all τ_g values. For the $P2_5$ case, cases with average τ_g less than one also see the medium and fine results being similar. However for the two cases of greatest average τ_g it is the coarse and medium results that generate almost identical results. The MTHB model has all three levels of grid refinement producing similar results over a wide range of τ_g values used. In some cases though it

was observed that a coarser level of grid refinement yielded a better L_2 norm than a finer one. This highlights a shortcoming of both models when the values of ρC_p are varied between material regions as already observed.

The physical parameters chosen for the $P2$ case lead to the steady-state being reached in a relatively short period of time and the discrepancies become apparent in the tests conducted here. The discrepancy in steady-state values for the $P2_5$ case is illustrated in Figure 3.20. It is important to note however that the magnitude of error presented at steady-state, seen in Figure 3.20, is similar to that presented in Karani and Huber [105].

In general, however, it can be concluded that the steady-state results for both models do show convergence towards the analytic results with grid refinement.

Two medium radial test

The layout, boundary and initial conditions used for the parametric two medium radial test case were very similar to those illustrated in Figure 3.3. The only difference was that R_1 was doubled in size to $0.4R_2$. The IWN results calculated for the two medium radial test are presented in Figure 3.21 and the corresponding convergence plots are given in Figure 3.22.

In a 2D radial setting, the IWN results are broadly similar to those discussed for the bar test. It should first be noted that in the $P1$ and $P3$ tests both models were unstable when the lowest average τ_g was used. These are represented in Figure 3.21 as an IWN of zero.

In this case, the MTHB method provides generally lower IWN values than the KH method. The most obvious difference between the two methods is the variation of the MTHB method with changing average τ_g values. In particular, the Reference and $P3$ cases showed the smallest error at the lowest values of τ_g. This is not ideal in practice as this state corresponds to those with the smallest Δt and hence longer simulation times for a desired physical time. Such implementations may also be problematic due to the linkage of the thermal and fluid domains by Δx and Δt. From this, τ_g approaching 0.5 may imply that τ_f would also be reduced towards values where hydrodynamics may become unstable [114]. This behaviour is dependent on the physical Prandtl number ($Pr = \nu/\alpha$) of the fluid being modelled.

Figure 3.22 illustrates the KH method generally displaying approximate first order convergence for most tests. The MTHB approach however shows improvement that is slightly greater than first order for the step between the coarse and medium grid spacings but generally negligible improvement between the medium and fine grids. This suggests that either the MTHB method is grid independent for this test case or the error becomes dominated by another source at further refinement. Again the

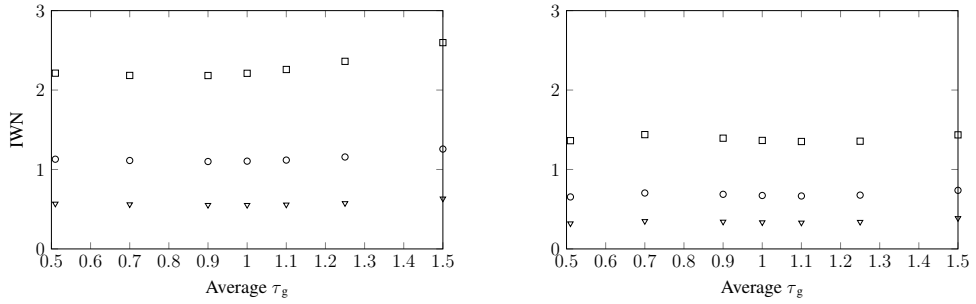

(a) Reference case

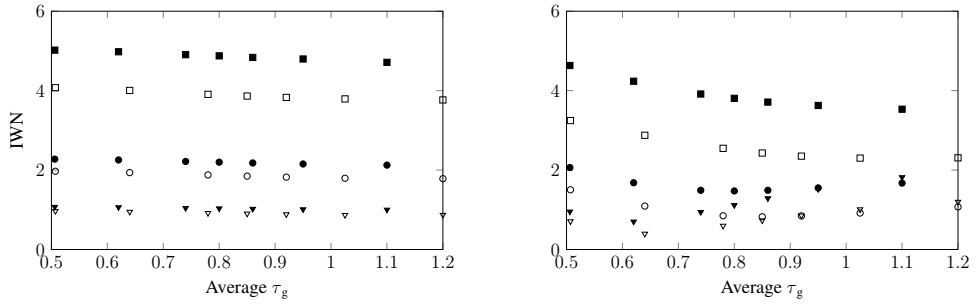

(b) P1 case

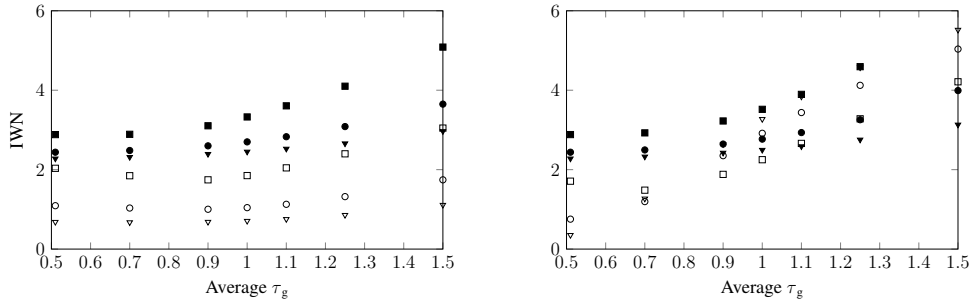

(c) P2 case

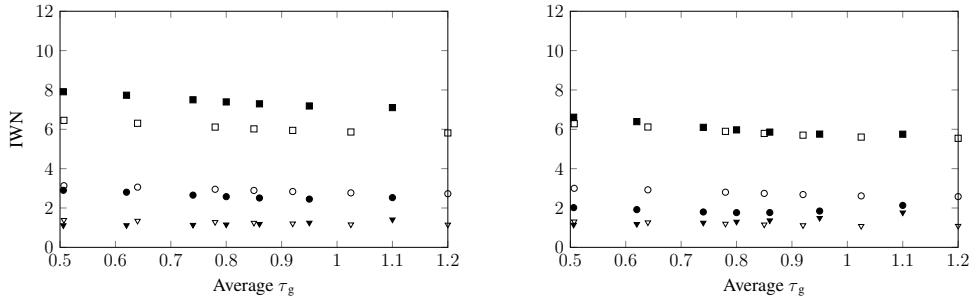

(d) P3 case

Figure 3.16: IWN calculated for the two medium bar test case at coarse (squares), medium (circles) and fine (triangles) grid resolutions plotted against the average τ_g of the two media. The plots on the left are the results for the KH method, those on the right are for the MTHB method. In the lower three plots, the hollow markers represent a property ratio of 2.5 and the filled markers a ratio of 5.

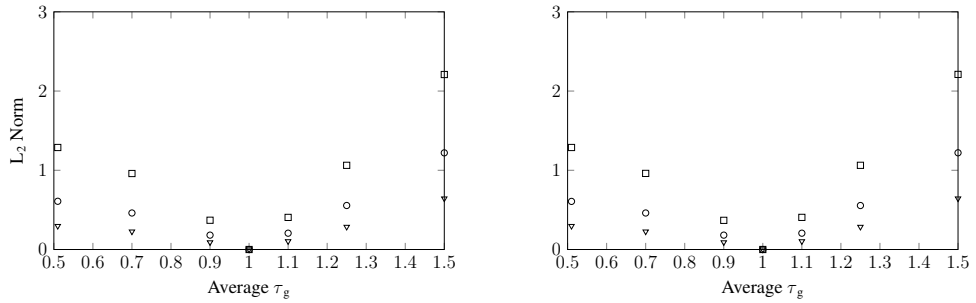

(a) Reference case

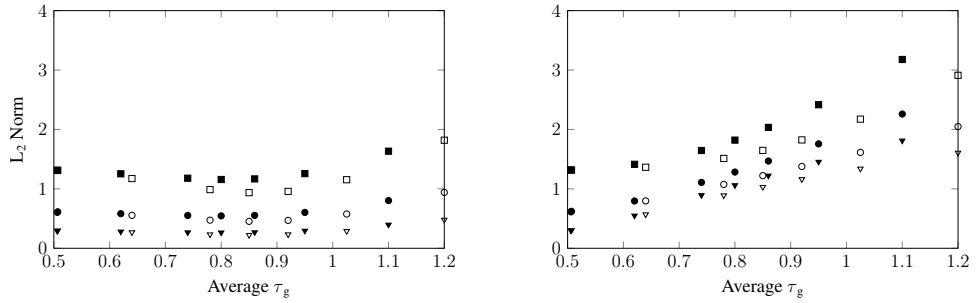

(b) P1 case

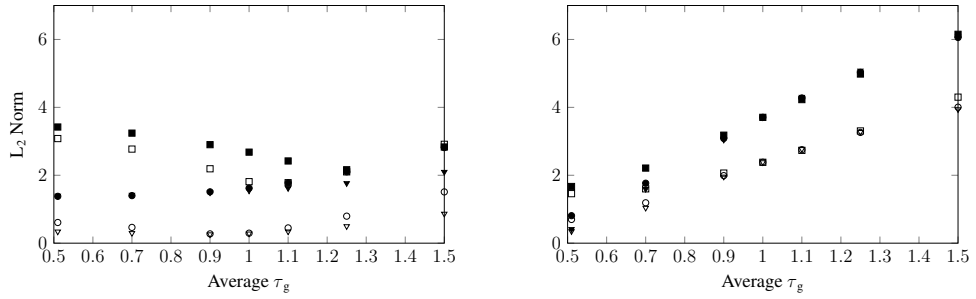

(c) P2 case

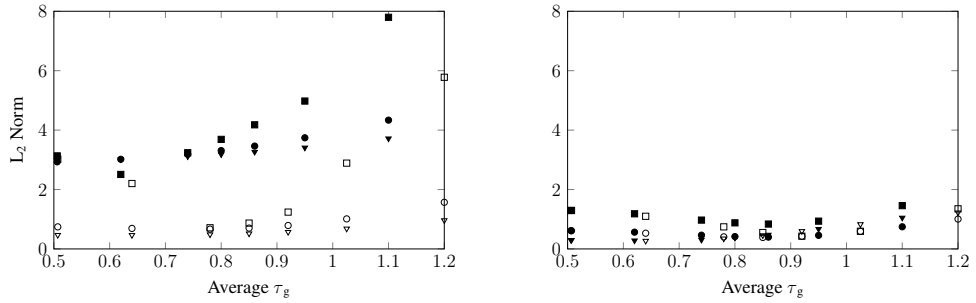

(d) P3 case

Figure 3.17: Steady-state L_2 norm calculated for the two medium bar test case at coarse (squares), medium (circles) and fine (triangles) grid resolutions plotted against the average τ_g of the two media. The plots on the left are the results for the KH method, those on the right are for the MTHB method. In the lower three plots, the hollow markers represent a property ratio of 2.5 and the filled markers a ratio of 5.

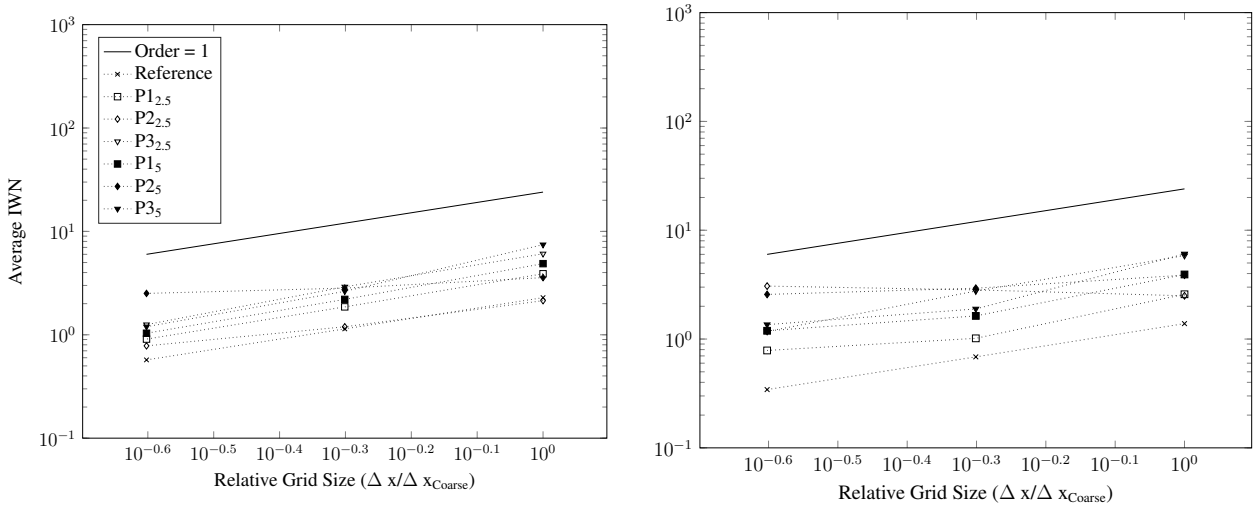

(a) KH Method

(b) MTHB Method

Figure 3.18: Variation in average IWN for stable bar tests against the level of grid refinement. The plot markers are labelled consistently for both methods. A solid line representing a convergence rate of one has been included for reference.

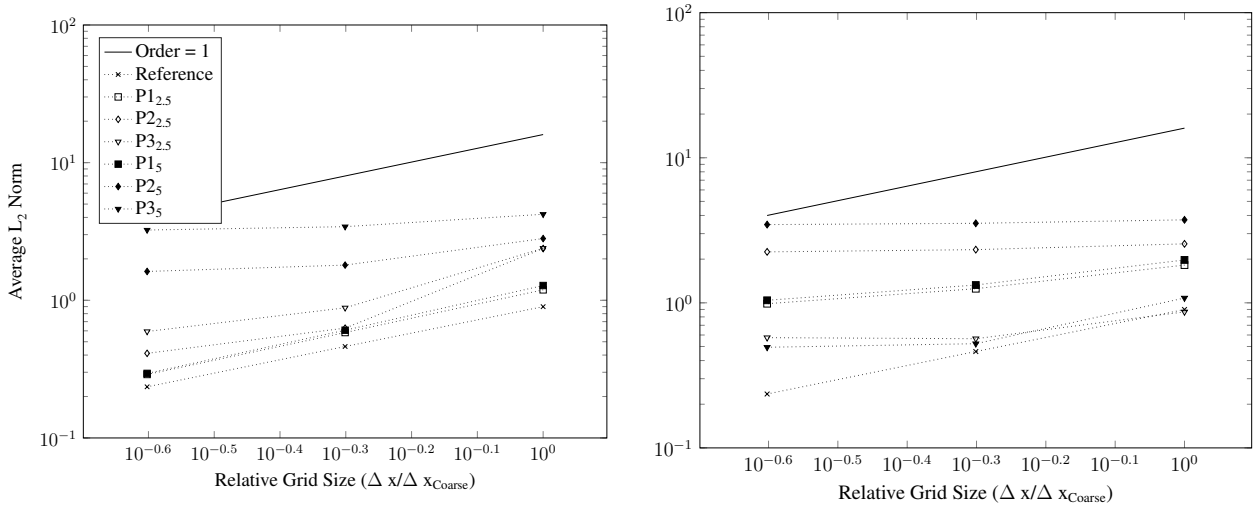

(a) KH Method

(b) MTHB Method

Figure 3.19: Variation in steady-state L_2 norm for stable bar tests against the level of grid refinement. The plot markers are labelled consistently for both methods. A solid line representing a convergence rate of one has been included for reference.

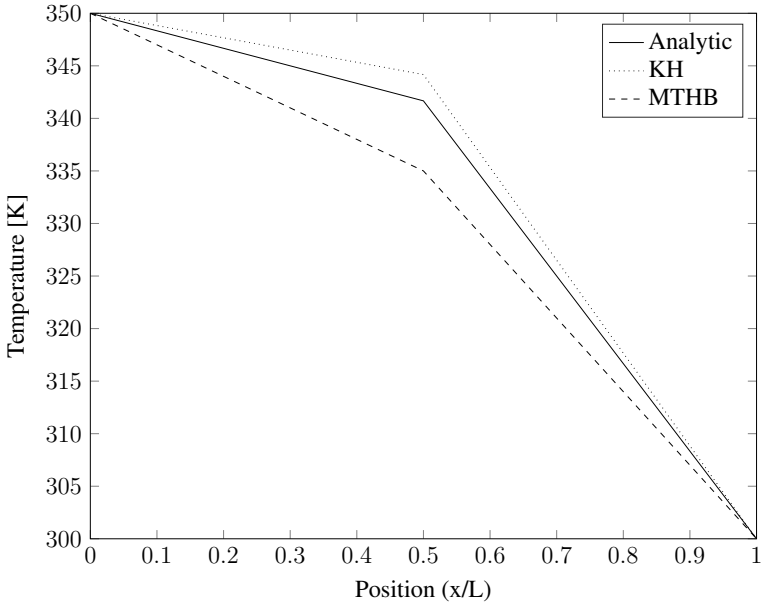

Figure 3.20: Comparison of the analytic, KH method and MTHB method steady-state temperature profiles for the $P2_5$ case. The numerical cases have been run with $\tau_g = 1$ for Medium 1.

$P2$ cases are observed to display consistently contrary convergence behaviour to that displayed by the majority of results. The reasoning for this behaviour would be similar to that discussed for the bar case and potentially be associated with the variation in ρC_p. However, as the steady-state condition for the radial problem is the entire domain becoming the same temperature as the outer wall, it would be the rate of temperature change which is in error in this case. It is also interesting to note that the variation in α between two media appears to be associated with some instability in the 2D models when a very low τ_g is used.

It is again reiterated here that IWN strongly favours performance at earlier time steps. As this is where the system is changing most rapidly, it may be viewed as a strict measure for evaluating how the model behaves. However, the transient behaviour of the models is a key consideration of this research.

Moving fluid test

The purpose of the moving fluid test case was to demonstrate the performance of the two models in the presence of both CHT and convective flow. Here, the set-up of Figure 3.2 was used in two examples with a constant flow of $U = 0.002m/s$ and $0.005m/s$, respectively, moving across the domain in the x-direction. The interface location remained fixed in this scenario. This test was run with $k_1/k_2 = 0.5$, $(\rho C_p)_1/(\rho C_p)_2 = 1.5$ and $\tau_{g,2} = 1.0$. These material values were chosen to correspond with those used in Section 3.3.2. A steady-state analytic solution,

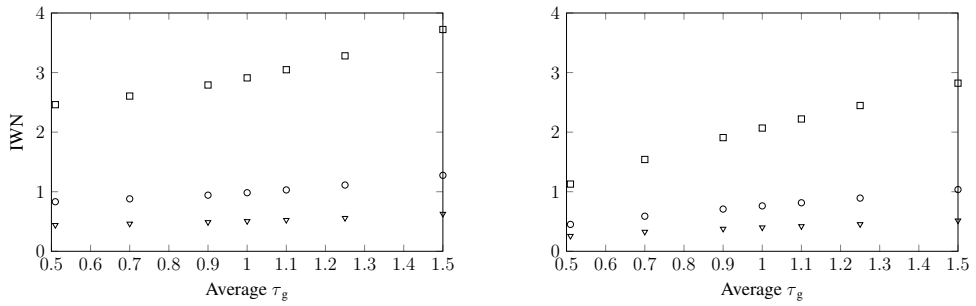

(a) Reference case

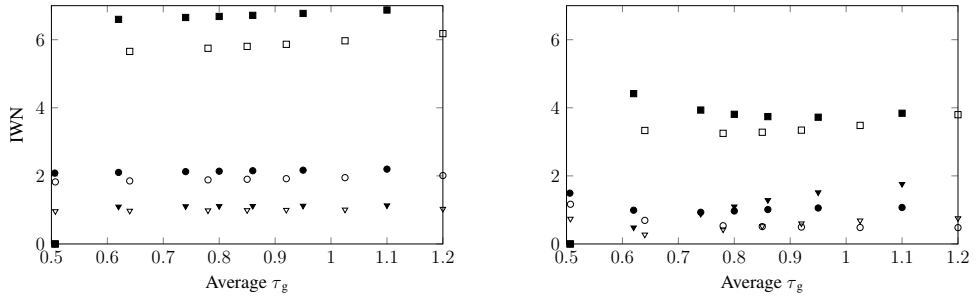

(b) P1 case

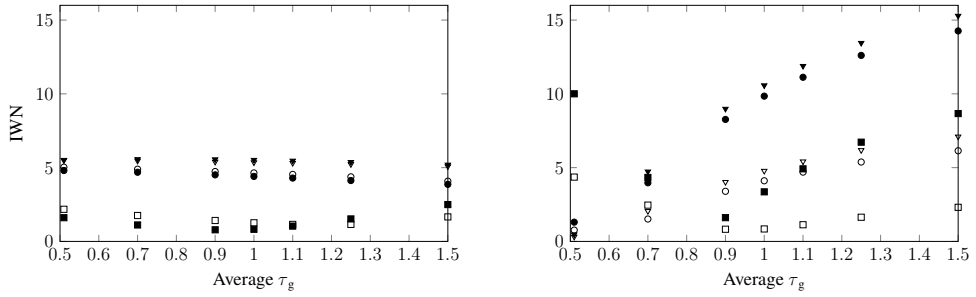

(c) P2 case

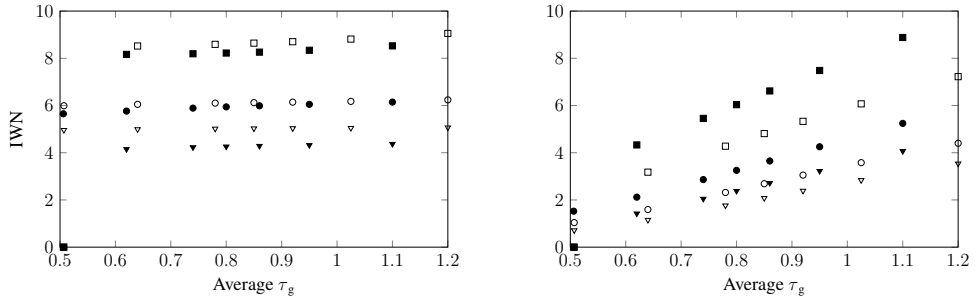

(d) P3 case

Figure 3.21: IWN calculated for the two medium radial test case at coarse (squares), medium (circles) and fine (triangles) grid resolutions plotted against the average τ_g of the two media. The plots on the left are the results for the KH method, those on the right are for the MTHB method. In the lower three plots, the hollow markers represent a property ratio of 2.5 and the filled markers ratio of 5. Markers with a value of IWN = 0 are due to unstable simulations.

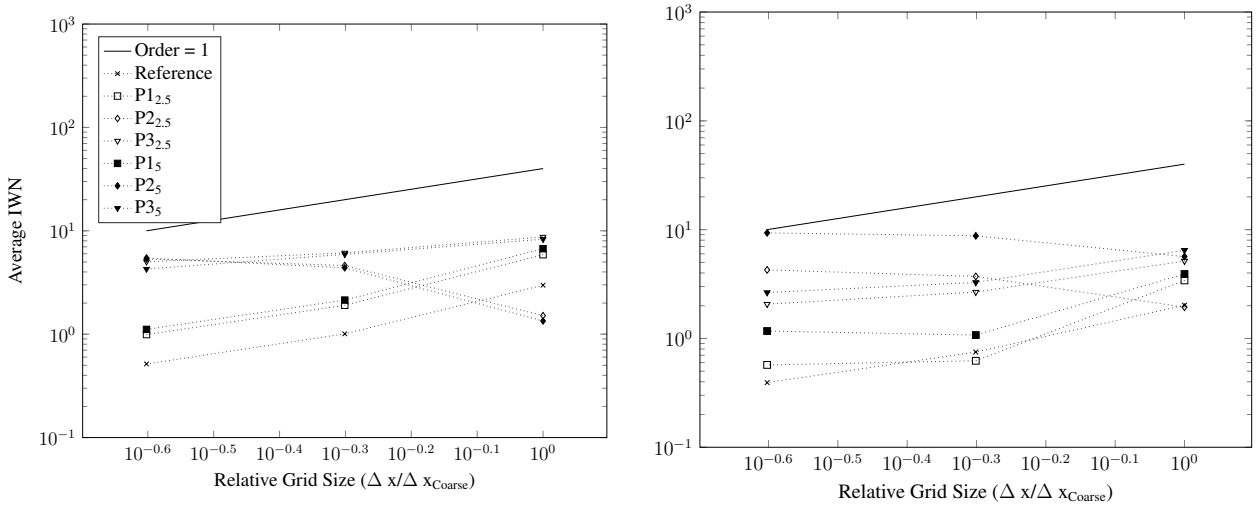

(a) KH Method

(b) MTHB Method

Figure 3.22: Variation in average IWN for stable radial tests against the level of grid refinement. A solid line indicated a representing rate of one has been included for reference.

$$T(x) = \begin{cases} T_H - \frac{C_1\alpha_1}{U}\left(1 - e^{\frac{Ux}{\alpha_1}}\right) & 0 \leq x \leq L/2 \\ T_C - \frac{C_2\alpha_2}{U}\left(e^{\frac{UL}{\alpha_2}} - e^{\frac{Ux}{\alpha_2}}\right) & L/2 < x \leq L \end{cases}, \tag{3.16}$$

was derived to judge the performance of the two LBM models at each of the velocity magnitudes tested. Here, C_1 and C_2 are constants found through application of the CHT relations at the interface of the two media. The results of the two methods at steady-state are presented in Figure 3.23. Here it can be seen that the KH method solves the problem acceptably, replicating the analytic solution well in both cases. The MTHB solution however appears to struggle to fully capture the solution despite the introduction of a velocity term to the calculation of the interface temperature (Equation 3.5).

3.3.2 Validation tests

Static particle suspension tests

A useful example of numerical suspension analysis is the work conducted by Yu *et al*. [116] using the fictitious domain method for simulating heat transfer in particle suspensions. Two of the test cases investigated in their study have been replicated and compared to the LBM methodologies proposed in the current work. These tests investigate heat conductivity properties of stationary suspensions at various levels of relative thermal conductivity and solid volume fraction.

The first test places a single particle with diameter, D, at the centre of a $16D \times 16D$ domain as an approximation of a dilute limit suspension (Figure 3.24a). The upper and lower wall of the domain are

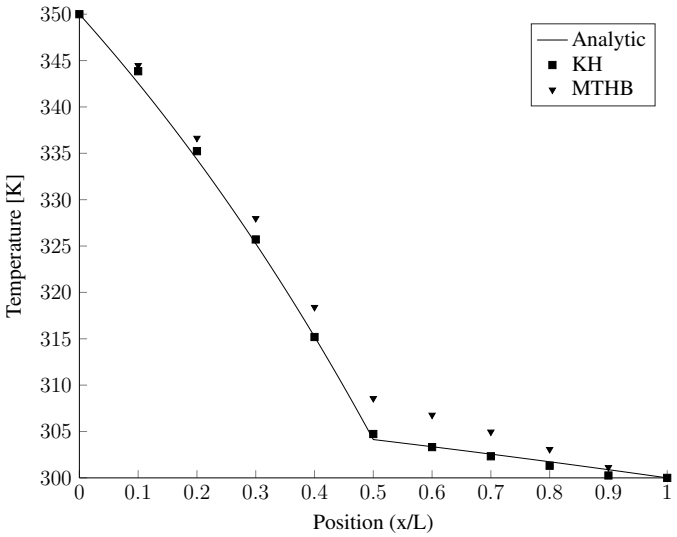

(a) $U = 0.002m/s$

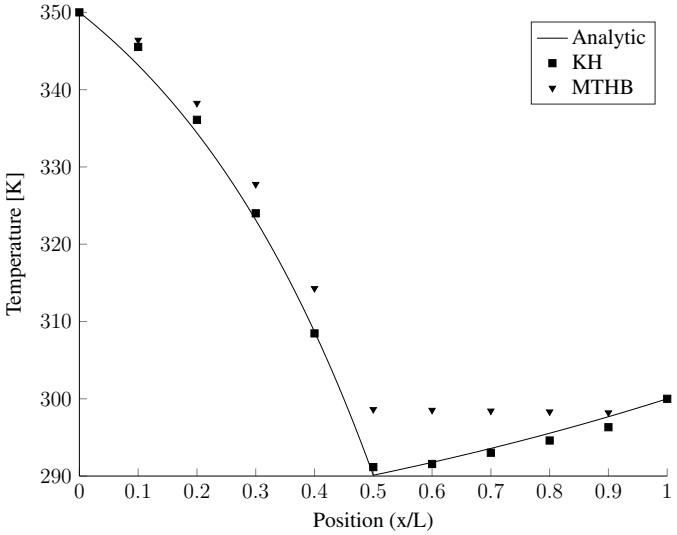

(b) $U = 0.005m/s$

Figure 3.23: Comparison of the steady-state KH and MTHB results with the analytic solution for a constant velocity imposed on the test case described in Figure 3.2.

held at a fixed, hot (T_H) and cold temperature (T_C), respectively. The model is run until steady-state is reached. A conductivity coefficient, c, can be defined that stipulates how the diffusive component of conductivity, k_d, varies compared to the fluid value via $k_d/k_F = 1 + c\phi$. Yu *et al.* [116] report a formula for calculating this value for a suspension of N particles as,

$$c = \frac{(k_R - 1)H}{(T_H - T_C)NS_p} \sum_{r=1}^{N} \int_{\partial P_r} n_y T_S dx. \tag{3.17}$$

Here $k_R = k_S/k_F$ is the conductivity ratio between the solid and fluid components, $H(= 16D)$ is the height of the domain, S_p is the area of a particle and P_r refers to the domain covered by particle r. Varying the value of k_R allows investigation of the ability of a model to calculate c. In the dilute limit, a simple analytic solution, $c = 2(k_R - 1)/(1 + k_R)$, is utilised by Yu *et al.* [116] to evaluate model performance. In the current study, the KH and MTHB models are compared against this solution and the results of Yu *et al.* [116].

The effective conductivity of suspensions of $k_R = 5$ was examined in the second test case from Yu *et al.* [116]. Here, a 4×4 array of circular particles was placed within a square domain (Figure 3.24b). The size of the domain and the spacing between particles were varied to obtain a range of solid volume fractions. As in the single particle test, the upper and lower walls were fixed at T_H and T_C, respectively, and the simulation was run to steady-state. Under the assumption that the heat flux input to the system by the upper wall is equal in all cases, the effective conductivity ratio of a suspension can be estimated in the current model by $k_e/k_F = (\Delta T_e H)/((T_H - T_C)\Delta x))$. Here ΔT_e is the average temperature difference between the upper wall and the row of nodes immediately below it. These relations are presented by Yu *et al.* [116] as a thermal analogue to the expressions for the viscosity of a suspension calculated by Batchelor [117].

In the single particle tests, the c parameter (Equation 3.17) has been calculated at various k_R using the proposed LBM models and compared with the results obtained in Yu *et al.* [116] as well as an analytic solution for the dilute limit. The LBM models used the fine mesh sizing from the previous tests and values for $\tau_{g,F}$ of 1 and 0.6. The results are presented in Figure 3.25. The reason for testing two different $\tau_{g,F}$ values is highlighted in Figure 3.26 which illustrates the difference in τ_g needed to capture materials with different values of thermal diffusivity. This figure is a result of the relationship between relaxation parameters and material properties of two components,

$$\alpha_2/\alpha_1 = (\tau_{g,2} - 0.5)/(\tau_{g,1} - 0.5). \tag{3.18}$$

The expected behaviour is successfully replicated at low conductivity ratios by both methodologies. However, when $\tau_{g,F} = 1$, ratios of $k_R = 2, 5, 10$ and 40 requires $\tau_{g,S} = 1.5, 3, 5.5$ and 20.5

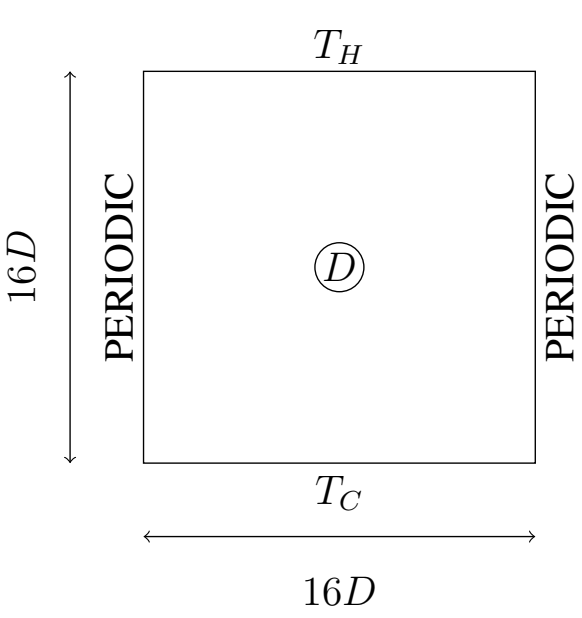

(a) Single particle test case

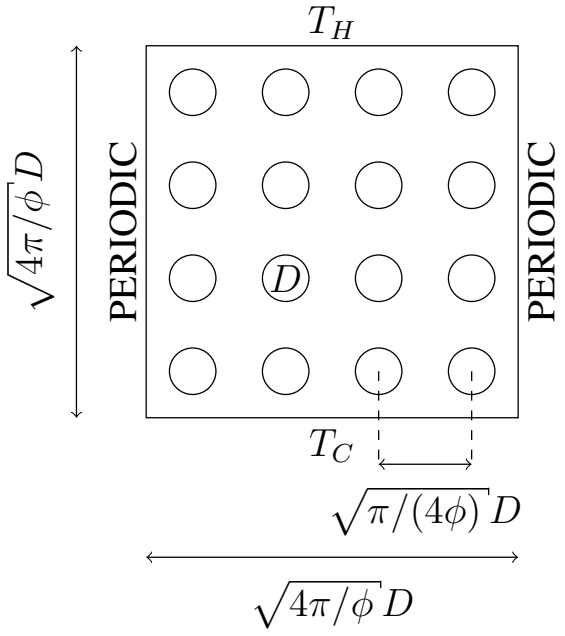

(b) Particle array test case

Figure 3.24: Schematic layouts used for comparison to the studies by Yu *et al*. [116]. The single particle test varies the ratio of thermal conductivities between the central particle and the surrounding fluid to compute the impact of the particle on the conductivity of the suspension. The array test varies the geometry to investigate the conductive properties of a suspension at different particle volume fractions.

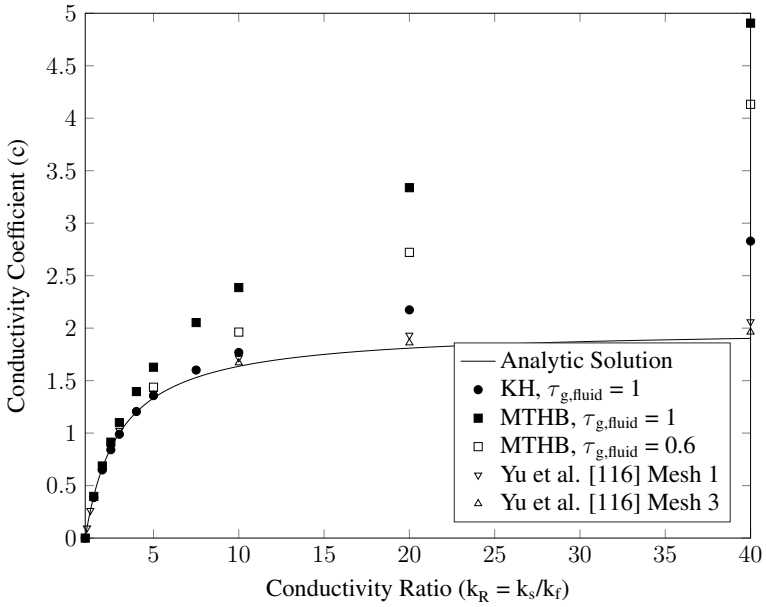

Figure 3.25: The variation of the conductivity coefficient of a dilute suspension with conductivity ratio as computed by the current model is compared to published results from Yu *et al*. [116] and the analytic result ($c = 2(k_R - 1)/(1 + k_R)$). The filled markers for the two LBM methods represent tests with $\tau_{g,F} = 1$, the hollow markers for these trials represent $\tau_{g,F} = 0.6$.

respectively. At larger values of k_R, it is this large $\tau_{g,S}$ that causes the significant deviation of the two LBM methods away from the analytic results. In particular, this is noticeable above $k_R \approx 10$ for the KH method and $k_R \approx 3$ for the MTHB method. This greater sensitivity to the relaxation parameters in the MTHB method is unsurprising as they contribute more significantly in this interface treatment than in the KH approach.

When the KH method was tested with $\tau_{g,F} = 0.6$ for $k_R = 5, 10, 20$ and 40 the model returned unstable results and so these are not plotted, this is consistent with the behaviour seen in the radial test cases. Further refinement of the value of $\tau_{g,F}$ chosen could serve to optimise the performance of this method for higher values of k_R. Using $\tau_{g,F} = 0.6$, the MTHB method exhibited notably improved behaviour than the $\tau_{g,F} = 1$ case however the results still deviated from the analytic solution. It could be anticipated that further reducing the value of $\tau_{g,F}$ would aid in reducing the error of this methodology however this comes with the requirement of extended simulation run times. In order to maintain a constant value for α for the fluid, Equation 2.12 dictates that the time step must be decreased in turn when the grid spacing is held constant. The level at which this becomes impractical is dependent on available computational resources.

For the particle array test scenario, Yu *et al*. [116] compared results from the two mesh grades implemented with their model and analytic (and experimentally validated) results from Perrins *et al*.

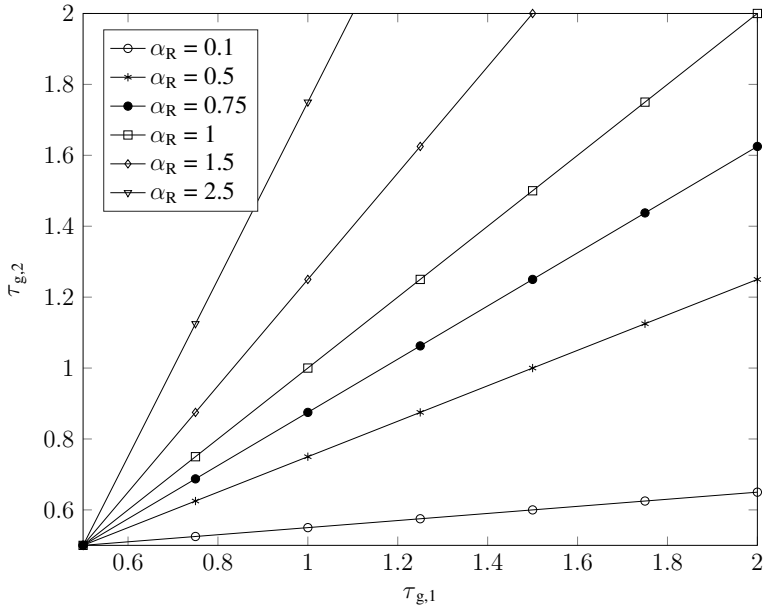

Figure 3.26: The value of $\tau_{g,2}$ needed for different values of $\tau_{g,1}$ and different property ratios $\alpha_R = \alpha_2/\alpha_1$. This plot is a graphical representation of Equation 3.18.

[118]. Figure 3.27 compares the results computed with the current model to these results. The LBM methods used here are calculated with $\tau_{g,F} = 1$.

For the LBM parameters tested here the KH method performs comparably to the fictitious domain method up to a solid volume fraction of approximately 0.5. Beyond this point it is believed that the assumptions made in the calculation of $\frac{\partial}{\partial x_j}(\frac{1}{\rho C_p})$ become inaccurate as particles become closer together. The MTHB method captures the general trend for the effective heat conductivity change however it is compromised by the choice of $k_R = 5$ and $\tau_{g,F} = 1$ as was discussed for the single particle tests. The data points presented in [116] for the highest solid fractions are not included here as the bounce-back walls limit the LBM models to a maximum value of $\phi \approx 0.7$ for the particle layout used.

Dynamic particle suspension tests

The second set of validation cases for suspensions were illustrations of particles moving through a domain. Two cases of a pair of hot particles of diameter $D = 0.0004m = 16\Delta x$ and $T = 325K$ moving through a fluid-filled channel of height $1.875D$ with fixed temperature cold walls ($T = 300K$) were used to highlight the capability of the model to capture interaction effects. In both cases the fluid kinematic viscosity was held at $\nu = 10^{-6}m^2/s$ and the simulation run for 15000 steps. The first case had the centres of the two particles aligned in the centre of the channel, whilst in the second the centres were offset above and below the centre of the channel by a factor of $0.1875D$. The particles were

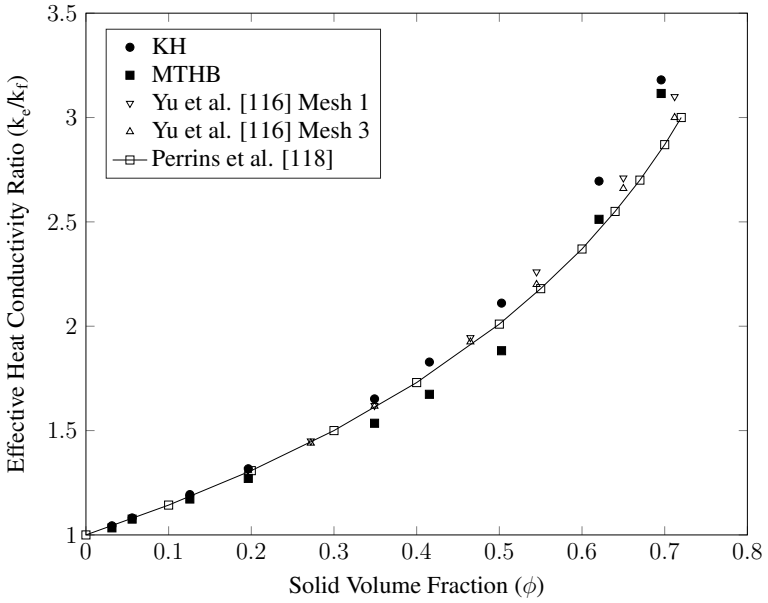

Figure 3.27: The variation of the effective conductivity (k_e/k_f) of suspensions with varying solid fractions in a fixed, square array as computed by the current model is compared to published results from Yu *et al*. [116] and Perrins *et al*. [118]. This test maintains $k_R = 5$.

separated by a distance of $1.25D$ along the length of the channel. In both of these tests the particles were given an initial velocity (corresponding to a Reynolds number of 1) and allowed to move freely under the influence of hydrodynamic interactions. In both the KH and MTHB methods, the temperature of a particle at a given point in time could be calculated based on a weighted average of the local nodal temperatures which it covers. This quantity was calculated via $T_p = (\sum_j B_j T_j)/(\sum_j B_j)$ where j is within the set of covered nodes.

The test case of two particles following each other moving through a channel was performed with both methods. As an example, the material properties tested were $k_R = 0.5$ and $\rho C_{p,S}/\rho C_{p,F} = 1.5$. It should be noted that with both k and ρC_p changing between the two components, this test case is closest to the $P2$ example used in the parametric studies. Temperature traces of the leading and trailing particles are given in Figures 3.29. Illustrative snapshots of the temperature fields part-way through the simulation are given in Figure 3.30.

Given both tests represent an infinite sequence of particles moving through a channel, the consistent cooling behaviour of the leading and trailing particles is to be expected. It can be noted in Figure 3.29 that the particles in the KH tests cooled faster than those using the MTHB method. In both test cases the bulk of the fluid is transported along the channel by the motion of the particles. This means that against the majority of a particle's surface, the relative incident velocity of the fluid is small. As such, there is minimal impact from the differences between the two LBM methods when fluid flow is

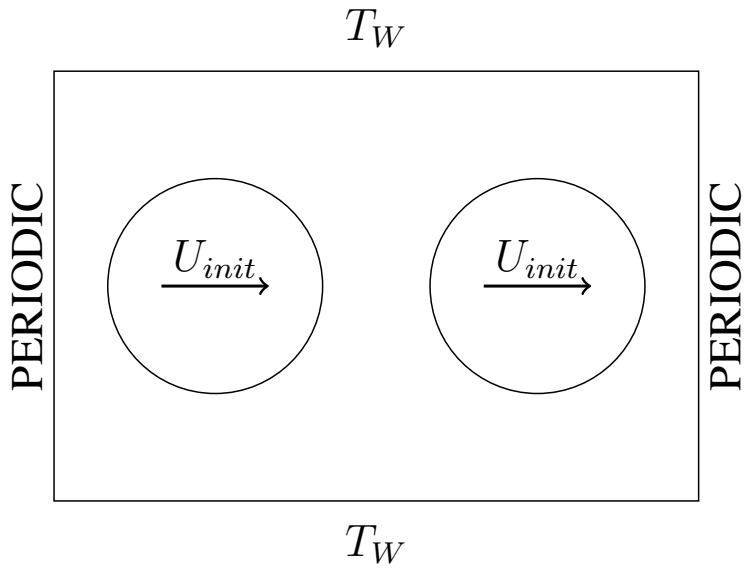

Figure 3.28: Schematic layout of the centreline paired moving particle test. The offset test has the trailing particle closer to the upper wall and the leading particle closer to the lower wall.

present, as highlighted in Section 3.3.1. The particles cool slightly faster in the offset test case where a greater proportion of the particles can be exposed to a convective heat transfer component from the fluid. From a qualitative perspective, it can be observed that the expected symmetry of results can be seen in the temperature distributions shown in Figure 3.30.

The variation between the two CHT methods in the moving particle tests may also be due to the relative impacts of a change in the solid coverage fraction on each method. It is the change in B at a node that is used to represent motion of a particle over a node from the viewpoint of the thermal population. In the MTHB approach, B is used in the calculation of the interface temperature whilst the KH method only uses this term to calculate material properties and relaxation parameters.

3.4 Summary

The inclusion of CHT between two media is necessary to correctly capture thermal behaviours in multicomponent problems. This chapter extends, verifies and validates two methods for CHT within a passive scalar thermal LBM framework. The KH method achieves this by adding a forcing term to the relaxation of nodal populations in a completely local format. The MTHB method, which is non-local, modifies the temperature at interface nodes based on those at neighbouring nodes to ensure that the conjugate conditions are met. It then relaxes the populations at these locations with the appropriate parameters to ensure the interface is properly represented.

The preliminary studies showed that the MTHB was able to capture steady-state behaviour for

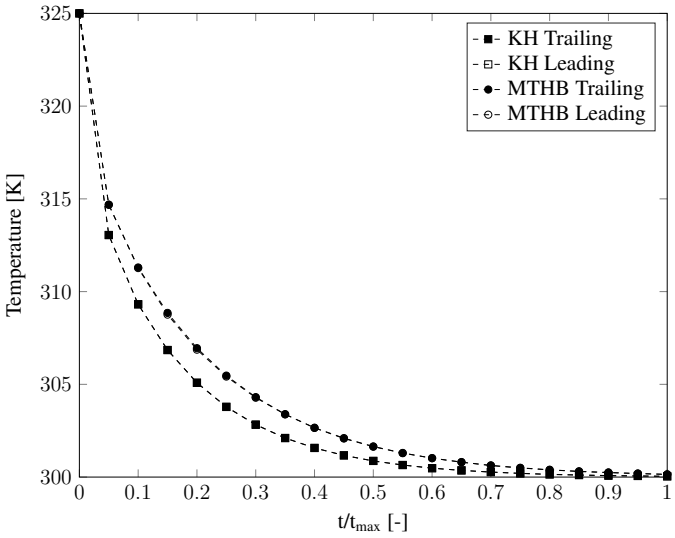

(a) Centreline test

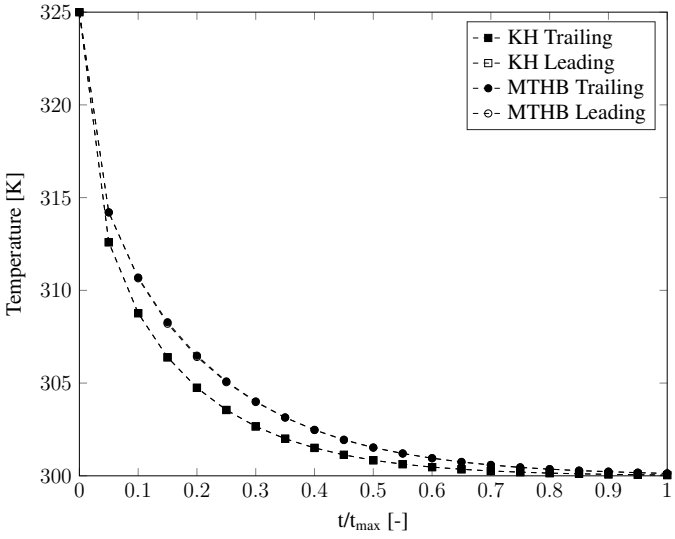

(b) Offset test

Figure 3.29: Temperature plot of particles moving through a channel. As expected, the periodic nature of the layout means that the leading and trailing particles cool in the same fashion.

a number of 2D layouts with both straight and curved boundaries within a TLBM framework. This provided justification to perform a more rigorous study of CHT schemes with differing formulations.

The parametric phase of study extended the KH and MTHB methods by implementing a PSM-style approach to curved boundaries and compared their performance using both static and moving test cases. These methods were firstly tested against analytic solutions for heat transfer through a two medium bar and radial layouts. Both methods generated acceptable results except in the case where physical properties varied between the materials but the thermal diffusivity remained constant. This is similar to results seen with more traditional numerical techniques such as SIMPLE-like algorithms.

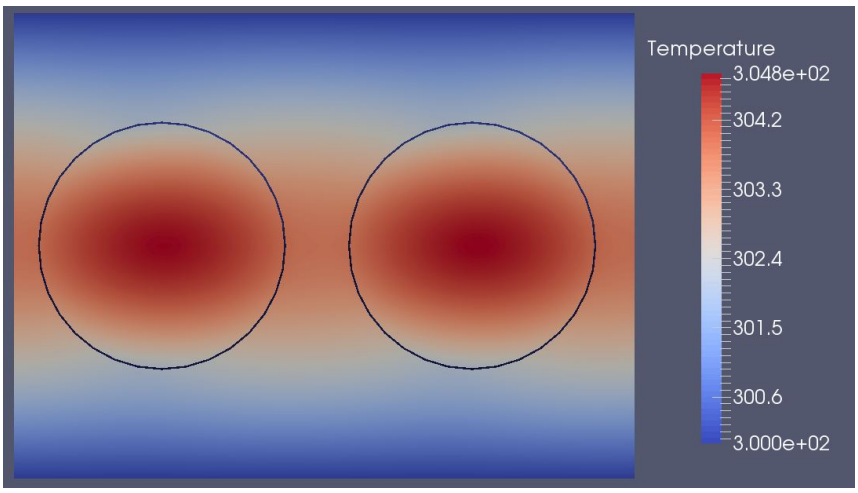

(a) KH method - centreline test

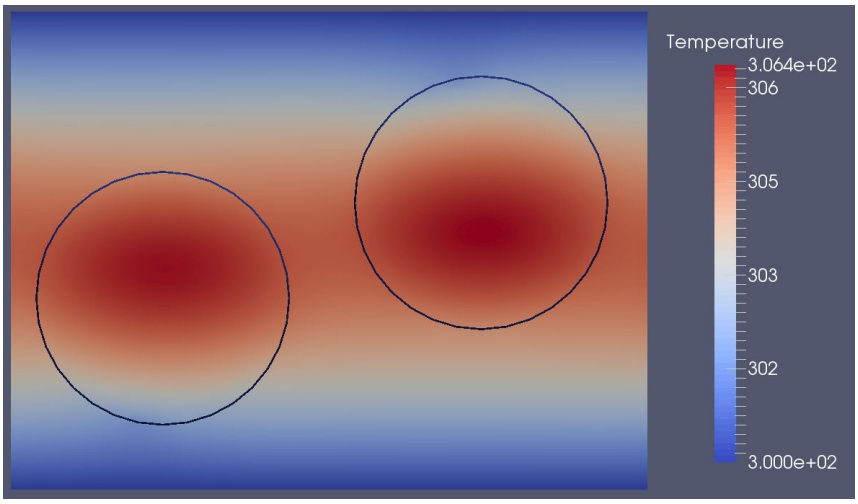

(b) MTHB method - offset test

Figure 3.30: Snapshots of the temperature [K] distribution of two particles moving through a channel. The symmetry of both problems can be noted.

The KH method was shown to continue to exhibit accurate results when a convective flow was introduced, however the MTHB method did not. The methods were then tested against results for static suspensions suggested by Yu *et al.* [116]. These again showed acceptable performance for both methods within limits provided by the physical properties of the two media and the relaxation parameters used. A final test case of a sequence of particles moving along a channel was used to qualitatively demonstrate the ability of these models to capture the transient cooling of such systems.

Based on the presented results it may be observed that non-local approaches for CHT, such as those presented by Mohamad *et al.* [104], can provide a robust and accurate approach to modelling problems where convective flow is not present. However, this performance may be more greatly de-

pendent on the LBM relaxation parameter and material properties than models such as that presented by Karani and Huber [105]. The KH method can also capture convective flows more accurately than the modified MTHB method. The method used should be chosen based on the problem being solved.

Chapter 4

Modelling of temperature-dependent viscosity in the LBM

In many scientific, engineering and industrial settings a working fluid is subjected to a thermal gradient. Such a gradient can be localised or distributed over a significant distance. These may be a result of intentional heat transfer to the fluid or a consequence of the operation of other components in the system. While all material properties of a fluid exhibit some variation due to temperature, it is changes in viscosity that often present the most obvious macroscopic evidence of this. It is of interest then that this temperature-dependence is neglected in favour of a constant viscosity in many studies of thermal LBM models (for example [79, 78, 74]). In some situations this may be an appropriate assumption to make, but it may not always be the case.

One situation where the influence of fluid viscosity is significant is in particle suspensions. When used in a practical setting, the motion and transport of the particles through the system is often the major focus of the application. Changing viscosity of the fluid component in these situations consequently alters the hydrodynamic forces acting on the particles and, as such, impacts the rate at which particles settle under gravity or are carried by the flow.

Given the change in material properties due to temperature can be highly localised, the modelling technique used to capture such behaviour needs to be formulated in a manner that can accommodate this. The implementation approach of the LBM provides a local framework for performing such calculations in an efficient and robust manner. The LBM is supported by a significant body of work relating to non-Newtonian fluids, where local changes in viscosity due to shear rate have been successfully modelled e.g. [119, 120, 121]. This indicates that similar methods can be used successfully in the situation where the viscosity change is a function of temperature. The study of temperature-dependent variations within an LBM framework has previously been conducted or discussed in a

relatively small number of prior works [122, 80, 123, 124].

The work presented in Chapter 3 analysed CHT for a passive scalar implementation of TLBM. In this chapter, it will be demonstrated that this formulation is not able to capture specific details associated with temperature-dependent viscosity flow. To resolve this, it is shown that a more detailed model that conserves total energy [80] is required. An approach for computing CHT within this framework will also be discussed.

4.1 Investigations of temperature-dependent viscosity

The numerical investigations undertaken with this model have been broken into two parts. The first section verifies the performance of D2Q9 TLBM models against analytical results for temperature-dependent flows. The second section examines the transport of single and multiple particles through a fluid with varying viscosity.

4.1.1 Model verification

The work of Myers *et al.* [125] developed analytical expressions for the velocity and temperature profiles generated for a temperature-dependent viscosity fluid within a Couette flow experiencing an applied temperature gradient. The layout of the channel used to compare the model performance against these results is presented in Figure 4.1. In these tests, the viscosity of the fluid is assumed to vary in an exponential fashion with respect to temperature,

$$\mu = \mu_0 e^{-\beta T}, \tag{4.1}$$

where μ_0 is a reference viscosity and β is a coefficient indicating the rate of temperature-dependence. This form is chosen as it allows for an analytic solution. In practice though, this dependence could be implemented with any suitable function of temperature. The velocity profile is given in a normalised form by,

$$U(y) = \sqrt{\frac{2e^{\beta T_m}}{\beta Br}} \left\{ tanh \left[y \sqrt{\frac{A^2 \beta Br}{2e^{-\beta T_m}}} - tanh^{-1} \sqrt{1 - e^{-\beta T_m}} \right] + \sqrt{1 - e^{-\beta T_m}} \right\}, \tag{4.2}$$

and the normalised (or dimensionless) temperature profile by,

$$T(y) = T_m + \frac{1}{\beta} ln \left\{ 1 - tanh^2 \left[tanh^{-1}(\sqrt{1 - e^{-\beta T_m}}) - y \sqrt{\frac{A^2 \beta Br}{2e^{-\beta T_m}}} \right] \right\}. \tag{4.3}$$

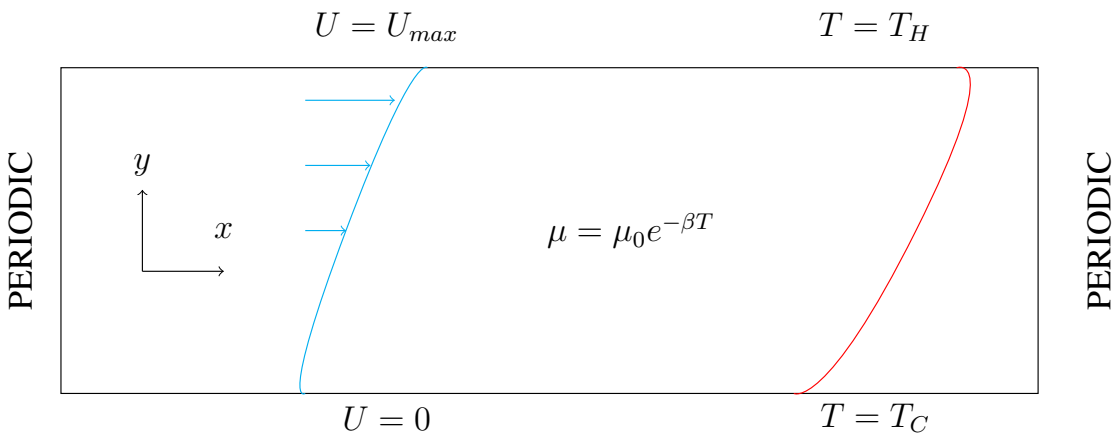

Figure 4.1: The Couette flow with temperature gradient used to test the numerical model of temperature-dependent viscosity. Analytical expressions for the velocity and temperature profiles across the height of the channel were developed by Myers *et al.* [125].

The terms T_m and A are found through application of the boundary conditions at the upper wall (normalised value of y = 1). Typically this requires these equations to be solved numerically. Here, the normalised temperature can be calculated from a physical temperature through,

$$T = \frac{T^{physical} - T_C^{physical}}{T_H^{physical} - T_C^{physical}}, \tag{4.4}$$

where $T_H^{physical}$ and $T_C^{physical}$ are, respectively, reference hot and cold temperature of the system. For physically sensible results, these should be suitable to the system being considered e.g. such that the Boussinesq approximation of small temperature differences still applies. In the following sections these may be considered to be $T_H^{physical}$ = 350K and $T_C^{physical}$ = 300K. Additionally, the non-dimensional Brinkman number of the flow can be defined as,

$$Br = \frac{\mu_0 U_{max}^2}{k(T_H - T_C)}, \tag{4.5}$$

using k as the thermal conductivity of the fluid, U_{max} the velocity of the shearing wall and T_H and T_C the respective dimensionless temperatures of the moving (hot) and stationary (cold) walls. This term relates to the amount of shear heating generated in the system.

To evaluate the performance of the passive scalar and total energy thermal LBM models a number of test cases with different values of Br and β, as presented in Table 4.1, were conducted. The reference lattice viscosity was set at a value of $1/6$, with this being set at the lower (cold) wall. Note that lattice values are calculated by setting Δx and $\Delta t = 1$. From a numerical point of view, the local viscosity of the LBM population was varied using the exponential relationship based on

Parameter	Br	β
Case 1	0.7	1
Case 2	0.7	1.25
Case 3	2	1
Case 4	0.275	1
Case 5	0.7	0.1

Table 4.1: Parameter values used for the assessing the performance of the LBM models at capturing temperature-dependent viscosity flow behaviour by comparison to analytic results.

the local LBM temperature (Equation 4.1). In the LBM models, this will impact the calculation of local fluid velocity as outlined in Chapter 2. In the total energy model, the changing velocity will feed back to the temperature calculation through the zeroth moment of the thermal population ($\sum_{i=0}^{m-1} g_i(\mathbf{x}, t) = \rho E = \rho(C_p T + 0.5u^2)$ as per Guo *et al.* [80] with C_p being the local heat capacity) and the equilibrium function. For the passive scalar model, in the absence of Boussinesq forcing, only the equilibrium function has an effect.

The height of the channels was set to $10\Delta x$ for the coarsest grid spacing test. This was then increased to achieve a medium ($20\Delta x$) and fine ($40\Delta x$) grid spacing. For each grid spacing, U_{max} was chosen such that the modelled shear rate was constant at $\dot{\gamma}$ = 0.01 in lattice units. The fixed temperature and velocity boundary conditions were implemented using the non-equilibrium extrapolation method similar to those described in Guo *et al.* [80] and Frapolli *et al.* [77]. Model accuracy was assessed by calculating an L_2 norm of the difference between the steady-state LBM and the analytic results. The results in Table 4.2 summarise the L_2 norm observed at the coarsest grid spacing and the average order of convergence as the grid spacing was refined. A positive value for convergence indicates that the L_2 norm decreased with a reduction in grid spacing. As can be observed in these results, and in Figures 4.2 and 4.3 for Case 1, the passive scalar model struggled to capture the temperature-dependence within the Couette flow. The total energy model, however, captured the complex temperature-dependent interactions accurately for a range of parameter values. The cause of this is due to the passive scalar model only being able to generate a linear temperature field between points of different temperature. The consequence is that features that are generated by more complex heating modes, shear heating for example, are not resolved in this model. This is reflected by the convergence data where the temperature population is unchanged with decreasing grid spacing. These results indicate that a total energy LBM model is required to accurately model systems where temperature-dependent viscosity is being considered. This model was used in the remainder of this

	Passive Scalar				Total Energy			
	Fluid		Temperature		Fluid		Temperature	
Case	L_2	Order	L_2	Order	L_2	Order	L_2	Order
1	3.1e-3	-0.2	5.5e-2	0.0	2.4e-3	2.0	3.9e-5	1.8
2	3.4e-3	-0.2	4.7e-2	0.0	3.9e-3	2.0	9.0e-5	1.6
3	9.6e-3	-0.1	1.4e-1	0.0	1.5e-3	2.1	2.0e-4	2.2
4	2.1e-3	0.2	2.3e-2	0.0	2.7e-3	2.0	1.4e-5	1.6
5	6.1e-4	0.0	9.1e-2	0.0	1.8e-5	2.0	1.4e-5	2.0

Table 4.2: L_2 norm results for the coarsest grid spacing and the approximate order of convergence for the tested LBM models with temperature-dependent viscosity when compared to the analytic results. A positive value for convergence indicates that the L_2 decreased with a reduction in grid spacing.

chapter and thesis when thermal models are discussed.

4.1.2 Model validation

After verifying the ability of the total energy LBM to capture the temperature-dependent behaviour of the fluid, it was then used to examine particle transport within a channel. This comprised cases containing single and multiple particles with the same thermal properties as the fluid. This meant that only the temperature-dependent effects of the fluid from the boundary temperatures were impacting the flow. DEM particles were coupled to the LBM using the PSM method discussed in Chapter 2.

Single particle transport

The first test consisted of a single particle located within the centre of channel experiencing Couette flow. It was constructed in a non-dimensional frame of reference. As per the verification test, the lower (stationary) wall was maintained at $T_C = 0$ and the upper (moving) wall was held at $T_H = 1$. This particle was prescribed a diameter of $D = H/4$, where H is the channel height, and an initial temperature of 0.5. It started at rest and was allowed to move freely with the flow. These tests were conducted with a channel height of $H = 40$ and thus a particle diameter of 10 lattice spacings. This layout is presented in Figure 4.4. This simulation was run for two cases, the first with the LBM viscosity varying exponentially with local fluid temperature as per the verification tests and the second with it being held constant at the lower wall value. This compared the impact of variable and constant viscosity on particle motion. This pair of simulations was also repeated with the temperature of the

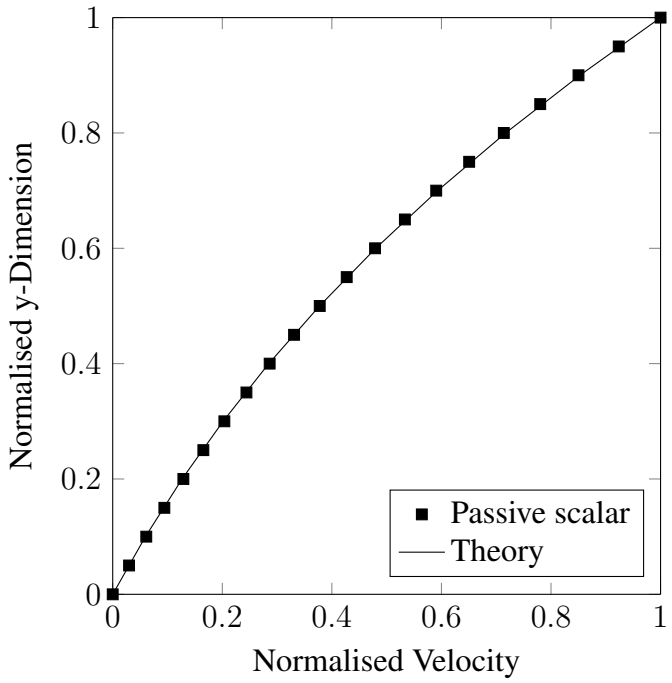

(a) Normalised velocity profile

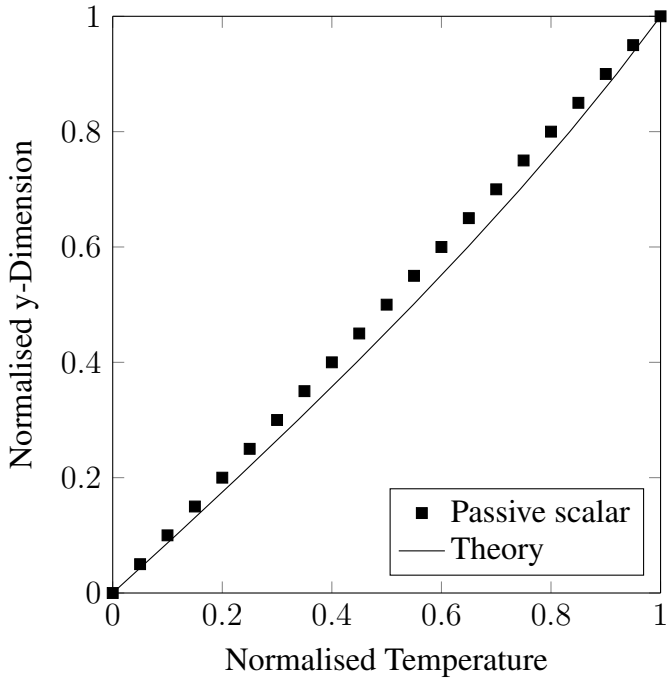

(b) Normalised temperature profile

Figure 4.2: An example comparison of the passive scalar LBM model with the analytic results of Myers *et al*. [125] for the normalised velocity and temperature profiles generated within a temperature-dependent Couette flow and applied temperature gradient.

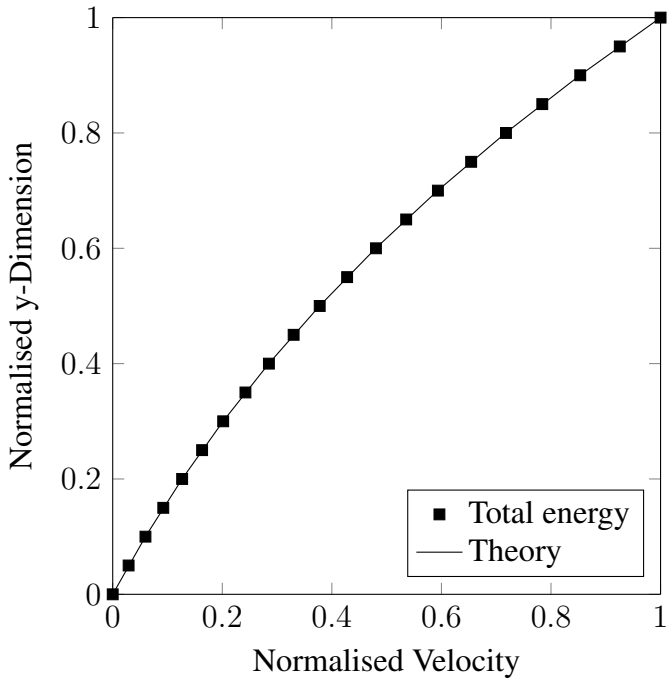

(a) Normalised velocity profile

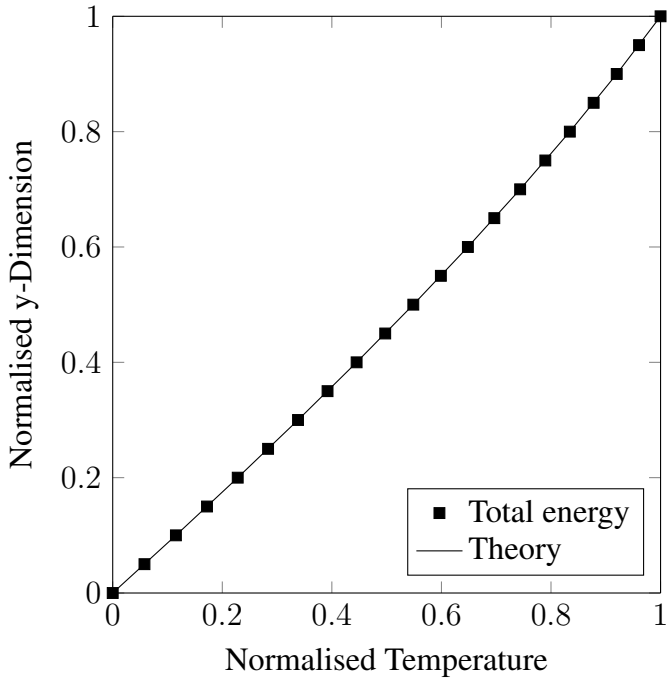

(b) Normalised temperature profile

Figure 4.3: An example comparison of the total energy LBM model with the analytic results of Myers *et al.* [125] for the normalised velocity and temperature profiles generated within a temperature-dependent Couette flow and applied temperature gradient.

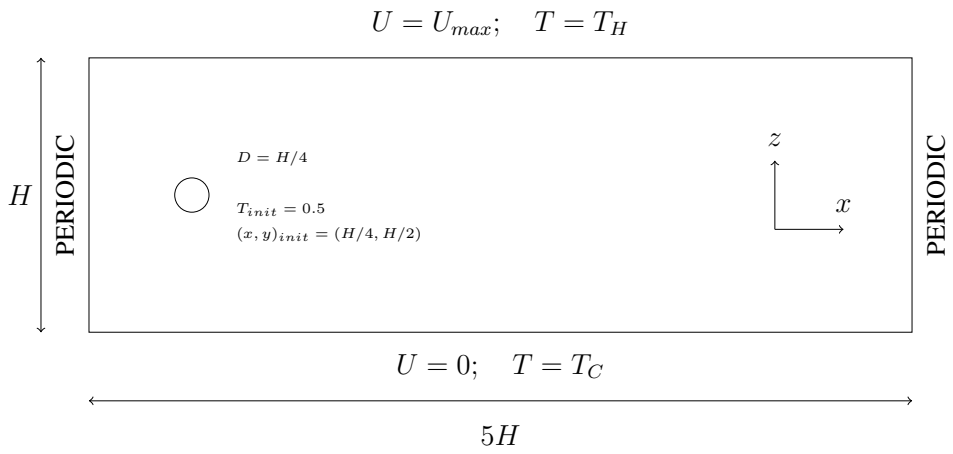

Figure 4.4: To investigate particle motion in a Couette flow with temperature-dependent viscosity, the verification test layout had a single particle placed in the centre of the channel. It was allowed to move freely with the flow. These tests were conducted with $H = 40$.

upper and lower boundaries swapped. This was used to determine whether the temperature effects on viscosity or the hydrodynamics of the Couette flow field was the primary contributor to particle motion.

Over the duration of each of the simulations (t_{max} = 20,000 steps) the velocity and vertical displacement of the particle was tracked. The normalised results of these are presented in Figure 4.5. Here it can be observed that after the initial state of rest had been overcome, the particle in the variable viscosity case migrated at a constant rate towards the upper boundary. By the end of the simulation the particle had moved a distance of $0.17D$ (approximately $0.0425H$). In comparison, when the viscosity is held constant the particle effectively remains in the same position in the centre of the channel. On initial inspection this can be attributed to the thinner (lower viscosity) fluid closer to the hot wall reducing the stress experienced by the particle on its upper surface compared to the lower surface. This imbalance causes the observed migration of the particle. It can also be noted that due to the relatively minor vertical motion of the particle in the constant viscosity case that, for the parameters in use in this study, hydrodynamic effects on particle motion are limited.

A similar argument can be made for the reduced magnitude of particle velocity in the variable viscosity case. In the centre of the channel, the viscosity of the fluid surrounding the particle in the variable viscosity case is less than that experienced with the constant viscosity case (which is taken at the cold lower wall value). This thinner fluid is unable to accelerate the particle as effectively and as such it takes longer to achieve a steady-state velocity matching that of the local flow.

In the simulations with the temperature conditions swapped (Figure 4.6), it can be seen from the vertical motion that the particle has again migrated towards the region of lower viscosity. It can also be

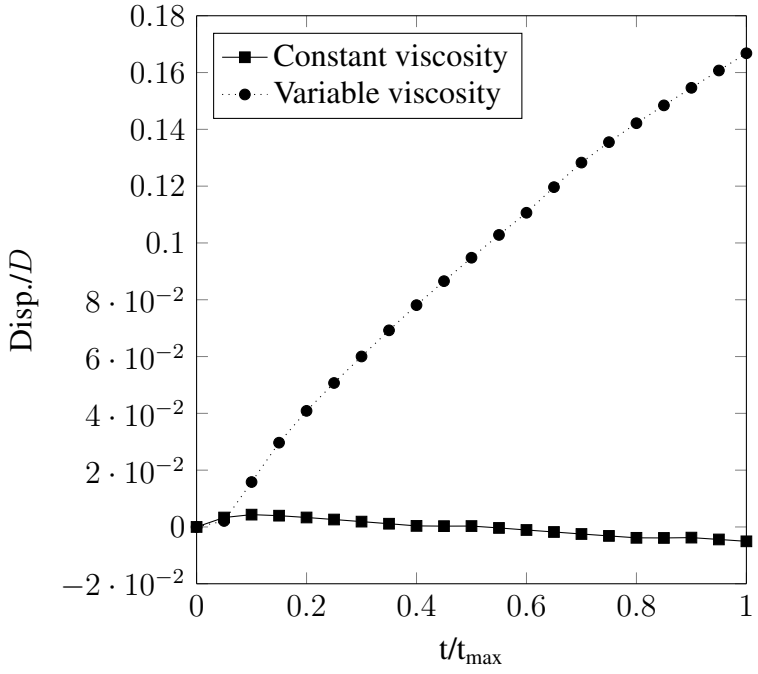

(a) Normalised particle vertical displacement

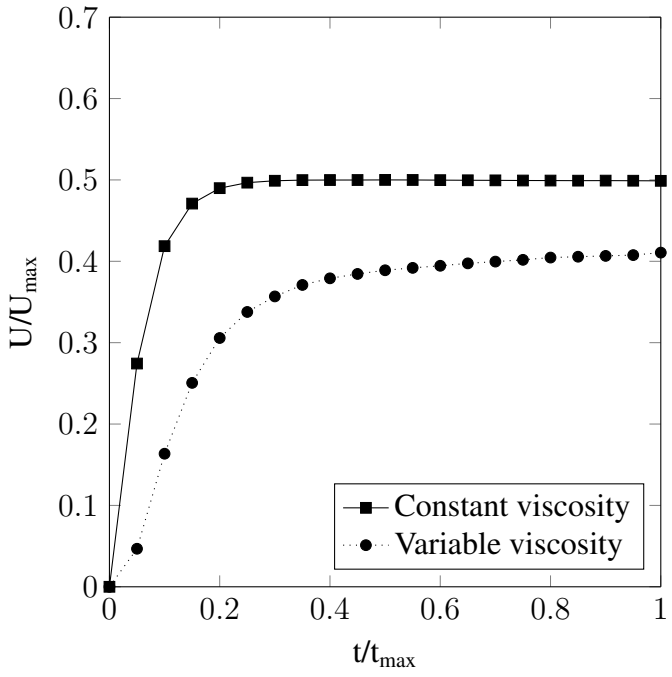

(b) Normalised particle velocity magnitude

Figure 4.5: Comparison of the vertical displacement (normalised by particle diameter) and velocity magnitude (normalised by wall velocity) of a single particle within a Couette flow influenced by a temperature gradient. Note that the constant viscosity results are identical to those in Figure 4.5 as the particle motion is independent from temperature in this case.

noted here that in Figures 4.5 and 4.6 the constant viscosity results are identical and can be used as a reference. In the swapped layout, particle migration has occurred at a slower rate than in the previous case. The magnitude of particle velocity is also significantly greater with the temperature boundary conditions swapped. Both of these observations can be associated with the change in temperature and velocity profiles that occur within the channel as a result of the temperature boundaries changing. This is illustrated in Figure 4.7. In particular, the fluid velocity in the second case is significantly faster over the entire height of the channel. This observation is due to the higher viscosity fluid being located at the moving plane of the upper wall. In the first case, the hot and thin fluid was less capable of transferring shear stress as a result it did not effectively accelerate the fluid below it. In the second case, the motion of the thick fluid by the wall is more readily able to accelerate the adjacent fluid layers and this continues over the height of the channel. The result is that the particle in the second case is driven by a higher local fluid velocity than when the viscosity is held constant, allowing it to achieve a greater overall velocity. The greater momentum of the particle along the length of the channel may also hinder vertical motion contributing to the reduced rate of migration observed in the second case.

Multiple particle transport

Whilst the motion of a single particle is of academic interest, the collective motion of a suspension of multiple particles is of greater interest to industrial and scientific applications. To investigate the influence of a temperature-dependent viscosity fluid on suspension transport, the Couette flow used elsewhere in this chapter was packed with a quasi-random distribution of 14 particles to give a 2D solid volume fraction of approximately 0.55. The initial layout of these particles is given in Figure 4.8. As for the single particle case, tests were conducted with either constant or temperature-dependent fluid viscosity. Again, these were repeated with the temperature boundary conditions swapped.

Figures 4.9 and 4.10 give the mean particle displacement and the mean particle velocity of the two suspension cases under the respective temperature conditions. However, before a discussion of the results for these tests is presented, it should be noted that these will be sensitive to the initial distribution of the particles within the channel. A different distribution may alter the specific behaviour seen in a simulation.

Generally speaking, some similar observations to the single particle cases can be observed in the suspension tests. For the case where the top wall is heated, the particles are observed to move, on average, slower within the temperature-dependent viscosity fluid than in the reference case. In the bottom heated simulation, the particles tend to move faster. This is likely to be related to the

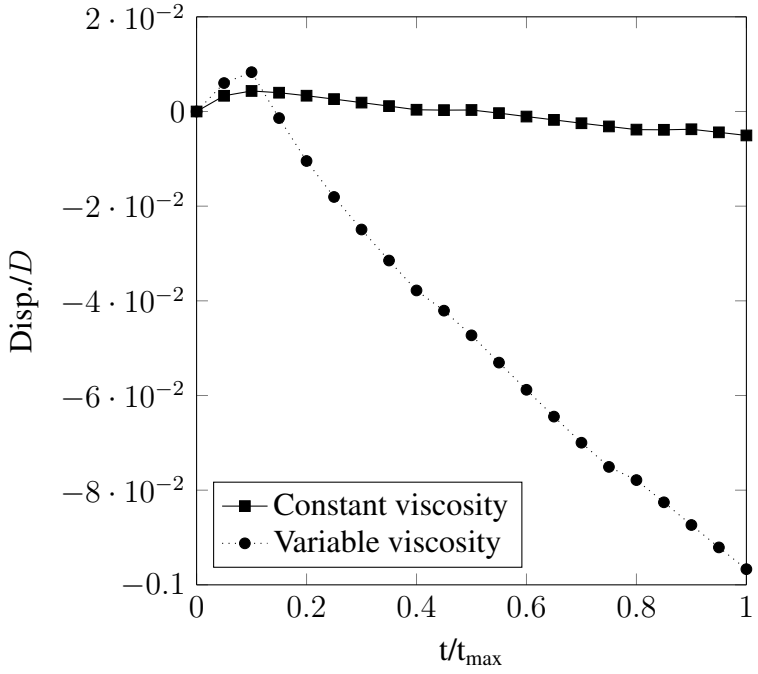

(a) Normalised particle vertical displacement

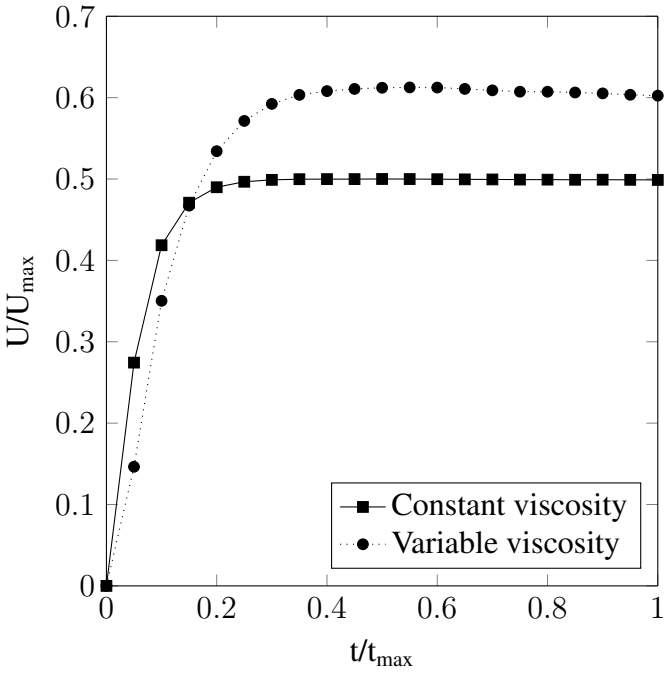

(b) Normalised particle velocity magnitude

Figure 4.6: Comparison of the vertical displacement (normalised by particle diameter) and velocity magnitude (normalised by wall velocity) of a single particle within a Couette flow of temperature-dependent viscosity influenced by a reversed temperature gradient.

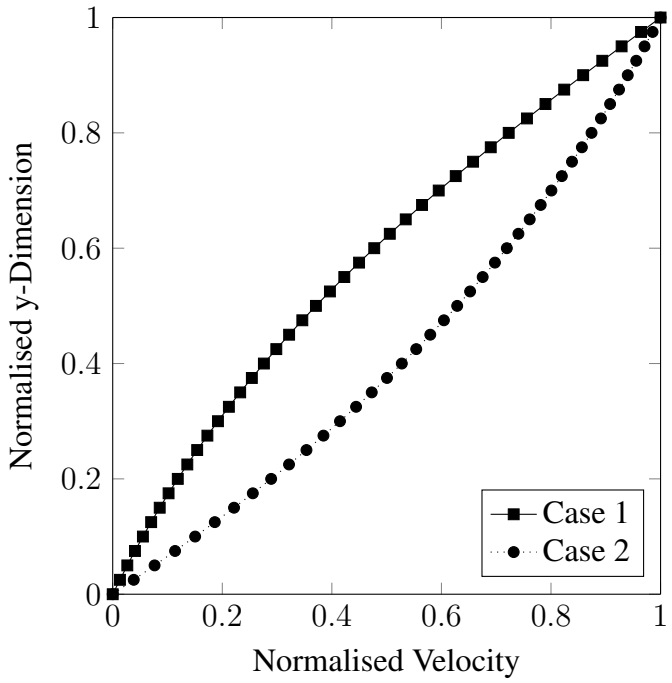

(a) Normalised velocity profile

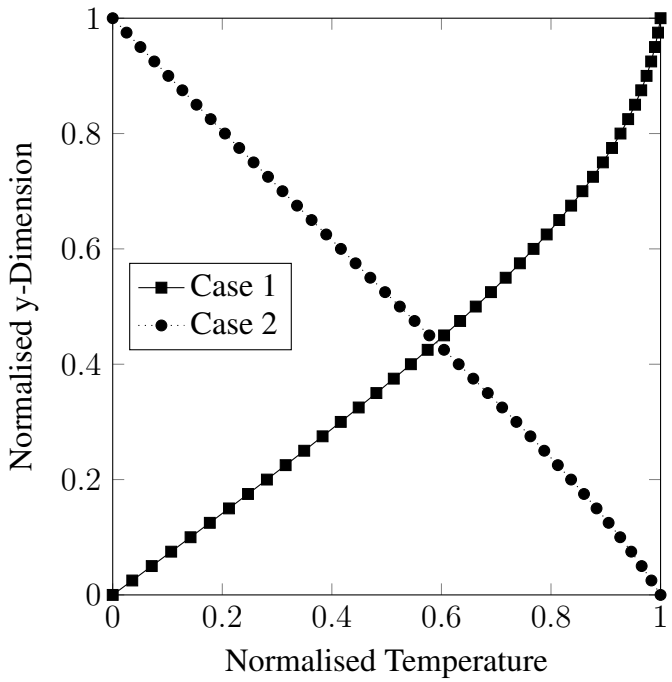

(b) Normalised temperature profile

Figure 4.7: Normalised velocity and temperature profiles observed within a Couette flow when the temperature boundary conditions are swapped (Case 2) from their original configuration (Case 1).

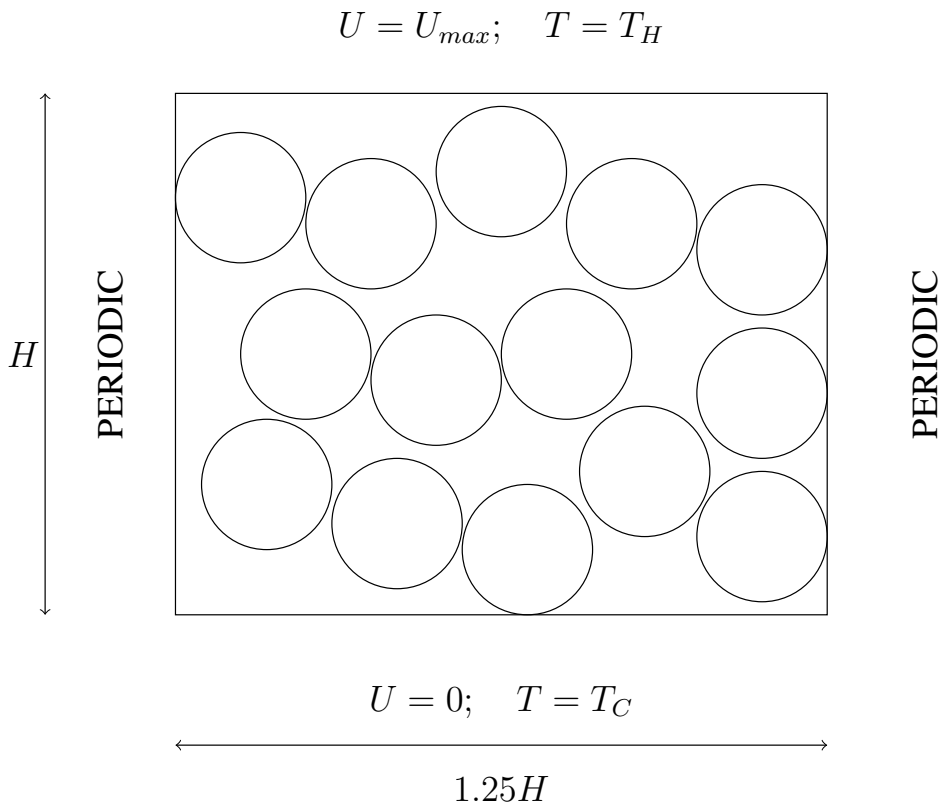

Figure 4.8: The initial distribution of the multiple particle test within a Couette flow of temperature-dependent viscosity fluid. The fraction of solids within the 2D channel is approximately 0.55.

difference in velocity profile within the fluid caused by the change in viscosity (as observed for the single particle case) and how this interacts with the structures of particles that have been formed.

When average particle position is considered, it appears that the collision of particles dominates the temperature-dependent transport effects seen for a single particle. This is evidenced by the more variable particle position seen in the pack tests. Up until about $0.3t_{max}$, the behaviour of the two temperature cases is qualitatively similar. This would be due to the initialisation of particle motion within the domain being controlled more by the shearing flow than the temperature changes, which caused a slight collective downwards motion of the particles. For the remainder of the simulation, the particles in the top heated case are generally at or below the positions of the reference case whilst they are generally higher in the bottom heated case. A suggestion as to the cause of this would be that the faster particle motion in the bottom-heated case leads to more energetic collisions occurring within the particle pack. With the distribution examined, these have driven the average particle position upwards for this example. The significant drop in average particle height during the last portion of the bottom heated test is due to a single particle migrating to a free space in a lower layer in this time frame. This is a unique effect of the particle distribution chosen.

This section has shown that the qualitative and quantitative motion of particles through a fluid can be fundamentally impacted by viscosity changing with temperature. In particular, this arises from the altered stress field and velocity profiles that are generated within a fluid by this effect.

4.2 Conjugate heat transfer for the total energy LBM

As noted in Chapter 3, temperature must be continuous across the boundary in order to ensure CHT conditions at interfaces of disparate media. The methods discussed in Chapter 3 are suitable for the passive scalar LBM where temperature is the conserved quantity. These methods are not applicable to the total energy LBM required to model temperature-dependent viscosity fluids. This is because of total energy being the conserved quantity (i.e. zeroth moment) of the thermal population. To illustrate why a CHT approach that conserves the zeroth moment is not useful, consider a stationary case where C_p, the local specific heat, varies between two adjacent nodes such as for a boundary between two media. The total energy model being used here, proposed by Guo *et al.* [80], conserves the quantity $\rho E = \rho(C_p T + 0.5\mathbf{u}^2)$. As the quantity ρE will be continuous between these two locations, there will be a step change in temperature that is proportional to the ratio of C_p values. To meet CHT requirements, this behaviour must be reversed such that temperature is continuous and there is a step change in total energy. Pareschi *et al.* [107] developed a CHT scheme for a total energy conserving form of the entropic LBM. In this section, this methodology has been adapted to the LBM construction

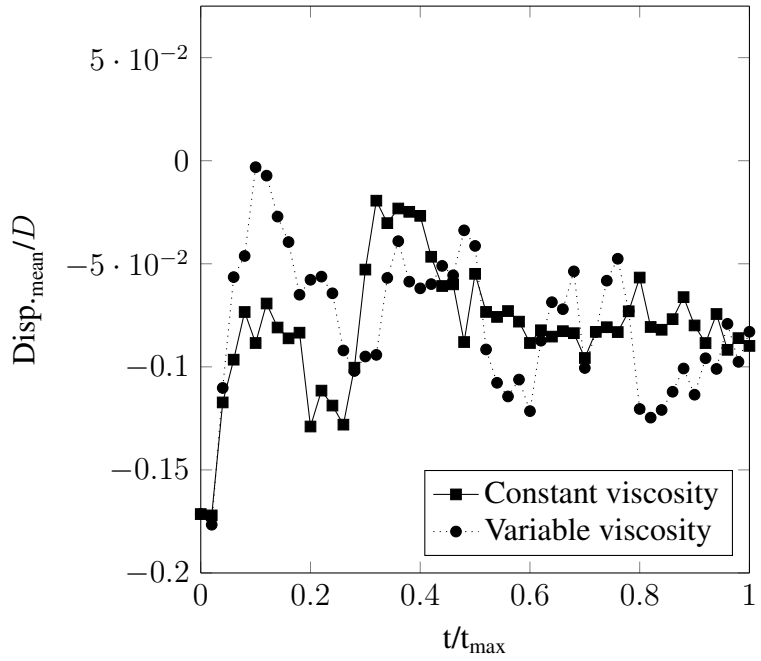

(a) Normalised mean particle vertical displacement

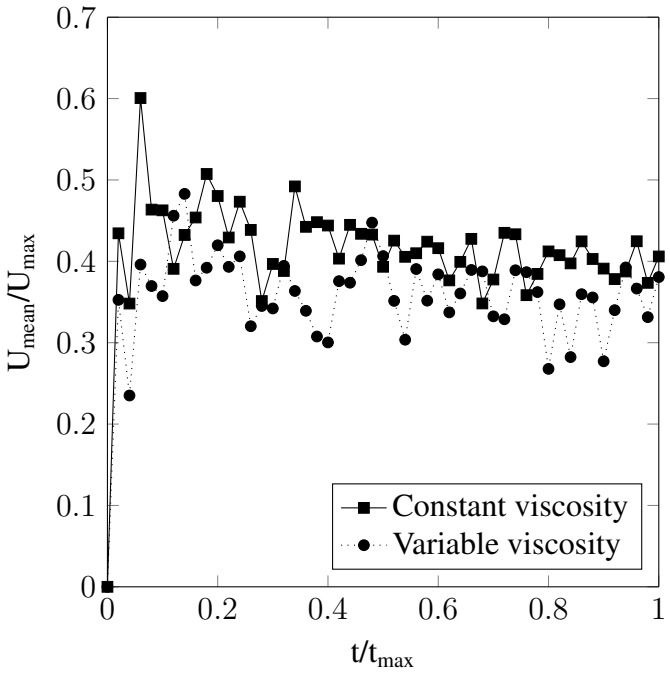

(b) Normalised mean particle velocity magnitude

Figure 4.9: Comparison of the mean vertical displacement and velocity magnitude of a dense particle suspension within a Couette flow of temperature-dependent viscosity fluid influenced by a temperature gradient.

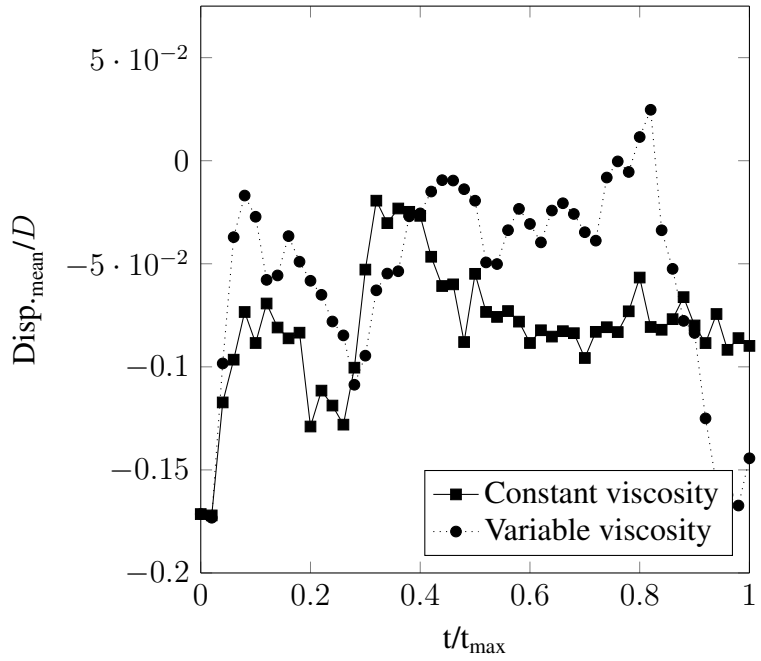

(a) Normalised mean particle vertical displacement

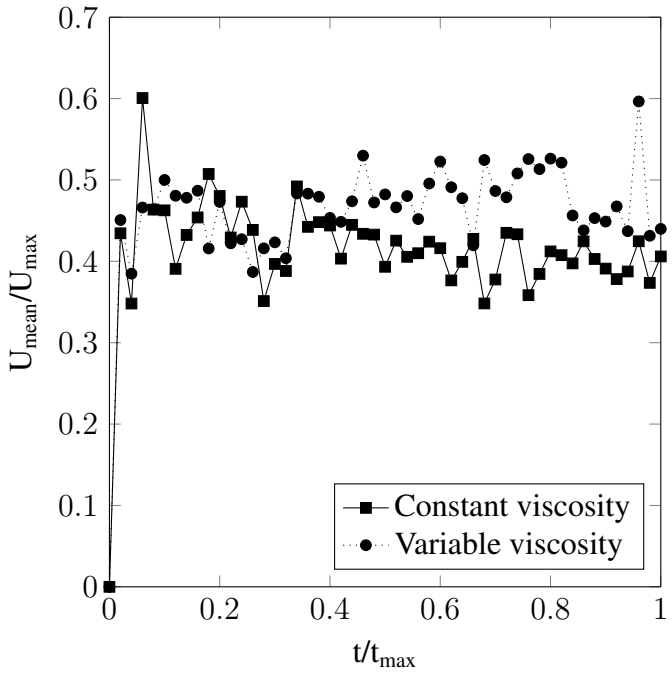

(b) Normalised mean particle velocity magnitude

Figure 4.10: Comparison of the mean vertical displacement and velocity magnitude of a dense particle suspension within a Couette flow of temperature-dependent viscosity fluid influenced by a reversed temperature gradient.

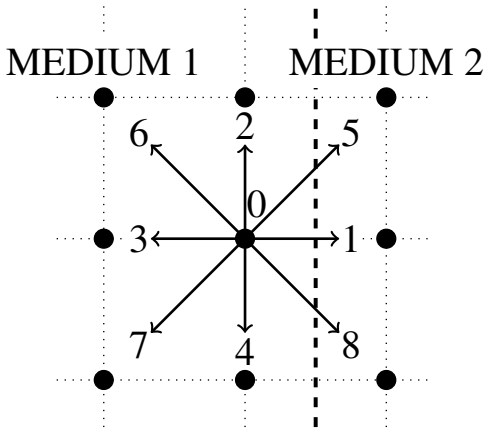

Figure 4.11: An example of finding temperatures within the total energy CHT model. To find the interface temperature along the dotted line, the CHT equations are solved between the '0' node and that in the '1' direction. The temperature at '0' is then estimated from the interface value and that at the node in the '3' direction.

used in this work.

Unlike the two CHT methods presented in Chapter 3, the approach of Pareschi *et al.* [107] is a strictly off-grid method. This is in the sense that the true interface of the two media is located between nodes. In the current implementation, the boundary is assumed to lie at the mid-point of these locations. The rationale of this method is that the interface between the two components is treated as a boundary between the respective regions. The CHT conditions are enforced by modification of the populations that are streamed across the boundary.

The first step in the procedure is to identify the temperature of the interface based on the CHT conditions. Given the interface is located off-grid, this computation will necessarily occur between the current node and its nearest neighbour with the adjacent media. This is then used to estimate the temperature at the local node by interpolating between the interface temperature and that at the node in the opposite direction to the interface. This is illustrated for a straight boundary in Figure 4.11. These values are then used to determine the local temperature gradients in the appropriate Cartesian directions of the lattice. Calculating these gradients is a non-local process which impedes the computational performance of this model. The key step in this implementation is using these values to add a correction term to the equilibrium expression of populations streaming across the boundary. This has the effect of modifying the populations such that they are streamed from a location with the computed interface temperature. The correction terms,

$$h_i^{eq,*} = \frac{w_i}{c_s^2}\left(c_s^2\tau_g\rho c_v K_\alpha \partial_\alpha T + 2u_\beta P_{\alpha\beta}\right) + \frac{w_i}{c_s^4}\left(c_s^2\tau_g\rho c_v\left(u_\alpha K_\beta \partial_\beta T + u_\beta K_\alpha \partial_\alpha T\right) + \left(2c_s^2 + 0.5\rho c_v T\right) P_{\alpha\beta}\right) \quad (4.6)$$

are added to the equilibrium values of the total energy energy population prior to the collision step occurring. Here α and β refer to the Cartesian directions of the lattice in Einstein notation and $P_{\alpha\beta} = \sum_i c_{i\alpha}c_{i\beta}\left(f_i - f_i^{eq}\right)$ is the local stress tensor. The K values are a conductivity correction term to be applied to the temperature gradient. This term takes a value of if the conductivity decreases between nodes in the indicated direction, -1 if conductivity increases or 0 if there is no change. Note that this overall correction is of a slightly different form to that presented by Pareschi *et al.* [107]. This is due to the zeroth moment of the energy population calculating $2\rho E$ in [107] compared to ρE in the model of Guo *et al.* [80] used in this thesis. An advantage of this strategy is that the form of the correction term is general for both two- and three-dimensional problems.

To quantify the performance of this implementation, three test cases were performed. The first was a two-medium bar similar to that used in Chapter 3, the second a case of flow parallel to an interface bound by sinusoidal temperature boundaries, and the final a case of radial heat transfer.

As in Chapter 3, a 1D bar was used as an initial test case to demonstrate the performance of the CHT method. For this model an end-heated bar was used as an example, as in Case 1 in Figure 3.2. In this investigation for a bar of length $L = 59\Delta x$, the left ($0 \leq x \leq L/2$) and right ($L/2 \leq x \leq L$) half domain values were 1/6 and 1/2 for conductivity, k, and 1 and 2 for heat capacity. Note that these are in lattice units. Consequently, $\Delta t = 1$ is used for this test as well as for the subsequent examples. The steady-state result for this situation can be determined from the CHT relations and the knowledge that linear temperature profiles will be created between the boundaries and the media interface. The interface temperature for this case is,

$$T_{Interface} = \frac{k_1 T_H + k_2 T_L}{k_1 + k_2}. \quad (4.7)$$

In Figure 4.12 it can be seen that the total energy LBM model is able to capture this behaviour accurately. The effect of the CHT correction creating a continuous temperature profile and step change in total energy at the interface can also been seen in this diagram. The transient performance of the LBM model was also examined by comparing the temperature development at $x = L/4, L/2$ and $3L/4$ to the analytic model [109] used in Chapter 3. As can be seen in Figure 4.12, this behaviour is also captured accurately. This is consistent with the results seen in Chapter 3, when a similar case was examined with different material properties. In particular, the model approaches the exact solution

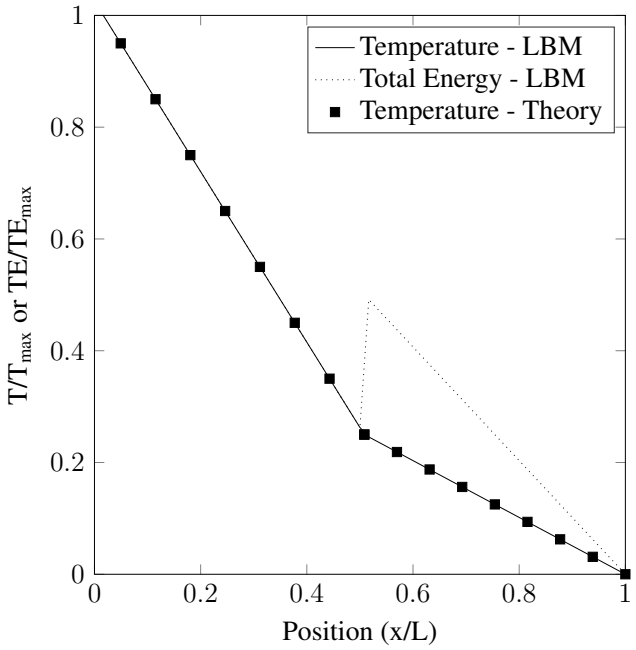

Figure 4.12: The steady-state bar results for temperature (compared to the analytic result) and total energy. The continuity of temperature and step change in total energy at the interface of the two material regions is clearly visible.

at the interface. The convergence of the model to steady-state can also be seen after approximately 7,500 steps.

The case of flow parallel to an interface has previously been used [108, 105] as an example of steady-state heat flow under complex bounding conditions. The domain used (Figure 4.14) is rectangular with length L and height H with $(x, y) \in ([0, L] \times [0, H])$. This is split at the point $y = H/2$ into two regions of differing material properties. The upper and lower boundaries of the full domain are held at a constant temperature profile described by $T(x, 0) = T(x, H) = cos(2\pi x/L)$. A constant horizontal velocity, U, flows through the entire domain in a periodic manner. The analytical solution for this problem at steady-state is given in Li *et al.* [108], although the term $(a_1^2 - 1)$ in the numerator of Equation 37 of this paper should read $(a_1^2 - 1)a_3$. This was confirmed via direct correspondence with the leading author, Like Li (31 January 2018). Dimensionless quantities were used to test the model within a domain of $(H \times L) = (64 \times 64)$. The upper and lower half domain values were 1/6 and 1 for conductivity, and 1/2 and 2 for heat capacity. Density, ρ, was held at unity throughout the entire test section. As per Li *et al.* [108], the velocity was chosen such that a Peclet number of $Pe = UHC_{p,lower}/k_{lower} = 20$ was enforced. LBM temperature profiles at $x/L = 0.0625, 0.25, 0.5$ and 0.75 have been generated and compared to the analytical solution at these locations. These are presented in Figure 4.15. As can be seen, the LBM results are able to very closely capture the analytic

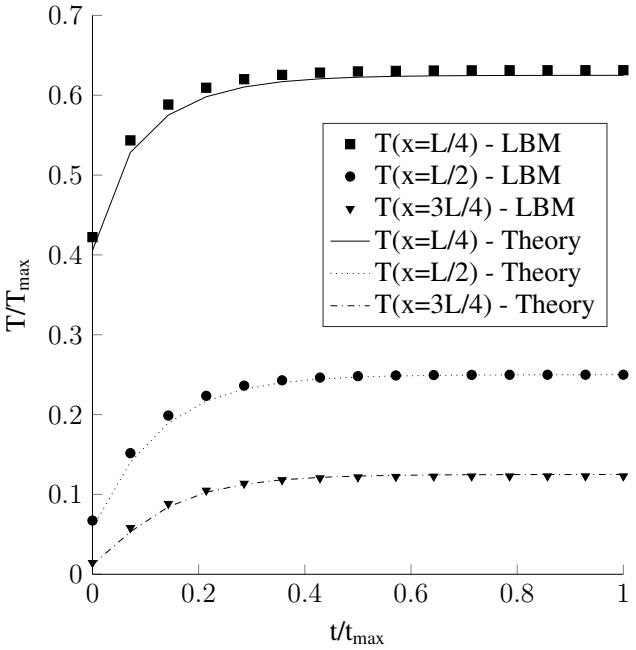

Figure 4.13: Transient results for temperature at three locations along the two medium bar. The total energy LBM model is able to accurately capture the theoretical behaviour.

results.

To demonstrate the model's ability to resolve CHT on curved boundaries, the radial test case presented in Li *et al.* [108] and Karani and Huber [105] has been analysed. This test case has a similar radial layout to that shown in Figure 3.3. Instead of having a constant temperature outer boundary, the temperature varies with radial position as $T(R_2, \theta) = cos(2\theta)$. The steady-state analytic solution for this problem is provided in Li *et al.* [108]. It should also be noted this test case was presented in Pareschi *et al.* [107] but with a slightly different fixed temperature boundary condition. This scenario was simulated until a steady-state was reached for four levels of grid resolution (between 16 and 128 lattice cells across the radius of the domain). In this model, the outer annulus had material properties of k = 100/6 and heat capacity of 10, while the inner region had k = 1/6 and heat capacity of 1. An example of the temperature contours generated by the model at steady-state can be seen in Figure 4.16. It should be noted here that the small circular contours around the edge of the interface of the two media can be viewed as artefacts associated with converting a circular boundary to a Cartesian lattice grid. In particular, this is believed to be associated with correctly identifying the missing populations at those locations. Also, these locations are where the assumption that the interface is midway between the nodes is most incorrect. The L_2 norm of these different grid resolutions were plotted against the radial resolutions to estimate the convergence properties of the implementation. The result of this is given in Figure 4.17. The order of convergence was noted to be 0.52, which is

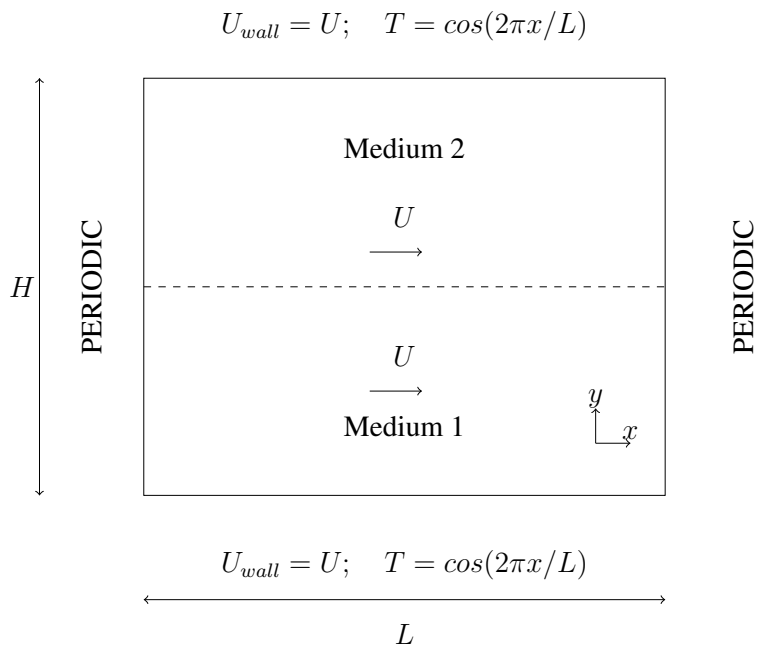

Figure 4.14: Layout for testing the steady-state LBM and analytic temperature profiles for flow across adjacent media with varying material properties as described in Li *et al.* [108].

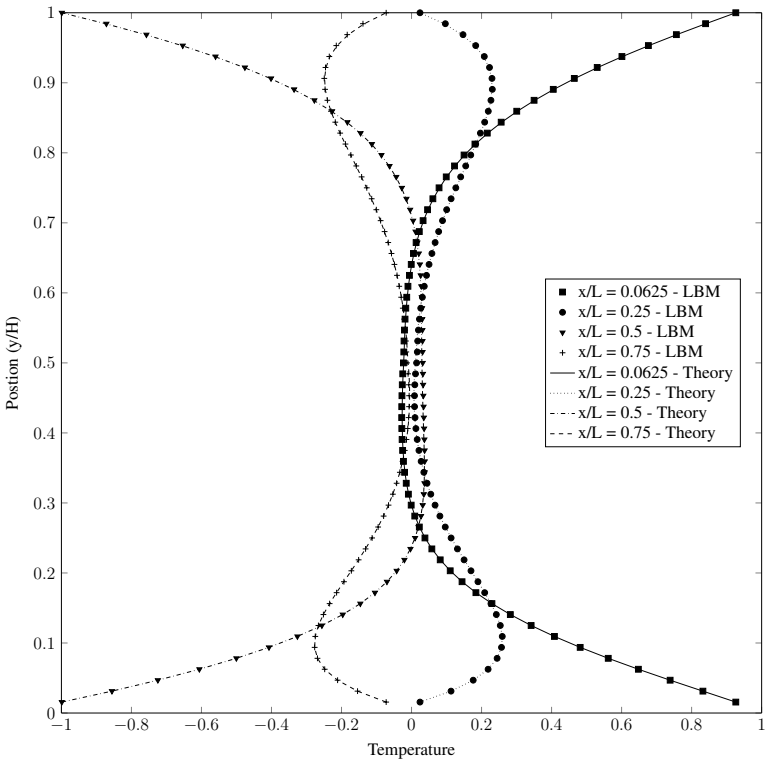

Figure 4.15: Comparison of steady-state LBM and analytic temperature profiles for flow across adjacent media with varying material properties as described in Li *et al.* [108]. The difference in profiles is due to the sinusoidal temperature profile along the upper and lower edges of the domain.

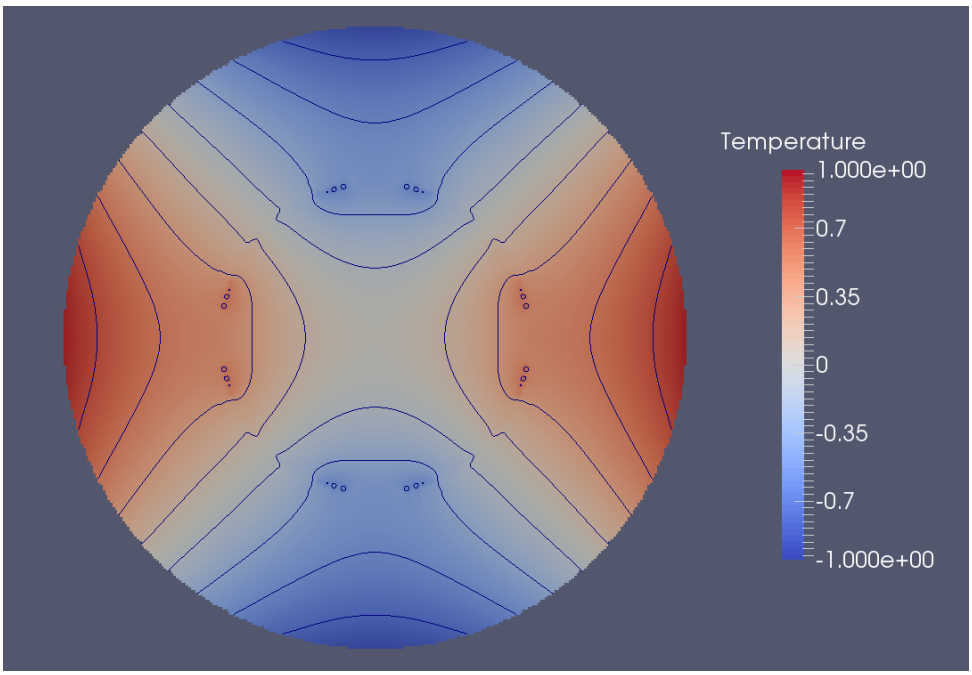

Figure 4.16: Temperature field and contours for the radial CHT test case. The small, round contour artefacts near the interface of the two media is believed to be associated with identifying the missing populations of the interface and locating a circular boundary onto a Cartesian lattice grid.

less than the results given by Pareschi *et al.* [107]. The difference in L_2 error magnitude between that and this work can be attributed to the different temperature measurements used to compile the L_2 figure. In Figure 4.17, the LBM profile was compared against the analytic solution along the radius of the full domain at $\theta = 0$. In Pareschi *et al.* [107], the temperature along the interface of the two regions was used to assess the model.

4.3 Summary

Firstly in this chapter, analytical results for a Couette flow with a temperature gradient were used to assess lattice Boltzmann models for flows with temperature-dependent viscosity. It was found that a total energy formulation of the thermal LBM was required to attain correct velocity and temperature profiles. The passive scalar LBM was not able to generate the complex thermal behaviour associated with changing viscosity. The total energy model was found to achieve approximately second order convergence towards the analytical results for both fluid velocity and temperature profiles. Furthermore, this model was coupled to the DEM to study the impact of temperature-dependent viscosity on the transport of suspended particles. In studies with a single particle within a Couette flow and temperature gradient, the presence of temperature-dependent viscosity was demonstrated to quan-

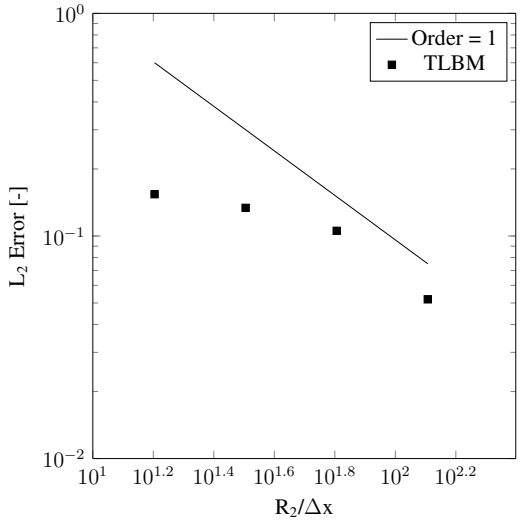

Figure 4.17: Convergence of the radial LBM results towards the analytic prediction. The order of convergence is estimated at 0.52.

titatively and qualitatively change how the particle moved through the flow. This variation can, in particular, be attributed to the change in the stress field and velocity profile throughout the fluid that is generated by changes in viscosity. Similar variations were observed when multiple particles were present in the domain, however collisions between particles were believed to reduce the impact of temperature-dependent viscosity.

Finally, a method for preserving CHT conditions within the total energy formulation was presented. This was verified using similar bar and radial test cases to those used for passive scalar CHT formulations in Chapter 3. A case of convective flow was also investigated. The results obtained demonstrated that the CHT method was able to resolve the temperature evolution of straight and curved boundaries in both steady-state and transient settings. It was also shown that the model could resolve CHT at boundaries in the presence of fluid flow. All of these were achieved with an acceptable level of accuracy.

Chapter 5

Suspension rheometry in three-dimensional flows

The work presented thus far in this thesis has been conducted in two dimensions. However, the models presented are general and can be directly extended to three-dimensional problems. This has been done for this chapter to firstly illustrate the capabilities of the model in realistic problems and to secondly conduct numerical rheometry tests of suspensions exposed to different temperature conditions. Numerical rheometry uses computational models to explore the properties and behaviours of fluids under a variety of complex conditions. In such a framework, a broad parametric space can be efficiently studied under repeatable conditions. The study of complex flow features, such as internal velocity profiles and fluid stresses, that are difficult to study experimentally can also be readily measured. Development of this model has occurred using the open-source codes of TCLB (LBM) and ESyS-Particle (DEM). Both LBM populations were implemented using a D3Q27 lattice.

5.1 Model capabilities

In this section, a number of the key features that demonstrate the capabilities of the model in three-dimensions are presented. In particular, these illustrate that the hydrodynamics of fluid-particle interactions are correct and CHT properties are preserved.

5.1.1 Calculation of particle coverage

As outlined previously, the partially saturated method of Noble and Torczynski [91] has been used to hydrodynamically couple the solid and fluid components. Central to this method is computing the fraction of the unit cell surrounding an LBM node that is covered by a solid particle (B, see

Figure 2.3). In stationary geometries, this is often straightforward and only needs to be performed during the initialisation of a simulation. For example, it can be achieved through application of an analytic description of a domain. Transient problems such as particle suspensions require this term to be recomputed regularly throughout a simulation. In 3D, this is most tractable for rigid spheres but can still be a time consuming task. Such approaches for computing this factor include Monte Carlo approximations, sub-division of lattice cells, edge intersection averaging or calculation of convex hulls [126]. Recently, Jones and Williams [126] proposed a linear approximation technique that significantly outperforms these methods both in terms of computation time for equivalent accuracy and accuracy for given computation time. They recognise that when mapping a sphere that is larger than an LBM cell, the coverage of a majority of cells varies linearly with the distance to the centre of the sphere. In their method, the coverage of a node-centred cell by a sphere, with radius r, is found through,

$$B = -\hat{D} + V_a - R + 0.5, \tag{5.1}$$

where $\hat{D}$ is the distance between the node and the surface of the sphere and $R = r/\Delta x$ is the sphere radius normalised by the grid spacing. The V_a term is the volume of the sphere contained within the cell. The authors present the solution to the associated integral as,

$$V_a = \left(\frac{1}{12} - R^2\right) \arctan\left(\frac{A}{1-2R^2}\right) + \frac{A}{3} + \left(R^2 - \frac{1}{12}\right) \arctan\left(\frac{1}{2A}\right) - \frac{4R^3}{3} \arctan\left(\frac{1}{4RA}\right), \tag{5.2}$$

where $A = \sqrt{R^2 - 0.5}$. This expression is constant for a given particle size and may be pre-computed prior to a simulation. The authors also give an equivalent expression for calculating the coverage of circles in 2D simulations. In practice, suspensions may be studied where multiple particle sizes are present. As such, when performing a calculation on a particle, V_a is not known *a priori*. From analysis of the function for V_a over a wide range of R, it was recognised that Equation 5.2 could be sufficiently approximated as,

$$V_a \approx R - K/R. \tag{5.3}$$

Here, K is a constant that was taken as 0.084 for 3D and noted to be 0.042 for the 2D case. In particular, this result is valid for $R > 2$. This is an acceptable outcome as larger values for R are needed for correct hydrodynamic behaviour to be computed. This means that the coverage of a cell by a sphere can be computed solely based on its distance from the centre of any given particle in the simulation as,

$$B = -\hat{D} - K/r + 0.5. \tag{5.4}$$

As in the work by Jones and Williams, this value is capped such that $B \in [0, 1]$ is maintained. For the results in the following section, only LBM nodes that were centred within a particle had their coverage mapped. This was found to yield superior results in the tests conducted for the particle resolution of interest.

5.1.2 Particle hydrodynamics

Terminal velocity of a single particle between parallel plates

To demonstrate that the hydrodynamics of a particle within a fluid is correctly captured by the 3D model, the test case of a particle settling between two parallel plates was used. In this scenario, a particle was placed between two plates and accelerated by a body force with the terminal velocity of the particle used as an evaluative measure. In the low Reynolds number regime of Stokes flow (i.e. $Re \ll 1$), the velocity of the particle is given by Wang *et al.* [127] as,

$$U_{sphere} = \frac{F\left(1 - 0.625(r/l) + 0.1475(r/l)^3 - 0.131(r/l)^4 - 0.0644(r/l)^5\right)}{6\pi\rho\nu r}. \tag{5.5}$$

Here, r is the radius of the sphere and l its distance from the nearest wall. F is the magnitude of the force applied to the particle. Looking forward, this analysis is relevant for proppant transport in hydraulic fracturing as flows in this regime are typical.

For the test case presented here, see Figure 5.1, the density of the particle was taken as ρ = 2,000 kg/m^3, and the particle was sized and placed such that r/l = 0.5. Typically, the upper boundary of the domain was placed at a height of $H = 4l$, and the periodic sides were spaced $4H$ apart. The fluid possessed a kinematic viscosity of $\nu = 10^{-6}m^2/s$. A constant acceleration of **a** = 0.01 m/s^2 was applied to the particle as the driving force parallel to the plates. This leads to a predicted terminal particle velocity of approximately U_{sphere} = 3.1 $\times$ $10^{-5}m/s$. This corresponds to a valid particle Reynolds number of about 0.01 for the particle radius of r = 0.0001 m. Figure 5.2 shows the absolute relative error of the measured terminal particle velocity. The results converge to this value at approximately order 2.8 with increasing radial resolution. The convergence of the model being slightly greater than second order is consistent with previous data presented for this test case [127, 128]. These authors suggest the approximations inherent in the analytical solution as a possible cause for this. It can also be noted that some minor variations in geometry: the periodic sides being spaced $8H$ apart for the $r/\Delta x$ = 2 case and the upper domain located at $H = 8l$ for the $r/\Delta x$

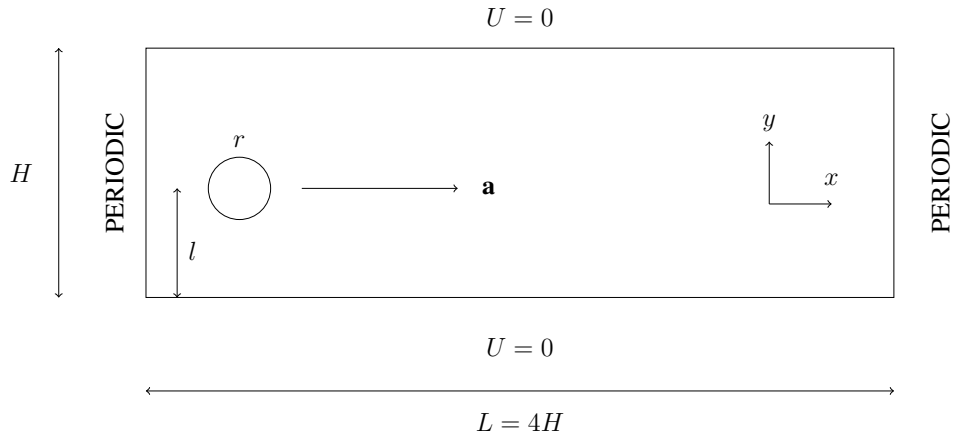

Figure 5.1: Mid-plane view of terminal velocity test used to verify the model's hydrodynamics. The model is periodic in the out-of-page direction which typically had a total depth of $4H$. The particle of radius r = 0.0001m was placed such that r/l = 0.5, while $l = H/4$ was typically used in testing.

= 6 case; do not impact the convergent trend. These modifications were needed for the test case to run on the available computational resources. In this chapter, a resolution of $r/\Delta x$ = 6.4 for free moving particles has been chosen as a compromise between resolving the hydrodynamics and computational speed. From Figure 5.2, the absolute relative error of the particle velocity of this case is approximately 1%. In particular, this highlights that the PSM requires a minimum resolution of particle radius compared to grid spacing to accurately capture the hydrodynamics of a sphere moving through a viscous fluid.

Relative viscosity of particle suspensions

To validate the model for suspension flow, the effective viscosity for a variety of solid volume fraction (SVF) cases is calculated and compared to previous results from the literature. In a general setting of spheres immersed within a Newtonian fluid, the presence of the solids causes the apparent viscosity of the suspension to increase. This is noted to occur rapidly as the SVF of the suspension approaches the maximum packing (for particles of the same size) of approximately 64% [36]. To test this, a numerical rheometer was designed such that a single layer of particles was located in the centre of the domain. These were set to half the radius of the free particles to allow better packing and a smoother platen surface. A constant force, $F_{applied}$, was applied to this platen to shear the fluid. The measured steady-state velocity of the platen indicated the velocity gradient, $\partial U/\partial y$, to the walls parallel to platen. This allowed the effective viscosity, μ_E, of the suspension to be measured using,

$$\tau = \frac{F_{applied}}{A} = \mu_E \frac{\partial U}{\partial y}, \tag{5.6}$$

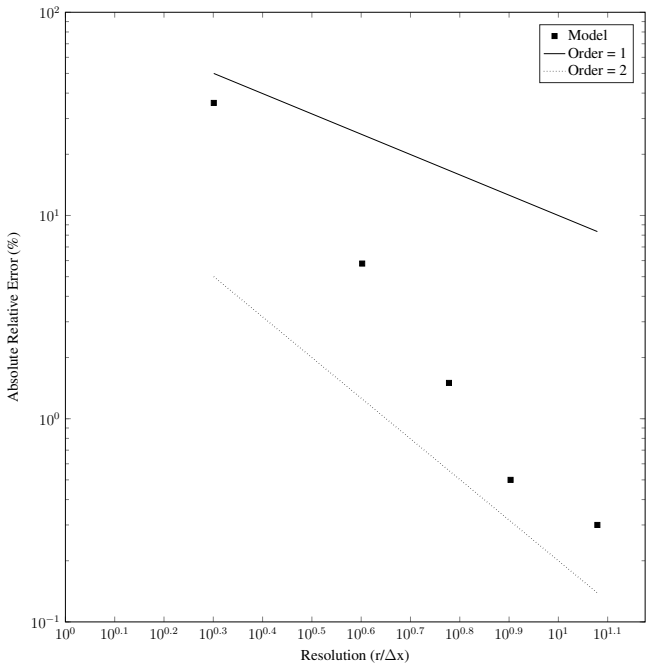

Figure 5.2: Convergence of the terminal velocity of a particle moving between parallel plates due to a constant acceleration. Slopes of first and second order convergence have been included for reference. The observed convergence order of approximately 2.8 is consistent with that observed in previous studies [127, 128].

with τ being the shear stress in the fluid over plan area A. The addition of particles to either one or both sides of the shearing platen alters the SVF of the suspension being tested. The relative viscosity, μ_R, of the suspension is the ratio of μ_E to the viscosity of the base fluid. A schematic layout of this test domain is illustrated in Figure 5.3. The physical grid spacing (Δx = 1.5625$\times$ $10^{-5}m$) and time step (Δt = 4μs) give a fluid viscosity of approximately ν = 1.02 $\times$ $10^{-5}m^2/s$. The domain height was set to H = 0.002m and the shearing force on the platen was set at 4 μN. Tests were run until a steady platen velocity was reached.

Due to fluid-particle and particle-wall interactions, the effective viscosity of the fluid increases with SVF. A number of empirical correlations for this behaviour can be found in the literature [16, 129, 130, 131, 132]. What can be noted from these correlations is that the behaviour of the suspension becomes more sensitive to experimental layout and material properties as the particle fraction increases. This is evidenced by the increasing spread of values for the correlations presented in Figures 5.4 and 5.5. In both cases, the 'Model 1' results calculate the relative viscosity by comparison to the input fluid viscosity. 'Model 2' compares the suspension viscosity against the viscosity of the fluid as calculated by repeating the test with no free particles present. These results are compared against a number of experimentally validated correlations for the relative viscosity of suspensions

from the literature. The correlations used here are the Krieger-Dougherty equation [130, 16, 133]:

$$\mu_R = \left(1 - \frac{\phi}{\phi_M}\right)^{-2.5\phi_M}; \tag{5.7}$$

the Eilers correlation [131, 130]:

$$\mu_R = \left(1 + \frac{1.5\phi}{1 - \frac{\phi}{\phi_M}}\right)^2; \tag{5.8}$$

the Mooney equation [16]:

$$\mu_R = exp\left(\frac{2.5\phi}{1 - \frac{\phi}{\phi_M}}\right); \tag{5.9}$$

and the correlation proposed by Morris and Boulay [129, 132]:

$$\mu_R = 0.133 + I + 2.5\phi_M\sqrt{\frac{4I}{3}}; \tag{5.10}$$

where $I = \frac{4}{3}\left(\frac{\phi_M}{\phi} - 1\right)$. In these expressions ϕ_M is used represent the maximum random packing fraction of spheres into a volume. A value of ϕ_M = 0.64 is used for the Krieger-Dougherty and Mooney equations, the Eilers equation uses ϕ_M = 0.58 while the Morris-Boulay expression takes ϕ_M = 0.68. Although used as a model fitting parameter in these correlations, ϕ_M should ultimately be a constant geometric property.

In these figures, four variations of simulations based on particle packing and shearing platen design are presented. Firstly, Figure 5.4 examines the case of free particles only being located on the lower side of the shearing platen. The stated SVF is calculated based on the volume below the platen only. This layout was examined as it more closely resembles the Couette-type rheometer that is used in many experimental studies. In this case, the relative viscosities predicted numerically are, generally speaking, at or below those determined by validated correlations. The results predicted by the Morris and Boulay correlation [129], however, are very well captured.

In Figure 5.5, the rheometer has particles on both sides of the shearing platen in order to provide a more symmetrical model. This has served to increase the effective relative viscosity of the suspension for a comparable SVF (this time calculated based on volume above and below the platen). The discrepancy between the numerical model and the correlations is however similar to that seen elsewhere in the literature e.g. [133]. It should also be noted that the correlations and numerical results presented by Thorimbert *et al*. [133] are developed using a smooth shearing platen. It is unsurprising that with the rougher platen used in this model that the suspension appears more viscous as both fluid and particle interactions with the platen are increased. The two sets of results in both figures further illustrate the difference in behaviour that the choice of platen can make. In Figure 5.5a, a densely packed platen has been used to more closely imitate a smooth surface shearing the fluid. This layout

will more strongly interact with the free particles, but it will also experience greater friction from the free fluid. In Figure 5.5b, the platen is more much more sparsely packed - the fraction of the shearing plane covered by particles is reduced by a factor of approximately nine. This reduces both the amount of particle interaction with the platen and the effective drag upon it. As the thickness of the effective shearing platen is the same through the height of the domain, these two layouts yield effectively similar velocity profiles through the sheared fluid. It can be seen that the sparser platen does serve to better match the correlation predictions, particularly at SVF below about 0.3.

Figure 5.6 presents the relative viscosity results for a rheometer with particles situated on both sides of a sparsely packed platen. Here the 'T' results represent simulations performed with a temperature thinning fluid,

$$\nu = \nu_0 e^{-T}, \tag{5.11}$$

at a constant dimensionless temperature of $T = 1$. As an incompressible fluid is being studied the conversion between dynamic and kinematic viscosities is valid. In the thinner fluid, the relative viscosity of the suspension is significantly increased over the isothermal case. This behaviour was observed experimentally by Konijn *et al.* [134] and highlights that the relative viscosity of a fluid may not solely be dependent on SVF. Of some potential reasons for this presented by Konijn *et al.* , grain-inertia effects are possibly the most likely explanation in the current setting. As particles can move more freely in the thinner fluid, more of the input shearing force is required to overcome particle momentum when they collide with the shearing platen. This results in a greater apparent viscosity of the suspension, especially with increasing SVF.

In all cases presented here, it is important to observe that the fundamental physics of suspensions is being captured accurately by the model.

5.1.3 Transient conjugate heat transfer modelling

In Chapter 4, the presented total energy approach for CHT supposed that the interface between two media was stationary. To model transient suspensions, the method needs to be adapted to accommodate changing interface positions. This was achieved by labelling the component of a given node based on its solid coverage at a given point in time. By comparing the value of this flag with that of its neighbours, the presence and orientation of component boundaries relative to the node can be identified. Once the directional orientation is known in terms of the closest lattice velocity direction, the interface is assumed to lie halfway between the current node and the neighbouring node in that direction. From this point, the presented CHT algorithm can be applied.

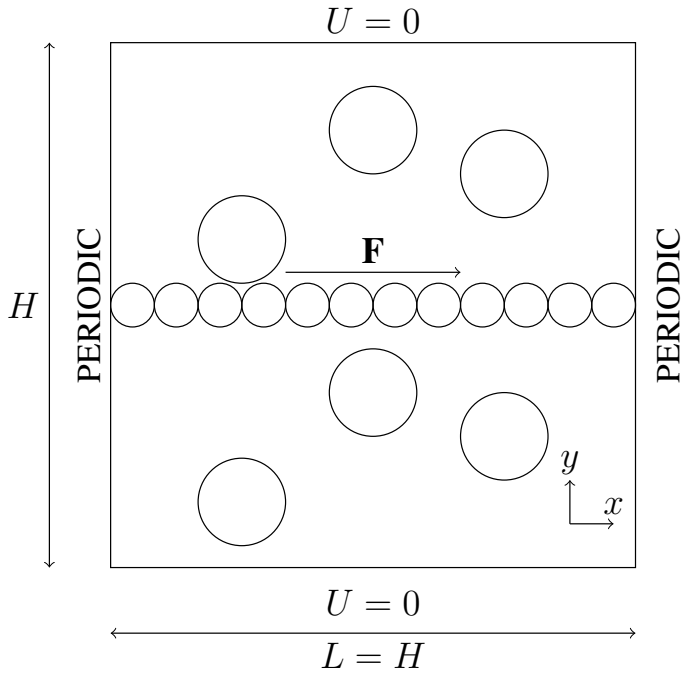

Figure 5.3: Mid-plane view of relative viscosity test used to validate the model's hydrodynamics. The model is periodic in the out-of-page direction which also had a total depth of $0.5H$. Free moving particles were placed either below or on both sides of the central shearing platen. The central platen had a constant force applied to it to shear the fluid, its steady-state velocity provided a measure of the effective viscosity of the suspension.

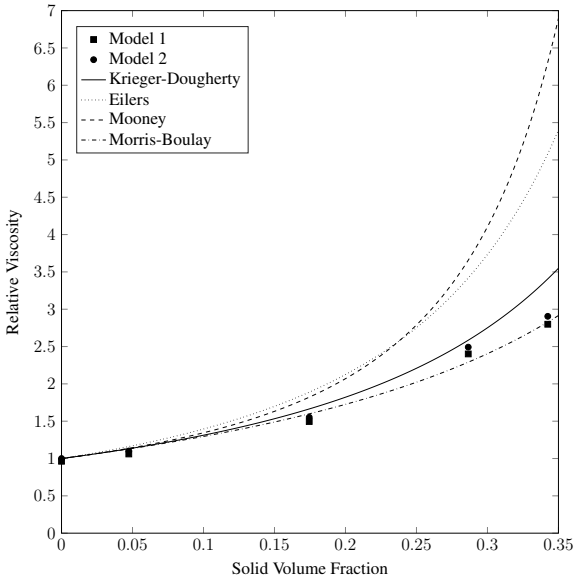

(a) Dense platen

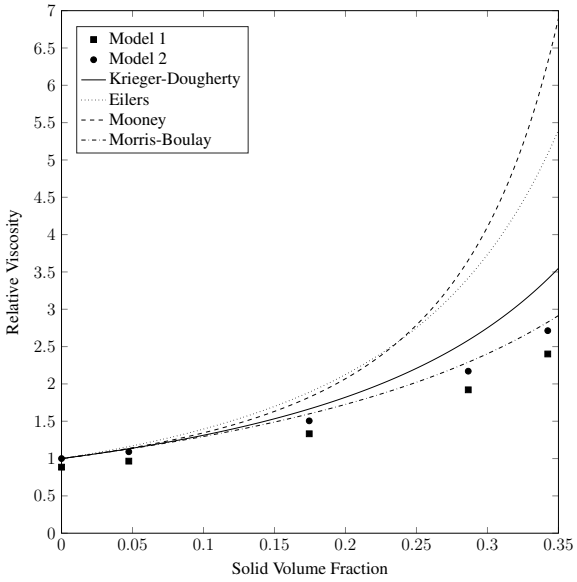

(b) Sparse platen

Figure 5.4: Relative viscosity results generated by the model with particles located only on the lower side of the platen. The 'Model 1' results calculate the relative viscosity by comparison to the input fluid viscosity. 'Model 2' compares against the viscosity determined with no free particles present. In (a) the platen is essentially fully covered by non-overlapping particles whereas in (b) the driving platen is sparsely populated with particles. These results indicated the sensitivity of the the relative viscosity to the layout of the rheometer.

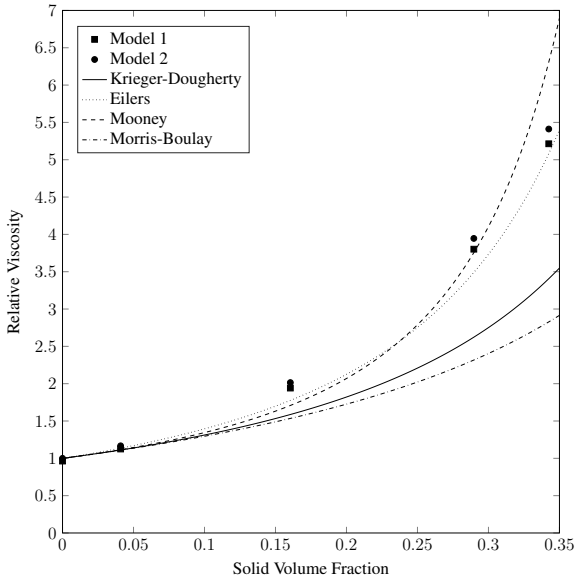

(a) Dense platen

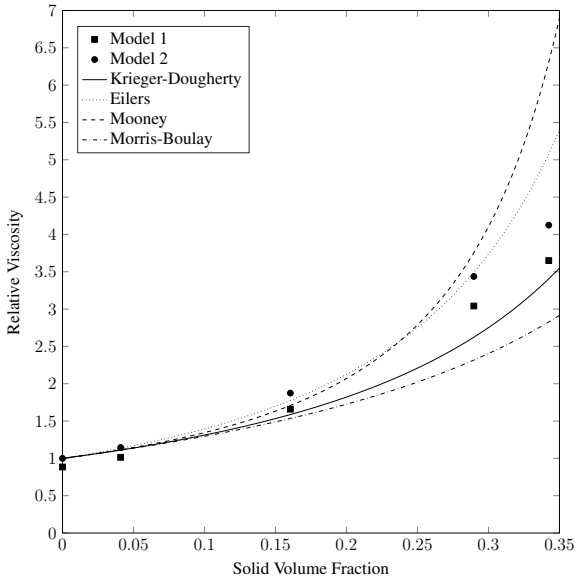

(b) Sparse platen

Figure 5.5: Relative viscosity results generated by the model with particles located only on the both sides of the platen. The sparse and dense platen layouts described in Figure 5.4 are again compared here. Again, these results indicate the sensitivity of the the relative viscosity to the layout of the rheometer.

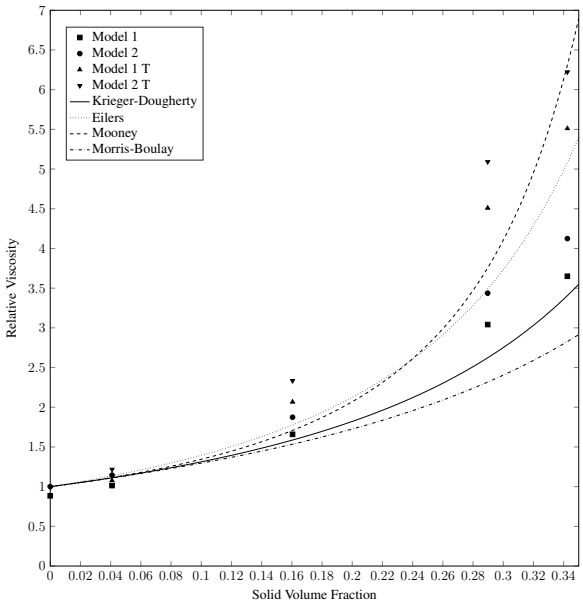

Figure 5.6: Relative viscosity results with particles on both sides of a sparsely packed platen. The 'T' results indicated simulations run with a temperature-dependent viscosity fluid at T=1 (i.e. $\nu = \nu_0 e^{-1}$).

To illustrate the calculation of the normal direction, a 2D example will be given for simplicity (see Figure 5.7). Here, positive flag values are assigned to the solid (S) and fluid (F) nodes. The normal located at node e can then be calculated with,

$$\hat{\mathbf{n}} = \frac{\mathbf{n}}{|\mathbf{n}|}, \tag{5.12}$$

where,

$$\mathbf{n} = \left((c+f+i)-(a+d+f)\,,(a+b+c)-(g+h+i)\right). \tag{5.13}$$

To ensure consistency in computations for the orientation of the normal, the sign of the vector is swapped if the sum of the surrounding nodes is less than the same number (eight in 2D) of the central node (here e). When the flag value of S is greater than F, this ensures that the normal is pointing towards the fluid. The lattice direction, i, closest to the normal can then be found by determining $max(\hat{\mathbf{n}} \cdot \mathbf{c}_i)$.

As a demonstration of CHT being observed, consider a particle moving through a channel of fluid that possesses differing conductivity and heat capacity. Here $k_{solid} = \frac{1}{2}$ and $C_{p,solid} = 3.0$ (lattice units), the respective fluid values are taken as one-third of these. A temperature gradient is applied across the channel with the entire domain intialised at the temperature of the hot wall. As the particle moves it will be cooled by the temperature gradient at a different rate to the surrounding fluid. The particle will represent a disturbance in the temperature field, however the CHT restrictions mean that this will be continuous with fluid's temperature field. This has been applied to a layout similar to the

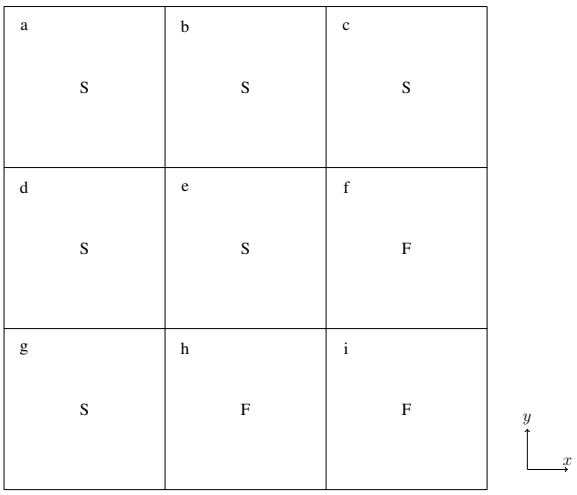

Figure 5.7: Example layout for determining the direction of the interface normal. Solid nodes are labelled S and fluid nodes F. Lower case letters are for identification.

hydrodynamic test case described in Figure 5.1. In Figures 5.8 and 5.9 the desired behaviours for temperature (continuous at particle boundaries) and total energy (step change at particle boundaries and $\frac{C_{p,solid}}{C_{p,fluid}} = 3$ times greater than temperature) can be observed.

5.2 Numerical rheometry

With the model validated, the behaviour of a sheared suspension under a variety of conditions was examined. Numerical rheometry allows a range of configurations and behaviours to be tested efficiently under repeatable conditions. These focused on different combinations of volume fraction, temperature gradient, fluid model and material properties. These demonstrate not only the behaviour of suspensions in an isothermal setting but also when the impacts of temperature-dependent viscosity and conjugate heat transfer are taken into account.

The rheometer model constructed to perform these tests consisted of a layer of regularly packed spheres at its upper and lower surface in the y-direction (see Figure 5.10). These are translated in opposite directions at a constant velocity to both shear the flow and to provide a boundary to the internal particles. The boundaries in the x- and z-directions are periodic for fluid flow, thermal effects and particle motion. The domain measures $0.002m$ in the x-direction and $0.001m$ in the z-direction. The centres of the spheres in the shearing platens are separated by $0.0018m$. The particles in these models are all of radius $100\mu m$ and resolved by 6.4 lattice spacings. A time step of $4\mu s$ implies that the kinematic viscosity of the base fluid is approximately ν = 1.02 $\times$ $10^{-5}m^2/s$ when the numerical viscosity of the total energy LBM is 1/6. The magnitude of shearing velocity of the two platens was

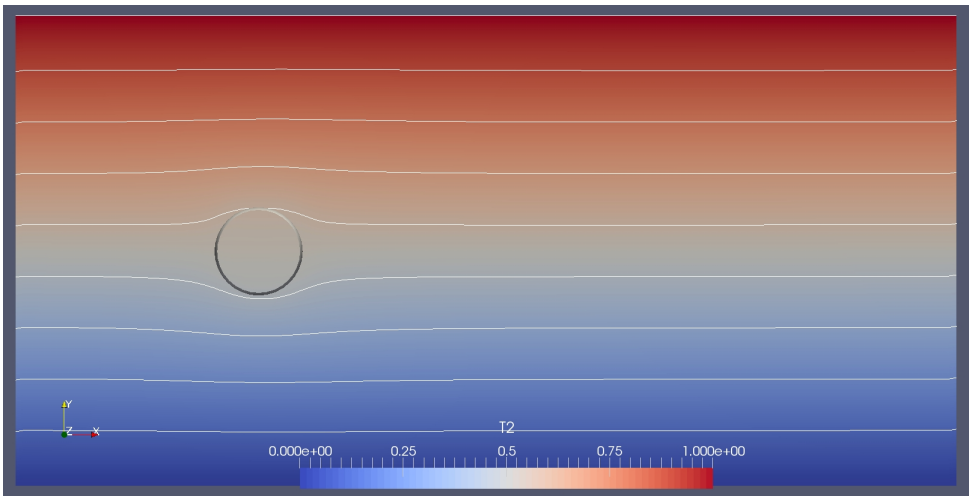

(a) Temperature distribution at $t^* = 0.85$

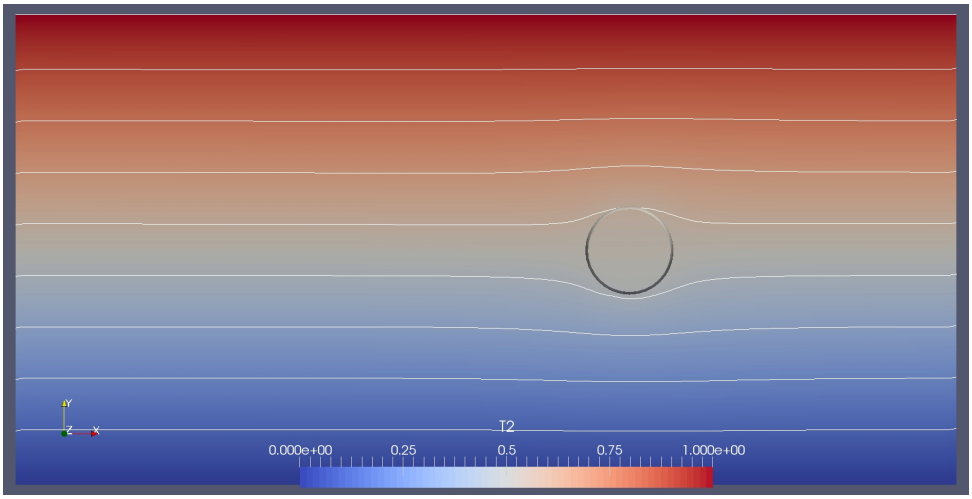

(b) Temperature distribution at $t^* = 1.0$

Figure 5.8: An example of the temperature distribution around a particle as it move through a fluid with an applied temperature gradient. The figures are coloured and contoured by dimensionless temperature. Because of the CHT implementation, the temperature field is continuous between media within the total energy conserving LBM model.

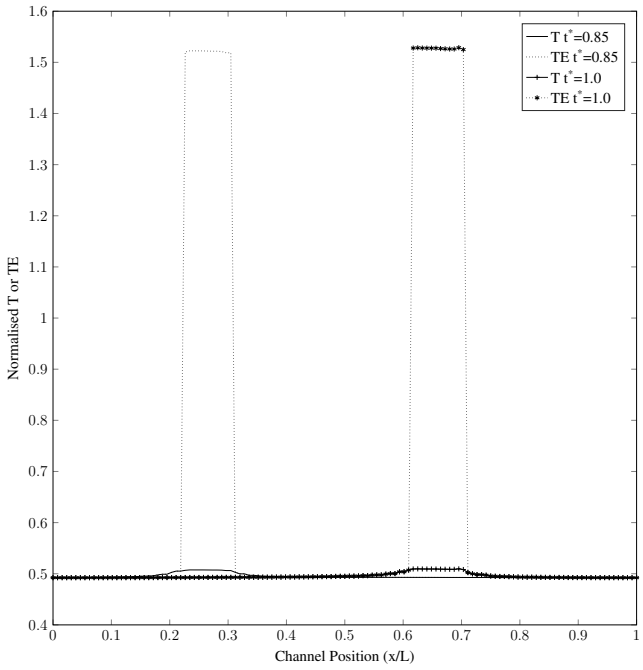

Figure 5.9: Traces of temperature and total energy along the centre line of the channel at the times presented in Figure 5.8. The continuity of temperature and step change in total energy are clearly evident.

set at $0.1m/s$, corresponding to a shear rate of $\dot{\gamma}$ = 111.11 s^{-1}. Five cases of particle SVF were examined, as summarised in Table 5.1. Note that in the base case, the 120 particles represents those in the two shearing platens. SVF has been calculated based on the freely moving internal particles only. All cases were run for 80,000 steps.

To examine thermal behaviour, the same combination of dimensionless temperature gradients and fluid viscosity as used in Chapter 4 were again applied and outlined in Table 5.2. As in Chapter 4, these can be interpreted based on $T_H^{physical}$ = 350K and $T_C^{physical}$ = 300K. It is noted here that for the layout of the rheometer used, the two non-isothermal cases are identical but subject to inverted initial

Name	**Total Particles**	**SVF**
Base	120	0%
SVF0	157	5%
SVF1	243	16%
SVF2	337	28%
SVF3	403	37%

Table 5.1: Solid volume fractions of different test cases examined in a shearing rheometer.

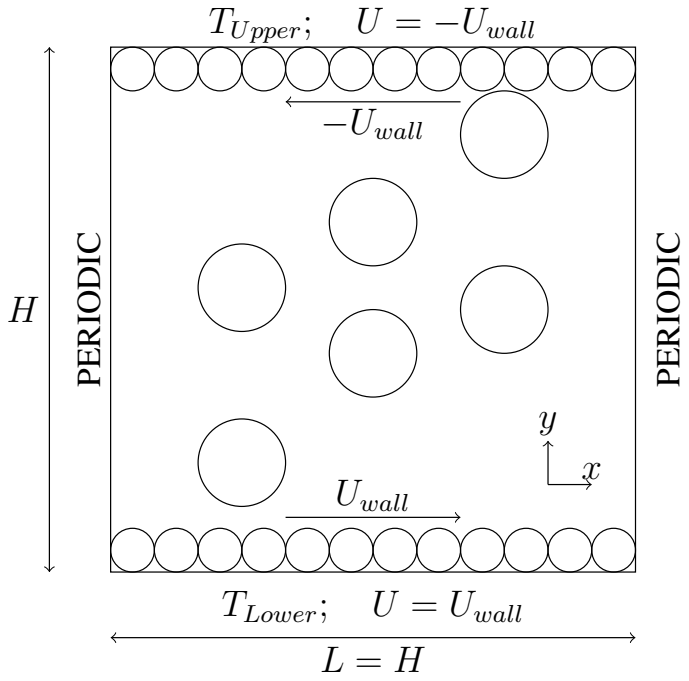

Figure 5.10: Mid-plane view of planar shearing test used to explore the macroscopic behaviour of suspensions. The model is periodic in the out-of-page direction which also had a total depth of $0.5H$. Free moving particles were placed between the upper and lower constant velocity shearing platens at various concentrations.

Case	T_{Upper}	T_{Lower}
NT	0	0
T	1	0
Ts	0	1

Table 5.2: Dimensionless temperature conditions at the walls for numerical rheometry tests.

Property	non-CHT	CHT - increase	CHT - decrease
k	$\frac{1}{6}$	$\frac{1}{2}$	$\frac{1}{18}$
ρC_p	1.0	3.0	$\frac{1}{3}$

Table 5.3: Thermal material data used for the solid component in the rheometer tests. The fluid component used the non-CHT values in all tests. All values here are in lattice units.

particle positions. The results from these cases should then be approximately symmetric. When a temperature gradient is being applied, the viscosity reduces with temperature according to $\nu = \nu_0 e^{-\beta T}$. Here ν_0 is the viscosity at the cold wall (set numerically as $1/6$) and $\beta = 1$.

To demonstrate the influence of conjugate heat transfer on the behaviour of the suspension, the material properties of the solid component were modified in two ways as indicated in Table 5.3. These changes in material property conserved the thermal diffusivity of the solid in all cases. The base fluid properties remained unmodified at non-CHT values. In these cases the solids and internal fluid was initialised at the same temperature as the hot wall.

5.2.1 Numerical rheometry results: non-CHT

To begin, the analysis of suspensions without CHT effects was performed. In practice, this means that the solid and fluid components have the same thermal properties. To establish a base from which the effects of temperature change and subsequently CHT can be quantified, baseline results for suspension behaviour were established. As presented in Figure 5.11, these illustrate the average velocity profiles recorded in the central plane of the domain in two ways. Firstly the profiles seen at all SVF cases without the effects of temperature-dependent viscosity (i.e. the isothermal case); and secondly the base temperature-dependent viscosity fluid profiles when no particles are present. In particular, it can be noted in Figure 5.11a that as the SVF increases, the presence of particles causes a non-linear perturbation of the velocity profile. The particles cause a reduction in flow velocity through the centre of the channel and steeper flow gradients adjacent to the shearing platens. In Figure 5.11b,

the recorded velocity profiles for a temperature-dependent fluid are consistent in nature with those observed and discussed in Chapter 4.

The first comparison that can be made is how the velocity profiles change when a temperature gradient is applied. These are provided in Figure 5.12. The most noticeable feature of these results is the deviation of the line of stationary flow away from the centre of the channel, consistent with the baseline results. This is particularly noticeable for SVF0 and SVF1. For both temperature gradient cases, the section of flow adjacent to the heated boundary is very similar for all SVF cases. This section of flow corresponds to the lowest viscosity region of the domain where the particles provide less of a disturbance to the flow imposed by the shearing platen. Adjacent to the cold boundary, the particle effects dominate for the higher SVF cases and the fluid effects at lower SVF. This is indicated by the SVF2 and SVF3 profiles remaining similar to those seen in the isothermal case whilst SVF0 and, to a lesser extent, SVF1 more closely resemble the base fluid profile in this region. This behaviour is further highlighted in Figure 5.13 where the variation of the flow profiles at each non-zero SVF case are presented. It can be observed here that as the SVF increases, the temperature-dependent behaviour of the fluid reduces and the velocity profile becomes more closely aligned with the base isothermal profile. A characteristic change in the flow profile can be noted to occur between SVF1 and SVF2 (SVF $\approx 20\%$). Around this point, the 'S'-shape of the isothermal profile becomes more pronounced compared to the monotonically varying gradient observed with the base temperature-dependent fluid. Figure 5.14 demonstrates that the presence of particles in the non-CHT case has only a minor impact on the temperature distribution within the fluid. Here the temperature profile becomes slightly non-linear and the temperature throughout the profile is increased. As, thermally speaking, there is no interaction between the solid and fluid in this test case, this variation must be associated with the changing hydrodynamics within the domain. In particular, it is believed that viscous heating of the fluid within the freely moving fluid generated by the particles is causing this. This is discussed further when considering the CHT results. Finally, it was also noted that the vertical migration of particles within the rheometer was negligible for each SVF case

5.2.2 Numerical rheometry results: CHT

The material parameters of the solid component were altered in two different ways in order to introduce CHT to the flow. In both cases the 'T' temperature case was simulated. In these cases the thermal relaxation constant, $\omega_g = \left(\frac{3k}{\rho C_p} + 0.5\right)^{-1} = 1.0$, was held constant between the solid and fluid components. In Figure 5.15, the increased properties from Table 5.3 were implemented, while in Figure 5.16 the decreased values were used. These investigations were performed to demonstrate

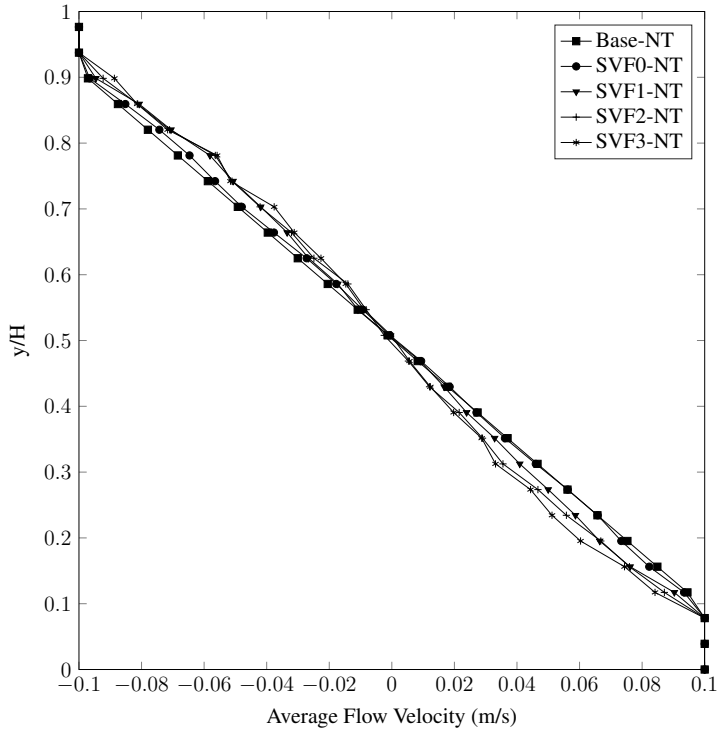

(a) Baseline SVF

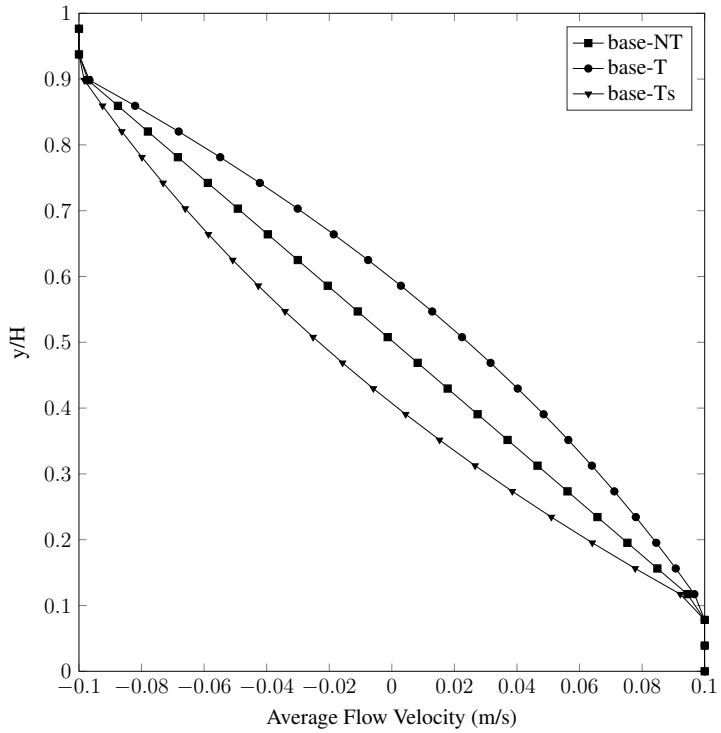

(b) Baseline temperature

Figure 5.11: Baseline results for the velocity profiles generated within the rheometer. The SVF results indicate the profiles generated without temperature-dependent viscosity or CHT effects. The temperature results indicate the profiles generated within the fluid with no particles present under the temperature conditions. The NT results refer to the isothermal model. T and Ts refer to the two temperature cases (see Table 5.2).

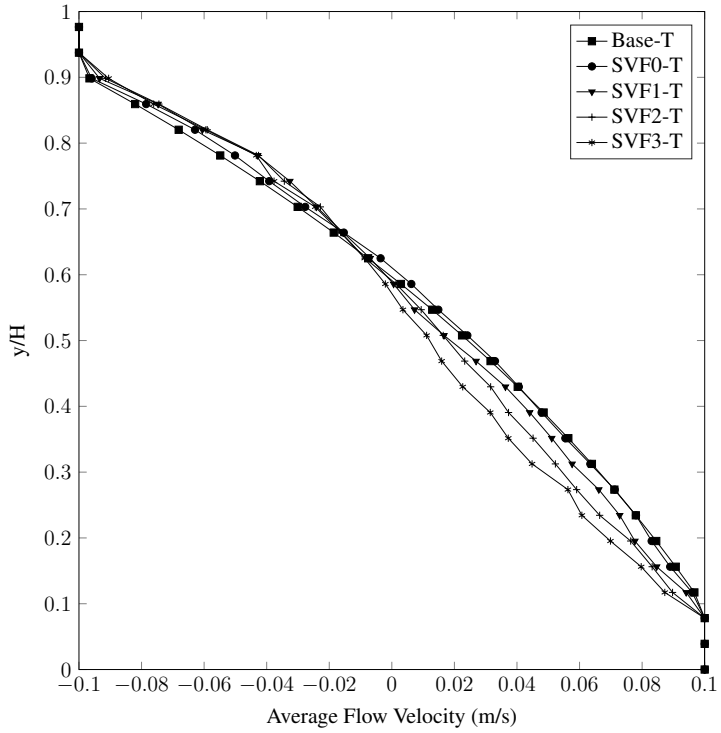

(a) Case ‘T’

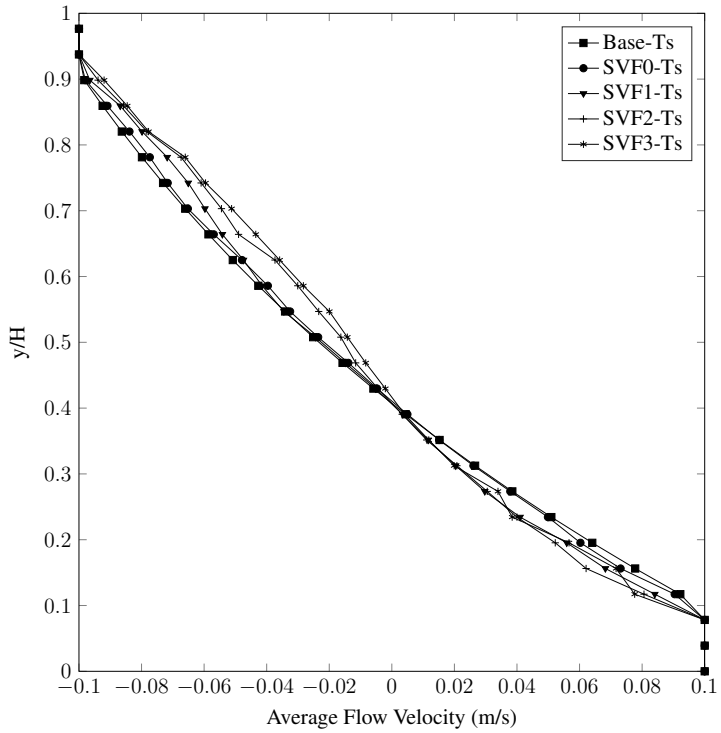

(b) Case ‘Ts’

Figure 5.12: Variation of flow profiles within the different SVF cases with applied temperature gradient. Note the change in the stationary velocity location away from the centre of the channel, particularly for the lower SVF cases.

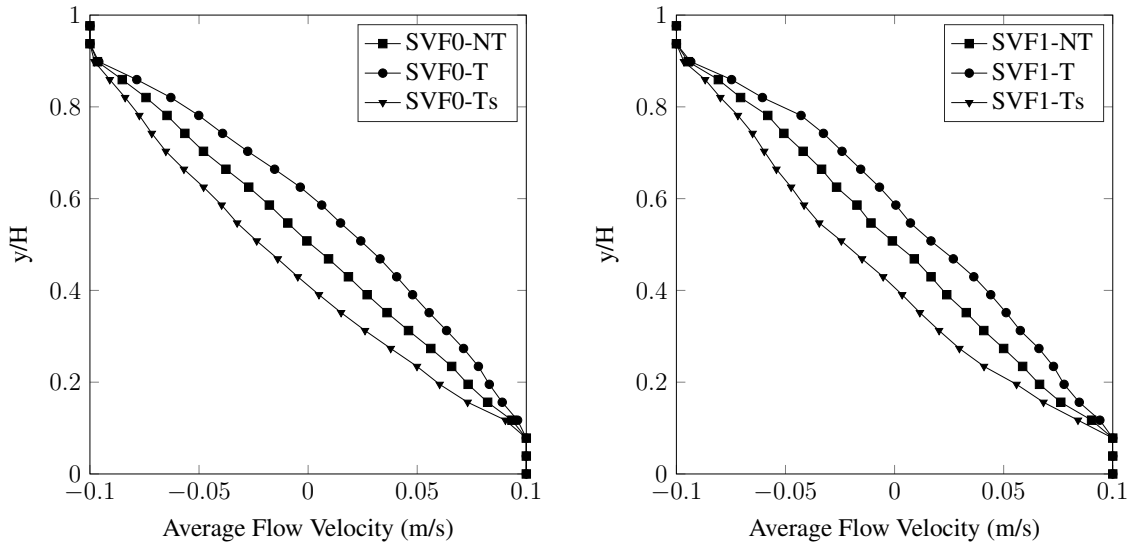

(a) SVF0

(b) SVF1

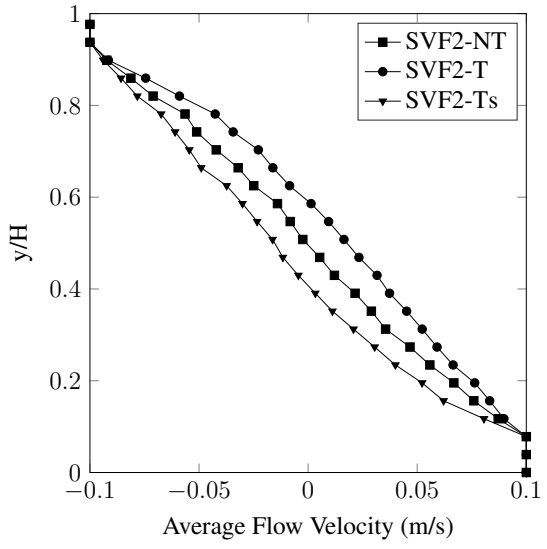

(c) SVF2

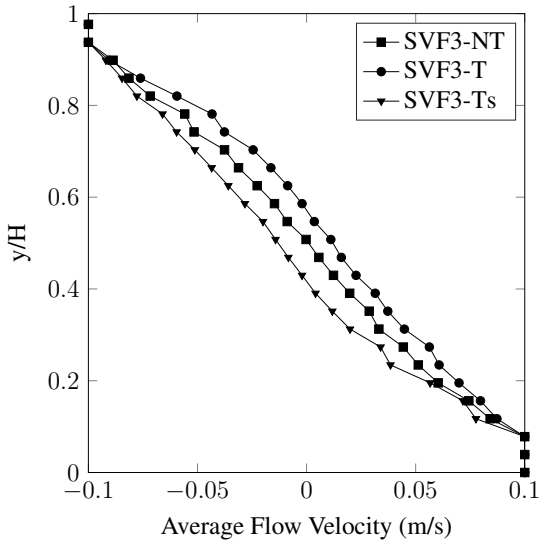

(d) SVF3

Figure 5.13: Variation of flow profiles within the different temperature cases for the non-zero SVF cases. Note that as the SVF increases, the relative impact of the temperature-dependent viscosity variation decreases.

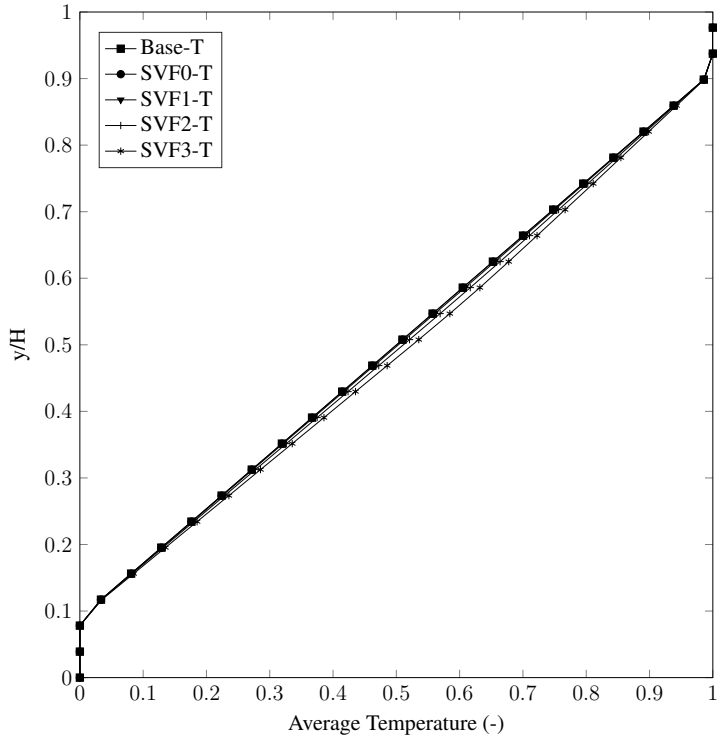

(a) Case ‘T’

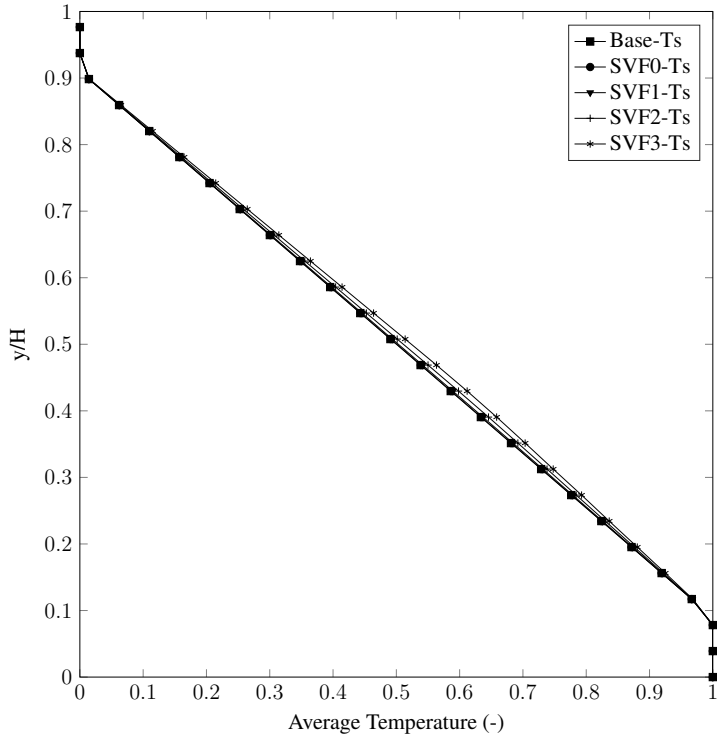

(b) Case ‘Ts’

Figure 5.14: Variation of temperature profiles within the different SVF cases with applied temperature gradient. The slight increase in temperature is likely due to viscous heating resulting from the effective increase in viscosity with SVF

CHT effects on the velocity and temperature profiles generated within the sheared rheometer model. Note that in these figures, the 'Base-T' case results have also been added for comparison even though CHT plays no part in this model.

Initially, it can be noted that the velocity profile of the flow remains fundamentally unaltered in the characteristic nature of each SVF result. The CHT test case with properties increased (Figure 5.15a) is virtually unchanged from the non-CHT scenario. However, compared to Figure 5.12a, in Figure 5.16a there is slightly greater uniformity in the flow of the various SVF cases in the upper half of the domain. Except for the SVF3 case, the CHT introduction has caused the average velocity profile to more closely represent the base case. These variations do not make any qualitative change to the overall behavioural description of the system. As could be expected, there is however a much more noticeable change in average temperature profiles when CHT is introduced to the flow. In both the CHT and non-CHT models the a small measure of the variation in temperature profiles between SVF cases may be attributed to viscous heating resulting from the increase in viscosity associated with particles in suspension. As noted in Chapter 4, the Brinkman number for a Couette flow is defined as,

$$Br = \frac{\mu_0 U_{max}^2}{k(T_H - T_C)}, \tag{5.14}$$

and corresponds to the ratio of viscous and conductive heat transfer effects. An increase in Br, such as through the increase in viscosity, corresponds to increased viscous heating. In both CHT cases, the temperature profiles are more widely distributed than in the non-CHT case (Figure 5.14a). The variations observed in Figure 5.15b occur mostly in the centre of the domain and are most significant for the SVF2 and SVF3 cases. Here, the variation is more likely to be associated with the increased heat capacity (C_p) of the particles compared to the surrounding fluid. This corresponds to a region of comparatively low speed flow, better allowing heat to accumulate in this region especially as the fraction of particles increases. In Figure 5.16b, the wider spread of temperature variation occurs for all SVF cases and is more noticeable in the upper half of the domain. This can be attributed to corresponding reduction in the k value for the suspension due growing proportion of solids in suspension. This serves to again slightly increase the Br of the flow and the corresponding viscous heating effect.

5.3 Summary

This chapter has presented verification and validation cases for the extension of the numerical concepts discussed in earlier chapters to a 3D model. To demonstrate that particle hydrodynamics was

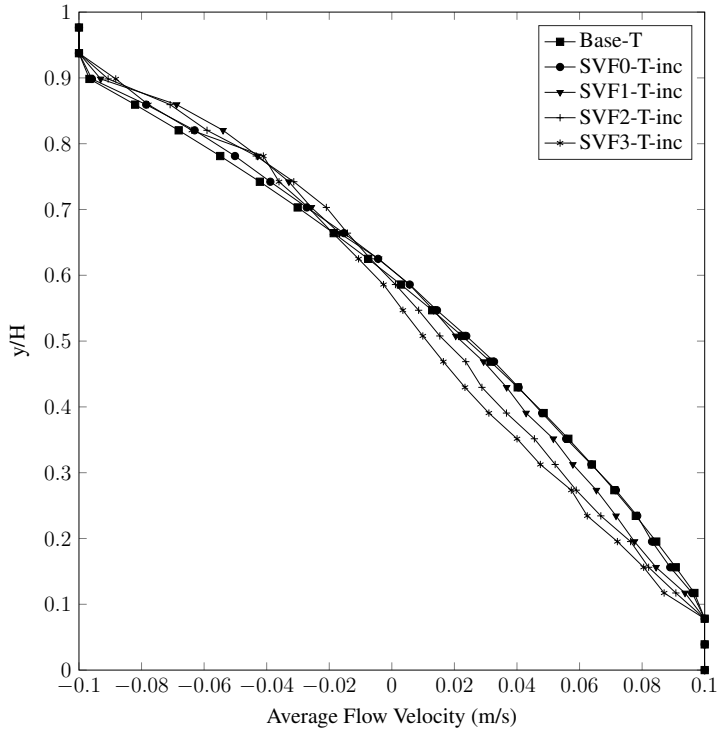

(a) VelocityCase ‘T’

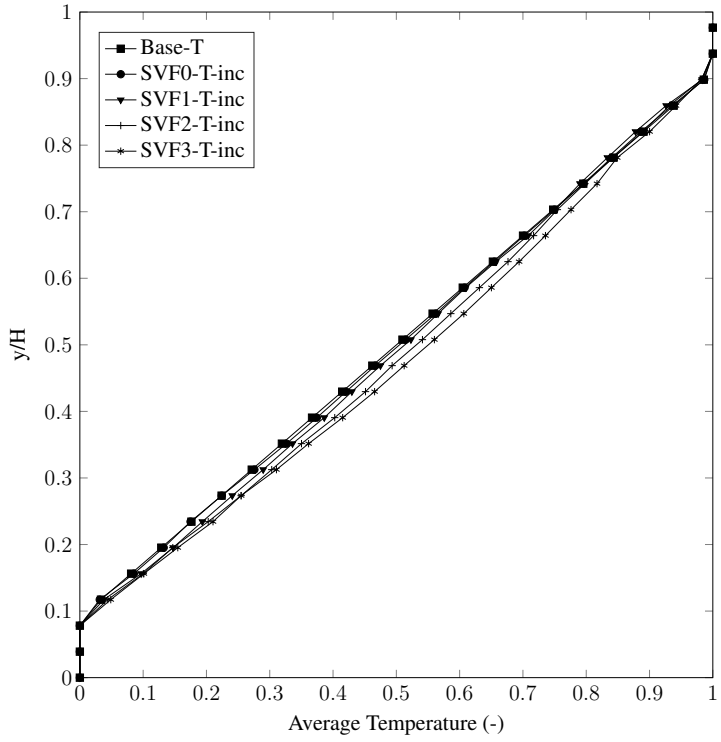

(b) Temperature Case ‘T’

Figure 5.15: Average velocity and temperature profiles of the sheared rheometer test model with the material parameters k and C_p increased by a factor of three over the non-CHT test values.

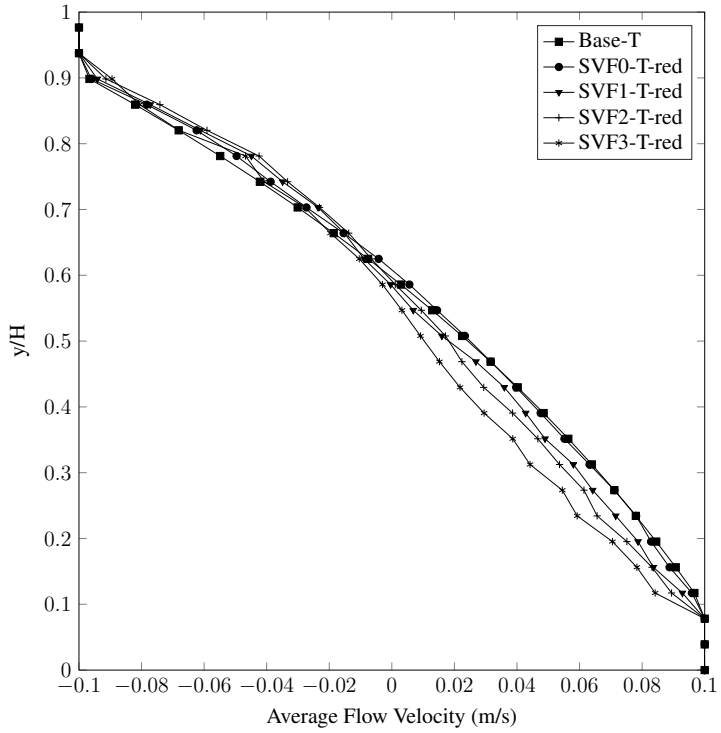

(a) Velocity Case 'T'

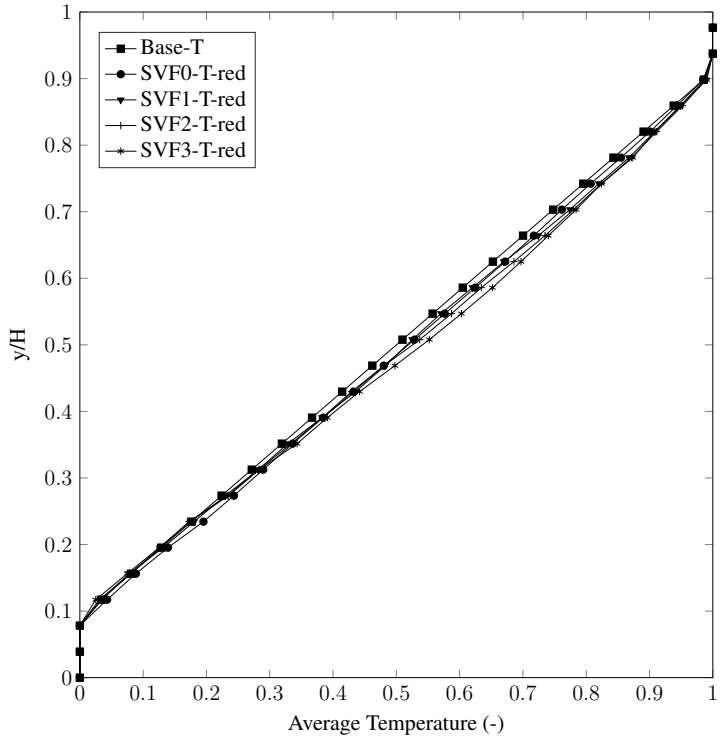

(b) Temperature Case 'T'

Figure 5.16: Average velocity and temperature profiles of the sheared rheometer test model with the material parameters k and C_p decreased by a factor of three over the non-CHT test values.

captured correctly, the steady-state velocity of a particle moving under a constant acceleration between two plates was studied. The model demonstrated convergence of results with increasing resolution of the particle within expected bounds. The ability of the model to capture suspensions flows was also demonstrated through comparison of relative viscosity of a suspension experiencing shear to experimentally validated correlations from the existing literature. The fundamental physics of these were captured by the current model to an acceptable level. The sensitivity of these results to rheometer layout was also highlighted within these tests, illustrating the uncertainty that exists in both the numerical and experimental analysis of suspension flows. The general CHT methods discussed in previous chapters were extended to 3D and demonstrated that desired behaviour was still captured.

This model was then employed to study the macroscopic velocity and temperature profiles generated within suspension using a fixed shear rate numerical rheometer. This was performed with material parameters that neglected or accentuated the effects of CHT between the solid and fluid components. All tests were conducted at a range of solid volume fractions of particles between the shearing planes up to a value of around 37%. It was observed that in the presence of a temperature thinning fluid, the perturbation in the average velocity of the field was reduced in regions of reduced viscosity. As the SVF of the flow was increased, the velocity profile was observed to more closely resemble that generated within a temperature-independent fluid. Similar behaviour for velocity profiles was seen when CHT was introduced to the flow. When the temperature field across the suspension was analysed, a non-linearity of the profile was observed in the non-CHT cases. This was likely induced by viscous heating due to increasing effective viscosity of the suspension with SVF. When CHT was allowed to occur through increasing or decreasing the thermal conductivity and heat capacity of the solid component, the non-linear profile became more pronounced. When properties were reduced, the increase is likely still attributable to viscous heating as this parameter change causes an overall reduction in the thermal conductivity of the suspension. When material properties were increased however, it is thought that the increased heat capacity of the particles were better able to retain heat in the slower central section of the channel. These observations may be used to better develop particle suspensions with desired properties for use in practical applications.

Chapter 6

Proppant transport in characteristic fracture geometries

This chapter takes the LBM-DEM model for suspension flow with temperature effects that has been developed through the previous chapters and applies it to models that are representative of proppant transport problems witnessed within hydraulic fracturing operations. The performance of a hydraulic fracturing treatment depends on the placement of sufficient quantities of proppant throughout a fracture to ensure that it does not close once the fluid is removed. Another problem that needs to be avoided is the blockage of a fracture feature with excessive proppant, preventing placement further along the fracture. Both of these issues may serve to prevent the permeability of an unconventional reservoir being increased sufficiently to allow viable production. Further treatments may be required to remedy such shortcomings. The case studies presented here aim to provide a contribution to the knowledge of proppant flow through representative features so that treatments can be better planned to minimise operational costs. These results will provide fully resolved particle flow through these features, a key point of distinction from the continuum based models often used to study such problems.

Previous numerical studies of proppant transport can be readily found in the existing literature [135, 136, 137, 138]. With improved computational resources becoming more widely available, more DEM-based studies are being published. These allow motion of proppant particles to be resolved and are often coupled to a finite volume fluid solver. This can be seen as an improvement in some respects over the use of continuum models which are still widely used (and are suitable for large scale studies). Despite this, some of these studies are still restricted to a quasi-two-dimensional model by setting the fracture width studied to being just wider than a single particle. The results presented in this chapter will be both fully resolved and fully three-dimensional.

In the works of Zhang *et al.* [135] and Baldini *et al.* [136], coupled models of finite volume fluid solvers and the DEM are used to study dune formation within a straight fracture. In both papers, this allows for fully resolved particles to be modelled. However, both of these studies only model a fracture with a width of around a single particle diameter. This prevents fully 3D motion of particles from occurring. In these studies, parameters relating to particle interactions (e.g. stiffness and friction coefficent) [135] and injection strategy [136] are investigated for their effect on dune formation. The flow mechanisms that generate specific transport behaviours are also identified in [135]. In his PhD dissertation, Blyton [137] studied a number of proppant transport problems using the same general approach. The studies presented here include flow through an open and closed straight channel and transport within a channel with a branch splitting off from it. Whilst a 3D implementation has been used, computational limitations have restricted many presented studies to models having a thickness of 1-2 particle diameters, with the largest featuring a thickness of 10 diameters. In the channel flows, the focus has been on the generation of Poiseuille profiles in horizontal (open) channels and settling velocity (closed) in vertical flows. Parametric investigation of slot width, particle size, particle density and fluid viscosity was completed. In branched channel studies, a so-called 'particle transport coefficient' is used to evaluate the effect of branch width, angle, Reynolds number, fluid viscosity and particle parameters on flow through the domain. This measure is the mass flow rate of particles travelling along the branch compared to that being inserted into the domain, normalised by the corresponding fluid flow ratio. Jamming of particles was observed in a number of the cases tested here. In the branched tests, the width of the channel was fixed at two particle diameters, this narrow domain may have had an influence on whether jamming occurred.

In an example from industry, Han *et al.* [138] studied the transport of proppant through a straight channel, and approaching a T-junction or a crossing junction using a commercial fluid dynamics solver. In that work, the solid component was treated from an Eulerian perspective as a continuum property of the fluid. This approach allowed large scale models to be studied (i.e. this paper presents an example of a straight channel measuring approximately $90m \times 12m \times 5mm$ being simulated for $295s$). However, this approach cannot detail how the individual particles are transported through the domain. The authors observe that increased turbulence at a junction can assist in the transport of particles along the side branches. Reducing proppant weight and increasing fluid viscosity were observed as ways to improve the proppant distribution in these cases. Increasing the pumping rate was not observed to improve distribution.

6.1 Numerical case studies

Three case studies of representative fracture models are studied in this chapter. The first examines the classic problem of particle settling within a straight fracture. Temperature-dependent viscosity effects are introduced to understand how particle motion varies under these conditions. The second case study consists of a channel with a leak-off point partway along it. This will examine how an undesired flow pathway can impact transport along the main fracture. Finally, a fracture geometry with a step along its propagation axis will study how blockage may be induced. In all three cases, the fracture is periodic in the vertical direction with gravity applied to each case. Particles of density 1000 kg/m^3 are continuously injected along the full height (w = 64Δx) of the fracture at the inlet of the domain with a horizontal velocity of U_{inject} = 0.1m/s and the same initial SVF. Particles are added to the domain when the leading w is vacant of particles. In the cases where pressure outlets are implemented, a lattice value of $p = 1/3$ is enforced. When dimensionless temperature is applied, it increases linearly between T = 0 at the inlet to T = 1 at the outlet along the main fracture direction. As in Chapter 4, these can be interpreted based on $T_H^{physical}$ = 350K and $T_C^{physical}$ = 300K. In all cases tested here, the LBM spacing has been set at Δx = 3.125 $\times$ $10^{-5}m$ with a time step of Δt = 40 μs, this corresponds to a kinematic viscosity of ν = 4.07 $\times$ $10^{-5}m^2/s$ when a numerical viscosity of 1/6 is used. Unless noted otherwise, the particles used in these studies have a radius of r = 6.4Δx = 0.0002m (diameter D = 0.0004m). As noted in Chapter 5, conjugate heat transfer has a relatively minor impact on particle trajectories through a fluid. For these studies, the solid and fluid components have the same thermal properties used in the non-CHT tests in the previous chapter.

6.1.1 Proppant transport within a straight fracture

The model domain to investigate the effects of temperature-dependent viscosity on the settling behaviour of proppant within a straight channel is presented in Figure 6.1. The fluid entered with fixed velocity and exited with a constant pressure boundary condition implemented using the well known Zou-He method [69]. This model was run for a total of 250,000 steps.

To compare the settling behaviour of the two cases, the particle velocities averaged along the length of the channel were computed. These results after 125,000 and 250,000 steps are presented in Figure 6.2. Firstly, it can be noted that the velocity along the length of the channel (x-direction) is essentially unchanged by the introduction of temperature-dependent viscosity. The magnitude of this is tending around the injection viscosity as expected from mass conservation. The variation between the data points is dependent on how many particles were located around that position at the time of interest. The most interesting measure though is the vertical (y-direction) velocity. In the absence of

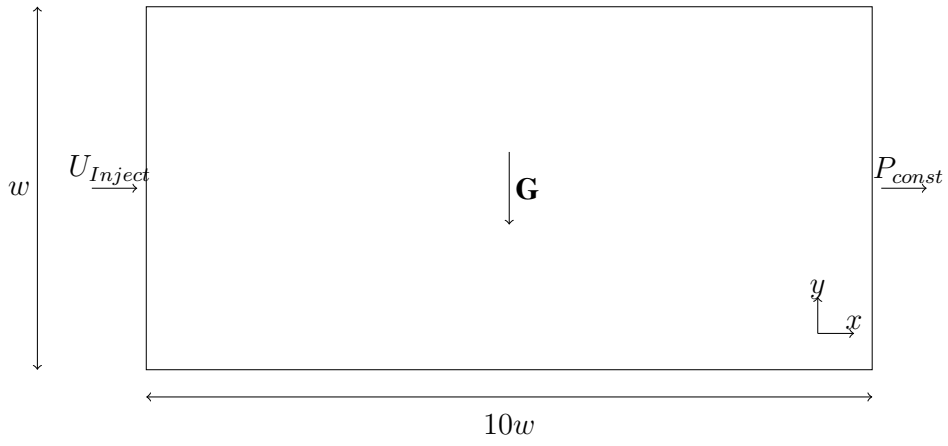

Figure 6.1: Layout of settling within a straight fracture geometry. The entire model has a thickness of w. The model is initially filled with particles of diameter $D = 0.2w$, these are continuously injected with the inlet velocity into the leading w of the domain. The upper and lower boundaries in the y direction are periodic.

changing viscosity, this slowly increases along the length of the channel due to the action of gravity. When a temperature-dependent viscosity is introduced, the magnitude of the settling velocity has increased by a factor of almost three. Similar trends were observed throughout the simulation, rather than just the example times given here. The distribution of particles and their velocities after 250,000 steps is presented in Figure 6.3. In particular, the increase in settling velocity can be noted in this figure. The same trend of behaviour can be observed when a higher initial SVF (33% compared to 8%) of particles was inserted into the fracture geometry (Figure 6.4). In this case, the magnitude of increase in vertical velocity is about a factor of two by the end of the channel. The distribution of particles and their velocities after 250,000 steps is illustrated more graphically in Figure 6.5. Again, the increase in settling velocity can be noted here. As an extra example, the tests at an elevated SVF were repeated with the size of the particles halved ($r = 3.2\Delta x = 0.0001m$). This change increased the initial SVF to approximately 39%. The reduction in resolution is still able to yield acceptably accurate results as shown in Figure 5.2. Due to computational limitations, this test could only be run for 160,000 steps. The results of this are presented in Figure 6.6 with data at 80,000 and 160,000 steps. Similar observations to that made for the larger particles can be made in this case. The factor of settling velocity increase at the end of the channel however is reduced with the smaller particles to approximately 1.75. The consequence of this in the context of hydraulic fracturing is that particles may settle onto the bottom of a fracture in an unanticipated way if a treatment is designed based on a poorly chosen constant viscosity. The distribution of particles and their velocities after 160,000 steps is further illustrated in Figure 6.7. To reduce congestion in the figure, only 10% of the total particles

are shown. The increased velocity around x/L = 0.5 in Figure 6.6 and density of particles in Figure 6.7 is due to the observed behaviour of the Poiseuille profile of the fluid flow through the channel dominating the motion of smaller particles. Newly injected particles move rapidly through the centre of the channel whilst those at the edges form a slow moving layer on each side. At 160,000 steps, a group of particles moving through the centre is located at around x/L = 0.5 whilst the remaining particles are located adjacent to the channel walls and are moving much more slowly (see Figure 6.8). Settling too fast, too slow or in an uneven manner can all have detrimental effects on the performance of a fracturing operation.

6.1.2 Proppant transport within a leaking fracture

To study a leaking fracture, as described in Figure 6.9, two cases were considered. The first contains a leak-off channel that is the same width as the main channel. The relative flow rates between the two pathways were varied such that ratios of leak:main = 1:1, 1:3 and 1:7 were enforced. This was enforced by velocity outlets at the exits of the main and leaking channels. The second case involved narrowing the leaking pathway such that its width was reduced to $2.5D$ and $1.25D$ with pressure boundaries at the exits. All tests were performed for 100,000 time steps. The initial SVF of these cases was approximately 26%.

As part of the analysis of both these cases, three key regions of the fracture domain were identified. The 'Entering' section is the region of length w immediately prior to the beginning of the leak channel, the 'Leaking' section is the entire volume of the side channel and the 'Continuing' section is the region of length w immediately after to the beginning of the leak channel. The cumulative total of particles moving through the domain were recorded to infer the passage of particles in a simulation.

Variation of flow ratio

The first case study being examined involved explicit variation of the flow rate exiting the main and leaking channels. This can be thought of as corresponding to the flow in the leaking channel being governed by a lower porosity region restricting the flow velocity. In this study, there was negligible difference observed between the distribution of particles of the isothermal and temperature-dependent viscosity simulations. As a result, Figures 6.10 and 6.11 only present the isothermal results. Figure 6.10 displays the cumulative total of particles moving through each region for the duration of the simulation in each flow case. Here it can be seen that, as expected, the number of particles flowing along the leaking path reduces with the corresponding flow rate. The bulk of the particles are travelling along the main channel. However, it can be observed in Figure 6.11, which compares the particle

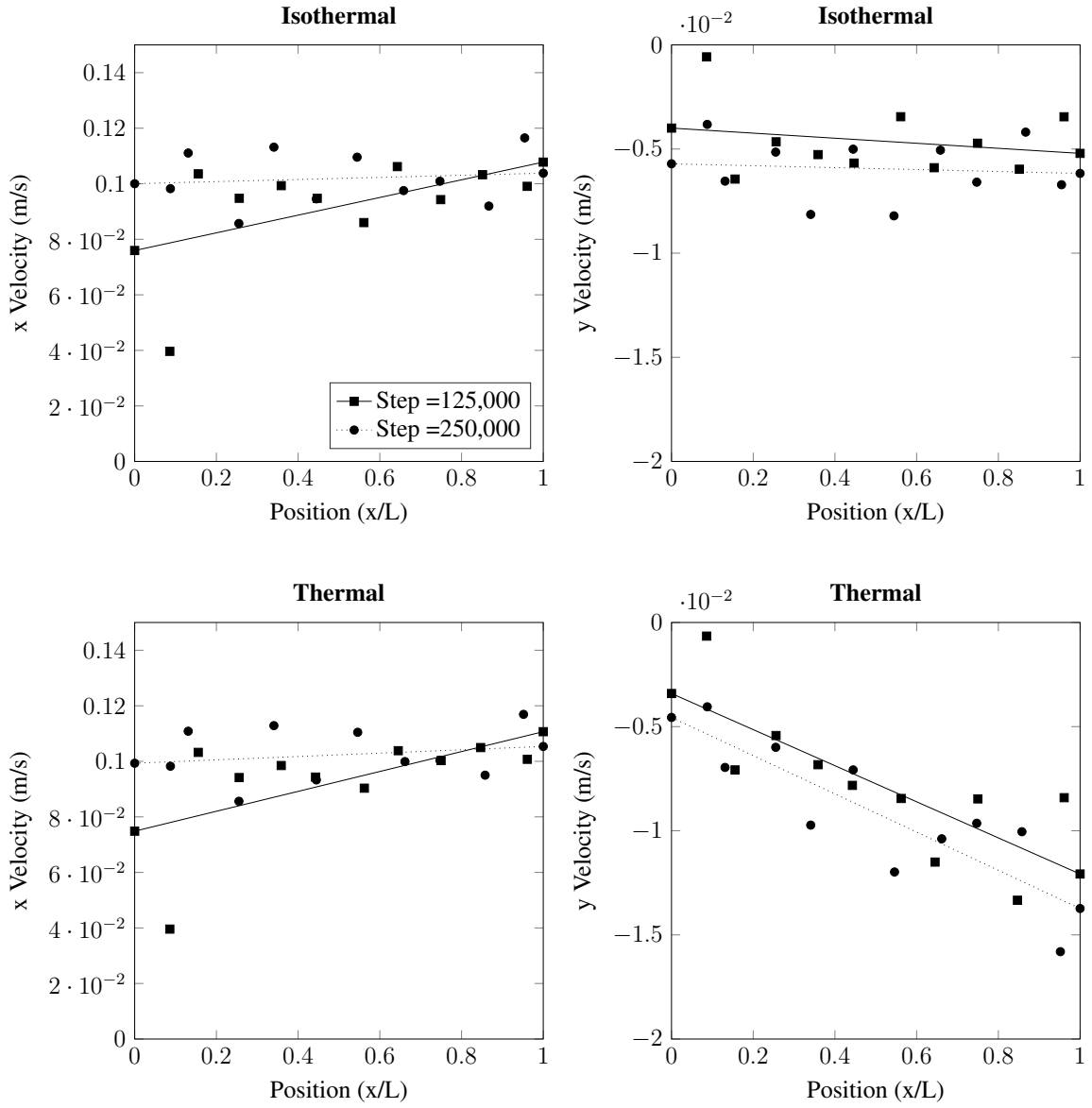

Figure 6.2: Velocity of the particles in the x- and y-directions averaged along the length of the straight channel (8% initial SVF) recorded at 125,000 and 250,000 steps. The isothermal plots have constant viscosity whilst the thermal results have temperature-dependent viscosity. The line represents a least-squares fit to the data points.

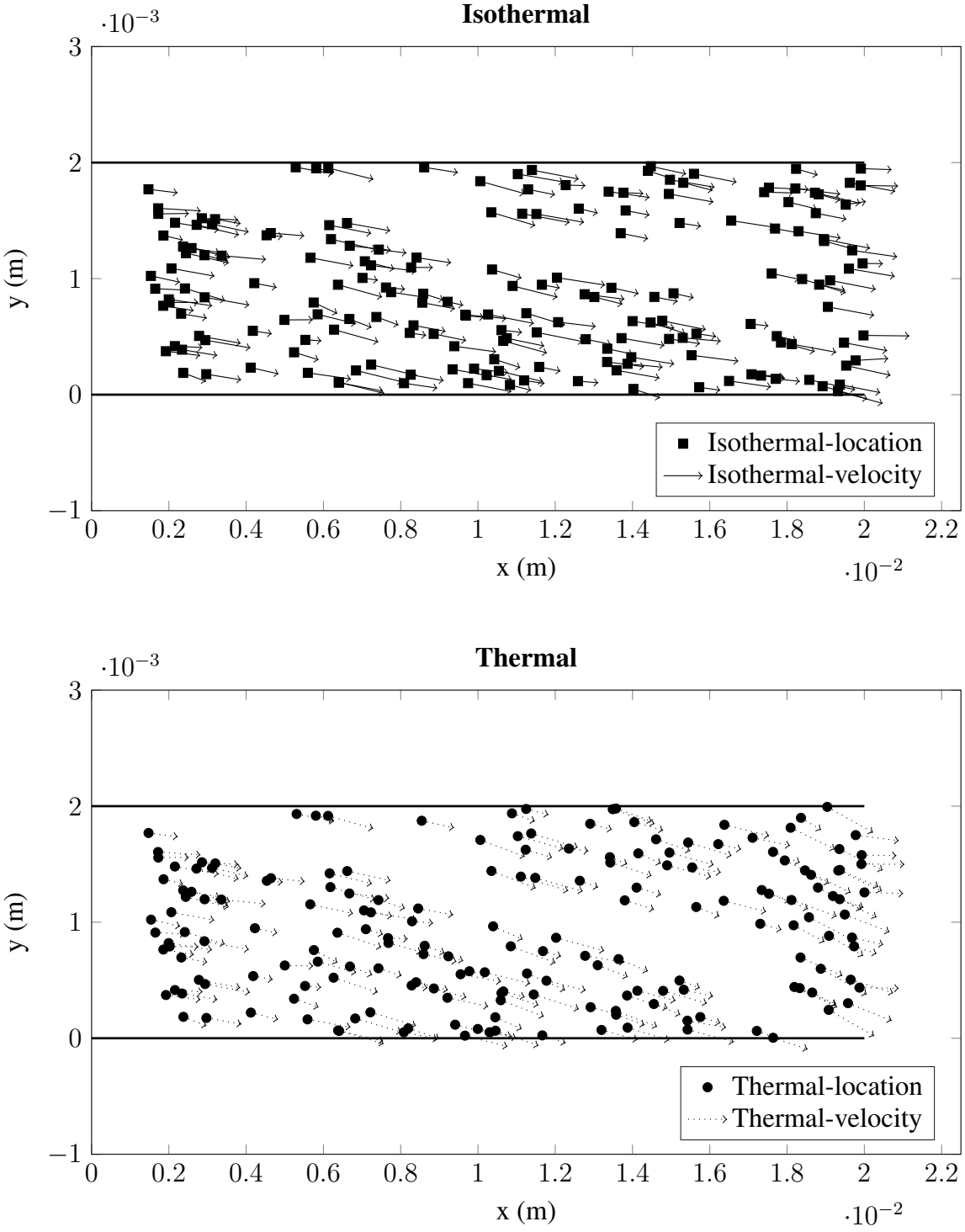

Figure 6.3: Comparison of the particle position and velocity vectors of the particles in a straight channel under both temperature conditions (8% initial SVF) recorded at 250,000 steps. The isothermal plots have constant viscosity whilst the thermal results have temperature-dependent viscosity. The increase in settling velocity can be noted in the Thermal case.

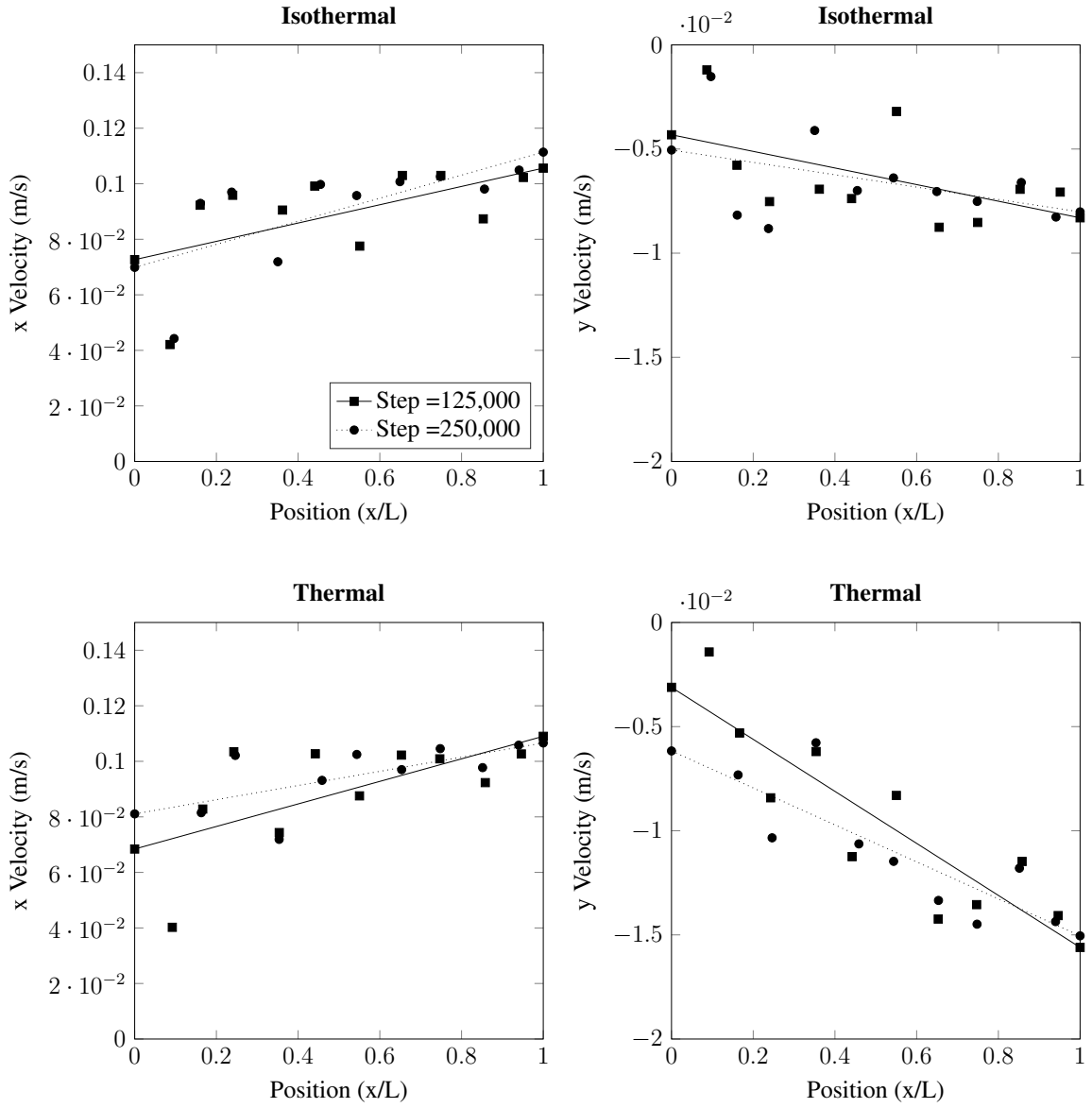

Figure 6.4: Velocity of the particles in the x- and y-directions averaged along the length of the straight channel filled with a 33% initial SVF of particles. Data here is recorded after 125,000 and 250,000 steps. The isothermal plots have constant viscosity whilst the thermal results have temperature-dependent viscosity. The line represents a least-squares fit to the data points.

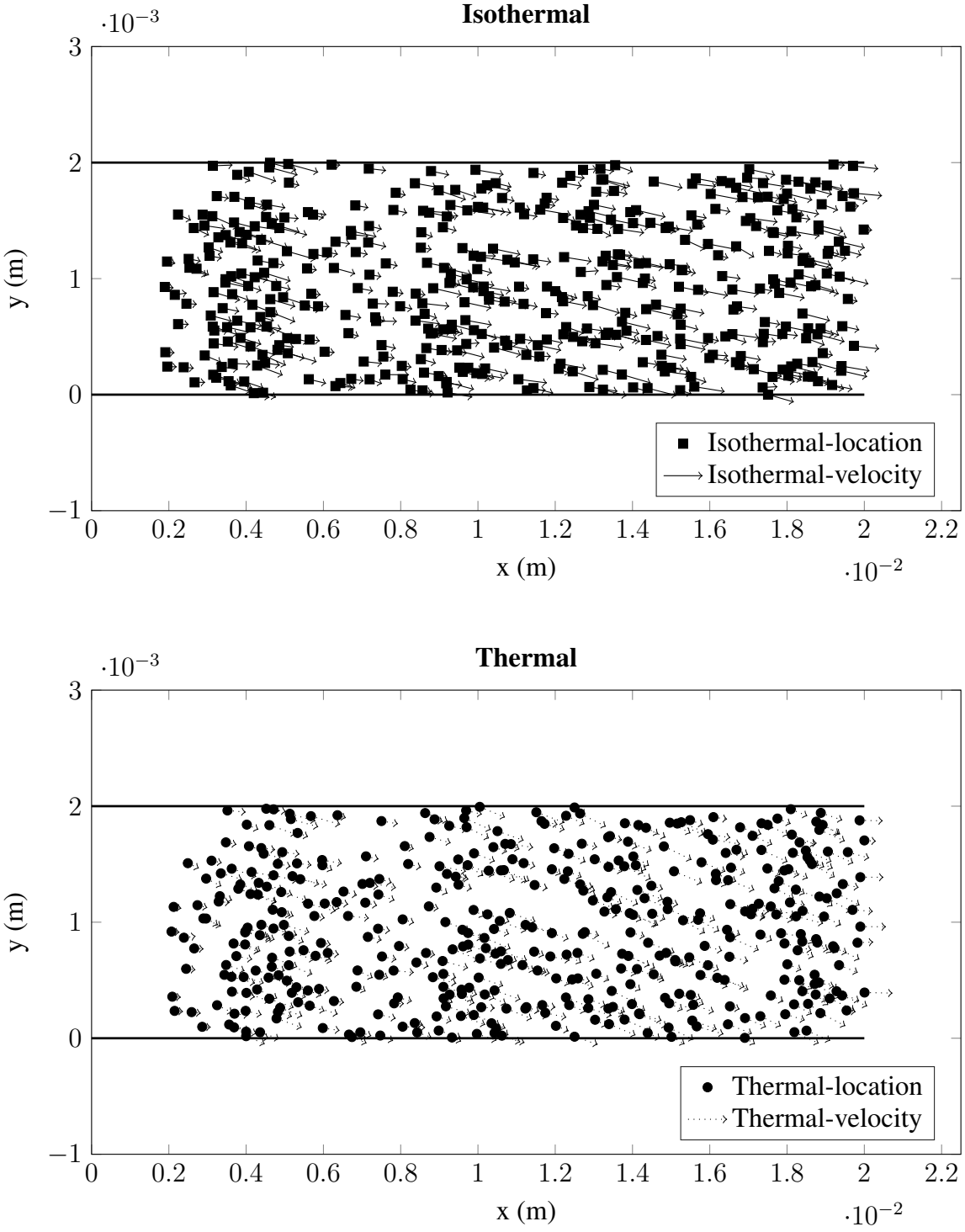

Figure 6.5: Comparison of the particle position and velocity vectors of the particles under both temperature conditions (33% initial SVF) recorded at 250,000 steps. The isothermal plots have constant viscosity whilst the thermal results have temperature-dependent viscosity. The increase in settling velocity can be noted in the Thermal case.

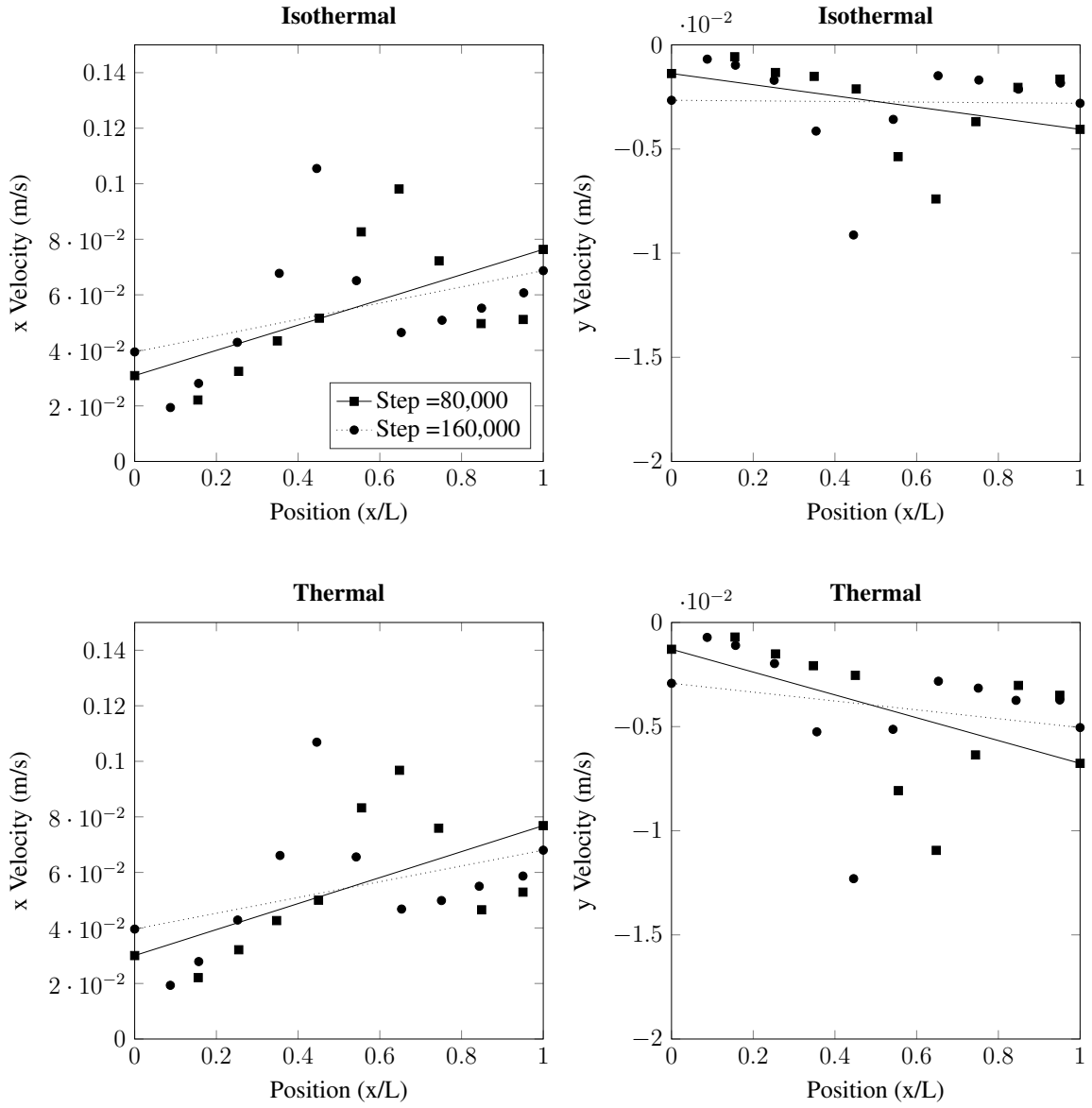

Figure 6.6: Velocity of the particles in the x- and y-directions averaged along the length of the straight channel filled with smaller particles. Data here is recorded after 80,000 and 160,000 steps. The isothermal plots have constant viscosity whilst the thermal results have temperature-dependent viscosity. The line represents a least-squares fit to the data points.

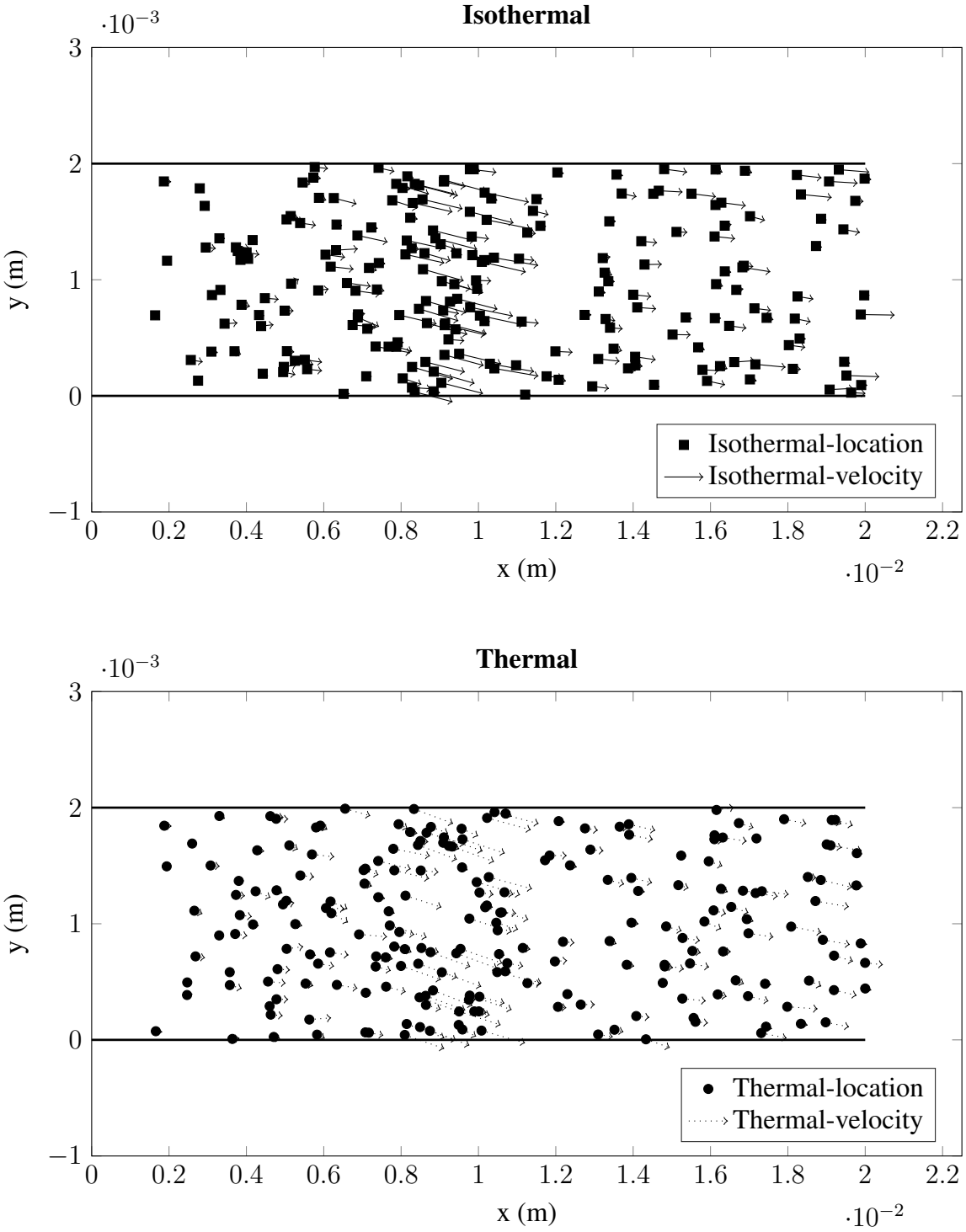

Figure 6.7: Comparison of the x-y (side view) particle position and velocity vectors of the small particles in a straight channel under both temperature conditions recorded at 160,000 steps. The isothermal plots have constant viscosity whilst the thermal results have temperature-dependent viscosity. The increase in settling velocity can be noted in the thermal case. To reduce congestion only 10% of the total particles are illustrated here.

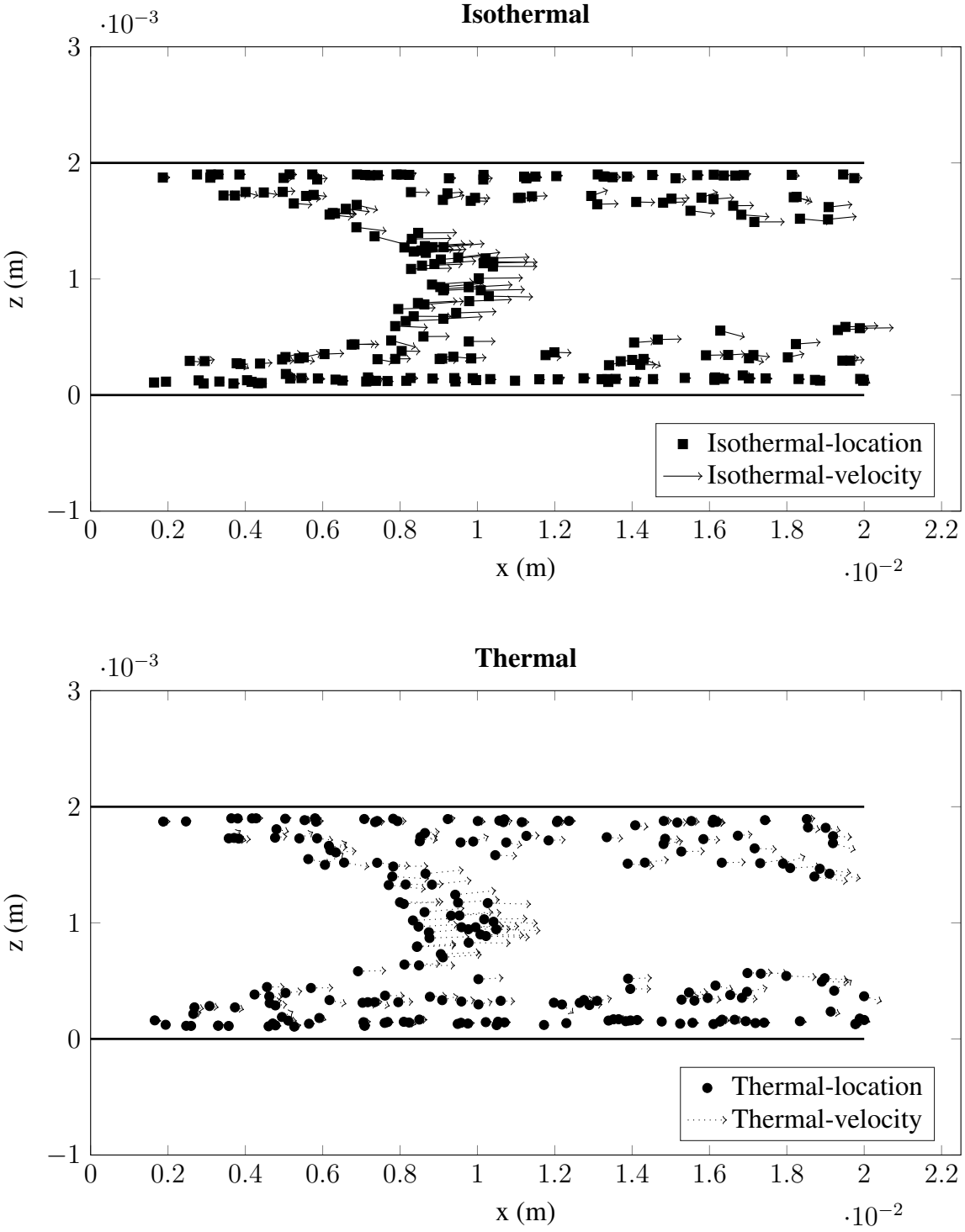

Figure 6.8: Comparison of the x-z (bottom view) particle position and velocity vectors of the small particles in a straight channel under both temperature conditions recorded at 160,000 steps. The isothermal plots have constant viscosity whilst the thermal results have temperature-dependent viscosity. To reduce congestion only 10% of the total particles are illustrated here. Note the domination of the particle motion by the Poiseuille profile of the fluid.

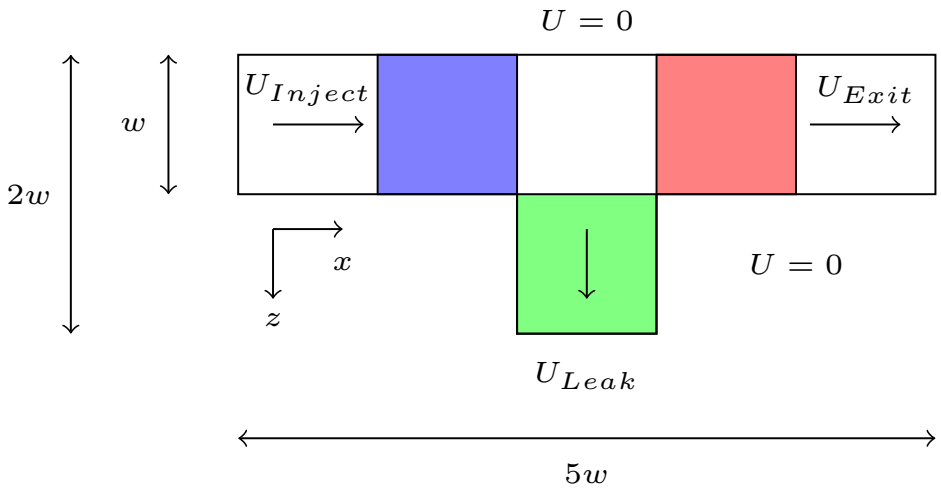

Figure 6.9: Layout for flow through a leaking fracture geometry. The model is initially filled with particles of diameter $D = 0.2w$, these are continuously injected with the inlet velocity into the leading w of the domain. The upper and lower boundaries in the y-direction (out-of-page) are periodic and space w apart. The width and flow rates of the leak and main channel are adapted to investigate their impact on flow. The blue section represents the 'Entering' section, green the 'Leaking' and red the 'Continuing' sections used for counting particles.

counts against flow rate, that there is not a linear decrease in the rate at which particles leak off. This is unsurprising as some particles would still be advected into the leak channel if there was no flow exiting this pathway. Figure 6.12 indicates the final locations of particles and their velocity vectors. Firstly, the significant variation in velocity magnitude between the three tests in both the leaking and main channels can be observed. The almost stagnant flow of the 1:7 test case in the leaking channel would assist in reducing the count of particles flowing through this region. The second feature of note is the direction of the velocity vector just prior to the leak channel. It can be noted here that particles much closer to the centre of the main channel are directed towards the leak in the 1:1 case as compared to the lower flow rates. For the 1:7 case it is only the particles immediately adjacent to the wall that are directed towards the leak channel. The Poiseuille profile of channel flow can also be observed in the particles prior to the leak.

Variation of leaking channel width

When a changing channel width was implemented to regulate flow through the leaking channel, variation was observed between the isothermal and thermal results. These can be observed in Figures 6.13, 6.14, 6.15 and 6.16. In Figure 6.13, it can be readily observed that the restriction of flow caused by the narrowed leak channel has made the main channel the strongly preferred path for the flow of

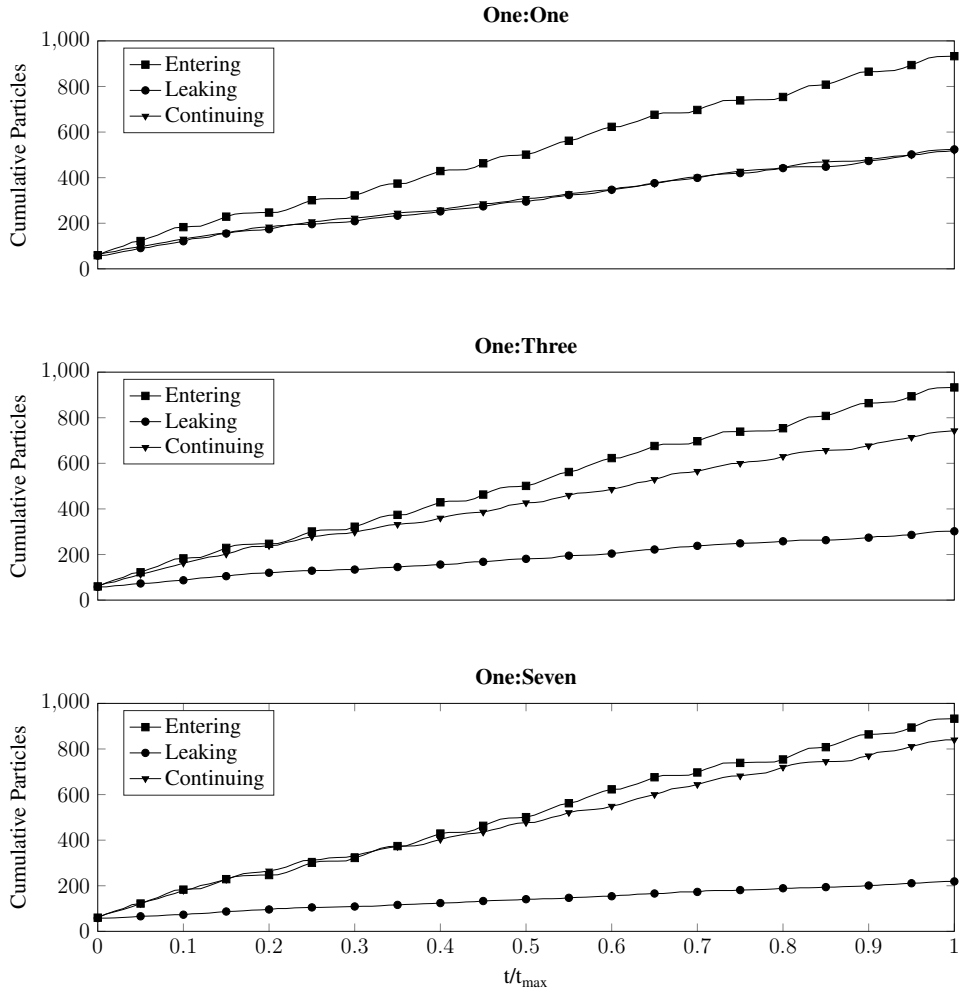

Figure 6.10: Cumulative totals of particles moving through the three characteristic sections of the fracture over the duration of the isothermal simulations. For each case the differing behaviour between the three flow ratios can be observed.

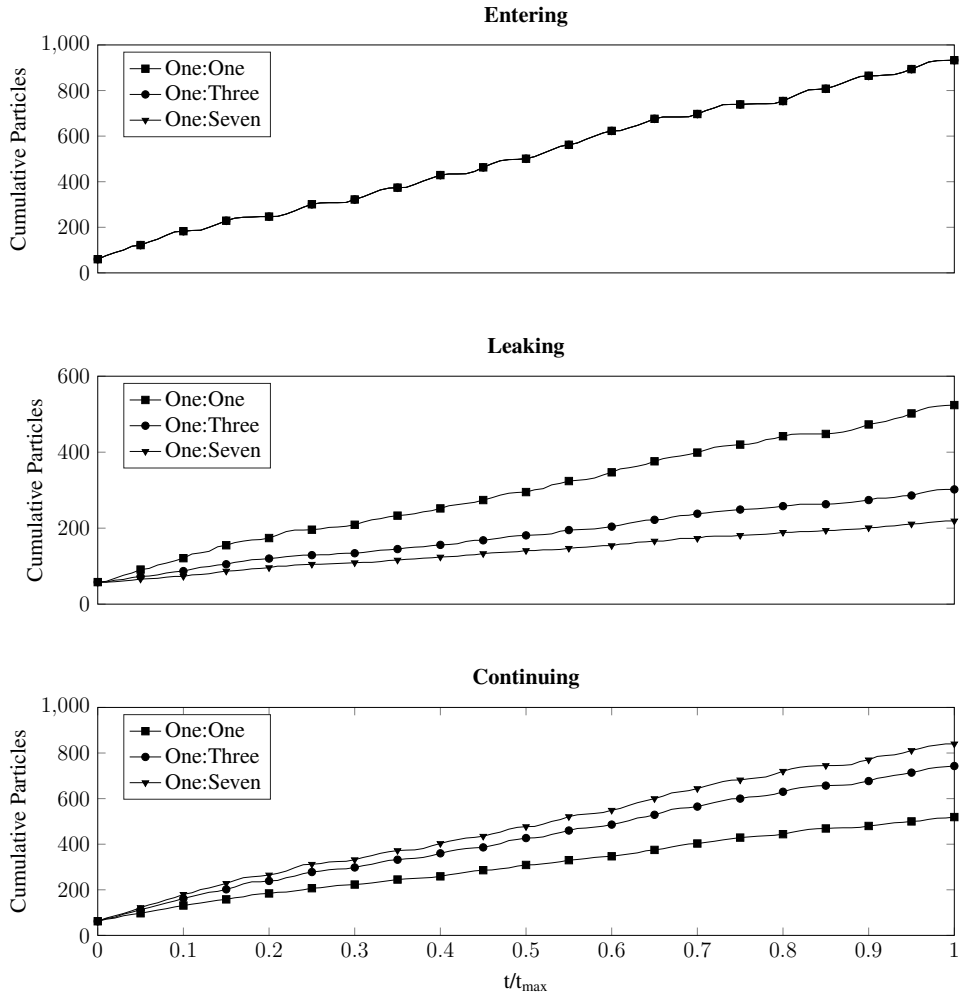

Figure 6.11: Comparison of cumulative totals of particles in each of the three flow cases over the duration of isothermal simulation. For each case the differing behaviour in each of the characteristic regions can be observed.

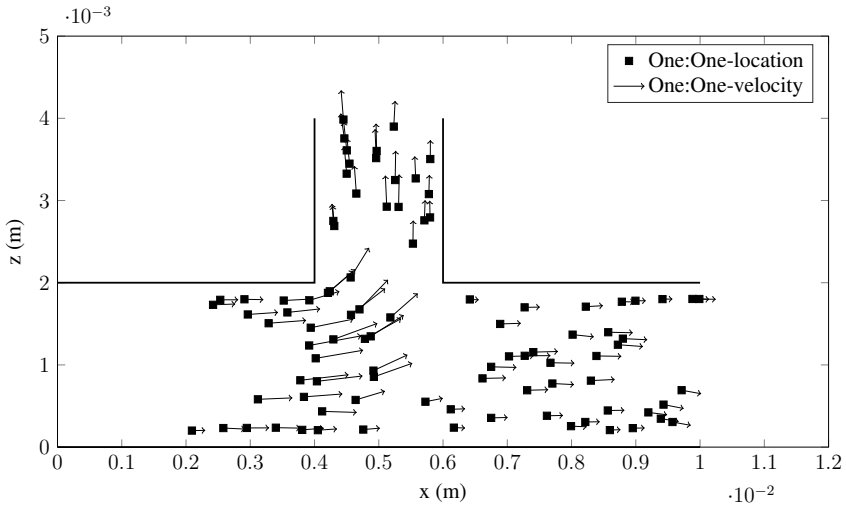

(a) One:One

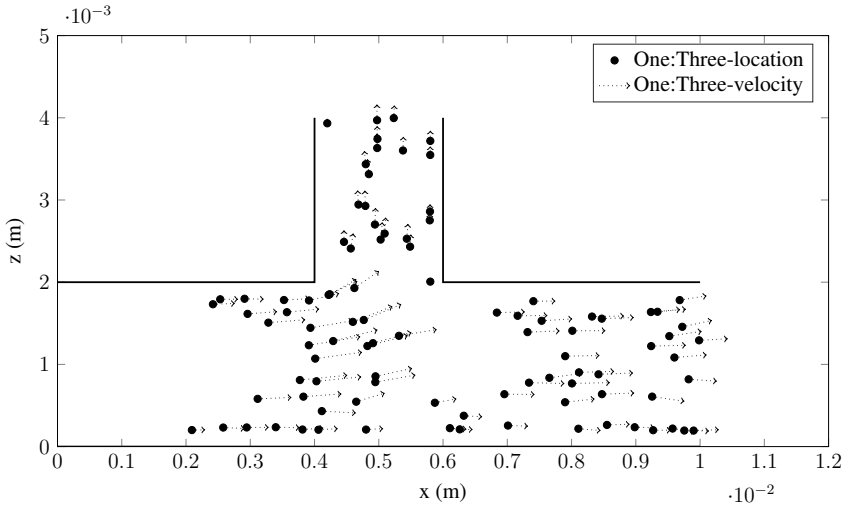

(b) One:Three

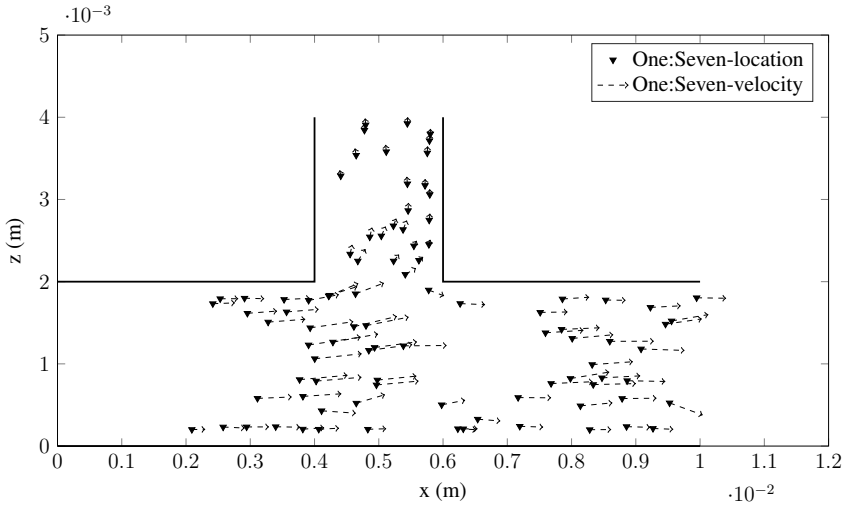

(c) One:Seven

Figure 6.12: Comparison of the particle position and velocity vectors after the 100,000 time steps for each of the three flow cases.

particles. In the case of the width being $1.25D$, the 'Continuing' region has slightly more particles than the 'Entering' region due to the simulation being initialised fully packed with particles. A number of these will begin between these to regions and contribute to the 'Continuing' count and not the 'Entering' one. The greater rate of leaking in the case of the wider channel overcame this in that case. Halving the channel width led to a proportionally greater drop in particles being extracted on the leaking pathway. In the wider channel the simulation concluded with over 200 particles travelling through this region, this reduced to less than 50 particles in the narrower channel. In Figure 6.14, the effect of the thermal model can be seen on the difference in leaking rate between the two channels. In both cases, the presence of temperature-dependent viscosity corresponds to a significant reduction in the number of particles travelling along the leaking channel. In the wider channel, the observed reduction is approximately 10% by the end of the simulation, whereas a 22% reduction is noted in the narrow channel. A possible explanation for this is that the reduced viscosity of the fluid, and corresponding reduced drag on the particle, makes it more difficult for a particle to change direction and travel along a narrow leaking pathway. As in the velocity controlled case, the velocity vector plots in Figures 6.15 and 6.16 highlight that only the particles very close to the leak channel are fed into the channel. It also appears that those particles in the leaking channel during the thermal case may have a reduced velocity compared to their isothermal counterparts. This would further reduce the flow rate of particles moving through the channel in this case. The case of the narrow leaking channel was repeated with the radius of particles halved, as a result the particles are of the same proportion compared to the wider leaking channel. This change caused the initial SVF to increase slightly to approximately 31%. The lattice spacing again remained the same as in the original case. It can be observed that the smaller particles have a reduced tendency to be extracted away from the main channel through examination of Figures 6.17 and 6.18. As for the larger particles, the presence of temperature-dependent viscosity reduces the number of particles travelling along the 'Leaking' path. The reduction is about 10%, similar to that seen in the wider channel for the larger particles. In Figure 6.19, it can be noted that the Poiseuille profile formed by the fluid dominates the distribution of particles through the channel. Particles become distributed along the walls in both temperature cases and this serves to delay injection of further particles.

None of the leaking channel cases presented here indicated the likelihood of forming a blockage due to a bridge forming across the mouth of the channel. This may be due to the flow rate through the main channel being too large or quantity of particles injected being too low for this to occur in a stable fashion. A second possibility is that the larger 3D height of the domains tested here meant that any such blockages were not able to fully seal off the leaking pathway. In 2D, or very low thickness 3D simulations, such behaviour may occur more readily.

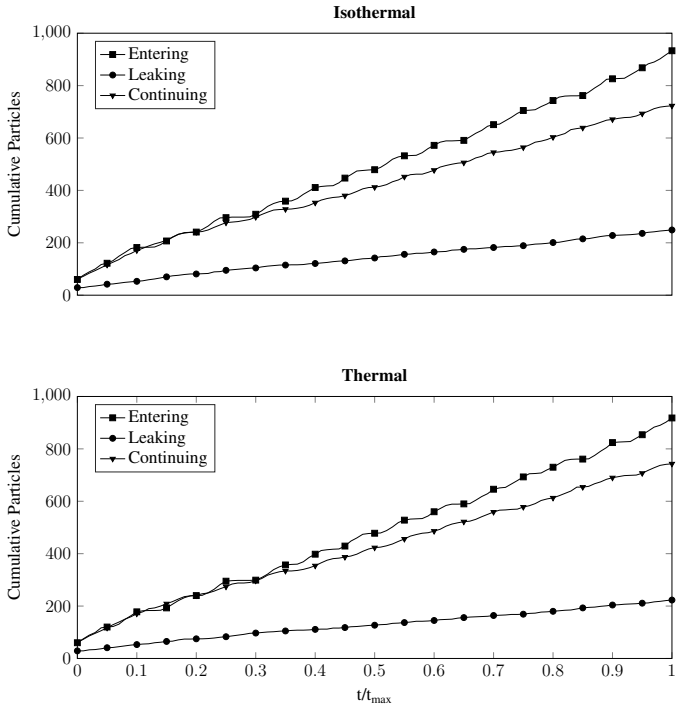

(a) Leak channel width = 2.5D

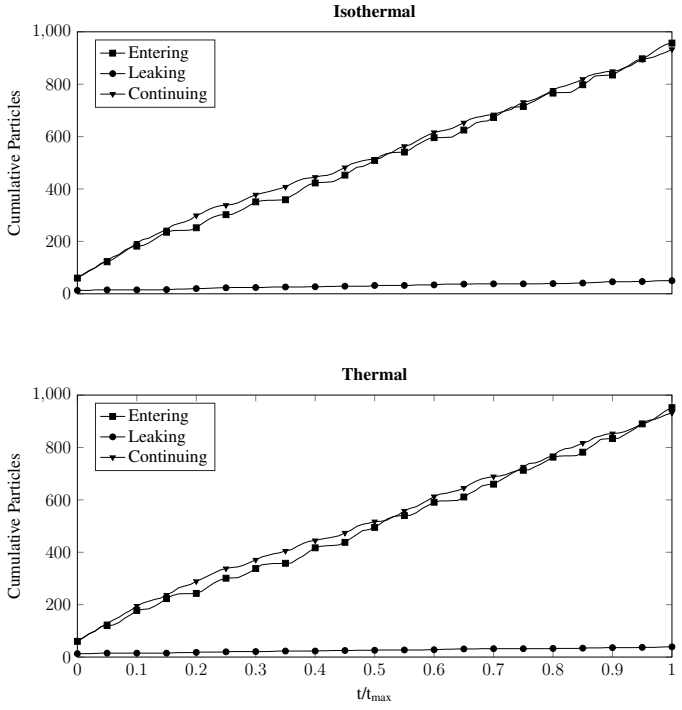

(b) Leak channel width = 1.25D

Figure 6.13: Cumulative totals of particles moving through the three characteristic sections of the fracture over the duration of simulations with differing leak channel widths.

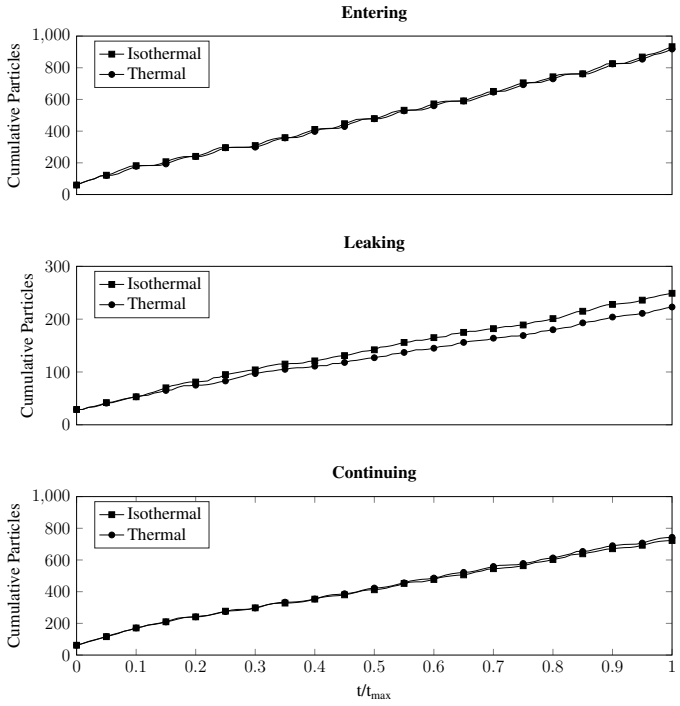

(a) Leak channel width = 2.5D

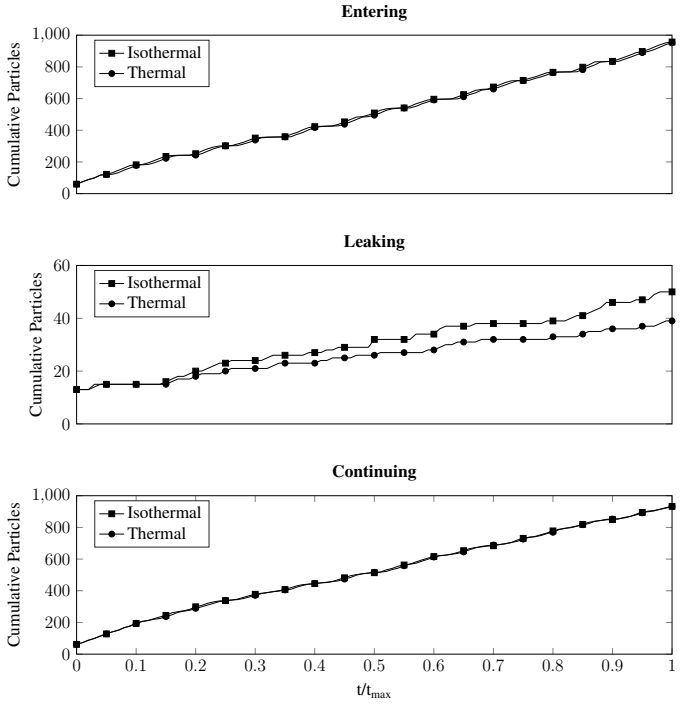

(b) Leak channel width = 1.25D

Figure 6.14: Section-based comparison of cumulative totals of particles moving through the leaking fracture with differing leak channel widths. For each width case the effect of temperature can be observed.

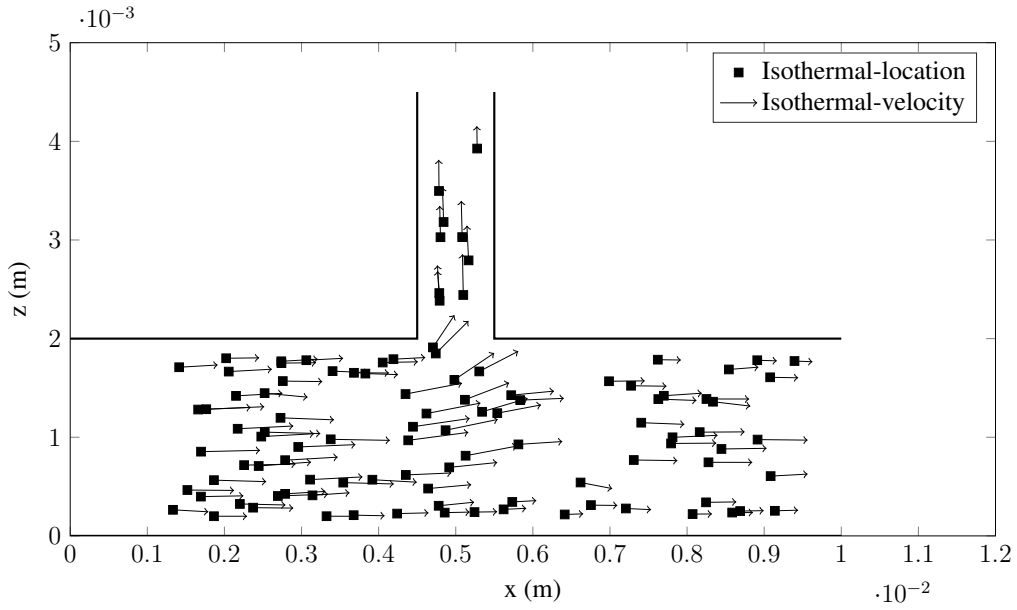

(a) Isothermal

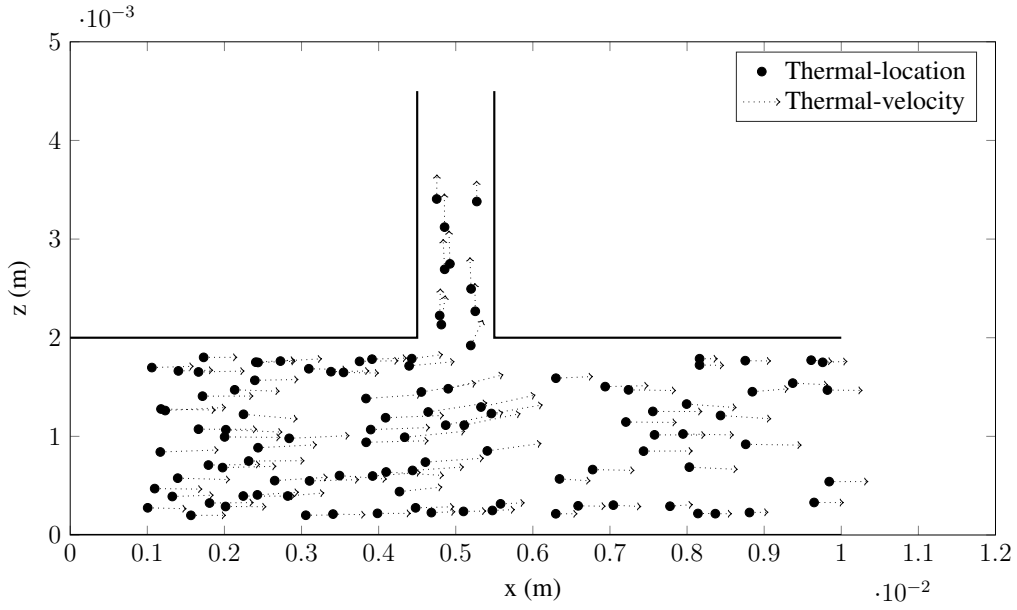

(b) Thermal

Figure 6.15: Comparison of the particle position and velocity vectors after the 100,000 time steps for each temperature case and leak channel width of 2.5D.

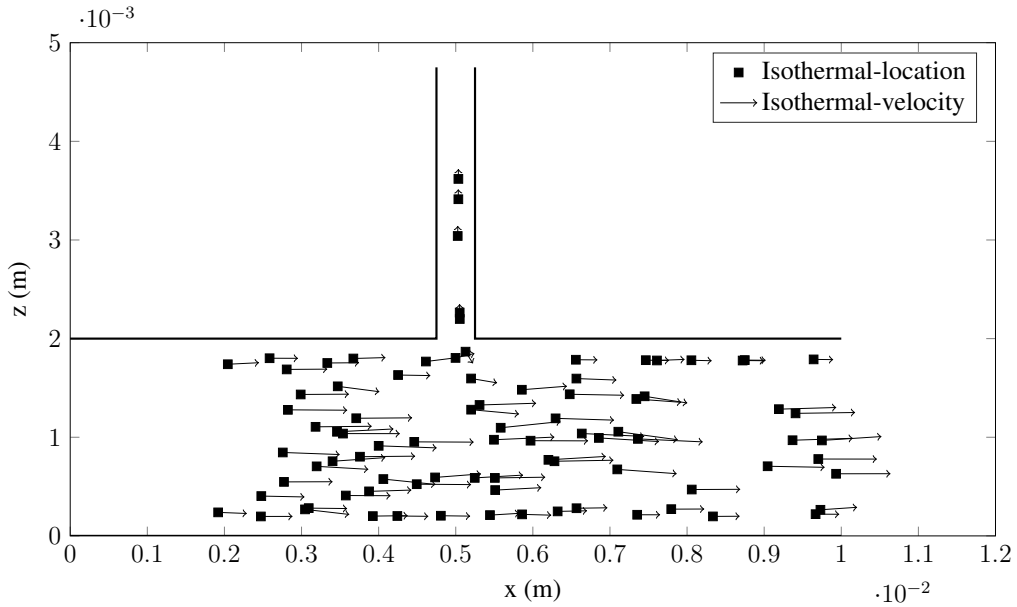

(a) Isothermal

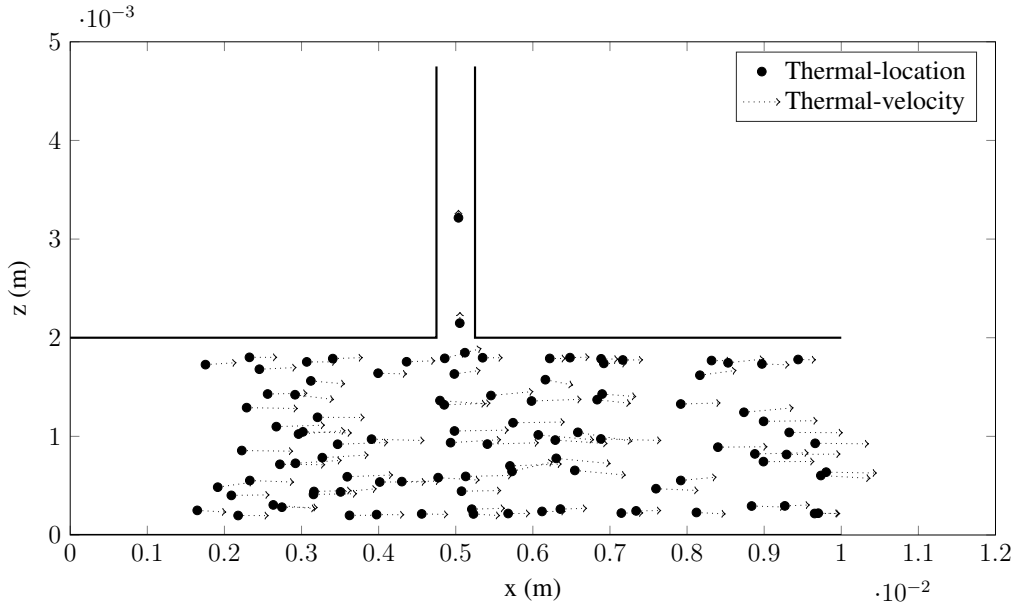

(b) Thermal

Figure 6.16: Comparison of the particle position and velocity vectors after the 100,000 time steps for each temperature case and leak channel width of 1.25D.

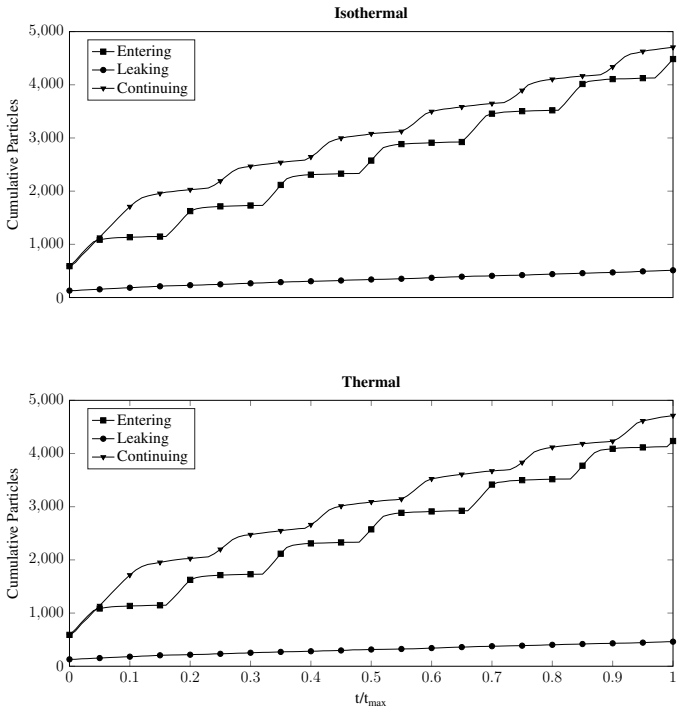

Figure 6.17: Cumulative totals of particles moving through the three characteristic sections of the fracture over the duration of simulations for the narrow leaking fracture with smaller particles.

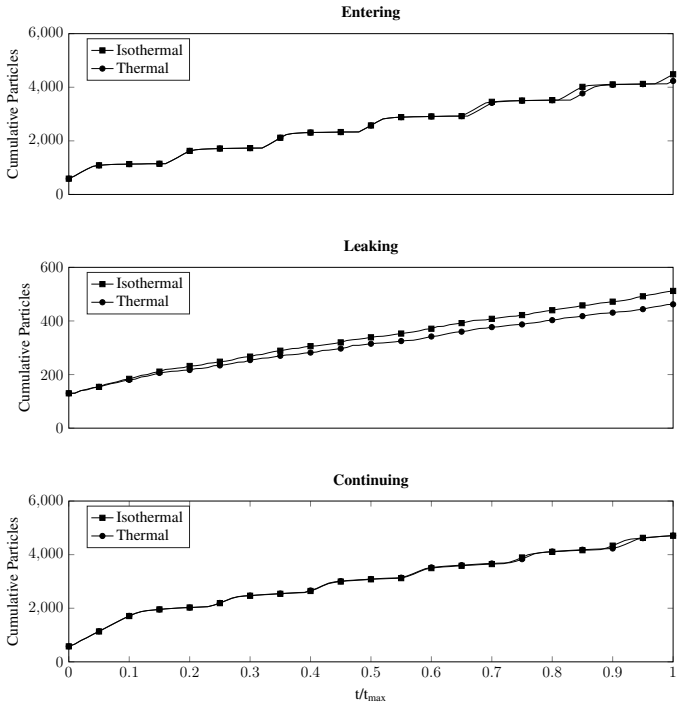

Figure 6.18: Section-based comparison of cumulative totals of particles moving through the narrow leaking fracture with smaller particles. For each temperature case the differing behaviour in each of the characteristic regions can be observed.

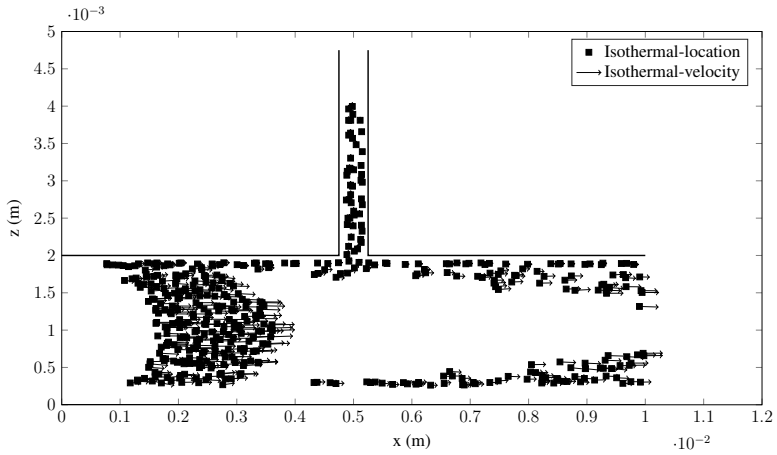

Figure 6.19: Comparison of the particle position and velocity vectors after the 100,000 time steps for each temperature case for the narrow leaking fracture with smaller particles. Only isothermal results are shown here. The dominating Poiseuille profile causes particles to remain trapped on the edges of the domain, this serves to delay further injection of particles.

6.1.3 Proppant transport within a stepped fracture

The final case study presented here examines the flow of proppant with distributed size flowing through the domain outlined in Figure 6.20. Cases of low (26%) and high (46%) initial solid volume fraction of particles with a range of diameters ($D \in [0.2w, 0.4w] = [0.0004m, 0.0008m]$) were examined to investigate the changes in flow produced by this change. The neck of the step direction change was then reduced $1.25D_{max}$ to bring a particular emphasis on identifying when blockages begin to occur in the fracture. A pressure exit condition was used at the outlet of the domain. As for the leaking channel test, three regions can be identified: 'Entering' section is the region prior to the beginning of direction change, 'Step' section is the entire width of the domain where the direction change occurs and the 'Continuing' section is the region beyond the step change. Again, these were run for 100,000 steps. The significant direction change experienced by particles in this domain was observed to lead to increased overlap between particles and walls that was not observed in the previous test cases. To alleviate this overlap, the contact stiffness between both particles and walls was increased by a factor of 10, which still allowed stable contact for DEM interactions to occur.

Changing solid volume fraction

The recorded outputs for flow through the step domain with changing initial SVF are presented in Figures 6.21, 6.22 and 6.23. From Figures 6.21 and 6.22, it can be noted that there is little difference between the isothermal and thermal cases. This is consistent with the settling tests in that the mass

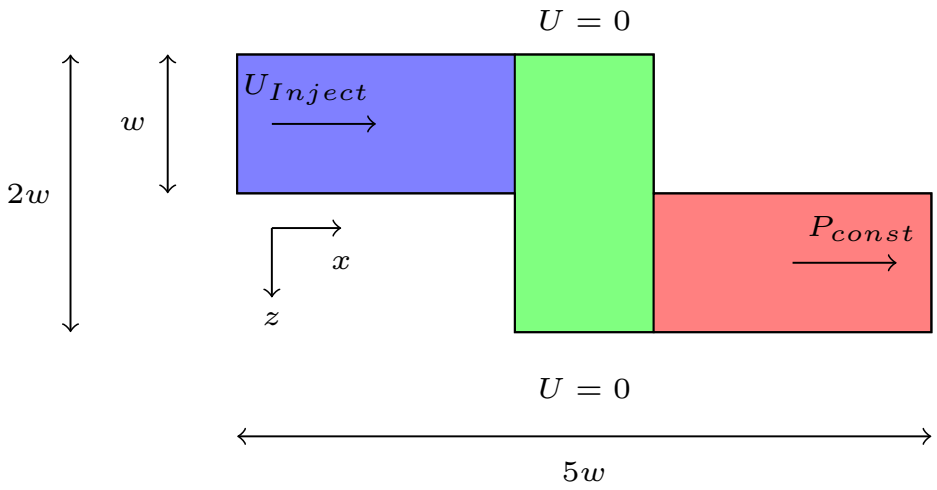

Figure 6.20: Layout for flow through a stepped fracture geometry. The model is initially filled with particles with diameters distributed in the range $D \in [0.2w, 0.4w]$, these are continuously injected with the inlet velocity into the leading w of the domain. The upper and lower boundaries in the y-direction (out-of-page) are periodic and are spaced w apart. The blue, green and red regions represent the 'Entering', 'Step' and 'Continuing' regions respectively for counting particles.

flow rate of particles through the channel was not impacted by the temperature-dependent viscosity. In Figure 6.21, the count of particles in the 'Entering' region is less smooth in its progression than compared to the other two regions. This is a consequence of the injection of particles not happening consistently through the simulation. Instead, the algorithm waits until the injection area is clear of previous particles before a new batch is inserted into the flow. Due to the nature of Poiseuille flow, it was observed that smaller particles would occasionally be caught in an area of low-speed flow near the walls, delaying further injection of particles. The more consistent gradient of the plots in the high SVF case suggests that the greater bulk of particles in this case is better able to overcome any potential blockages or entrainment of particles caused by the change in direction within the domain. This behaviour is made clear in the velocity vector plots in Figure 6.23. In the low SVF case, the transition of particle direction through the direction change is much smoother than seen in the high SVF case. This allows for pockets of the channel (e.g. near (x, y) = (0.006m, 0.000m) and (0.004m, 0.004m)) to be empty of particles as they follow the natural fluid flow path through the domain. In the high SVF case, particles in these regions can be observed to collide with and follow the wall as they move through the 'Step' region. In both cases, a much greater velocity magnitude can be observed in particles moving through the constriction provided by the neck of the step change.

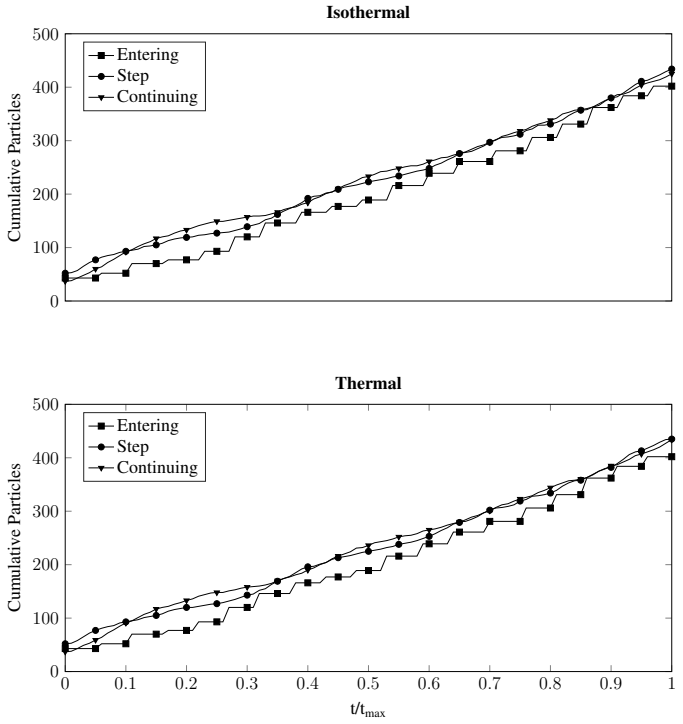

(a) Low SVF (26%)

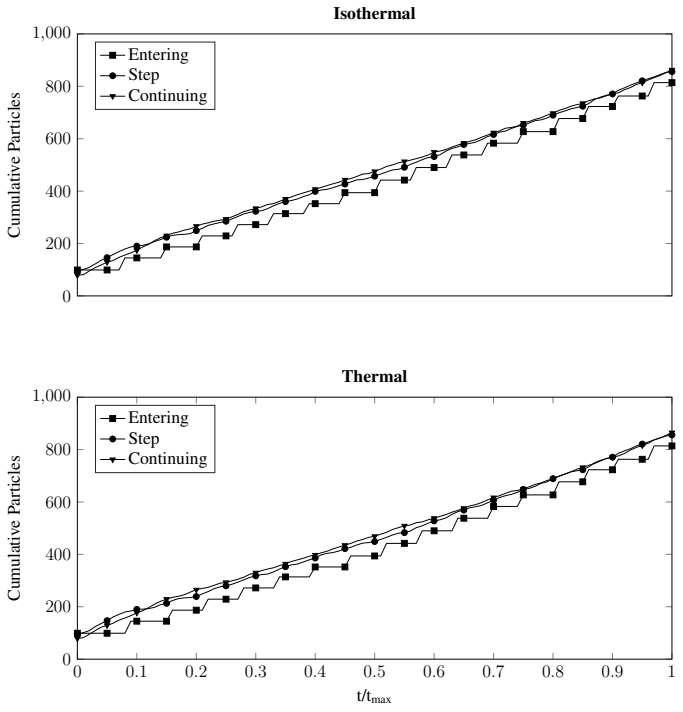

(b) High SVF (46%)

Figure 6.21: Cumulative totals of particles moving through the three characteristic sections of the fracture over the duration of simulations with differing initial SVF in the stepped domain.

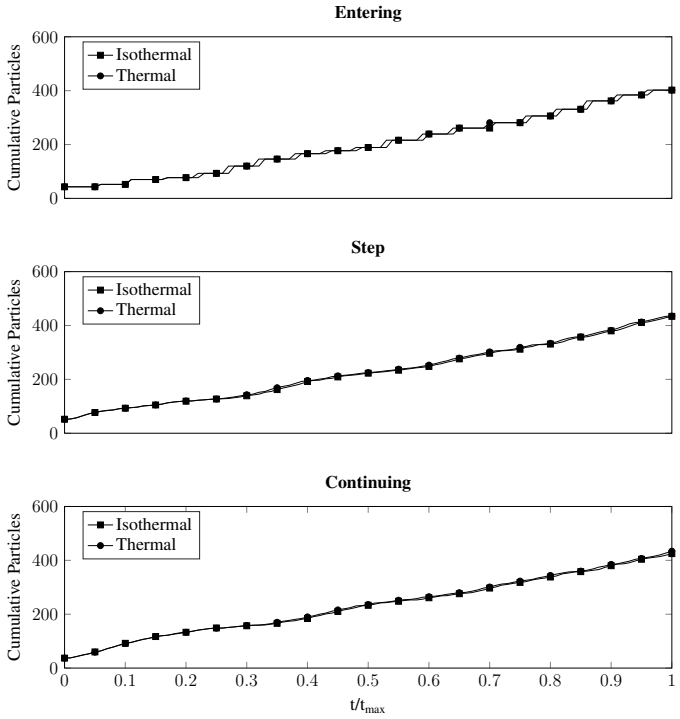

(a) Low SVF (26%)

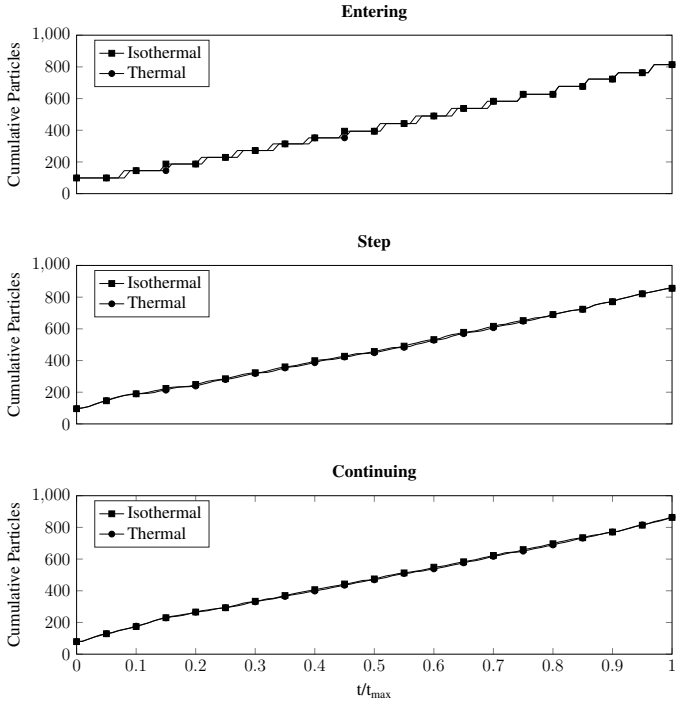

(b) High SVF (46%)

Figure 6.22: Section-based comparison of cumulative totals of particles moving through the fracture with differing initial SVF in the stepped domain. For each SVF case the effect of temperature in each of the characteristic regions can be observed.

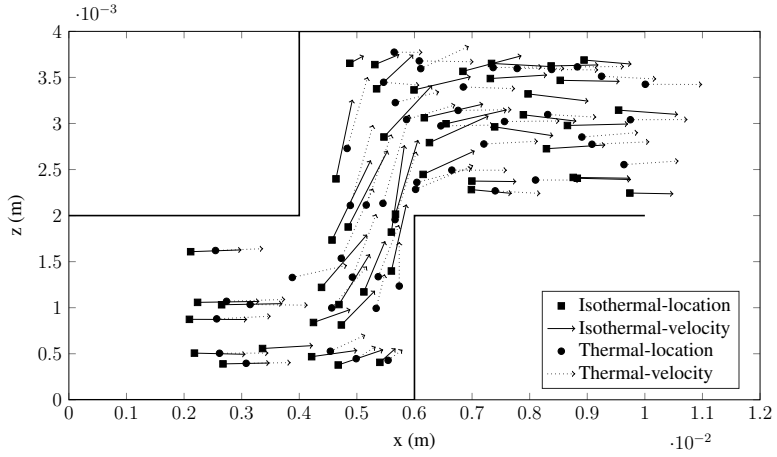

(a) Low SVF (26%)

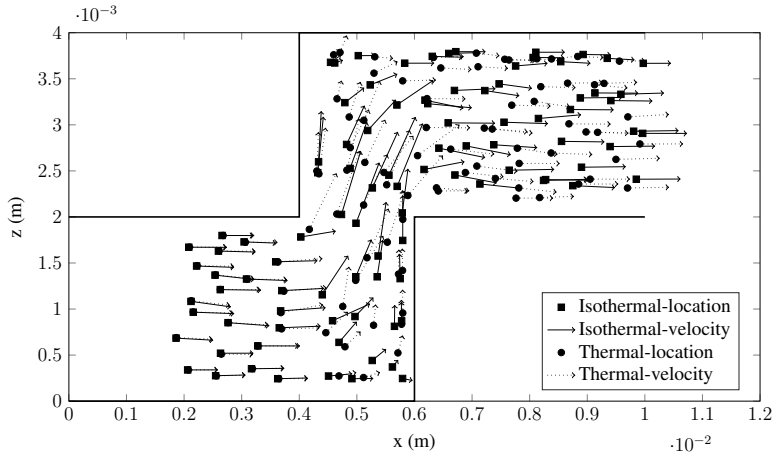

(b) High SVF (46%)

Figure 6.23: Comparison of the particle position and velocity vectors after the 100,000 time steps for each temperature case and each initial SVF in the stepped domain.

Narrowed step change

The previous study was then repeated in a geometry with the neck of the step change narrowed. As in some previous tests, the cumulative particle counts are similar for both temperature models. Figure 6.24 compares the counts observed for the low and high SVF cases whilst Figure 6.25 compares the particle position and velocity vector plots. The initial SVF values remain approximately the same in the modified geometry. In Figure 6.24 the inconsistent gradients of the counts over time indicate the changing pattern of particle motion through the regions. The increase in SVF has served to reduce the variations in the 'Step' and 'Continuing' regions, while delays in particle injection can be noted based on the 'Entering' plot. An explanation for this can be seen in Figure 6.24, and in particular the high SVF case. On the inlet side of the neck, particles move with their initial inlet velocity direction until they reach the end of the inlet channel where they make almost a right-angle turn to travel through the neck. It is only after passing through the neck that particles follow flow along a natural fluid path through the channel. The difference in quantity of particles before and after the neck as well as the associated velocity change can be clearly noted. So while the passage of particles through the neck is slowed a complete blockage does not occur. Further investigation is required to identify the conditions that result in blockage.

The final study conducted halved the size of particles flowing through the stepped domain with a narrow neck in both low and high SVF configurations. Initial SVF values altered to approximately 21% and 51% respectively for the low and high cases. The lattice spacing remained consistent with the previous tests as in the straight and leaking test cases. Again there was minimal difference between the temperature models and only the isothermal results are presented in Figures 6.26 and 6.27. With the introduction of smaller particles, the neck of the channel is relatively wider than that studied previously. What can be noted in Figure 6.26 is the more stepwise nature of the progression of particles through the domain, particularly in the 'Step' and 'Continuing' regions. Similar to the leaking case, the reduction in particle size has seen the Poiseuille profile of the flow dominate particle trajectories. This leads to slowly moving particles remaining adjacent to the walls of the channel, delaying the injection of the next group of particles (see Figure 6.27). When injected the bulk of these move through the domain rapidly leading to the steps in the cumulative counts. The behaviour of small particles being isolated at the edges of the fractures indicates that unexpected distributions of proppant may occur when a variety of particle sizes are being deployed in an operation.

Taken in conjunction with the similar behaviour observed in the straight and leaking fracture tests, this is particularly relevant to the use of graded proppant within the hydraulic fracturing process. This approach utilises particle of multiple sizes to increase the number of fracture pathways that are

being propped and further increase permeability of a reservoir [139, 140, 141]. Further studies of the performance of different proppant sizes could be systematically investigated with this model to better understand the effectiveness of the approach and how proppant is distributed throughout a fracture network.

6.2 Summary

This chapter has presented a number of case studies of proppant flow through characteristic fracture geometries of a straight fracture, a leaking fracture and a stepped fracture. In each case, flows with and without temperature-dependent viscosity have been compared. In the case of settling in a straight fracture, the progression of particles along the length of the fracture remained unchanged in the presence of temperature-dependent viscosity however a significant increase in the settling rate (vertical velocity) was noted with increasing fluid temperature. In practice, this may lead to proppant settling earlier than expected if a treatment was based on too low a fluid temperature. To investigate leaking of particles through a side channel, two cases based on velocity and geometric control were examined. In the velocity cases the variation between the isothermal and thermal results were minimal. However, when temperature effects were introduced to the leaking cases by narrowing the aperture of the leak channel, there was a reduction in particles travelling this pathway. This may indicate that lower viscosity fluids be used to help prevent loss of proppant through side channels that may interfere with an intended fracture pathway. Again in the stepped channel, the progression of particles along the length of the domain did not vary in the presence of temperature-dependent viscosity. This was observed for both low and high SVF simulations with particles of varying size. The behaviour of a partial blockage was observed when the neck of the stepped domain was narrowed. Finally, a selection of tests were repeated with the size of particles halved. In the leaking and stepped geometries, the transport of particles became more strongly dominated by the Poiseuille flow of the channel. This variation in behaviour with particle size may have consequences on the operation of graded proppant hydraulic fracturing treatments using particles of variable size. These models were chosen to provide some examples of how the flow of proppant through a fracture can be influenced by changing viscosity. There remains significant scope for future parametric analyses to further understand how particles travel through a confined geometry such as a fracture under these conditions and how this can be controlled to benefit an operation.

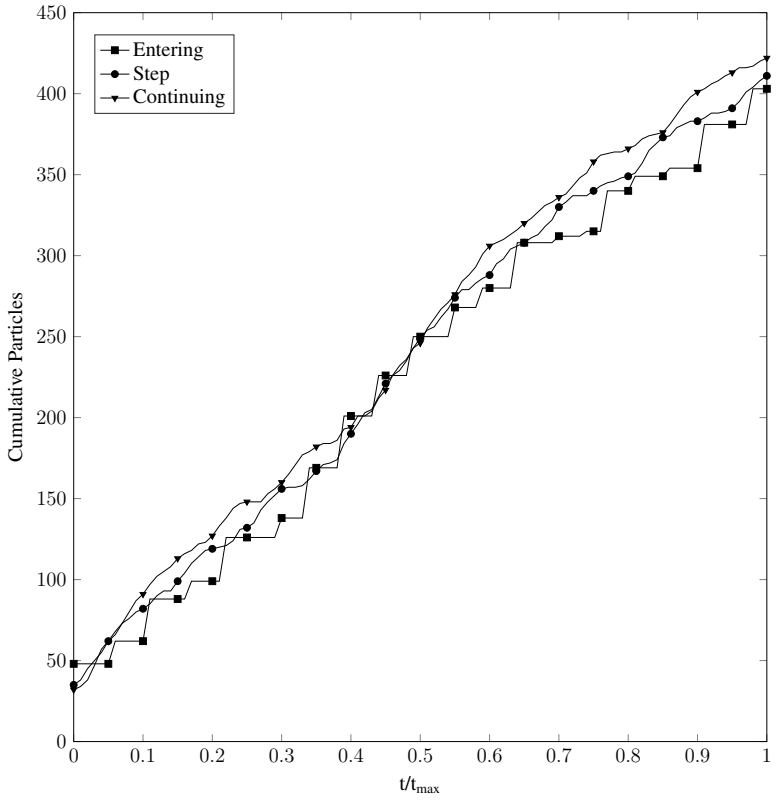

(a) Low SVF (26%)

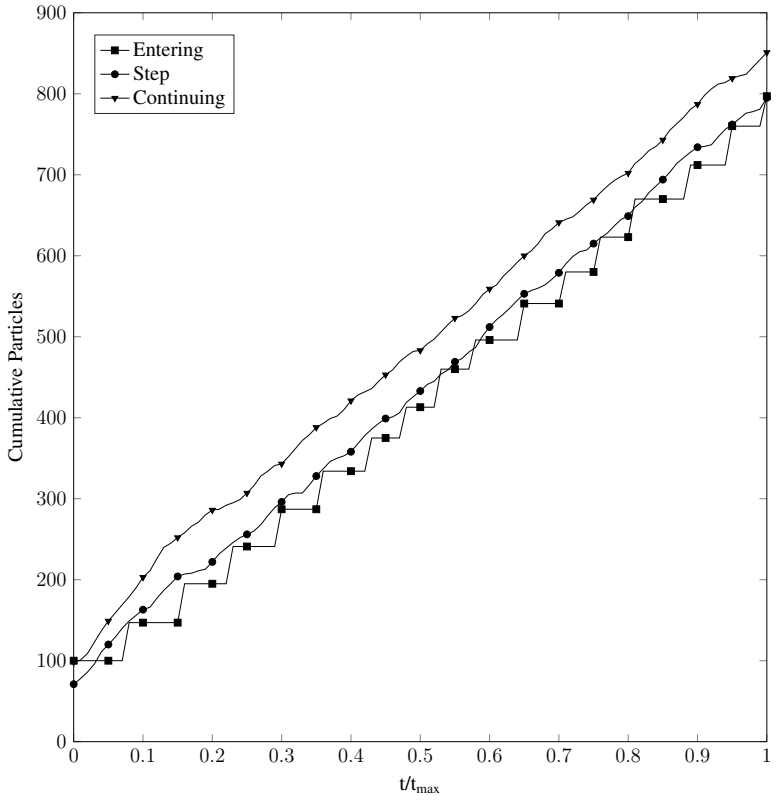

(b) High SVF (46%)

Figure 6.24: Cumulative totals of particles moving through the three characteristic sections of the fracture over the duration of the isothermal simulations with low and high initial SVF for the step domain with a narrow neck.

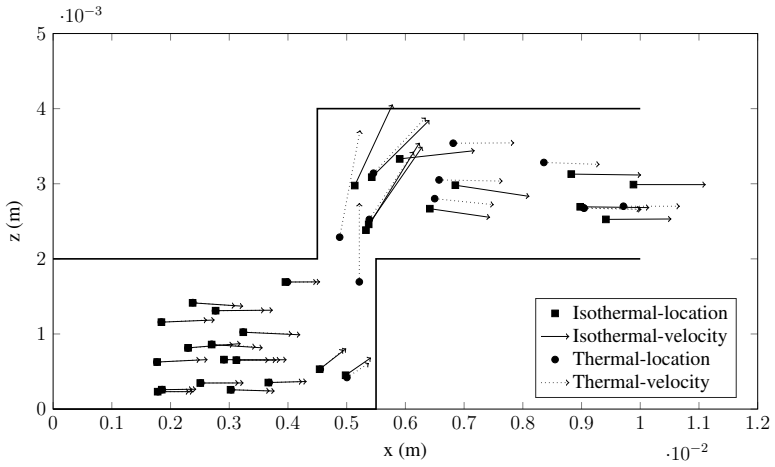

(a) Low SVF (26%)

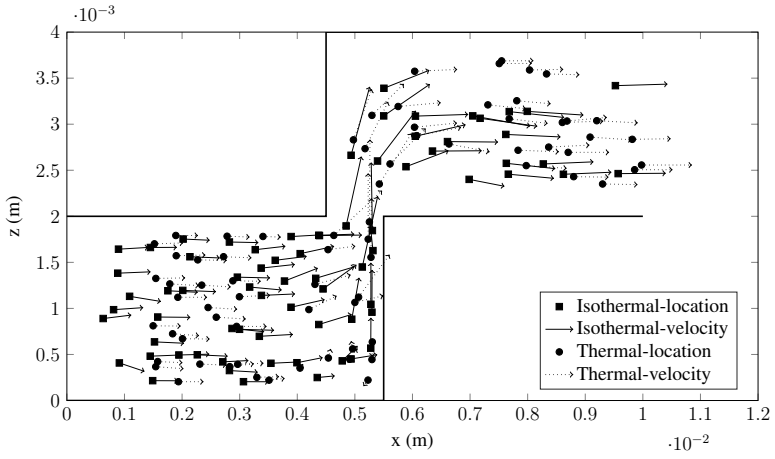

(b) High SVF (46%)

Figure 6.25: Comparison of the particle position and velocity vectors after the 100,000 time steps for each temperature case and each initial SVF in the stepped domain with a narrow neck.

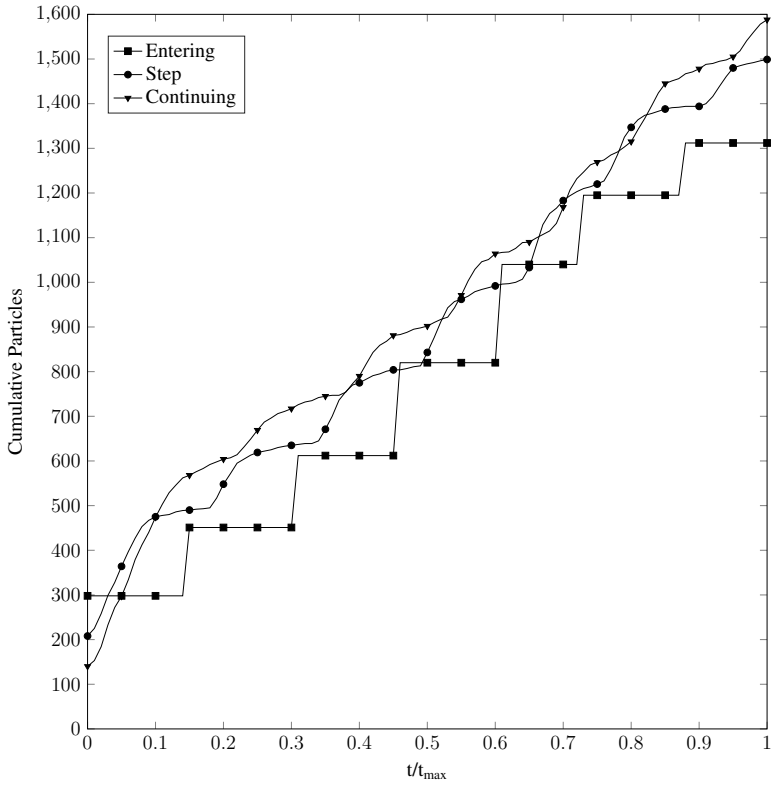

(a) Low SVF (21%)

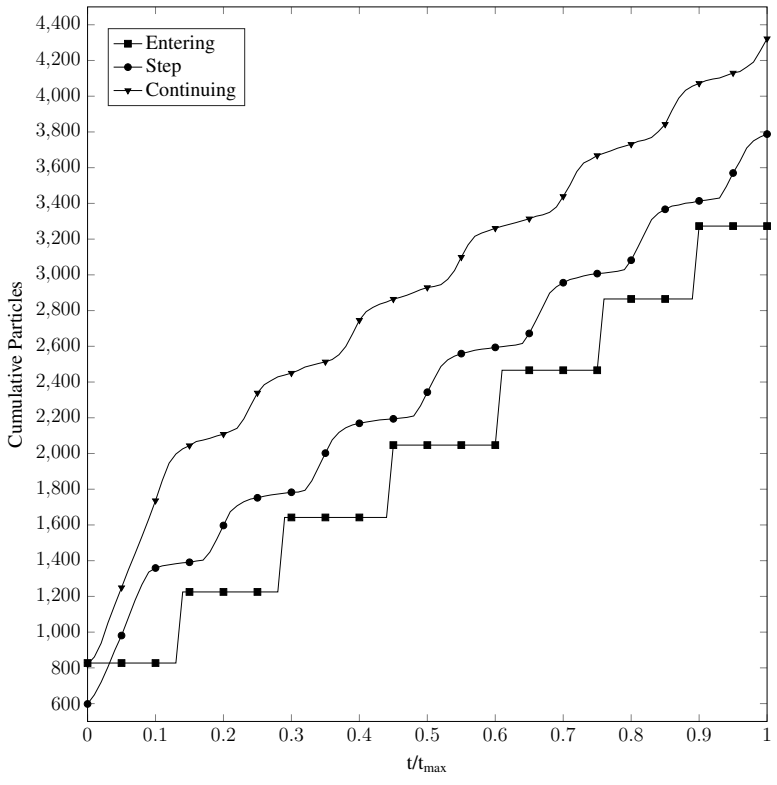

(b) High SVF (51%)

Figure 6.26: Cumulative totals of particles moving through the three characteristic sections of the fracture over the duration of the isothermal simulations with low and high initial SVF for the step domain with a narrow neck and reduced particle size.

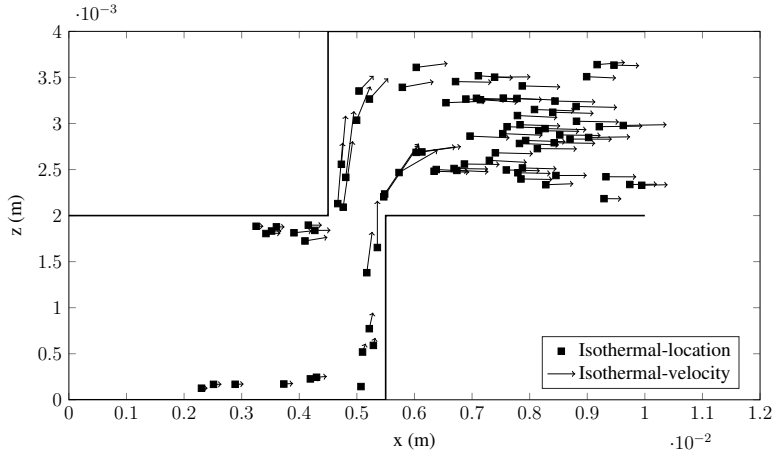

(a) Low SVF (21%)

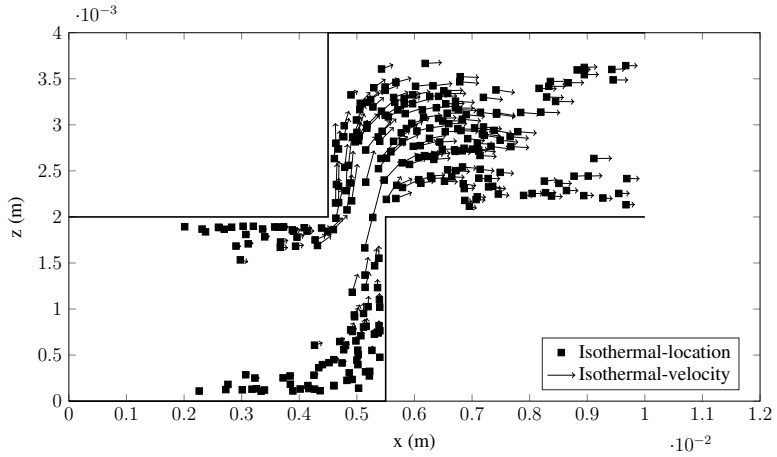

(b) High SVF (51%)

Figure 6.27: Comparison of the particle position and velocity vectors after the 100,000 time steps for the isothermal case and each initial SVF in the stepped domain with reduced particle size.

Chapter 7

Conclusions and avenues for further work

In brief, the major contributions of this thesis can be summarised as:

- Implementation and testing of conjugate heat transfer within coupled LBM-DEM simulations using a coverage-weighted interpretation of material properties.
- Development and evaluation of models studying temperature-dependent viscosity within the LBM and its interaction with conjugate heat transfer within transient suspensions.
- Investigation of confined suspensions flows in the presence of temperature-dependent viscosity with practical applications relevant to proppant transport.

In summary, the work presented in this thesis has sought to further the modelling of particle suspensions under the influence of thermal effects. In particular, approaches utilising thermal lattice Boltzmann methods coupled to the discrete element method were developed and implemented to study problems relating to conjugate heat transfer between components and temperature-dependent viscosity of the fluid. These two sets of behaviour have often been neglected in previous numerical studies of suspension flows. The localised operations of the LBM assists in being able to model the complex interactions of these two thermodynamic phenomena within the inherently transient setting of a particle suspension.

Whilst particle suspensions can be identified within a number of engineering and scientific fields the model that has been developed within this work has been focussed on the setting of hydraulic fracturing within the oil and gas industry. First developed in the years following the end of the second world war, the hydraulic fracturing process is a technique to increase the porosity of oil and gas reservoirs to make resource production a viable prospect. Its use has increased recently due to the decline in production of conventional reservoirs and the development of unconventional reservoirs such as shale gas and coal seam gas. A hydraulic fracturing treatment begins with the initiation

of fractures using small explosive charges at predetermined locations along a wellbore. Initially, fluid is pumped into the well at high pressure to cause growth of the fractures throughout a low porosity reservoir. Following this, proppant particles are added to the fluid being pumped. These are transported along the fractures where they eventually settle along their length. Removal of the fluid component leads to closure of the fractures, however the proppant pack serves to fully prevent this. As the porosity of the pack is greater than that of the surrounding reservoir, preferential pathways for flow of hydrocarbons are generated leading back to the wellbore and, thus, the surface. In a typical treatment, the fluid is water and the proppant sand. Some additives may be introduced to the treatment to prevent corrosion of pipework and obtain desirable fluid properties for proppant transport. The effectiveness of a hydraulic fracturing treatment primarily relies on how well proppant is distributed through a fracture. This is dependent on, among other things, the viscosity of fluid and geometry of the fracture. Enabling better understanding of proppant transport under the influence of complex thermodynamic effects is a motivating factor for the research presented in this thesis.

The implementation of conjugate heat transfer within a thermal lattice Boltzmann model comprises the basis for the first part of this thesis. To be meaningfully applied to use in modelling a particle suspension, transient variation of temperature and moving boundaries need to be considered. In Chapter 3, these were considered for a passive scalar interpretation of the thermal lattice Boltzmann method. Here a local and non-local approach for computing CHT were compared in a number of cases involving straight, curved and moving boundaries and with a parametric comparison of material parameters. In the settings discussed, the local method was better suited to the study of convective flows. The non-local method was more suited to stationary problems. In Chapter 4, a model was presented for CHT within a total energy based formulation of the thermal LBM. This is numerically more complicated than the previous methods due to total energy being the conserved quantity within this framework rather than temperature (as in the passive scalar approach). This implementation was shown to capture the steady and transient CHT behaviours for straight and curved boundaries to an acceptable degree.

A passive scalar interpretation of the thermal LBM is, generally, a technique that is able to resolve a wide range of phenomena relevant to fluid flows. However, as shown in Chapter 4, it is unable to accurately capture the non-linear temperature behaviour generated within the flows of a fluid with temperature-dependent viscosity. To capture this a total energy formulation of the thermal LBM is required, in particular to capture behaviour related to shear heating. This was shown to achieve second order accuracy in achieving this. Capturing temperature-dependent viscosity was further shown to qualitatively and quantitatively contribute to changing transport of individual particles through a fluid. In denser particle suspensions, these variations were still present however the magnitude of effects

were reduced.

The development of this model was extended into a fully three-dimensional version implemented within a coupled framework of the open-source codes TCLB and ESyS-Particle. In Chapter 5, this was utilised to study the behaviour of sheared suspensions at various solid volume fractions. In these cases, it was observed that the presence of particles, both with and without CHT in effect, reduced the velocity variations within a fluid that result from changing viscosity with temperature. The temperature profile was observed to become increasingly non-linear with SVF. This occurred without CHT being present due to the increase of effective viscosity with SVF leading to viscous heating. With CHT present temperature increases were still observed and related to viscous heating or material parameters used for the solid component. It is believed that this work is among some of the first contributions to the study of particle suspensions with both temperature-dependent viscosity and CHT, particularly utilising a coupled LBM-DEM approach.

The final chapter of the thesis focused on case studies relevant to hydraulic fracturing, in particular proppant flow through a fracture. Three cases were examined, namely the settling of particles within a straight fracture, proppant flow in the presence of a side channel, and transport through a stepped fracture profile. In all cases, observed behaviour for the suspending fluid with and without temperature-dependent viscosity was compared and contrasted. In the settling test this was related to deposition of proppant along a fracture. In the latter two cases the focus was on how variations in geometry, flow conditions and particle size distribution could lead to fundamental changes in flow behaviour. Prevention of blockages for example is an imperative for improving proppant placement through a fracture and enhancing the performance of a hydraulic fracturing treatment. This study involved fully resolved 3D particles, a component not often present in similar studies in the literature. In the settling tests, the settling velocity of particles was observed to greatly increase in the presence of a fluid with temperature-dependent viscosity. This was observed to be a magnitude of between two and three depending on the SVF of particles within the fracture. For studies of a leaking fracture, it was observed that under a velocity-controlled flow regime there was little difference between isothermal and thermal flows. However when the leaking channel was physically narrowed, the quantity of particles travelling along the leaking pathway was reduced when thermal effects were introduced. Finally, for a stepped fracture, the progression of particles through the domain was unaffected by the introduction of the thermal model even with a suspension of a variety of particle sizes. When the neck of the stepped domain was narrowed the partial blockage of the flow was identified. In both the leak and step cases, smaller particles were observed to be dominated by the Poiseuille flow within the channel. The led to particles remaining positioned along the edges of the channel well after the bulk progressed through the domain.

7.1 Avenues for further work

During the compilation of this research, a number of potential areas of continuing work have been identified. These relate to both the study of thermally influenced particle suspensions and the development of the model described in this work. These include:

- **Parametric studies of fracture flow**: The case studies presented here aim to provide some examples of how thermal effects can impact proppant transport through a fracture. There still remains significant scope to conduct more detailed parametric studies of flow behaviour through a variety of geometries. Further specific applications within hydraulic fracturing could include the study of graded proppant injection, non-Newtonian carrier fluids, and particle straining in porous media.

- **Further application of the model**: Whilst the model has been applied to problems relating to the context of hydraulic fracturing, its development has been very general. The principles developed here could be adapted to model problems such as industrial processing, water treatment and fluidised bed reactors.

- **Optimisation of TCLB-ESyS coupling**: Whilst functional, the current state of the coupling between the two codes is not optimal in terms of computational performance. Optimising this to improve performance with large numbers of particles would better allow the model to be deployed to study large-scale suspensions.

- **Transiently variable Prandtl number suspensions**: In the 3D model presented in this work, to avoid non-physical shear heating of suspensions with temperature-dependent viscosity, the thermal diffusivity of the solid and fluid components needs to be kept the same. However, when the viscosity is held constant the diffusivity can vary between components and still return accurate results. Further development of the model to allow this behaviour would widen the possible domain of material parameters that can be investigated.

- **Introduction of lubrication forces**: As suspensions become more densely packed with particles, lubrication forces arising from the interactions between both particles and walls can influence how transport occurs. The model presented here does not contain lubrication forces and the introduction of these would allow the model to provide further insight to confined suspension flows.

References

[1] Australian energy update 2016, Tech. rep., Australian Government - Department of Industry, Innovation and Science (2016).
URL https://www.industry.gov.au/Office-of-the-Chief-Economist/Publications/Documents/aes/2016-australian-energy-statistics.pdf

[2] MagentaGreen (Wikimedia Commons), (Non) Conventional Deposits, viewed 8 May 2018 (2014).
URL https://commons.wikimedia.org/wiki/File:(Non)_Conventional_Deposits.svg

[3] Queensland's unconventional petroleum potential, Tech. rep., Queensland Government (2017).
URL https://www.dnrm.qld.gov.au/__data/assets/pdf_file/0018/291330/unconventional-petroleum-potential-2017.pdf

[4] Queensland Government, Petroleum and gas production statistics (June 2017), viewed 10 May 2018 (January 2018).
URL https://data.qld.gov.au/dataset/petroleum-gas-production-and-reserve-statistics/resource/9746212a-e0c6-484d-95ad-b2be1c46027d

[5] Key statistics 2017, Tech. rep., Australian Petroleum Production and Exploration Association (APPEA) (2017).
URL https://www.appea.com.au/wp-content/uploads/2017/05/APPEA_Key-Stats-2017_web_revised.pdf

[6] Queensland Government - Department of Environment and Heritage Protection, Fraccing, viewed 10 May 2018 (2014).
URL https://www.ehp.qld.gov.au/management/non-mining/fraccing.html

[7] Annual energy outlook 2018, Tech. rep., U.S. Energy Information Administration (2018).
URL https://www.eia.gov/outlooks/aeo/pdf/AEO2018.pdf

[8] Review of well operator files for hydraulically fractured oil and gas production wells: Hydraulic fracturing operations, Tech. rep., U.S. Environmental Protection Agency (2016).
URL https://www.epa.gov/sites/production/files/2016-07/documents/wfr2_final_07-28-16_508.pdf

[9] Review of well operator files for hydraulically fractured oil and gas production wells: Well design and construction, Tech. rep., U.S. Environmental Protection Agency (2015).
URL https://www.epa.gov/sites/production/files/2015-05/documents/wfr_1_final_5-8-15_508_km_5-13-15_sb.pdf

[10] U.S. Energy Information Administration, Shale gas and oil plays: Lower 48 states, viewed 23 May 2018 (June 2016).
URL https://www.eia.gov/maps/maps.htm#shaleplay

[11] Hydraulic fracturing ('fraccing') techniques, including reporting requirements and governance arrangements, Tech. rep., Australian Government - Department of Energy (2014).
URL http://www.environment.gov.au/system/files/resources/de709bdd-95a0-4459-a8ce-8ed3cb72d44a/files/background-review-hydraulic-fracturing_0.pdf

[12] Shale gas extraction in the UK: a review of hydraulic fracturing, Tech. rep., The Royal Society (2012).
URL https://royalsociety.org/~/media/policy/projects/shale-gas-extraction/2012-06-28-shale-gas.pdf

[13] M. Economides, K. Nolte (Eds.), Reservoir Stimulation, Wiley, 2000.

[14] R. Jeffrey (Ed.), Effective and Sustainable Hydraulic Fracturing, Intech, 2013.
URL https://www.intechopen.com/books/effective-and-sustainable-hydraulic-fracturing

[15] A. Einstein, Investigations on the Theory of the Brownian Movement, Dover, 1956.
URL http://www.maths.usyd.edu.au/u/UG/SM/MATH3075/r/Einstein_1905.pdf

[16] R. Pal, Rheology of suspensions of solid particles in power-law fluids, The Canadian Journal of Chemical Engineering 93 (1) (2015) 166–173.

[17] K. Ben-Naceur, P. Stephenson, Models of heat transfer in hydraulic fracturing, in: SPE/DOE Low Permeability Gas Reservoirs Symposium, 19-22 March, Denver, Colorado, no. SPE/DOE 13865, Society of Petroleum Engineers, 1985, pp. 163–179.

[18] M. Biot, L. Masse, W. Medlin, Temperature analysis in hydraulic fracturing, Journal of Petroleum Technology (1987) 1389–1397.

[19] R. Clifton, J.-J. Wang, Multiple fluids, proppant transport, and thermal effects in three-dimensional simulation of hydraulic fracturing, in: SPE Annual Technical Conference and Exhibition, 2-5 October, Houston, Texas, no. SPE 18198, Society of Petroleum Engineers, 1988.

[20] K. G. Nolte, Fluid flow considerations in hydraulic fracturing, in: SPE Eastern Regional Meeting, 1-4 November, Charleston, West Virginia, no. SPE 18537, Society of Petroleum Engineers, 1988, pp. 145–156.

[21] R. Barree, M. Conway, Experimental and numerical modeling of convective proppant transport, Journal of Petroleum Technology (1995) 216–222.

[22] C. Blyton, D. Gala, M. Sharma, A comprehensive study of proppant transport in a hydraulic fracture, in: SPE Annual Technical Conference and Exhibition, no. SPE-174973-MS, Society of Petroleum Engineers, 2015.

[23] B. Kong, E. Fathi, S. Ameri, Coupled 3-D numerical simulation of proppant distribution and hydraulic fracturing performance optimization in Marcellus shale reservoirs, International Journal of Coal Geology (147-148) (2015) 35–45.

[24] J. Adachi, E. Siebrits, A. Peirce, J. Desroches, Computer simulation of hydraulic fractures, International Journal of Rock Mechanics and Mining Sciences 44 (5) (2007) 739 – 757.

[25] C. Detournay, J. Lemos, F. Zhang, Development of a proppant transport logic in 3DEC, in: P. Gomez, C. Detournay, R. Hart, M. Nelson (Eds.), Applied Numerical Modeling in Geomechanics 2016, Itasca, 2016, pp. 573–585.
URL https://www.itascacg.com/training-events/symposium/4th-itasca-symposium-on-applied-numerical-modeling

[26] B. Kong, S. Chen, K. Zhang, M. E. G. Perdomo, Proppant transport simulation in hydraulic fractures and fracture productivity optimization, in: SPE Asia Pacific Uncoventional Resources Conference and Exhibition, no. SPE-176873-MS, Society of Petroleum Engineers, 2015.

[27] T. Olsen, M. Debonis, Real-time optimization of fracturing fluid viscosity changing fracture conditions, in: SPE Rocky Mountain Regional Meeting, 11-13 May, Casper, Wyoming, no. SPE 17540, Society of Petroleum Engineers, 1988, pp. 533–540.

[28] I. Tomac, M. Gutierrez, Numerical study of horizontal proppant flow and transport in a narrow hydraulic fracture, in: 47th US Rock Mechanics/Geomechanics Symposium, no. ARMA 13-342, American Rock Mechanics Association, 2013.

[29] B. Meyer, Heat transfer in hydraulic fracturing, SPE Production Engineering 4:4 (1989) 423–429.

[30] A. M. Linkov, On comparison of thinning fluids used for hydraulic fracturing, International Journal of Engineering Science 77 (2014) 14 – 23.

[31] D. Eskin, M. J. Miller, A model of non-Newtonian slurry flow in a fracture, Powder Technology 182 (2) (2008) 313 – 322.

[32] D. Eskin, Modeling non-Newtonian slurry flow in a flat channel with permeable walls, Chemical Engineering Science 123 (0) (2015) 116 – 124.

[33] X. Chen, Y. C. Lam, Z. Wang, Non-isothermal analysis of concentrated suspension slip flow with particle migration, Composites Science and Technology 68 (2) (2008) 398 – 409.

[34] J. Richardson, R. Chhabra, Non-Newtonian Flow and Applied Rheology - Engineering Applications, Elsevier, 2008.

[35] J. J. Wylie, D. L. Koch, A. J. C. Ladd, Rheology of suspensions with high particle inertia and moderate fluid inertia, Journal of Fluid Mechanics 480 (2003) 95–118.

[36] J. J. Stickel, R. L. Powell, Fluid mechanics and rheology of dense suspensions, Annual Review of Fluid Mechanics 37 (1) (2005) 129–149.

[37] A. Ladd, R. Verberg, Lattice-Boltzmann simulations of particle-fluid suspensions, Journal of Statistical Physics 104 (5-6) (2001) 1191–1251.

[38] A. Mohamad, Lattice Boltzmann Method: Fundamentals and Engineering Applications with Computer Codes, Springer London, 2011.

[39] S. Chen, G. D. Doolen, Latttice Boltzmann method for fluid flows, Annual Review of Fluid Mechanics 30 (1) (1998) 329–364.

[40] G. R. McNamara, G. Zanetti, Use of the Boltzmann equation to simulate lattice-gas automata, Physical Review Letters 61 (1988) 2332–2335.

[41] F. J. Higuera, J. Jimenez, Boltzmann approach to lattice gas simulations, Europhysics Letters 9 (7) (1989) 663–668.

[42] C. K. Aidun, J. R. Clausen, Lattice-Boltzmann method for complex flows, Annual Review of Fluid Mechanics 42 (1) (2010) 439–472.

[43] A. Prosperetti, G. Tryggvason (Eds.), Computational Methods for Multiphase Flow, Cambridge University Press, 2007.

[44] R. G. M. van der Sman, Simulations of confined suspension flow at multiple length scales, Soft Matter 5 (2009) 4376–4387.

[45] K. Han, Y. T. Feng, D. R. J. Owen, Three-dimensional modelling and simulation of magnetorheological fluids, International Journal for Numerical Methods in Engineering 84 (11) (2010) 1273–1302.

[46] C. Leonardi, J. McCullough, B. Jones, J. Williams, Electromagnetic excitation of particle suspensions in hydraulic fractures using a coupled lattice Boltzmann-discrete element model, Computational Particle Mechanics 3 (2) (2015) 125–140.

[47] Z.Guo, C.Shu, Lattice Boltzmann Method and Its Applications in Engineering, World Scientific Publishing, 2013.

[48] S. Arcidiacono, J. Mantzaras, I. V. Karlin, Lattice Boltzmann simulation of catalytic reactions, Physical Review E 78 (2008) 046711.

[49] G. Li, M. Aktas, Y. Bayazitoglu, A review on the discrete Boltzmann model for nanofluid heat transfer in enclosures and channels, Numerical Heat Transfer, Part B: Fundamentals 67 (6) (2015) 463–488.

[50] D. R. J. Owen, C. R. Leonardi, Y. T. Feng, An efficient framework for fluid-structure interaction using the lattice Boltzmann method and immersed moving boundaries, International Journal for Numerical Methods in Engineering 87 (1-5) (2011) 66–95.

[51] P. L. Bhatnagar, E. P. Gross, M. Krook, A model for collision processes in gases. I. Small amplitude processes in charged and neutral one-component systems, Physical Review 94 (1954) 511–525.

[52] Y. H. Qian, D. D'Humieres, P. Lallemand, Lattice BGK models for Navier-Stokes equation, Europhysics Letters 17 (6) (1992) 479.

[53] H. Chen, S. Chen, W. H. Matthaeus, Recovery of the Navier-Stokes equations using a lattice-gas Boltzmann method, Physical Review A 45 (1992) R5339–R5342.

[54] D. d'Humieres, Generalized lattice Boltzmann equations, in: B. Shizgal, D. Weaver (Eds.), Rarefied gas dynamics: theory and simulations, Vol. 159 of Progress in Astronautics and Aeronautics, AIAA, 1992, pp. 450–458.

[55] D. d'Humieres, I. Ginzburg, M. Krafczyk, P. Lallemand, L. Luo, Multiple-relaxation-time lattice Boltzmann models in three dimensions, Philosophical Transactions of the Royal Society of London A: Mathematical, Physical and Engineering Sciences 360 (1792) (2002) 437–451.

[56] X. He, L. Luo, Theory of the lattice Boltzmann method: From the Boltzmann equation to the lattice Boltzmann equation, Physical Review E 56 (6) (1997) 6811–6817.

[57] T. Kruger, H. Kusumaatmaja, A. Kuzmin, O. Shardt, G. Silva, E. Viggen, The Lattice Boltzmann Method: Principles and Practice, Springer, 2017.

[58] I. V. Karlin, A. Ferrante, H. C. Ottinger, Perfect entropy functions of the lattice Boltzmann method, Europhysics Letters 47 (2) (1999) 182–188.

[59] J. Kang, N. I. Prasianakis, J. Mantzaras, Lattice Boltzmann model for thermal binary-mixture gas flows, Physical Review E 87 (2013) 053304.

[60] S. Chikatamarla, I. Karlin, Enropic lattice Boltzmann method for turbulent flow simulations: Boundary conditions, Physica A: Statistical Mechanics and its Applications 392 (2013) 1925–1930.

[61] S. Ansumali, I. Karlin, Entropy function approach to the lattice Boltzmann method, Journal of Statistical Physics 107 (1-2) (2002) 291–308.

[62] M. Geier, A. Greiner, J. G. Korvink, Properties of the cascaded lattice Boltzmann automaton, International Journal of Modern Physics C 18 (04) (2007) 455–462.

[63] M. Geier, M. Schonherr, A. Pasquali, M. Krafczyk, The cumulant lattice Boltzmann equation in three dimensions: Theory and validation, Computers & Mathematics with Applications 70 (4) (2015) 507 – 547.

[64] P. Lallemand, L.-S. Luo, Lattice Boltzmann method for moving boundaries, Journal of Computational Physics 184 (2) (2003) 406 – 421.

[65] A. J. C. Ladd, Numerical simulations of particulate suspensions via a discretized Boltzmann equation. Part 1. Theoretical foundation, Journal of Fluid Mechanics 271 (1994) 285–309.

[66] A. J. C. Ladd, Numerical simulations of particulate suspensions via a discretized Boltzmann equation. Part 2. Numerical results, Journal of Fluid Mechanics 271 (1994) 311–339.

[67] S. D. Walsh, H. Burwinkle, M. O. Saar, A new partial-bounceback lattice-Boltzmann method for fluid flow through heterogeneous media, Computers & Geosciences 35 (6) (2009) 1186 – 1193.

[68] E. Michaelides, Heat and Mass Transfer in Particulate Suspensions, Springer New York, 2013.

[69] Q. Zou, X. He, On pressure and velocity boundary conditions for the lattice Boltzmann BGK model, Physics of Fluids 9 (6) (1997) 1591–1598.

[70] J. Latt, B. Chopard, O. Malaspinas, M. Deville, A. Michler, Straight velocity boundaries in the lattice Boltzmann method, Physical Review E 77 (2008) 056703.

[71] G. McNamara, B. Alder, Analysis of the lattice Boltzmann treatment of hydrodynamics, Physica A: Statistical Mechanics and its Applications 194 (14) (1993) 218 – 228.

[72] G. McNamara, A. Garcia, B. Alder, Stabilization of thermal lattice Boltzmann models, Journal of Statistical Physics 81 (1-2) (1995) 395–408.

[73] G. McNamara, A. Garcia, B. Alder, A hydrodynamically correct thermal lattice Boltzmann model, Journal of Statistical Physics 87 (5-6) (1997) 1111–1121.

[74] P. Lallemand, L.-S. Luo, Hybrid finite-difference thermal lattice Boltzmann equation, International Journal of Modern Physics B 17 (1-2) (2003) 41–47.

[75] O. Malaspinas, B. Chopard, J. Latt, General regularized boundary condition for multi-speed lattice Boltzmann models, Computers & Fluids 49 (1) (2011) 29–35.

[76] J. Meng, Y. Zhang, Diffuse reflection boundary condition for high-order lattice Boltzmann models with streaming-collision mechanism, Journal of Computational Physics 258 (0) (2014) 601 – 612.

[77] N. Frapolli, S. S. Chikatamarla, I. V. Karlin, Multispeed entropic lattice Boltzmann model for thermal flows, Physical Review E 90 (2014) 043306.

[78] X. He, S. Chen, G. D. Doolen, A novel thermal model for the lattice Boltzmann method in incompressible limit, Journal of Computational Physics 146 (1) (1998) 282 – 300.

[79] I. V. Karlin, D. Sichau, S. S. Chikatamarla, Consistent two-population lattice Boltzmann model for thermal flows, Physical Review E 88 (2013) 063310.

[80] Z. Guo, C. Zheng, B. Shi, T. S. Zhao, Thermal lattice Boltzmann equation for low Mach number flows: Decoupling model, Physical Review E 75 (2007) 036704.

[81] R. H. Khiabani, Y. Joshi, C. K. Aidun, Heat transfer in microchannels with suspended solid particles: Lattice-Boltzmann based computations, Journal of Heat Transfer 132 (4) (2010) 041003–041003.

[82] B. Metzger, O. Rahli, X. Yin, Heat transfer across sheared suspensions: role of the shear-induced diffusion, Journal of Fluid Mechanics 724 (2013) 527–552.

[83] K. Guo, L. Li, G. Xiao, N. AuYeung, R. Mei, Lattice Boltzmann method for conjugate heat and mass transfer with interfacial jump conditions, International Journal of Heat and Mass Transfer 88 (0) (2015) 306 – 322.

[84] J. Huang, Z. Hu, W.-A. Yong, Second-order curved boundary treatments of the lattice Boltzmann method for convection-diffusion equations, Journal of Computational Physics 310 (2016) 26 – 44.

[85] A. E. F. Monfared, A. Sarrafi, S. Jafari, M. Schaffie, Linear and non-linear Robin boundary conditions for thermal lattice Boltzmann method: Cases of convective and radiative heat transfer at interfaces, International Journal of Heat and Mass Transfer 95 (2016) 927 – 935.

[86] P. Cundall, O. Strack, A discrete numerical model for granular assemblies, Geotechnique 29 (1) (1979) 47–65.

[87] J. Williams, R. O'Connor, Discrete element simulation and the contact problem, Archives of Computational Methods in Engineering 6 (4) (1999) 279–304.

[88] B. K. Cook, D. R. Noble, J. R. Williams, A direct simulation method for particle-fluid systems, Engineering Computations 21 (2/3/4) (2004) 151–168.

[89] L. Jahanshaloo, N. A. C. Sidik, S. Salimi, A. Safdari, The use of thermal lattice Boltzmann numerical scheme for particle-laden channel flow with a cavity, Numerical Heat Transfer, Part A: Applications 66 (4) (2014) 433–448.

[90] F. White, Fluid Mechanics, 7th Edition, McGraw-Hill, 2011.

[91] D. R. Noble, J. R. Torczynski, A lattice-Boltzmann method for partially saturated computational cells, International Journal of Modern Physics C 9 (8) (1998) 1189–1201.

[92] N.-Q. Nguyen, A. J. C. Ladd, Lubrication corrections for lattice-Boltzmann simulations of particle suspensions, Physical Review E 66 (2002) 046708.

[93] I. Ginzburg, D. d'Humieres, Multireflection boundary conditions for lattice Boltzmann models, Physical Review E 68 (2003) 066614.

[94] B. Chun, A. J. C. Ladd, Interpolated boundary condition for lattice Boltzmann simulations of flows in narrow gaps, Physical Review E 75 (2007) 066705.

[95] R. Verberg, A. J. C. Ladd, Lattice-Boltzmann model with sub-grid-scale boundary conditions, Physical Review Letters 84 (2000) 2148–2151.

[96] C. K. Aidun, Y. Lu, E.-J. Ding, Direct analysis of particulate suspensions with inertia using the discrete Boltzmann equation, Journal of Fluid Mechanics 373 (1998) 287–311.

[97] Z. Hashemi, O. Abouali, R. Kamali, Three dimensional thermal lattice Boltzmann simulation of heating/cooling spheres falling in a Newtonian liquid, International Journal of Thermal Sciences 82 (0) (2014) 23 – 33.

[98] Z. Hashemi, O. Abouali, R. Kamali, Thermal three-dimensional lattice Boltzmann simulations of suspended solid particles in microchannels, International Journal of Heat and Mass Transfer 65 (0) (2013) 235 – 243.

[99] Y. Feng, K. Han, D. Owen, Advances in computational modelling of multi-physics in particle-fluid systems, in: E. Onate, R. Owen (Eds.), Particle-Based Methods, Vol. 25 of Computational Methods in Applied Sciences, Springer Netherlands, 2011, pp. 51–88.
URL http://dx.doi.org/10.1007/978-94-007-0735-1_2

[100] X. Chen, P. Han, A note on the solution of conjugate heat transfer problems using SIMPLE-like algorithms, International Journal of Heat and Fluid Flow 21 (4) (2000) 463 – 467.

[101] J. Wang, M. Wang, Z. Li, A lattice Boltzmann algorithm for fluid-solid conjugate heat transfer, International Journal of Thermal Sciences 46 (3) (2007) 228 – 234.

[102] M. Wang, J. He, J. Yu, N. Pan, Lattice Boltzmann modeling of the effective thermal conductivity for fibrous materials, International Journal of Thermal Sciences 46 (9) (2007) 848 – 855.

[103] M. Seddiq, M. Maerefat, M. Mirzaei, Modeling of heat transfer at the fluid-solid interface by lattice Boltzmann method, International Journal of Thermal Sciences 75 (2014) 28 – 35.

[104] A. A. Mohamad, Q. W. Tao, Y. L. He, S. Bawazeer, Treatment of transport at the interface between multilayers via the lattice Boltzmann method, Numerical Heat Transfer, Part B: Fundamentals 67 (2) (2015) 124–134.

[105] H. Karani, C. Huber, Lattice Boltzmann formulation for conjugate heat transfer in heterogeneous media, Physical Review E 91 (2015) 023304.

[106] Y. Hu, D. Li, S. Shu, X. Niu, Full Eulerian lattice Boltzmann model for conjugate heat transfer, Physical Review E 92 (2015) 063305.

[107] G. Pareschi, N. Frapolli, S. S. Chikatamarla, I. V. Karlin, Conjugate heat transfer with the entropic lattice Boltzmann method, Physical Review E 94 (2016) 013305.

[108] L. Li, C. Chen, R. Mei, J. F. Klausner, Conjugate heat and mass transfer in the lattice Boltzmann equation method, Physical Review E 89 (2014) 043308.

[109] Y. Sun, I. S. Wichman, On transient heat conduction in a one-dimensional composite slab, International Journal of Heat and Mass Transfer 47 (67) (2004) 1555 – 1559.

[110] P. K. Jain, S. Singh, Rizwan-uddin, Analytical solution to transient asymmetric heat conduction in a multilayer annulus, Journal of Heat Transfer 131 (1) (2008) 011304–011304.

[111] A. Caiazzo, Analysis of lattice Boltzmann initialization routines, Journal of Statistical Physics 121 (1) (2005) 37–48.

[112] R. Mei, L.-S. Luo, P. Lallemand, D. d'Humieres, Consistent initial conditions for lattice Boltzmann simulations, Computers & Fluids 35 (89) (2006) 855 – 862, Proceedings of the First International Conference for Mesoscopic Methods in Engineering and Science.

[113] F. Zhao, Optimal relaxation collisions for lattice Boltzmann methods, Computers & Mathematics with Applications 65 (2) (2013) 172 – 185, Special issue on Mesoscopic Methods in Engineering and Science (ICMMES-2010, Edmonton, Canada).

[114] P. Lallemand, L.-S. Luo, Theory of the lattice Boltzmann method: Dispersion, dissipation, isotropy, Galilean invariance, and stability, Physical Review E 61 (2000) 6546–6562.

[115] L. Wang, Z. Guo, B. Shi, C. Zheng, Evaluation of three lattice Boltzmann models for particulate flows, Communications in Computational Physics 13 (4) (2013) 1151–1172.

[116] Z. Yu, X. Shao, A. Wachs, A fictitious domain method for particulate flows with heat transfer, Journal of Computational Physics 217 (2) (2006) 424 – 452.

[117] G. Batchelor, The stress system in a suspension of force-free particles, Journal of Fluid Mechanics 41 (3) (1970) 545–570.

[118] W. T. Perrins, D. R. McKenzie, R. C. McPhedran, Transport properties of regular arrays of cylinders, Proceedings of the Royal Society of London A: Mathematical, Physical and Engineering Sciences 369 (1737) (1979) 207–225.

[119] A. Vikhansky, Construction of lattice-Boltzmann schemes for non-Newtonian and two-phase flows, The Canadian Journal of Chemical Engineering 90 (5) (2012) 1081–1091.

[120] C. Leonardi, D. Owen, Y. Feng, Numerical rheometry of bulk materials using a power law fluid and the lattice Boltzmann method, Journal of Non-Newtonian Fluid Mechanics 166 (12) (2011) 628 – 638.

[121] S. Gabbanelli, G. Drazer, J. Koplik, Lattice Boltzmann method for non-newtonian (power-law) fluids, Physical Review E 72 (2005) 046312.

[122] Z. Guo, T. Zhao, Lattice Boltzmann simulation of natural convection with temperature-dependent viscosity in a porous cavity, Progress in Computational Fluid Dynamics 5 (1/2).

[123] X.-R. Zhang, Y. Cao, A lattice Boltzmann model for natural convection with a large temperature difference, Progress in Computational Fluid Dynamics, an International Journal 11 (5) (2011) 269–278.

[124] Y. Cao, Variable property-based lattice Boltzmann flux solver for thermal flows in the low Mach number limit, International Journal of Heat and Mass Transfer 103 (2016) 254 – 264.

[125] T. Myers, J. Charpin, M. Tshehla, The flow of a variable viscosity fluid between parallel plates with shear heating, Applied Mathematical Modelling 30 (9) (2006) 799 – 815.

[126] B. D. Jones, J. R. Williams, Fast computation of accurate sphere-cube intersection volume, Engineering Computations 34 (4) (2017) 1204–1216.

[127] D. Wang, C. R. Leonardi, S. M. Aminossadati, Improved coupling of time integration and hydrodynamic interaction in particle suspensions using the lattice Boltzmann and discrete element methods, Computers & Mathematics with Applications 75 (7) (2018) 2593 – 2606.

[128] O. E. Strack, B. K. Cook, Three-dimensional immersed boundary conditions for moving solids in the lattice-Boltzmann method, International Journal for Numerical Methods in Fluids 55 (2) (2007) 103–125.

[129] J. F. Morris, F. Boulay, Curvilinear flows of noncolloidal suspensions: The role of normal stresses, Journal of Rheology 43 (5) (1999) 1213–1237.

[130] J. R. Clausen, D. A. Reasor, C. K. Aidun, The rheology and microstructure of concentrated non-colloidal suspensions of deformable capsules, Journal of Fluid Mechanics 685 (2011) 202–234.

[131] I. E. Zarraga, D. A. Hill, D. T. Leighton, The characterization of the total stress of concentrated suspensions of noncolloidal spheres in Newtonian fluids, Journal of Rheology 44 (2) (2000) 185–220.

[132] B. Lecampion, D. I. Garagash, Confined flow of suspensions modelled by a frictional rheology, Journal of Fluid Mechanics 759 (2014) 197235.

[133] Y. Thorimbert, F. Marson, A. Parmigiani, B. Chopard, J. Latt, Lattice Boltzmann simulation of dense rigid spherical particle suspensions using immersed boundary method, Computers & Fluids 166 (2018) 286 – 294.

[134] B. Konijn, O. Sanderink, N. Kruyt, Experimental study of the viscosity of suspensions: Effect of solid fraction, particle size and suspending liquid, Powder Technology 266 (2014) 61 – 69.

[135] G. Zhang, M. Gutierrez, M. Li, A coupled CFD-DEM approach to model particle-fluid mixture transport between two parallel plates to improve understanding of proppant micromechanics in hydraulic fractures, Powder Technology 308 (2017) 235 – 248.

[136] M. Baldini, C. M. Carlevaro, L. A. Pugnaloni, M. Sanchez, Numerical simulation of proppant transport in a planar fracture. A study of perforation placement and injection strategy, International Journal of Multiphase Flow (2018) In Press, https://doi.org/10.1016/j.ijmultiphaseflow.2018.08.005.

[137] C. Blyton, Proppant transport in complex fracture networks, Ph.D. thesis, The University of Texas at Austin (2016).

[138] J. Han, P. Yuan, X. Huang, H. Zhang, A. Sookprasong, C. Li, Y. Dai, Numerical study of proppant transport in complex fracture geometries, in: SPE Low Perm Symposium, no. SPE-180243-MS, Society of Petroleum Engineers, 2016.

[139] A. Khanna, A. Keshavarz, K. Mobbs, M. Davis, P. Bedrikovetsky, Stimulation of the natural fracture system by graded proppant injection, Journal of Petroleum Science and Engineering 111 (2013) 71 – 77.

[140] A. Keshavarz, Y. Yang, A. Badalyan, R. Johnson, P. Bedrikovetsky, Laboratory-based mathematical modelling of graded proppant injection in CBM reservoirs, International Journal of Coal Geology 136 (2014) 1 – 16.

[141] A. Keshavarz, A. Badalyan, R. Johnson, P. Bedrikovetsky, Productivity enhancement by stimulation of natural fractures around a hydraulic fracture using micro-sized proppant placement, Journal of Natural Gas Science and Engineering 33 (2016) 1010 – 1024.